Development of a Biophysically Detailed Mathematical Model of a Mouse Atrial Cell for the Study of Cellular Proarrhythmic Mechanisms

A thesis submitted to The University of Manchester

for the degree of Doctor of Philosophy

in the Faculty of Engineering and Physical Sciences

2015

Weijian Shen

School of Physics and Astronomy

Contents

List of Tables

List of Figures

Abstract

University of Manchester

Weijian Shen

Degree Programme: Doctor of Philosophy

Thesis Title: Development of a Biophysically Detailed Mathematical Model of a Mouse Atrial Cell for the Study of Cellular Proarrhythmic Mechanisms

School of Physics and Astronomy

Atrial fibrillation (AF), the most common sustained arrhythmia, is associated with abnormal intracellular Ca^{2+} handling. Understanding AF requires comprehensive understanding of ionic currents, Ca^{2+} handling, phosphorylation regulation and related signalling pathways, but appropriate models are limited. The aim of this thesis is to develop an ionic model of the mouse atrial myocyte to investigate the cellular proarrhythmic mechanisms.

We have developed the first mouse atrial myocyte model that incorporates mathematically detailed ion channels, cellular Ca^{2+} and Na^{+} handling and their regulation by Ca^{2+}-calmodulin-dependent protein kinase II (CaMKII) and protein kinase A. For the first time, the inositol 1,4,5-trisphosphate (IP_3) production system and its effects on excitation-contraction coupling have also been described. The validated model predicted that: 1) hyperactivity of CaMKII and elevated intracellular Na^{+} concentration are the crucial factors that induce sarcoplasmic reticulum (SR) Ca^{2+} spontaneous release and delayed afterdepolarisations; 2) β-adrenergic stimulation may have proarrhythmic effects by exacerbating Ca^{2+} overload; and 3) enhanced activity in ryanodine receptors during IP_3-induced Ca^{2+} release is the major cause of the arrhythmogenesis in IP_3 signalling.

Declaration

I, the undersigned, declare that no portion of the work referred to in the thesis has been submitted in support of another degree or qualification of this or any other university or other institute of learning.

Weijian Shen

Copyright Statement

Acknowledgement

I would like to take this opportunity to express my appreciation to my supervisor, Professor Henggui Zhang. Thank him for allowing me the opportunity to conduct research in this vast and interesting field and his patient and impartial direction for my study.

I would also like to thank Chen Li, Ruoxi Wang, Haibo Ni, Kun Jian, Yang He, and Bo Zhu. Thank you all for your warm support.

Finally, I want to thank my parents for their financial and spiritual support.

Chapter 1 - Introduction

1.1 The Heart

1.1.1 Anatomy and Function of the Heart

The heart drives the circulatory system of humans and other vertebrates. It is located above the diaphragm, in between the lungs in the mediastinum of the thorax in human. The deoxygenated blood from the body is collected in the right atrium and flows into the right ventricle during diastole. During systole, the blood is pumped into the lungs, where it becomes oxygenated, and travels back into the left atrium (Figure 1.1A). The blood is then transported into the left ventricle and is ejected into the body circulation during the contraction of the left ventricle [1].The four valves within the heart (tricuspid, pulmonic, aortic and mitral), keep the unidirectional flow of the blood [2]. The human heart weighs about 250-300g with a heart rate of 60-70 beats per minute (bpm), whereas the mouse heart weighs only about 0.2g with a heart rate of around 500-600 bpm [3].

The electrocardiogram (ECG) provides a visual representation of electrical activity of the heart. The P wave in the ECG indicates that the atria are contracting to pump out blood, while the QRS complex indicates ventricular contractions. The PR interval measures the time period from where the P wave begins until the beginning of the QRS complex, indicating AV conduction time. The T wave indicates the resting period of the ventricles. The ST segment measures the end of the S wave and the beginning of the T wave, indicating the time interval between ventricular depolarisation and repolarisation [2]. Compared with human ECG, Q wave and ST segment in the mouse ECG are absent or shorter.

The cardiac cycle can be divided into ventricular systole and ventricular diastole (Figure 1.1B). During the beginning of systole in human, the volume of blood in the ventricle is unchanged and the ventricular pressure is sharply increased to ~120mmHg.

Once the pressure in the ventricle exceeds the aortic pressure, the aortic valve opens and ventricular ejection occurs. As the ventricular pressure falls below aortic pressure, the aortic valve closes. This is the end of the ejection phase or the left ventricular ejection time (LVET). The atrial contraction causes the small rise in left atrial pressure ("a wave"). Bulging of the mitral valve into the left atrium during the beginning of systole, causes a slight transient increase in left atrial pressure ("c wave"). After left ventricular ejection, blood has been accumulating in the left atrium, results in the elevation in the left atrial pressure ("v wave") [4].

1.1.2 The Cardiac Electrical Conduction System

The cardiac electrical conduction system primarily includes the sinoatrial node (SAN), the atrioventricular node (AVN), bundle branch, and Purkinje fibres (PF) (Figure 1.1A). It serves to generate and conduct the electrical activities throughout the heart. Excitation is initiated in the SAN and rapidly travels to the left atrium through Bachmann's bundle, and to the AVN via internodal pathways. After a delay in the AVN while the atria to complete their contraction, excitation moves through the bundle of His to the Purkinje network that rapidly spreads excitation to the entire working cells in the endocardium such that ventricles contract in a coordinated manner [5].

The heart rate is normally controlled by the SAN in mammalian heart. However, myocytes within the AVN and bundle of His are also able to depolarise spontaneously, but they have low rates and are suppressed by the SAN. If the SAN fails to function or heart block occurs, ventricles then contract at this lower independent rate [2].

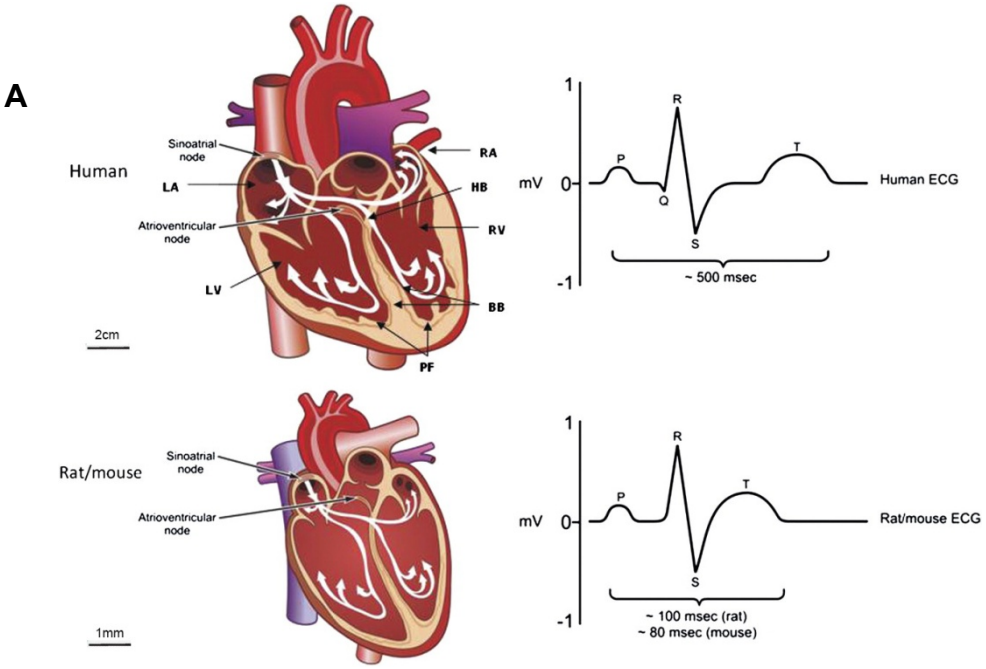
A
Human
Sinoatrial node
LA
Atrioventricular node
LV
RA
HB
RV
BB
PF
2cm
1
mV
0
-1
R
P
Q
S
T
~ 500 msec
Human ECG
Rat/mouse
Sinoatrial node
Atrioventricular node
1mm
~ 100 msec (rat)
~ 80 msec (mouse)
Rat/mouse ECG

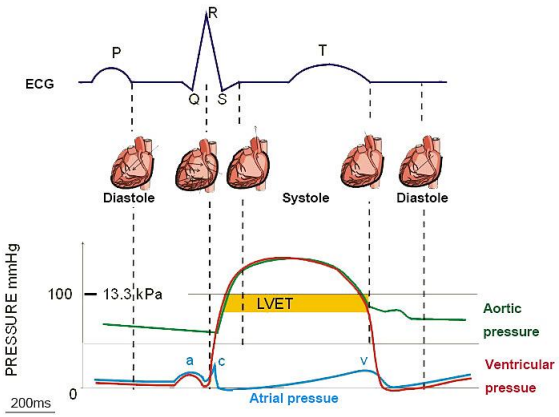
B
ECG
P
R
Q
S
T
Diastole
Systole
Diastole
PRESSURE mmHg
100
13.3 kPa
LVET
Aortic pressure
a
c
v
Ventricular pressue
Atrial pressue
0
200ms

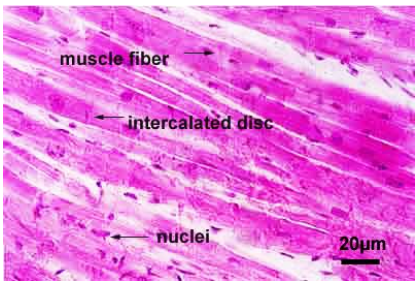
C
muscle fiber
intercalated disc
nuclei
20µm

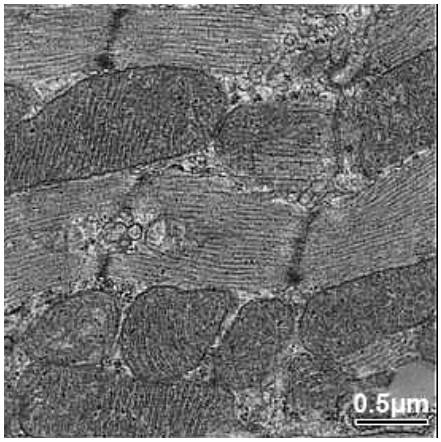
D
0.5µm

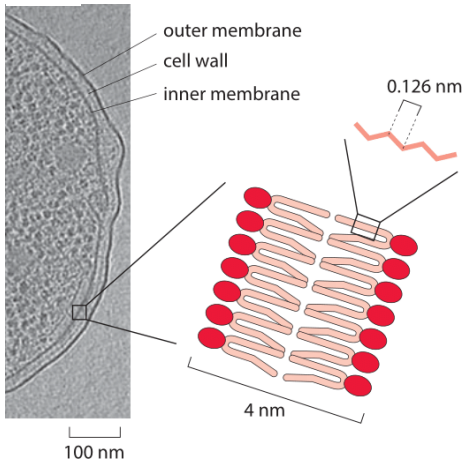
E
outer membrane
cell wall
inner membrane
0.126 nm
4 nm
100 nm

Figure 1.1 Illustrations of the heart and myocytes. A: Schematic illustration of the human heart, rat/mouse hearts and electrocardiogram. Figure adapted from [6]. B: Electro-mechanical events in the cardiac cycle. Figure adapted from [7]. C: Histological sections of cardiac muscle fibres. Figure adapted from [8]. D: Electron micrograph of mouse atrial myocyte. Note the highly specific labelling confined to the mitochondria. Figure adapted from [9] E: Electron micrograph of cell membrane and schematic of the lipid bilayer. Figure adapted from [10]. RA, right atrium; RV, right ventricle; LA, left atrium; LV, left ventricle; HB, His bundle; BB, bundle branches; PF, Purkinje fibres; LVET, left ventricular ejection time.

1.2 The Cardiac Myocytes

Cardiac myocytes are a type of highly specialised muscle cell. They occupy the majority of the myocardium (80%-90% of the heart volume [11]) in such a way that they are mechanically and electrically connected by intercalated discs (Figure 1.1C). The dimensions, volume, and surface area can vary depending on the region. The length of a myocyte ranges from 50 to 120 μm with a diameter between 5 and 25 μm [12]. Similar to skeletal muscle cells, cardiac myocytes are striated with narrow dark and light bands, for the reason that actin and myosin filaments are arranged in parallel discs (Figure 1.1D). However, cardiac myocytes are narrower and shorter than skeletal muscle cells.

1.2.1 The Cell Membrane

The cell membrane (or sarcolemma) is composed of a selective permeable phospholipid bilayer, membrane bound and transmembrane proteins. The bilayer contains hydrophilic heads that are grouped on either side of the membrane, and hydrophobic tails that are connected to each other inside (Figure 1.1E). There are two specialised regions of the myocyte in the sarcolemma: the intercalated disks and the transverse tubular system. The former ensures the rapid conduction of the AP between myocytes (conduction velocity in mouse atria: 38-58 cm/s [13-15]) and the latter ensures the quick penetration of depolarisation to the interior of the cell [12].

The cell membrane works as a selective filter which allows only certain substances to pass across it, thus facilitating the transport of required materials. The movement of objects across the membrane can occur without the input of cellular energy (e.g. passive osmosis or diffusion), or with energy (e.g. adenosine triphosphate-powered pumps). The membrane also maintains electrochemical gradients. For most cells, Na^+ concentration is significantly higher outside the cell than inside and the exact reverse is true for K^+ concentration. The gradient where fewer positive ions are inside a cell favours the movement of positively charged ions into the cell, and the movement of negative ions out of the cell.

1.2.2 Ion Channels

The flow of ions across the cell membrane is driven by the electrochemical gradient or energy from adenosine triphosphate (ATP), and is controlled by ion channels. Ion channels not only selectively permit a specific ion type to pass through the cell membrane, but also determine whether these specific ions can flow through the channel by the activation and inactivation processes of their gates.

The gate usually opens in response to a specific stimulus (Figure 1.2). The main types of stimuli are a change in the voltage across the membrane (voltage-gated channels), a mechanical stress (mechanically gated channels), or the binding of a ligand (ligand-gated channels). The gating kinetics in many ion channels is altered by protein phosphorylation and dephosphorylation. Moreover, with prolonged stimulation, most channels go into the inactivated state with no further opening until the stimulus has been removed [8].

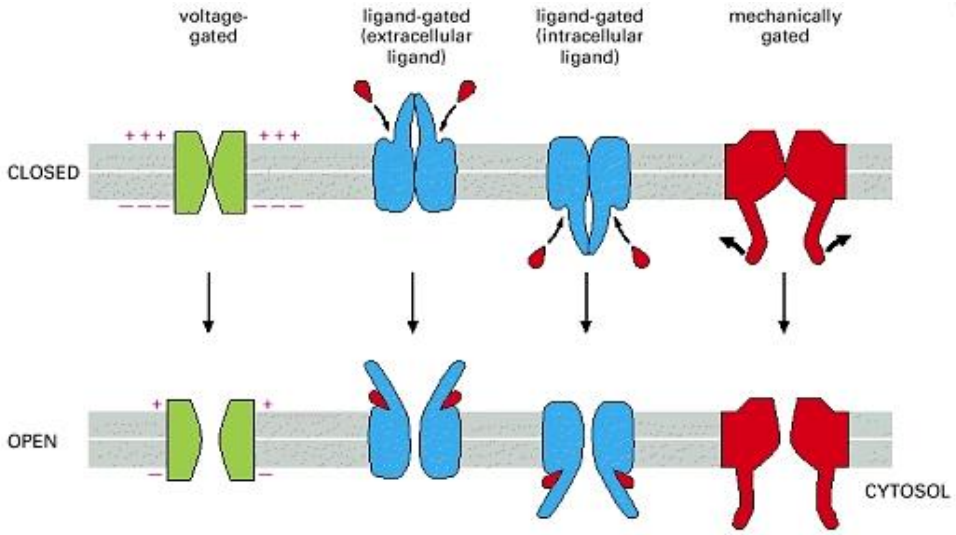

Figure 1.2 Illustration of the gating of ion channels. Figure adapted from [16]

1.2.3 The Cardiac Action Potential

When the membrane potential exceeds a certain threshold, it will rapidly rise and fall, initiating an AP in an all-or-nothing fashion. APs vary in shape, amplitude and time course for different cell types, as shown in Figure 1.3A. A representative AP of the human ventricular myocyte is shown in Figure 1.3B. During phase 0, the rapid upstroke largely depends on the Na^+ influx via the fast Na^+ channels. During phase 1, rapid inactivation of the Na^+ channels and slower activation of the transient outward channels are the bases to form a needle pattern in the AP. The formation of the plateau in phase 2 is primarily determined by the influx of Ca^{2+} via the L-type Ca^{2+} channels (LTCCs) and the outward K^+ current flowing for counterbalancing. Repolarisation accelerates during phase 3 primarily due to the increased K^+ conductance and the inactivation of all other inward currents. The resting membrane potential in phase 4 is maintained primarily by the inward K^+ rectifier and is secondarily affected by the Na^+-K^+-ATPase (NKA), the Na^+-Ca^{2+} exchanger (NCX) and the Ca^{2+} pump. The concentration of ions is then restored to the level at the resting potential [17].

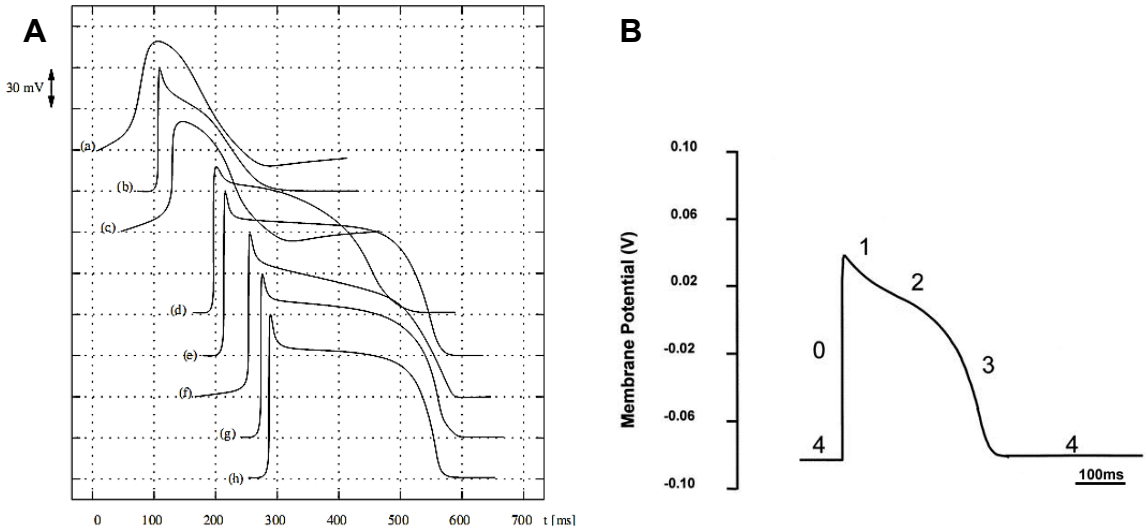

Figure 1.3 AP of human cardiac myocytes. **A**: APs with basic cycle length of 700ms recorded from (a) SAN, (b) atrium, (c) AVN, (d) His bundle, (e) Tawara bundle branch, (f) Purkinje fibres, (g) endocardial and (h) epicardial ventricles. Figure adapted from [18]. **B**: A diagram of the typical five phases in a mammalian ventricular AP. Figure adapted from [17].

1.2.4 Excitation-Contraction Coupling

The process in which electrical excitation initiates the myocyte to contract is called *excitation-contraction coupling* (ECC). The ECC process for mammalian ventricular myocytes is illustrated in Figure 1.4. During an AP, Ca^{2+} enters the cell via LTCCs located in the sarcolemma (SL) and triggers a fraction of the ryanodine receptors (RyRs) to release Ca^{2+} from the sarcoplasmic reticulum (SR). This subcellular process is known as *Ca^{2+}-induced Ca^{2+} release* (CICR). CICR plays a critical role in ECC. The elevation of $[Ca^{2+}]_i$ to activate mechanical contraction of myofilaments is primarily dependent on the SR release, as the amount of Ca^{2+} released from the SR is about ten times larger than that entering via LTCCs [19]. The released Ca^{2+} from the SR binds to the subunit of the thin filament protein to activate the contraction by shortening the sarcomere. Once contraction is complete, Ca^{2+} dissociates from the troponin-C (TnC) and the sarcomere restores to its original length. Cytosolic Ca^{2+} is then removed primarily by sarco/endoplasmic reticulum Ca^{2+} ATPase (SERCA) back to the SR, and also by

extruding from the cell via NCX and an ATP dependent Ca^{2+} pump to a smaller extent [20].

The intracellular calcium dynamics also involves several buffering mechanisms. Calsequestrin (CSQN), localised closely related to RyRs, is a SR Ca^{2+} binding protein with relatively low affinity and high capacity (40-50 Ca^{2+} ions per CSQN [21]). Its main function is to sequester Ca^{2+} into the lumen of the SR, and it may play an important role in regulation of the SR Ca^{2+} release [22, 23].

In the cytosol, two predominant buffers of Ca^{2+} exist: calmodulin (CaM) and troponin. Upon binding to Ca^{2+}, CaM is able to modulate various downstream processes, such as enzyme kinetics (e.g. Ca^{2+}/CaM-dependent protein kinase II, CaMKII) [24]. (The ECC regulation by CaM/CaMKII will be detailed in Section 1.3.) Troponin is the Ca^{2+} binding protein of the myofilaments, which consists of three functional proteins: 1) troponin I (TnI) occupies the binding sites to inhibit the contraction; 2) troponin T (TnT) binds to tropomyosin and helps position it on actin; and 3) TnC binds to Ca^{2+} to destabilise the link between TnI and actin, thus to initiate the contraction.

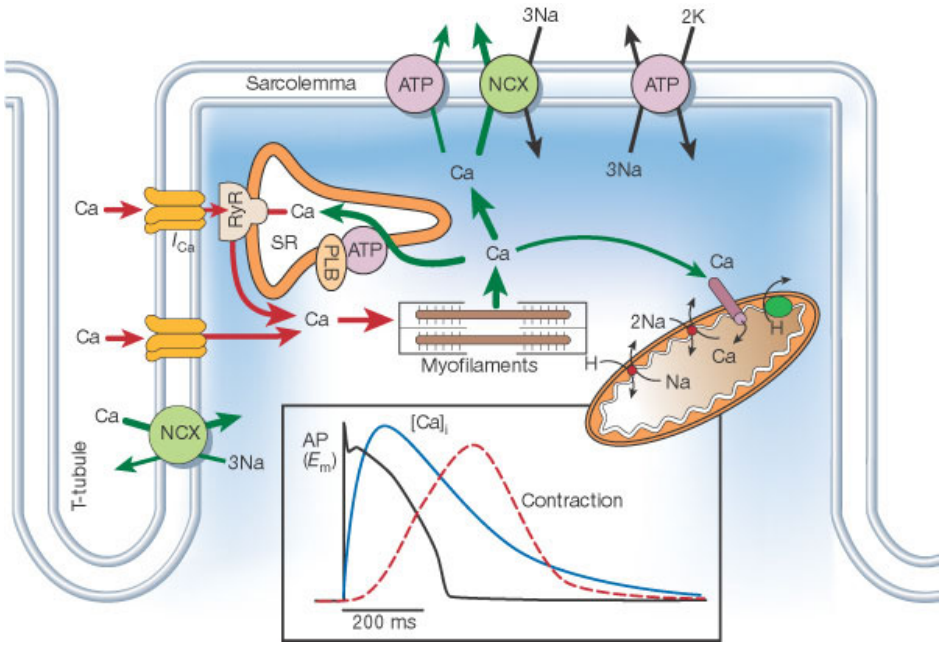

Figure 1.4 Schematic diagram of Ca^{2+} transportations in mammalian ventricular myocytes. Figure adapted from [25].

1.3 Calmodulin Modulation of ECC

1.3.1 Structure and Function of Calmodulin

CaM is a messenger protein expressed in all eukaryotic cells capable of binding four Ca^{2+} ions [26]. It is composed of N- and C-terminal lobes (each containing two Ca^{2+} binding EF-hands) (Figure 1.5A) and is able to react to changes in $[Ca^{2+}]_i$ over a wide range. CaM can sense rapid changes in the local domain of Ca^{2+} concentration with the high affinity C-lobe. In addition, it can sense slow lasting changes in the global $[Ca^{2+}]_i$ with its low affinity N-lobe [27], which makes it a dynamic Ca^{2+} buffer contributing ~3% of the total Ca^{2+} buffering during ECC [20]. When CaM binds Ca^{2+}, it changes conformation, exposing hydrophobic residues that can, in turn, interact with other proteins. Consequently, binding of Ca^{2+} by CaM causes both the CaM to change and, more importantly, other proteins to be affected (Figure 1.5B). In this way, Ca^{2+}-CaM is able to mediate many proteins, causing either activation or inhibition of related functions [28].

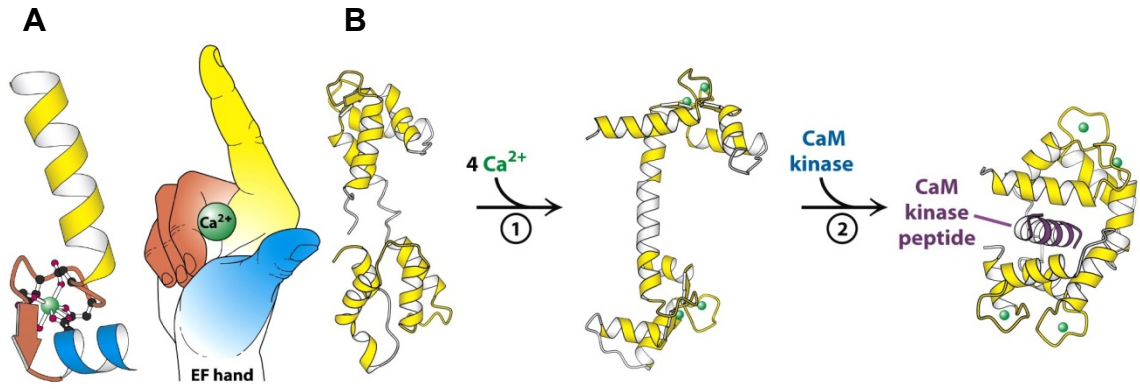

Figure 1.5 Illustration of CaM structure and its conformation changes. **A**: Illustration of EF hand of a CaM lobe. **B**: CaM conformation changes initiated by Ca^{2+} bindings. Figure adapted from [29].

1.3.2 Structure and Activation of CaMKII

CaMKII is a serine (Ser) or threonine (Thr) specific protein kinase which is regulated by the Ca^{2+}-CaM complex. There are three main domains of the CaMKII monomer: an amino-terminal catalytic domain, a central regulatory domain and a carboxy-terminal association domain (Figure 1.6 top). CaMKII forms homo- or hetero-multimers (6-12 subunits) in a wheel-like structure (Figure 1.6 middle). The activation of CaMKII is enabled by the binding of Ca^{2+}-CaM complex to the auto-inhibitory region on the regulatory domain. After activation, CaMKII can auto-phosphorylate its own $Thr^{286/287}$ site. As a result, CaMKII keeps active (20-80%) for several seconds, even when $[Ca^{2+}]_i$ declines to the resting level or CaM dissociates from the autonomous state (Figure 1.6 bottom) [25]. In addition, the calcineurin-activated protein phosphatase 1 (PP1) is able to dephosphorylate the active states of CaMKII [30].

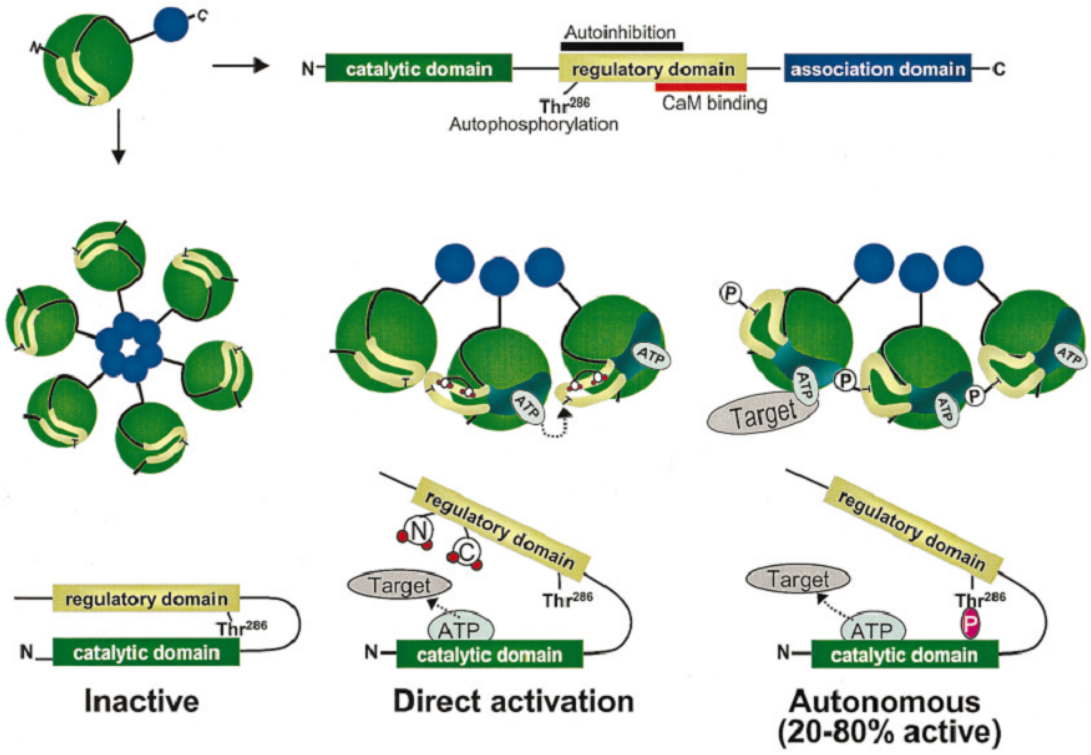

Figure 1.6 Domain layout of CaMKII. **Top row**: Three main domains of the CaMKII monomer. **Middle row**: The wheel-like structure formed by multiple monomers. **Bottom row**: Activation and auto-phosphorylation of CaMKII. Figure adapted from [31].

1.3.3 CaMKII Dependent Regulation

ECC in the cardiac myocyte is mediated by numerous highly cooperative mechanisms where membrane depolarisation controls the Ca^{2+} influx into the myocyte, initiating CICR and activating the contraction. The CaM is a primary mediator for Ca^{2+}-dependent modulation via direct Ca^{2+}-CaM binding or activation of CaMKII and phosphatases (e.g. calcineurin, CaN). CaMKII activity is dynamically controlled by Ca^{2+}, CaM and phosphatases. It can regulate proteins that are involved in the ECC, most importantly the LTCC, RyR and SERCA [25].

Studies on rat ventricular myocyte suggest that LTCCs are modulated via CaMKII-dependent L-type calcium current (I_{CaL}) facilitation, which results in a larger peak current and slower inactivation of the channel kinetics [32, 33].

CaMKII phosphorylation of RyR at Ser^{2809} and Ser^{2815} in human ventricular myocyte has been shown to contribute to the increase in the SR Ca^{2+} release by sensitising the RyR to Ca^{2+} [34]. Transgenic mouse study demonstrates that overexpression of CaMKII in ventricular myocytes increases the fractional SR Ca^{2+} release, and diastolic and spontaneous SR Ca^{2+} release [35].

SERCA can be phosphorylated directly by CaMKII. Upon phosphorylation, the maximum Ca^{2+} transport capacity of SERCA is increased [25]. In addition, CaMKII is also capable of phosphorylating the phospholamban (PLB), which is an inhibitor of SERCA [36]. Upon phosphorylation of PLB at Thr^{17}, the sensitivity for Ca^{2+} of SERCA in rabbit ventricular myocytes has been shown to be enhanced [37].

Studies have shown that CaMKII may also phosphorylate Na^+ channels in rabbit or dog ventricular myocytes [38, 39]. Overexpression of CaMKII slows recovery from inactivation and shifts steady-state inactivation to more negative voltages in the fast Na^+ current (I_{Na}) [38]. The phosphorylation effects on late Na^+ current (I_{NaL}) have shown that CaMKII slows the decay of I_{NaL}, but shifts steady-state inactivation to more positive voltages [39].

Evidence has been provided that phosphorylation of CaMKII may regulate K^+ channels as well. In mouse and rabbit ventricular myocytes, recovery from inactivation in transient outward K^+ current (I_{to}) is shown to be accelerated when CaMKII is overexpressed [40]. A reduction in amplitude of inward rectifier K^+ current (I_{K1}) has been observed in a transgenic study of chronic CaMKII overexpression in mouse ventricular myocytes [40].

1.4 Intracellular Signalling Pathways

An extracellular signal activates a specific cell surface receptor, which in turn propagates and amplifies the signal to the intracellular enzymes to trigger a chain of reactions inside the cell [41]. In this way, one signalling molecule can initiate a variety of intracellular targets causing many responses. This process is called *intracellular signal transduction* [42].

Dozens of intracellular signalling pathways responsible for transmitting information have been found [41]. Most of them respond to an external stimulus arriving at the cell surface and transfer information across the membrane to reach targets inside the cell (Figure 1.7, pathways 1-18). Other pathways are activated by signals generated from within the cell (Figure 1.7, pathways 19 and 20).

Several signalling pathways affect cardiac intracellular Ca^{2+} handling, and thus play an important role in the regulation of ECC. Voltage-operated channels (VOCs) and receptor-operated channels (ROCs) contribute to Ca^{2+} signals by controlling Ca^{2+} entry. The effectors of the 3'-5'-cyclic adenosine monophosphate (cAMP) signalling pathway, such as protein kinase A (PKA), are capable of up- or down-regulating ECC targets upon phosphorylation. Phospholipase C (PLC) and PtdIns 3-kinase (PI 3-K) related signalling pathways can utilise their intermediate inositol 1,4,5-trisphosphate (IP_3) to mobilise Ca^{2+} from the SR [43].

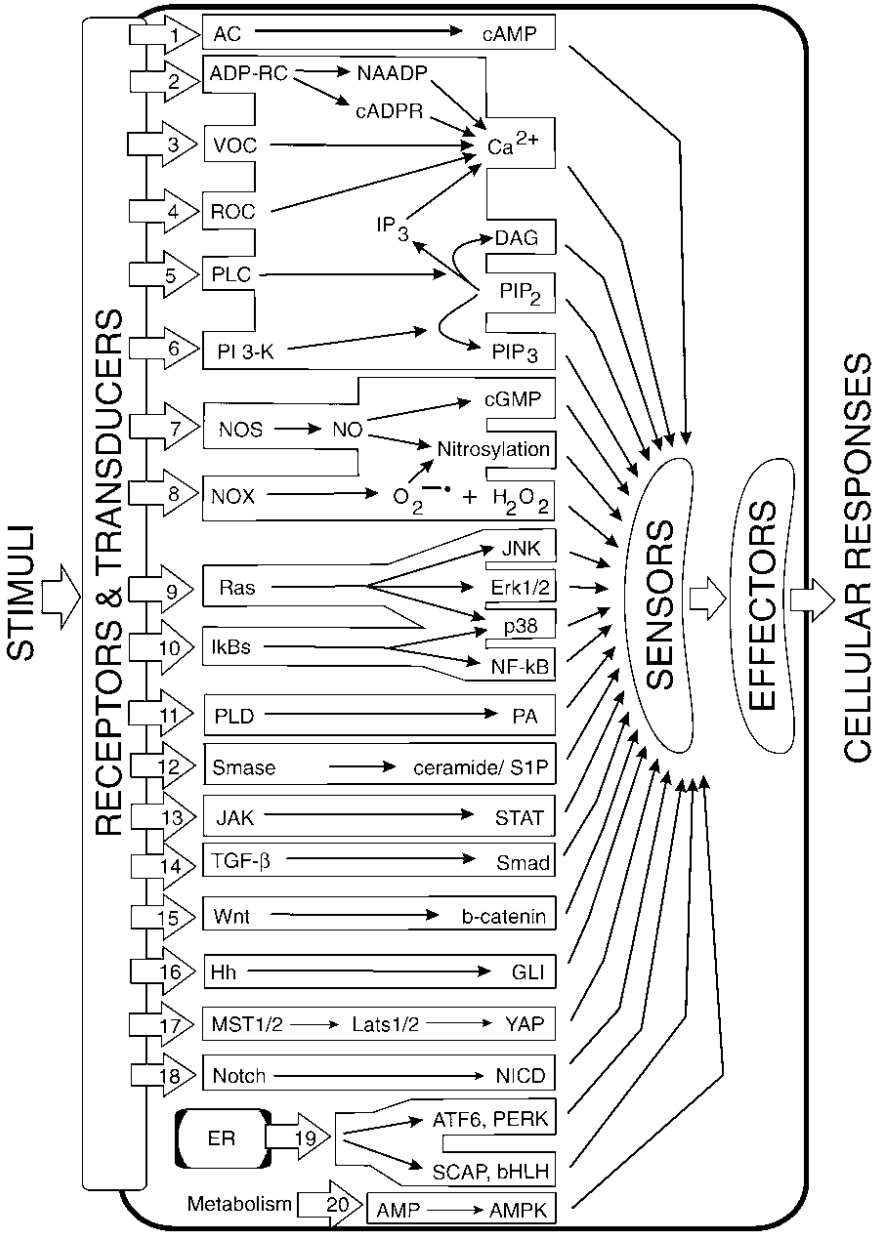

Figure 1.7 Summary of major signalling pathways used by cells to regulate cellular processes. 1: Cyclic AMP signalling pathway. 2: Cyclic ADP-ribose signalling and nicotinic acid–adenine dinucleotide phosphate signalling systems. 3: Voltage-operated channels. 4: Receptor-operated channels. 5: Phospholipase C signalling pathway. 6: PtdIns 3-kinase signalling pathway. 7: Nitric oxide /cyclic GMP signalling pathway. 8: Redox signalling pathway. 9: Mitogen-activated protein kinase signalling pathway. 10: Nuclear factor κB signalling pathway. 11: Phospholipase D signalling pathway. 12: Sphingomyelin signalling pathway. 13: Janus kinase /signal transducer and activator of transcription signalling pathway. 14: Smad signalling pathway. 15: Wnt signalling pathway. 16: Hedgehog signalling pathway. 17: Hippo signalling pathway. 18: Notch signalling pathway. 19: Endoplasmic reticulum stress signalling. 20: Metabolic messengers. Figure adapted from [43].

1.4.1 G-protein Coupled Receptors

G-protein coupled receptors (GPCRs) comprise the largest protein family of receptors in eukaryotes. They are able to recognise different ligands outside the cell, activate inside signal transduction pathways and affect cellular process in different ways. Ligands for GPCRs are heterogeneous molecules, including ions, hormones, neurotransmitters, peptides and proteins. Stimuli such as light, taste or odour can activate sensory GPCRs [44].

All GPCRs share the same molecular architecture that consists of a single polypeptide embedded in the membrane, seven transmembrane domains, and the extra- and intra-cellular intervening portions loop. The extracellular loop comprises the binding site for signalling molecules [45].

The G protein is composed of three subunits: G_α, G_β and G_γ. When inactive, the G protein is fully assembled with the G_α bound to guanosine diphosphate (GDP). Upon activation, as the ligand binds to the receptor, the G protein induces a conformational change to facilitate the exchange of a GDP for a guanosine-5'-triphosphate (GTP) at G_α. This causes the subunits to dissociate from the receptor, releasing a G_α-GTP monomer and a $G_{\beta\gamma}$ dimer, which are now free to modulate the downstream activities (Figure 1.8). The inherent GTPase activity of the G_α causes the GTP to be hydrolysed to GDP and inactivates the subunit, eventually allowing the heterotrimeric G-protein to reform.

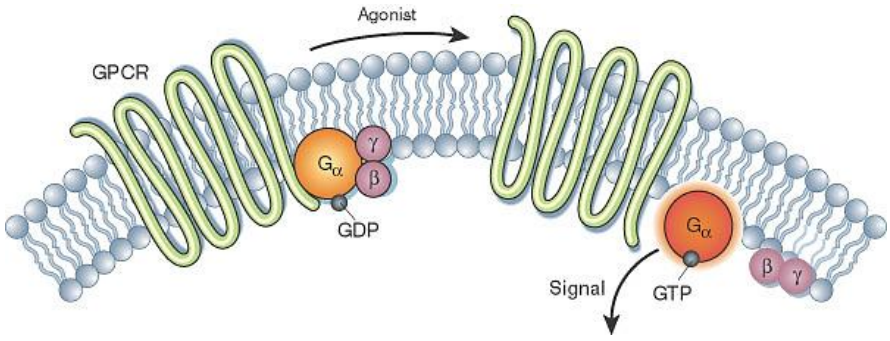

Figure 1.8 Activation of the G_α subunit of a G-protein coupled receptor. Figure adapted from [46].

1.4.2 cAMP Signalling Pathway

The cAMP signalling pathway is responsible for the regulation of various functions in almost all mammals. In the heart, the cAMP signalling pathway plays an important role in regulating cardiac contractility, relaxation, automaticity, metabolism and gene expression [47].

The cAMP signalling pathway is initiated from the surface of the cell where GPCR is activated by the binding of ligand, which results in the dissociation of the trimeric G-protein into the active G_{α}-GTP monomer and a $G_{\beta\gamma}$ dimer (Figure 1.9). The adenylyl cyclase (AC) is then activated by the G_{α}-GTP, using ATP to generate cAMP which is a ubiquitous second messenger [48]. The resultant cAMP binds to the regulatory subunits (R) of the protein kinase A (PKA) and induces dissociation of the holoenzyme. The catalytic subunits (C) can then phosphorylate downstream effectors. Phosphodiesterases (PDE) hydrolyse cAMP into AMP, which is one of the mechanisms that deactivate the cAMP/PKA pathway.

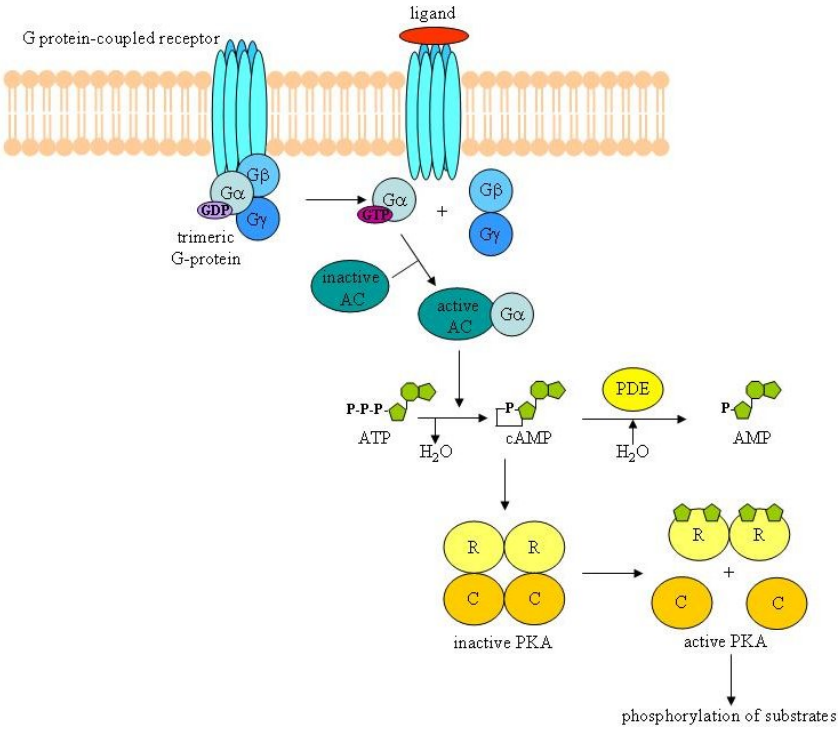

Figure 1.9 Schematic diagram of the cAMP signalling pathway. Figure adapted from [49].

1.4.3 β-adrenergic Regulation of ECC

In the cardiac myocyte, the β-adrenergic signalling pathway plays an important role in coordinated regulation of myocardial contractility through its effector PKA. As discussed in Section 1.4.2, activation of the β-adrenergic receptor promotes synthesising of the cAMP, which in turn dissociates the PKA whose catalytic subunits phosphorylate a wide range of target proteins. Consequently, it exerts a positive inotropic and chronotropic effect on the myocardium.

LTCC phosphorylation at Ser^{1928} on α_{1c} subunit and Ser^{478} and/or Ser^{479} on β_{2a} subunit by PKA results in a significant increase in I_{CaL} [50], and shifts the voltage-dependent activation and inactivation to more negative membrane potentials [51]. Single-channel experiments have shown that this phosphorylation increases channel availability and mode 2 gating [52]. A study on PDE suggested that phosphorylation of LTCCs causes a low activity of PDE which normally dephosphorylate the LTCC [53].

RyR phosphorylation at Ser^{2808} or Ser^{2809} by PKA has shown to cause dissociation of the FKBP12.6 proteins (regulatory subunits) from the RyR complex, resulting in the altered channel kinetics where the channel's open probability and sensitivity to Ca^{2+} activation are enhanced [54].

PLB can be phosphorylated at Ser^{16} by PKA, leading to an increase in the SERCA turnover rate of Ca^{2+} from the cytosol into the SR [55-57]. PP1 acts to dephosphorylate the PLB [58].

TnI, an inhibitory subunit of troponin complex, can be phosphorylated at Ser^{150} or $Ser^{23/24}$, leading to the increase in the Ca^{2+} unbinding rate, therefore accelerating the rate of muscle relaxation and maintaining cardiac output during fast heart rates [59, 60]. The protein phosphatase 2A (PP2A) is capable of dephosphorylating the TnI [61, 62].

Phospholemman (PLM), an inhibitory substrate, can be phosphorylated at Ser^{68}, resulting in the inhibition of NKA, therefore decreasing the affinity for intracellular Na^{+} [63].

PKA phosphorylation may also exert functional changes on other ion channels. Upon phosphorylation by PKA, an increase in the amplitude is observed in the I_{Na} [64, 65], the slow delayed rectifier K^+ current (I_{Ks}) [66] and the ultrarapidly activating delayed rectifier K^+ current (I_{Kur}) [67], while a decrease in the amplitude is shown in the I_{to} [68] and the delayed rectifier potassium current (I_{Kr}) [69].

1.4.4 Role of Inositol 1,4,5-trisphosphate in ECC

IP_3 is a ubiquitous secondary messenger regulating various functions in almost all eukaryotic cells. In cardiac myocytes, it is able to release Ca^{2+} from the SR through activation of IP_3 receptors (IP_3Rs), thus affecting Ca^{2+} homeostasis. IP_3 is generated by the PLC signalling pathway. When a GPCR on the cell surface binds to the specific ligand, the G_α subunit is then dissociated to induce activity in the PLC, which liberates IP_3 from phosphatidylinositol 4,5-bisphosphate (PIP_2) (Figure 1.10). This process is called the *PLC signalling pathway*, which generates two secondary messengers: IP_3 and diacylglycerol (DAG) [70].

The IP_3 receptor is the main target for IP_3 in the cytosol. There are three IP_3R isoforms expressed in the heart, but with different ratios in different species. In human atria and rat Purkinje myocytes, the isoform that is predominantly expressed is type 1, [71, 72], whereas myocytes from other species are particularly rich in type 2 IP_3Rs and, to a lesser extent, type 3 IP_3Rs [73, 74]. Studies have shown that the expression of RyRs outnumber IP_3Rs by a factor between 50:1 and 100:1 in ventricular myocytes [75], and the density of IP_3R is ~5-80 times less than that of RyR [70]. In atrial myocytes, the expression of IP_3Rs is ~3-10 times larger than that in ventricular myocytes [68, 69].

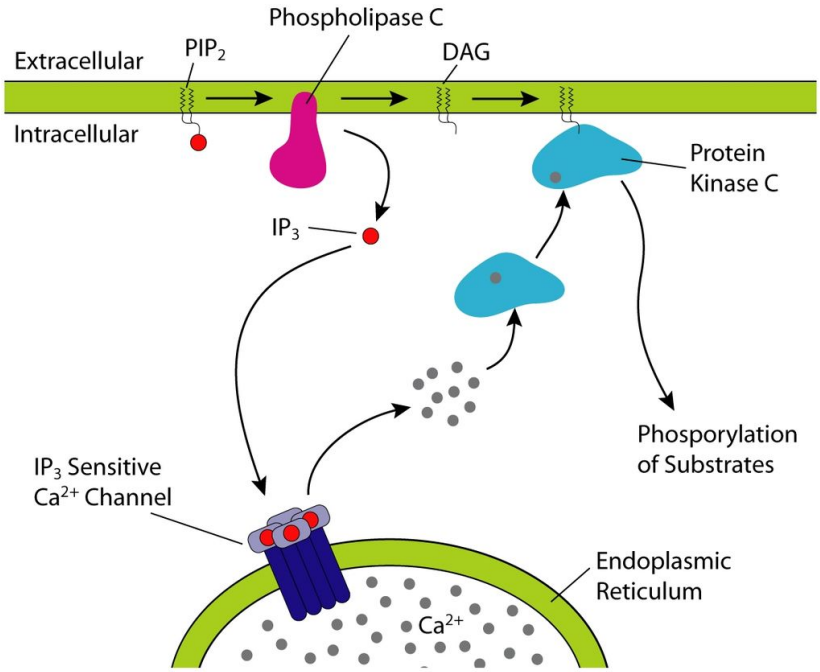

Figure 1.10 Schematic diagram of PLC signalling pathway and IP_3 induced Ca^{2+} release. Figure adapted from [76].

During ECC, IP_3 is able to exert a positive inotropic effect in the myocardium by means of increasing SR Ca^{2+} release without the modification of myofilaments Ca^{2+} responsiveness [77]. The IP_3-induced Ca^{2+} release shows an increase in the fractional Ca^{2+} release from the SR without alteration of the Ca^{2+} load in atrial myocytes[78].

IP_3-dependent elementary Ca^{2+} release events have also been characterised from several studies using confocal microscope [79-82]. Different from RyR-mediated Ca^{2+} sparks, IP_3-evoked Ca^{2+} puffs show 75-80% smaller amplitude, two-fold slower rise time and three-fold longer duration. Thus, IP_3Rs provide a significantly smaller Ca^{2+} release pathway compared to RyRs. However, IP_3-induced Ca^{2+} release may also induce arrhythmogenic alterations. In the human atrial myocardium, upon activation of PLC and IP_3Rs by application of endothelin-1 (ET-1), extra contractions can be observed and the frequency of spontaneous Ca^{2+} sparks is increased [83].

1.5 Cardiac Arrhythmia

An arrhythmia refers to any deviation from the normal sinus rhythm of the heart, which affects the origin, rate, rhythm, conduction velocity and sequence of activation [2]. It has been reported that about half of sudden deaths may be attributed to cardiac-related disorders [84].

Arrhythmia can be classified by the rate, site of origin or mechanism. An abnormally increased resting heart rate (commonly greater than 100 and 600 bpm, in human and mouse respectively [85]) is called *tachyarrhythmia*, while a decreased heart rate (commonly greater than 15% decrease in heart rate [86]) is called *bradyarrhythmia*. The mechanisms responsible for inducing cardiac arrhythmias are generally divided into two major categories: abnormal impulse formation and abnormal impulse conduction (Figure 1.11).

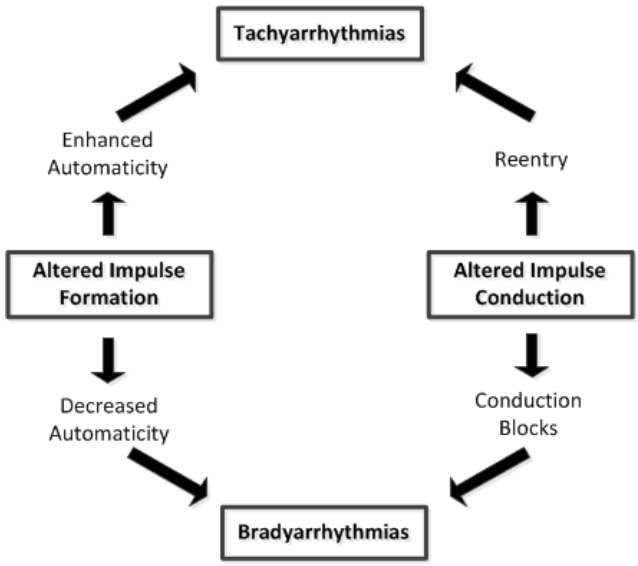

Figure 1.11 Overview of mechanisms of cardiac arrhythmias.

1.5.1 Abnormal Impulse Formation

In the heart, myocytes that are capable of triggering an excitation are classified into two groups, known as the *native pacemakers* (SAN) and *latent pacemakers* (AVN or Purkinje

system). Latent pacemakers may begin to initiate impulses and set the heart rate at their relatively slower intrinsic rate (~30-60 bpm) if the native pacemakers fail or the impulses are blocked [2].

Abnormal automaticity can also occur where non-pacemaker cells generate spontaneous depolarisations, which is believed to be the result of reduced resting membrane potential bringing it closer to the threshold potential, seen most commonly in myocardial ischemia [87].

Sometimes APs may trigger abnormal depolarisations before another original AP, which is called *afterdepolarisation*. If the membrane potential has already returned to the diastolic level prior to the depolarisation, it is a delayed afterdepolarisation (DAD), whereas if it takes off from somewhere on the plateau or late repolarisation phase it is an early afterdepolarisation (EAD) (Figure 1.12).

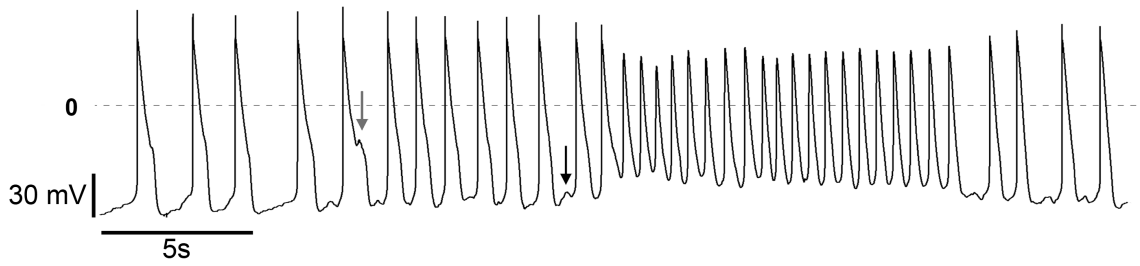

Figure 1.12 Afterdepolarisations in mouse ventricular myocyte. The first arrow indicates a EAD and the second arrow indicates a DAD. Figure adapted from [88]

EADs can occur either at the plateau phase or in late repolarisation. Abnormal reactivation of Ca^{2+} channels, especially with a long action potential duration (APD), is responsible for the EAD occurring at the plateau phase [89]. Mechanism of the EAD that occurs in late repolarisation may have more in common with DADs described below.

DADs are most frequently observed under conditions of intracellular Ca^{2+} overloading. The high SR Ca^{2+} load and elevated $[Ca^{2+}]_i$ cause spontaneous SR Ca^{2+} release events and activate Ca^{2+}-dependent currents (e.g. NCX) to depolarise the membrane transiently, causing a DAD [90].

1.5.2 Abnormal Impulse Conduction

Abnormal impulse conduction may lead to conduction block and reentry, the most common mechanism of arrhythmias.

Conduction block can have many causes, including ischemia, infection, fibrosis, and surgery [91]. Blocks can be transient or permanent, unidirectional or bidirectional, and can occur anywhere within the pacemaking and conducting systems. Atrioventricular (AV) block, the most common conduction block, can be classified as first, second, or third degree. In first-degree AV block, the time interval between the onset of depolarisation in the atria and ventricles is prolonged, but each wave of atrial depolarisation is eventually conducted to the ventricles. In second-degree AV block, some atrial depolarisations are blocked before reaching the ventricles. In third-degree AV block, complete conduction block prevents any supraventricular impulses from reaching the ventricles.

Reentry is another conduction disorder: it is the mechanism responsible for the most common and clinically relevant tachyarrhythmias. Reentrant tachycardia is such that an excitation wave travels around a circuit, depolarising adjacent tissue along the way, and eventually returning to the point of origin to reactivate that site [92].

In the classical description of reentry, two discrete pathways exist: one conducts slowly with a relatively short refractory period (α-pathway), and another conducts quickly with a relatively long refractory period (β-pathway). Under normal conditions, an AP reaches the reentrant circuit, separates, and travels down both pathways. The impulse travelling down the β-pathway reaches the final common pathway first, and continues to conduct, while the other impulse travelling down the α-pathway is blocked at the final common pathway, since the β impulse is within the refractory period (Figure 1.13A) [93].

Reentry occurs when an AP reaches the junction of the reentry circuit at which the β-pathway is still refractory. It then travels down the α-pathway. Since its conduction is slow, by the time it reaches the final common pathway, the β-pathway has already

recovered. In addition to continued conduction, the wave of depolarisation travels back through the β-pathway. When it reaches the junction, the AP conducts again down the α-pathway, as it has already recovered due to its short refractory period. If this mechanism persists, the circuit continues to repeat, leading to a reentrant tachycardia (Figure 1.13B) [93].

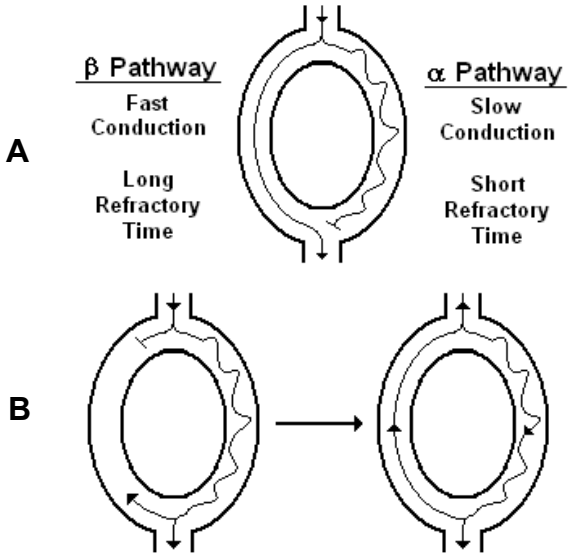

Figure 1.13 Schematic diagrams of conduction in normal and reentrant conditions.

1.6 Mathematical Modelling of Electrophysiology

Over the past few decades, extensive laboratory experiments have provided us with detailed information for the different types of ion channels, pumps, exchangers, and subcellular regulation processes. Biophysically detailed mathematical descriptions of these individual cellular components have integrated into the sophisticated cardiac cell models (Figure 1.14), establishing powerful mathematical platforms to address fundamental questions about the physiology and pathology of the heart. The power and utility of these integrative models enables us not only to verify further the experimental observations, but also to make quantitative predictions, and to guide the design of future experiments.

Our present day understanding of modelling neural and cardiac excitability has been significantly influenced by the landmark work of Hodgkin and Huxley (HH). They

presented the experimental data into a comprehensive theoretical framework which forms the basis of views of excitability. The HH concept was first applied to cardiac cells by Noble [94]. His model of cardiac Purkinje fibres was relatively simple, with five variables. With more experimental data available, the model was then updated twice, in the 1970s by McAllister, Noble and Tsien [95] and in the 1980s by DiFrancesco and Noble [96]. The latter two models formed the basis for the development of ventricular, atrial and sinoatrial cell models.

With increasing experimental data available since the mid-1990s, the emphasis in the development of myocyte models began to move from general mammalian models to more detailed models, based on data from specific cells and from particular species. As shown in Figure 1.14, the rabbit is the species that has been extensively modelled, and the most popular cell type for modelling is the ventricular myocyte.

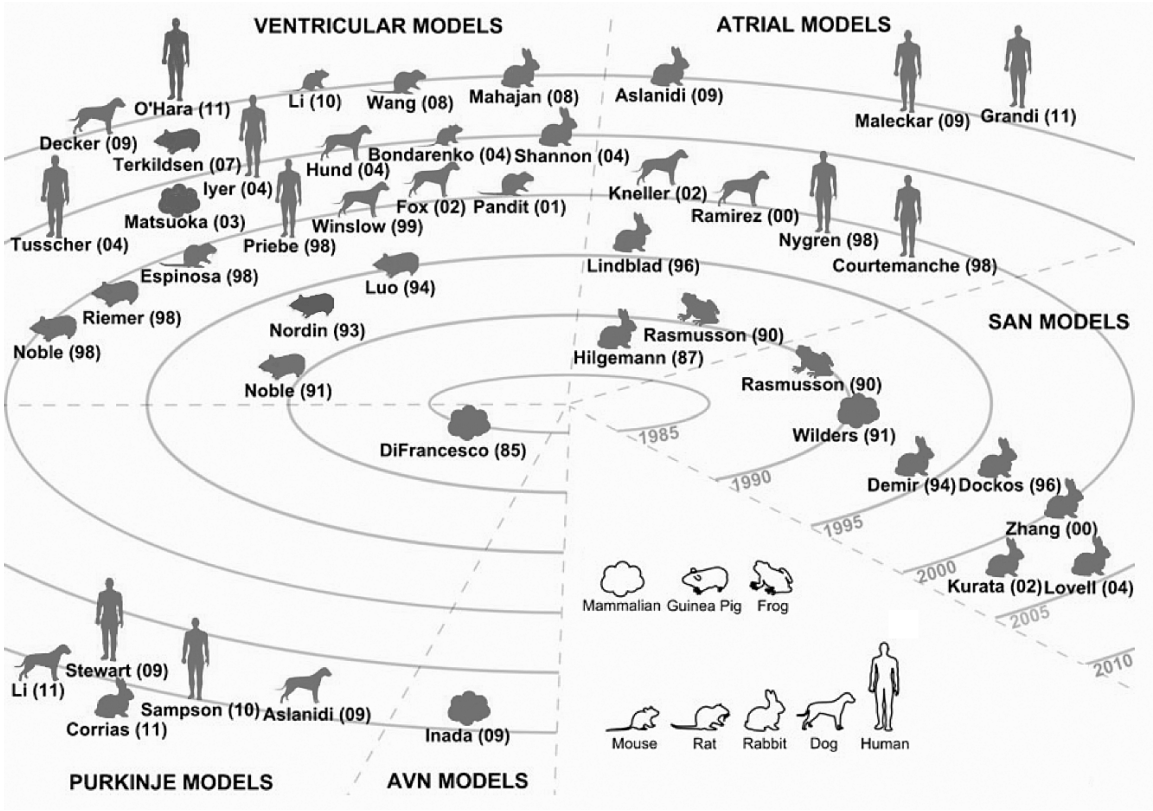

Figure 1.14 Electrophysiological models of myocytes of a variety of species in the SAN, atria, AVN, Purkinje fibre and ventricles. Figure adapted from [97].

1.6.1 The Hodgkin-Huxley Formalism

The pioneer mathematical model for the electrical behaviour of membrane ion channels of the squid giant axon was established by HH [98]. The HH model was based on the idea that the electrical properties of the nerve membrane can be modelled by an equivalent circuit. Three types of ionic current flow across the membrane in the equivalent circuit: I_{Na}, I_K, and a leakage current (I_L). Figure 1.15 shows the fundamental concept of the HH model from the original paper [98].

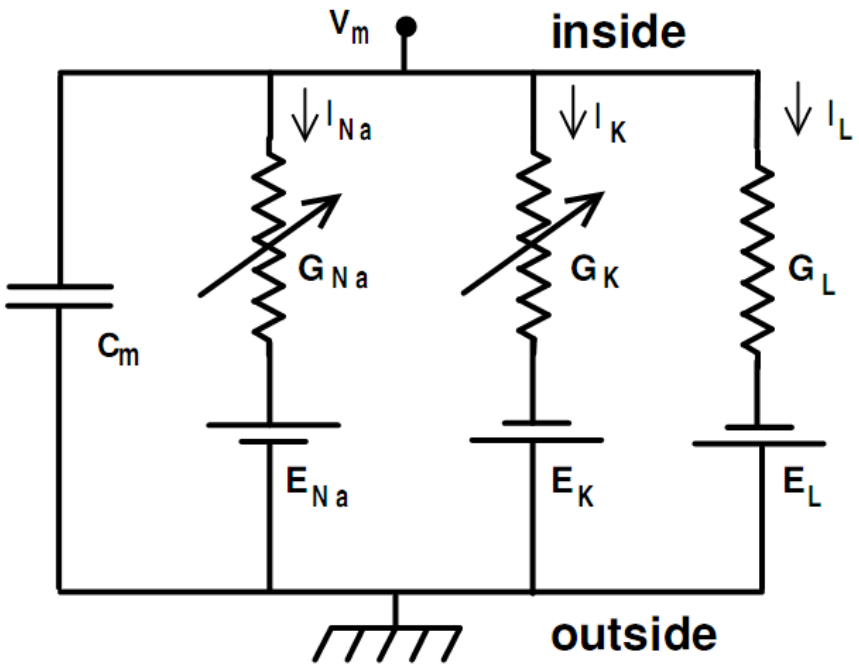

Figure 1.15 Electrical equivalent circuit of the cell membrane describing the electrophysiology of a squid giant axon. V_m, membrane potential; C_m, the membrane capacity; I_{ion}, ionic currents; E_{ion}, equilibrium potential; G_{ion}, ionic conductance (the reciprocal of resistance, $G_{ion}= 1/ R_{ion}$) [98].

The differential equation for AP is:

$$C_m \frac{dV}{dt} = -g_k n^4 (V_m - V_k) - g_{Na} m^3 h (V_m - V_{Na}) - g_L (V_m - V_L) \qquad (1.1)$$

where C_m is the capacitance per unit area of the membrane; g_K, g_{Na} and g_L are the maximum conductance of each ion channel per unit area of the membrane; n and m represent the activation variable of potassium and sodium, respectively; h is the inactivation variable of the sodium channel. The gating variable x (x represents n, m and h) is expressed in:

$$\frac{dx}{dt} = \alpha(1-x) - \beta x \tag{1.2}$$

or, equivalently,

$$\tau_x \frac{dx}{dt} = x_\infty - x \tag{1.3}$$

where α is the transfer rate coefficient for particles from closed to open state [1/s], and β is the transfer rate coefficient for particles from open to closed state [1/s]. τ_x is the time constant of variable x, and x_∞ is the steady state value of variable x.

1.6.2 The Markov Chain Formalism

Traditionally, Cardiac cell models mainly adopted the HH formulation concept of ion channel gating, where the state of an ion channel is a result of one or several independent gates that could be either open or closed. More specifically, the number of possible states for a channel with n different gates is 2^n (Figure 1.16A). However, some researchers argue that state diagrams offer a more accurate interpretation of ionic currents than the HH formulation concept. One of the most famous interpretations, the generic Markov chain model, was offered by the Russian mathematician Andrei Markov (1856–1922). The generic Markov chain model takes into account the interactions among the open, closed and inactive states of ion channels (as illustrated in Figure 1.16B), which gives a more accurate description of the conformation and underlying structure of the ion channel proteins, providing a generic basis for further modelling of agent binding. Despite these advantages, the generic Markov chain formalism requires a much longer computation time due to the numerous differential equations it introduced to the model.

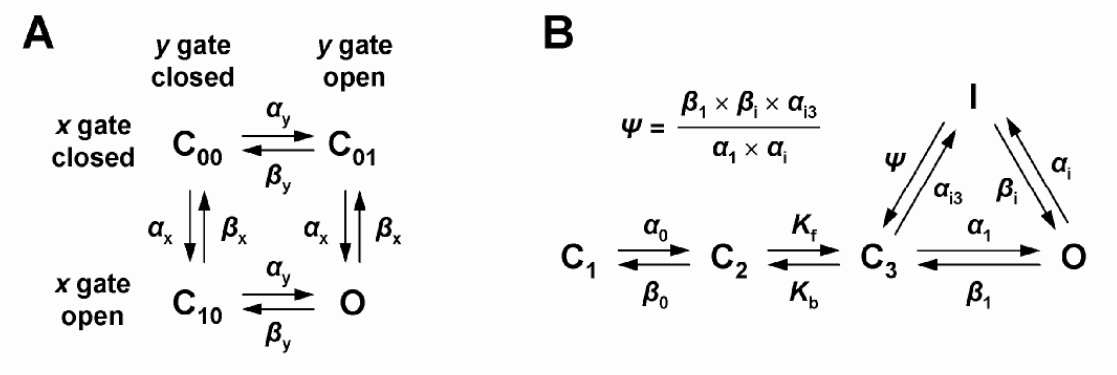

Figure 1.16 Example of Hodgkin-Huxley and Markov chain models of I_{Kr} channel gating. **A**: State diagram of classical HH type model. The open and closed states of the two gates (x and y) result in four possible conductive states for the channel. **B**: State diagram of Markov chain scheme. C_1, C_2, and C_3 are in closed states, O is in an open state, and I is in an inactivated state. All transition rates, except K_f and K_b, are a function of membrane potential. Ψ is defined as a function of other transition rates to satisfy the microscopic reversibility.

Chapter 2 - Modelling of a Mouse Atrial Myocyte

2.1 Introduction

Computer modelling of cardiac myocytes has been thriving over the past few decades. Models have been developing from the pioneering model of DiFrancesco and Noble [96] which purely included ionic membrane currents, to the later model of Luo-Rudy [99] that incorporated Ca^{2+} handling, and to the recent model of Soltis and Saucerman [100] that introduced CaMKII substrates and β-adrenergic signalling regulation. With the development of technique and increasing experimental findings, models of cardiac myocytes have become more and more complex and accurate.

Mice are the most commonly used mammals in medical research. They are inexpensive, easily maintained, and can reproduce quickly. Therefore, a wide range of physiological and pathological studies have been carried out using mice, providing an experimental data basis for computational simulations. Mangoni et al. [101] developed the first mathematical model of mouse SAN; this was updated with biophysical properties of membrane ionic currents and intracellular mechanisms by Kharche et al. [102]. Mouse ventricular models were first developed by Bondarenko et al. [103] and were refitted to the newer data by Li et al. [104]. Recently, mouse ventricular models with β-adrenergic signalling regulation and with CaM mediating Ca-dependent regulation were developed by Yang et al. [105] and Morotti et al. [106] respectively. These models provided further insights into the regulation of Ca^{2+} handling in physiological and pathological conditions.

The aim of this study is to develop a computational model of a mouse atrial myocyte that will provide new insight into the basis of atrial AP behaviour, and establish a cell platform for the study of cellular proarrhythmic mechanisms. The main objective of this chapter is to provide a complete description of the development of the biophysically detailed mathematical model of a mouse atrial cell.

2.2 Methods

The mouse atrial myocyte model was developed based on the mouse ventricular model of Morotti et al. (body temperature) [106], with parameters modified to match the experimental data of mouse atria. The ionic channels of I_{to}, I_{Kur} and I_{Kr} were replaced with Markov chain models for a better reflection of states transitions and gating kinetics. Some parameters of the activation of CaMKII and β-adrenergic activation of PKA, and their phosphorylation on ECC targets, were modified based on the atrial experimental findings. The main changes to the original model of Morotti et al. [106] are summarised in Table 2.1, Table 2.2 and Table 2.3,and will be described in detail in the following subsections.

	Ventricle	Atrium	Reference
Cell Length (μm)	100	90	[107]
Cell Radius (μm)	10.25	6.5	[107]
Cell Volume (pL)	33	11.95	[107]†
Cell Surface Area A_{cell} (μm^2)	20000	8290	[107]†
Cell Capacitance V_{cell} (pF)	200	50	[108]
Cytosol Volume (V_{myo} / V_{cell})	65%	79%	[109]
SR Volume (V_{sr} / V_{cell})	3.5%	1.76%	[109]
SL Volume (V_{SL} / V_{cell})	2%	1.7	[109]
Cleft Volume (V_{junc} / V_{cell})	0.0539%	0.01997%	[109]

Table 2.1 Changes of cell geometry to the ventricular model of Morotti et al. [106]. Parameters denoted with '†' were derived from experimental sources.

Target	Changes	Reference
I_{Na}	Conductance reduced from 10 mS/μF to 4 mS/ μF.	[110]§
I_{to}	Adapted Markov chain model and matched kinetics to the experimental data.	[111, 112]
I_{Kur}	Adapted Markov chain model and matched kinetics to the experimental data.	[112, 113]
I_{Kr}	Adapted Markov chain model and matched kinetics to the experimental data.	[114, 115]
I_{K1}	Matched kinetics to the experimental data.	[111]
I_{Ks}	Removed.	

Table 2.2 Changes of parameters for ECC ionic channels to the ventricular model of Morotti et al. [106]. Parameters denoted with '§' were determined by estimation against data from cited sources.

Target	Changes	Reference
I_{CaL}	Current magnitude decreased by 50%; steady-state activation rate was modified to fit the experimental data.	[116, 117]
I_{pCa}	Current magnitude reduced by 28%.	[118]§
I_{NKA}	Current magnitude reduced by 30%.	[119]§
SERCA	V_{max} increased by 65%.	[118, 120]§
PLB_{tot}	Total PLB reduced by 40%.	[118, 120]§

Table 2.3 Changes of parameters for Ca^{2+} handling. Parameters denoted with '§' were determined by estimation against data from cited sources.

A schematic plot of the ionic currents, fluxes, signalling pathways and physical compartments of the model is shown in Figure 2.1 and Figure 2.2. Active CaMKII dynamically phosphorylates LTCCs, RyRs and PLB. Under the condition of CaMKII overexpression, I_{Na}, I_{NaL}, I_{to}, I_{K1} and NCX current (I_{NCX}) were phosphorylated by CaMKII as acute or chronic effects (see Chapter 3). PKA was able to phosphorylate LTCCs, RyRs, PLB, PLM, I1, TnI and I_{Kur} (see Chapter 4). The IP_3 production system and its regulation on ECC were developed in our model (see Chapter 5).

The original MATLAB code of the ventricular model was rewritten in C language. The C code of modules for ECC, CaM, CaMKII and PKA were validated and verified by their abilities to generate the same results at every time step as MATLAB code. Nonlinear curve fittings were performed using Python language with the LMFIT package. Ordinary differential equations were solved by Sundials CVODE package. APs were obtained by pacing digital cells at indicated frequencies at steady state, unless stated otherwise.

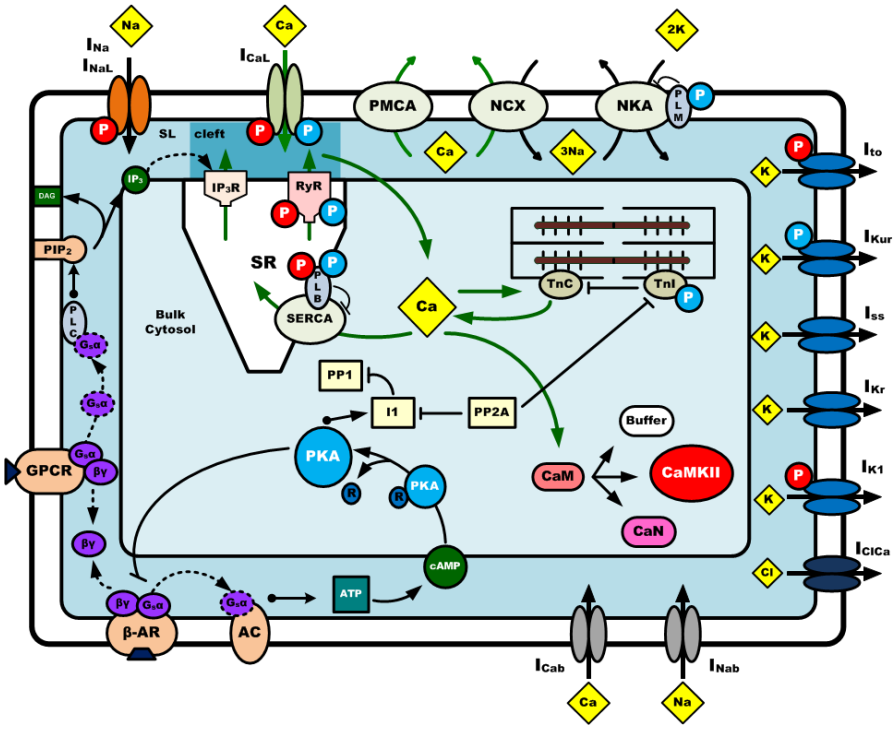

Figure 2.1 Schematic diagram of the computational model of a mouse atrial myocyte. The model includes detailed electrophysiology and Ca^{2+} cycling, their regulation by CaMKII, PKA and IP_3 signalling pathways.

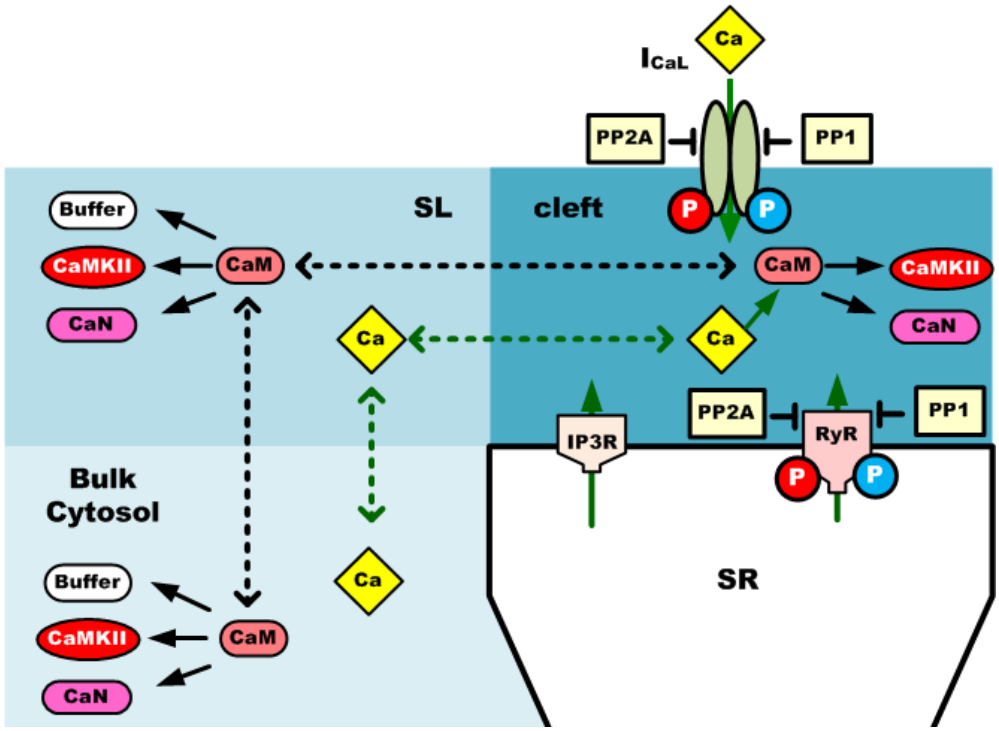

Figure 2.2 Diffusion of Ca^{2+} and CaM in three compartments. CaMKII is activated by Ca^{2+}-CaM binding in the dyadic cleft, subsarcolemma (SL), and bulk cytosol. Phosphatases 1 and 2A (PP1 and PP2A) oppose phosphorylation by either kinase. Ca^{2+} and CaM can diffuse across these three regions at different diffusion coefficients.

2.3 Modelling of Membrane Currents

The cell membrane was considered as a capacitor in parallel with variable resistances and batteries acting as the ionic channels and driving forces. The membrane potential (V) was determined by the following differential equation:

$$-Cm\frac{dV}{dt} = I_{Na} + I_{NaL} + I_{NaK} + I_{Nab} + I_{CaL} + I_{pCa} + I_{NCX} + I_{Cab} + I_{to} + I_{Kur} + I_{ss} + I_{K1} + I_{Kr} + I_{ClCa} + I_{stim} \quad (2.1)$$

where C_m is the membrane capacitance per unit area of the membrane, I_{Na} is the fast Na^+ current, I_{NaL} is the late Na^+ current, I_{NaK} is the Na^+/K^+ pump current, I_{CaL} is the L-type Ca^{2+} current, I_{pCa} is the Ca^{2+} pump current, I_{NCX} is the Na^+-Ca^{2+} exchange current, I_{to} is

the transient outward K^+ current, I_{Kur} is the ultrarapidly activating delayed rectifier K^+ current, I_{ss} is the non-inactivating steady-state voltage-activated K^+ current, I_{K1} is the time-independent inwardly rectifying K^+ current, I_{Kr} is the rapid delayed rectifier K^+ current, I_{ClCa} is the Ca^{2+}-activated Cl^- current, I_{Cab} and I_{Nab} are the background Ca^{2+} and Na^+ currents, and I_{stim} is the external stimulation current. Current densities are in unit of current per unit area.

2.3.1 Cell Geometry

In ventricular myocytes, the well-developed transverse tubules (T-tubules) uniformly spread depolarisation into the cell (Figure 2.3A), resulting in a nearly synchronous SR Ca^{2+} release throughout the entire cell [121]. Atrial myocytes in small species, however, either lack a well-developed T-tube network or have only a rudimentary T-tube network (Figure 2.3A). As a result, the initial rise of the Ca^{2+} transient starts from the periphery of the cell and then the inner Ca^{2+} are released sequentially towards the cell centre with decreasing amplitude [122].

Our mouse model of a single atrial myocyte did not take this into consideration, since the cytosol compartment was designed to be a point model, in which the Ca^{2+} transient was the overall result of all cytosolic Ca^{2+} activities. To simulate the effects of a diffusion barrier due to a 2 μm gap between the junctional and non-junctional RyRs in the atrial myocytes [123], the diffusion coefficient between SL and cytosol was reduced by 10%.

A mouse atrial myocyte is smaller than a ventricular myocyte, and has well-developed T-tubes [124]. Compared with the ventricular myocyte, both the cell length and the cell width are smaller for the atrial myocyte. Based on experimental measurements [107, 109, 118], the cell length in our model was reduced from 100 μm in the ventricular myocyte to 90 μm, and the cell width was reduced from 21 μm to 13 μm (Figure 2.3B).

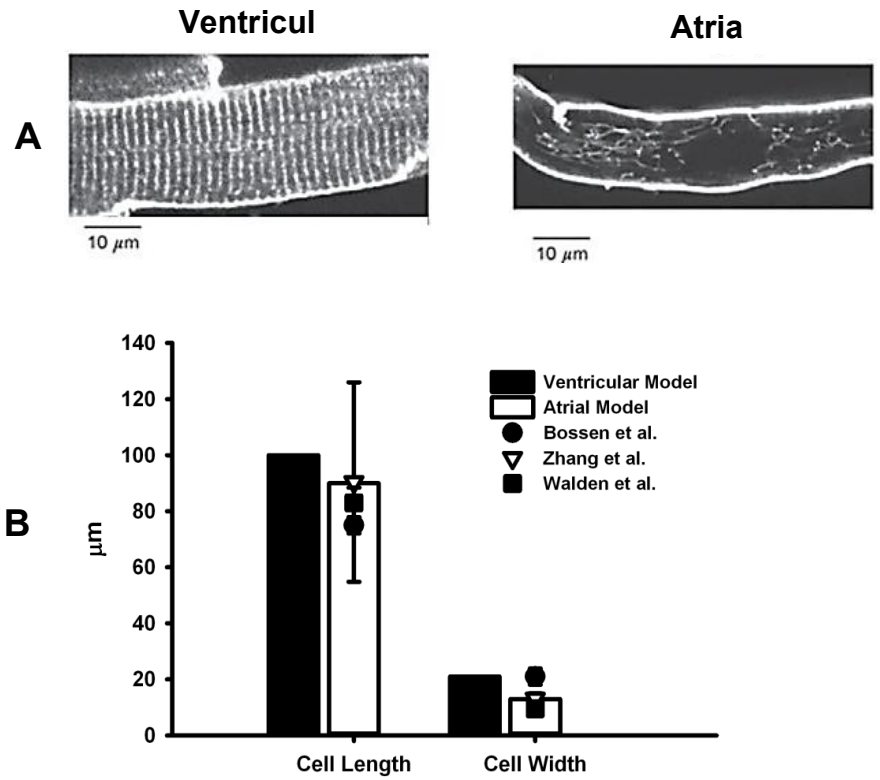

Figure 2.3 Cell geometry differences between ventricular and atrial myocytes. **A**: Membrane staining of rat ventricular and atrial myocytes showing a regular T-tube network in ventricular myocytes, and an atrial myocyte where T-tubes are absent. Figures are cited from [122]. **B**: Cell dimension differences. The filled bar is the value used in the ventricular model of Morotti et al. [106]. The empty bar is the one used in our atrial model. Experimental measures for murine atrial cells are from Bossen et al. [109], Zhang et al. [107] and Walden et al. [118].

2.3.2 Fast and Late Na^+ Currents, I_{Na} and I_{NaL}

The fast Na^+ current has extremely fast kinetics with times to peak of less than 500 μs [125], causing rapid depolarisation at the upstroke of the AP; its inactivation is also relatively quick (up to several millisecond) [126]. The I_{Na} channel kinetics were unaltered from the mouse ventricular model of Morotti et al. [106], due to the absence of experimental data. The conductance of I_{Na} was decreased from 10 nS/pF to 4.5 nS/pF to reproduce the AP amplitude (APA) and the dV/dt_{max} that matched the experimental observation (see Figure 2.19A and B).

The kinetics of the late Na^+ current were identical to the formulation described in Morotti et al. [106], due to the lack of experimental data for the mouse atrium. The conductance of I_{NaL} was increased by 68% from the mouse ventricular model to fit the peak current density observed from the experiment [127].

2.3.3 L-type Ca^{2+} Current, I_{CaL}

LTCCs provide the main Ca^{2+} influx for myocytes and act as a trigger for Ca^{2+} release from the SR. There are four types of LTCCs: $Ca_v1.1$ to $Ca_v1.4$, where $Ca_v1.2$ and $Ca_v1.3$ play the main role during cardiac ECC [128]. I_{CaL} has the kinetics of a fast activation with a time constant of 2-3 ms and a slower inactivation time course of 30 - 300ms [129].

The formulation of LTCC in our model was based on a previous model developed by Mahajan et al. [117], with related CaMKII and PKA phosphorylation modules updated for mouse ventricles by Morotti et al. [106]. The LTCC model of Mahajan et al. [117] has a minimum scheme of seven states, but incorporates both calcium-dependent inactivation (CDI) and voltage-dependent inactivation (VDI) (Figure 2.4A), where the transitions between C2 and C1 are strongly voltage-dependent, and the transitions from C1 to O are voltage-independent and determine the steady-state open probability.

In order to fit the experimental measures, the formulation of voltage-dependent steady-state activation rate was modified from

$$\alpha = 1/(1+e^{-V/8.0}) \tag{2.1}$$

to

$$\alpha = 1/(1+e^{-(V+4.4)/6.14}) \tag{2.2}$$

Thus, the half activation voltage reduced from 0mV to -4.5mV. We implemented the same voltage-clamp protocol as described in the related literature [108]: the I_{CaL} was activated by a series of 250-ms depolarisation pulses from a holding potential of -90 mV, to test potentials ranging from -40 mV to +40 mV (10 mV step). The integrated I_{CaL} was recorded and normalised to the peak value (Figure 2.4C). The peak current density of

3.56 pA/pF, the I-V relationship and the current traces all showed agreements with experimental observations (Figure 2.4 B-D).

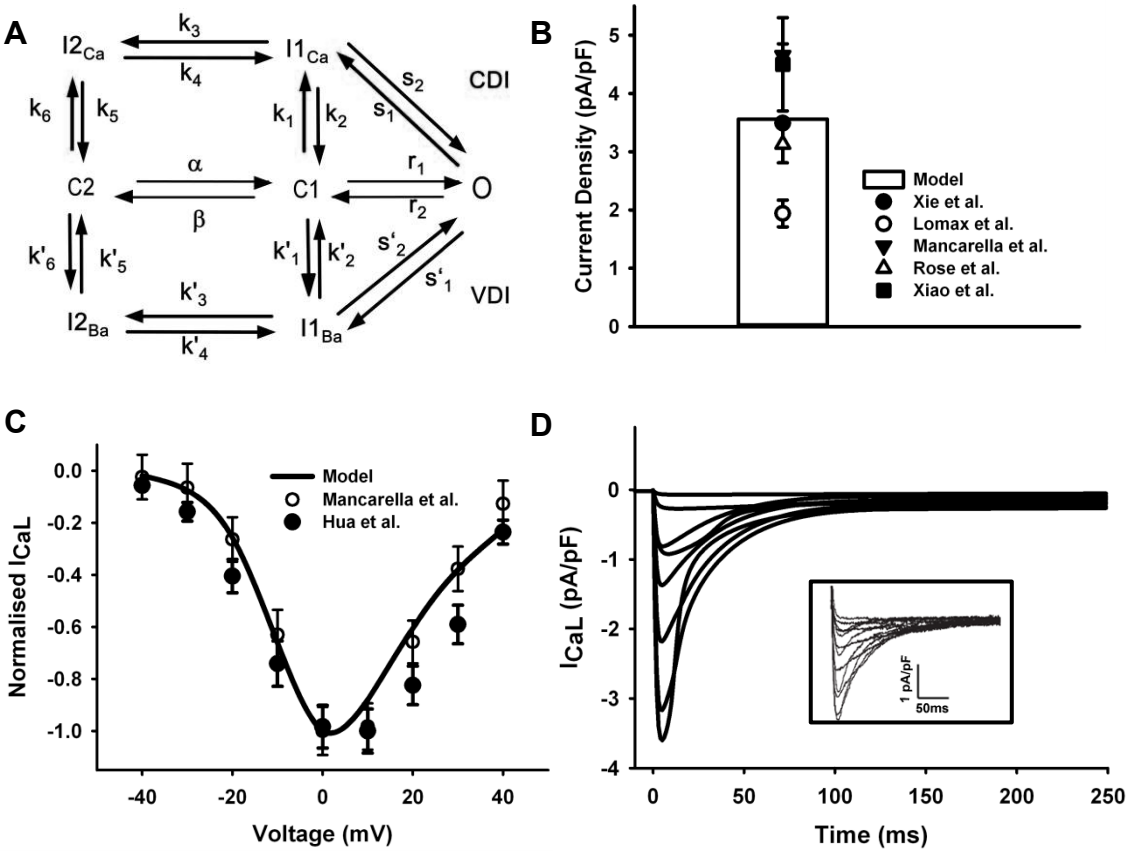

Figure 2.4 I_{CaL} in the atrial myocyte model and experiments. **A**: Schematic diagram of the Markov chain model of the L-type Ca^{2+} channel [117]. **B**: Peak simulated current density compared with experimental data. **C**: Normalised I-V relationship of ICaL. **D**: Current traces of the voltage clamp: the inset shows the experimental records from Mancarella et al. (Experimental data: Xie et al.[116], Lomax et al. [111], Mancarella et al. [108], Rose et al. [130], Xiao et al. [131])

2.3.4 Transient Outward K^+ Current, I_{to}

The transient outward K^+ current, I_{to}, is a rapidly activating and inactivating K^+ current, encoded by Kv1.4 and Kv4.2-Kv4.3 [132]. Xu et al. [133] reported that the elimination of I_{to} gave rise to substantial increases in atrial APD, suggesting that I_{to} plays a prominent role in mouse atrial repolarisation.

The HH equations for I_{to} in the mouse atrial myocyte were replaced with the Markov chain model of Campbell et al. [134] that comprised seven states (Figure 2.5A). The I-V relationship was determined by using a protocol of 500-ms voltage steps in 10-mV increments between -75 mV and +45 mV from a holding potential of -75 mV. The results show a peak current density of 12.1 pA/pF. Simulated normalised I-V curve and related current traces were similar to those seen in experiments (Figure 2.5B-D).

To plot the steady-state inactivation curve for I_{to}, a two-pulse of 500ms protocol was applied. The first was from the holding potential of -75 mV to potentials between -105 mV and +35mV in 10-mV increments; the second was from the holding potential of -75 mV to potentials between -105 mV and +50mV. The peak amplitudes after applying the second stimulus were recorded and normalised to their maximum value (Figure 2.5E). The simulated inactivation curve reproduced the experimental findings well.

To plot the recovery from the inactivation curve, two 500-ms pulses to +35mV from a holding potential of -75mV were applied. The first pulse (P1) was followed by the second pulse (P2) after an interstimulus interval of 0-500ms, in 25ms increments. The peak amplitudes after applying P2 were recorded and normalised to their maximum value (Figure 2.5F). The simulated results were close to the experimental values.

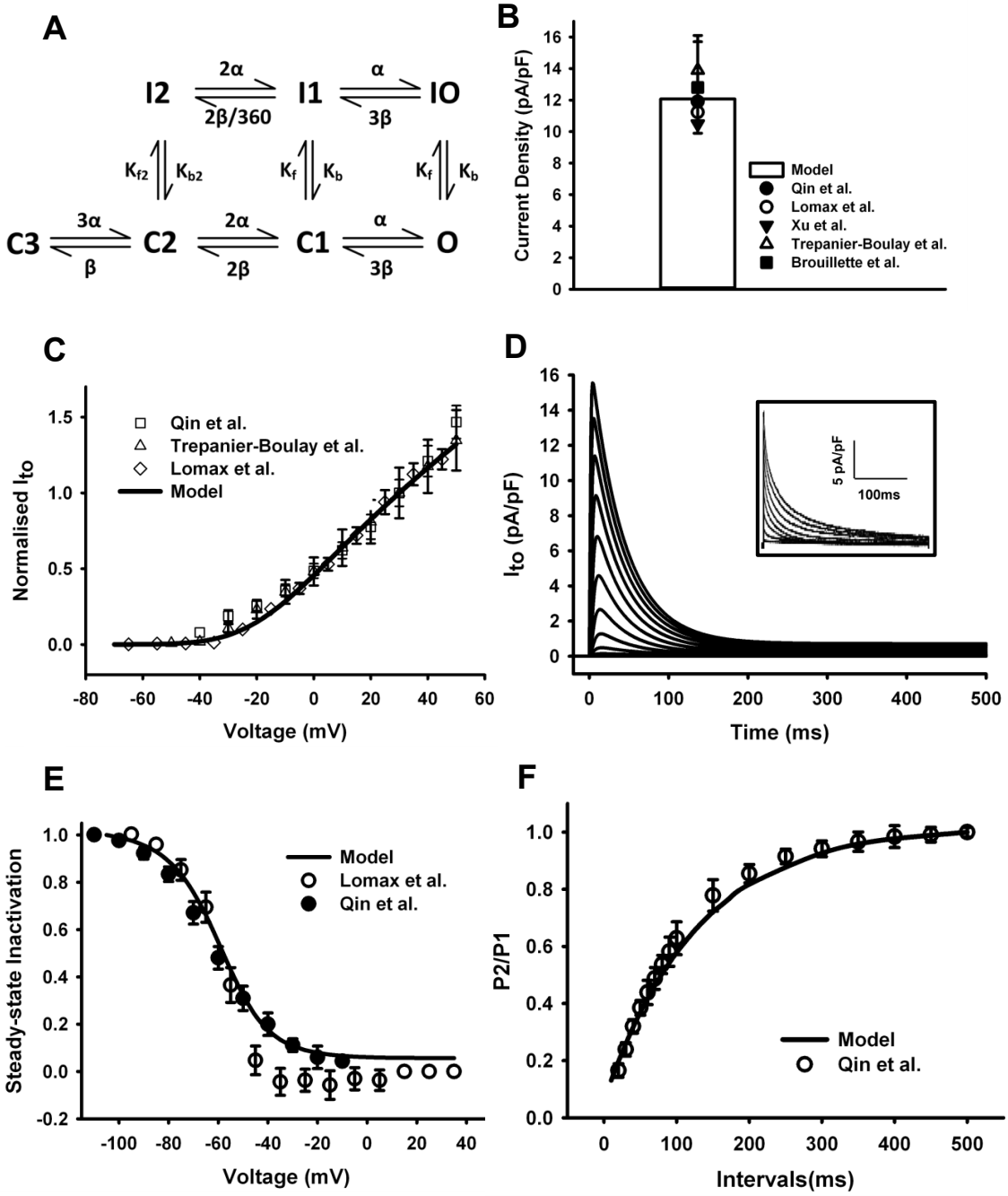

Figure 2.5 I_{to} in the atrial myocyte model and experiments. **A**: Schematic diagram of seven-state Markov chain model of I_{to} [134]. **B**: Current density at +30mV. **C**: I-V relationship, current normalised to the current at +30mV. **D**: Current traces for the corresponding voltage clamp protocol. The inset shows the experimental record. **E**: Steady-state inactivation curve. **F**: Recovery curve from inactivation. (Experimental data: Qin et al. [135], Trepanier-Boulay et al. [113], Lomax et al. [111])

2.3.5 Ultrarapidly Activating Delayed Rectifying K^+ Current, I_{Kur}

The ultrarapidly activating delayed rectifying K^+ current, I_{Kur}, encoded by Kv1.5, was identified in atrial myocytes from several species. The kinetics of rapid activation and slow inactivation were reflected in the early current nomenclature, such as rapidly activating slowly inactivating current $I_{K,s}$[136], sustained current I_{sus} [137], or ultrarapid K^+ current I_{Kur} [113], which is the currently accepted name for this current.

The HH formulations of I_{Kur} for the mouse ventricular myocyte were replaced with the six-state Markov chain model of Zhou et al. [112] (Figure 2.6A). The transition rates were adjusted to match the experimental data. The I-V relationship was determined by using a protocol of 500-ms voltage steps in 10-mV increments between -70 mV and +50 mV from a holding potential of -80 mV. The peak current density of 4.68 pA/pF, simulated the normalised I-V curve, and related current traces were similar to those seen in experiments (Figure 2.5B-D).

2.3.6 Non-inactivating Steady-state K^+ Current, I_{ss}

The non-inactivating steady-state K^+ current, I_{ss}, was found in the mouse ventricles and atria by Xu et al. [133, 138]. It is a 4-AP-resistant current, which is distinctly different from I_{to} and I_{Kur} [139].

I_{ss} in the model of mouse atrial myocytes was completely reformulated to match the experimental measures. The I-V relationship was determined by using a protocol of 500-ms voltage steps in 10-mV increments between -80 mV and +60 mV from a holding potential of -80 mV. The peak current density of 11.9 pA/pF, simulated normalised I-V curve and related current traces are similar to those seen in experiments (Figure 2.7A-C).

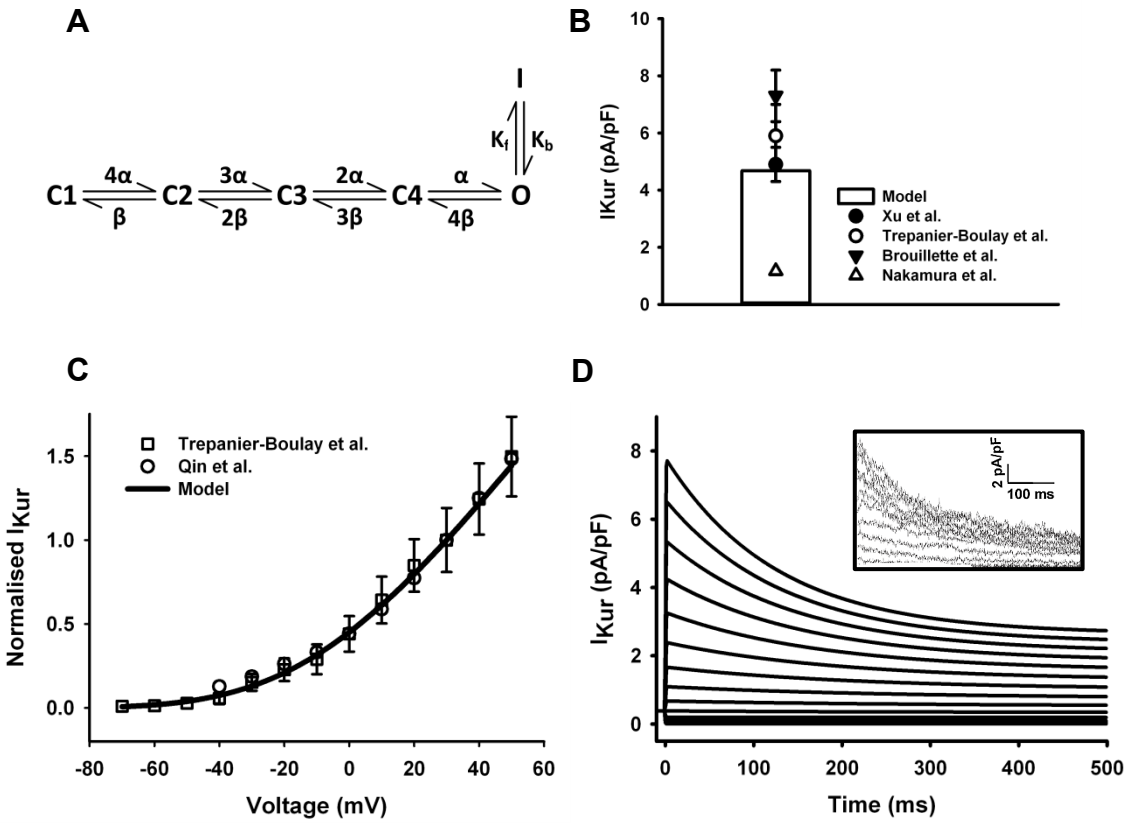

Figure 2.6 I_{Kur} in the atrial myocyte model and experiments. **A**: Schematic diagram of six-state Markov chain model of I_{Kur} [112]. **B**: Current density at +30mV. **C**: I-V relationship, current normalised to the current at +30mV. **D**: Current traces for the corresponding voltage clamp protocol. The inset shows the experimental record. (Experimental data: Xu et al. [133], Trepanier-Boulay et al. [113], Brouillette et al. [139], Nakamura et al. [114], Qin et al. [135])

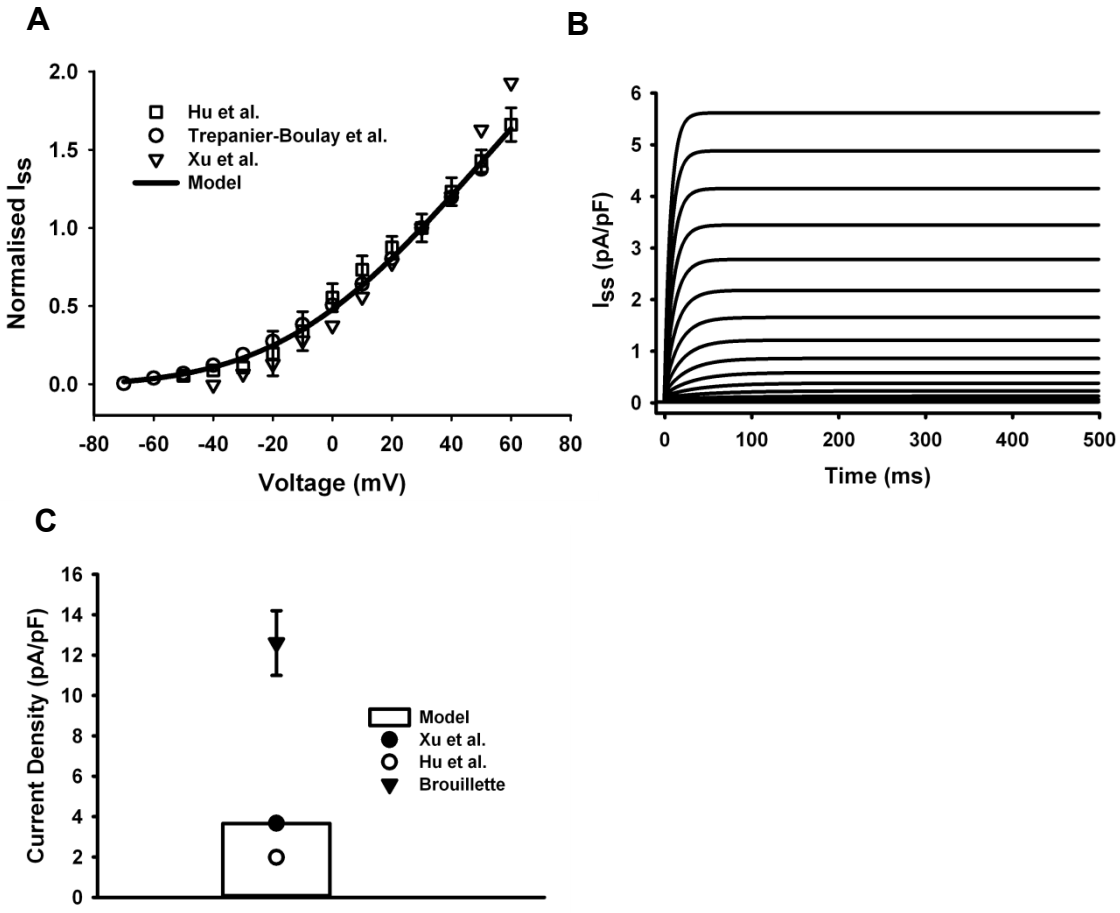

Figure 2.7 I_{ss} in the atrial myocyte model and experiments. **A**: I-V relationship, current normalised to the current at +30mV. **B**: Current traces for the corresponding voltage clamp protocol. **C**: Current density at +30mV. (Experimental data: Xu et al. [133], Hu et al. [140], Brouillette et al. [139])

2.3.7 Rapid Delayed Rectifying K^+ Current, I_{Kr}

The rapid delayed rectifying K^+ current, I_{Kr}, encoded by ERG (KCNH2, KV11.1), has been proved to have a key role in the late repolarisation of AP in several mammalian species [141-143]. The presence and function of I_{Kr} in the mouse atrium has been demonstrated by Nakamura et al. [114].

The HH formulations of I_{Kr} for the mouse ventricular myocyte were replaced with the five-state Markov chain model of Clancy et al. [115] (Figure 2.8A). All transition rates were modified to fit the experimental measures. The I-V relationship was determined by using a protocol of 500-ms voltage steps in 10-mV increments between

-45 mV and +45, following a 200-ms prestep potential of -35 mV, and the tail currents were measured on return to -40mV. The resultant tail I-V curve and time constants for inactivation and activation were in agreement with the experiment [114] (Figure 2.8 B-C). The simulated steady-state I-V curve and current traces are shown in Figure 2.8 D-E.

2.3.8 Inward Rectifying K^+ Current, I_{K1}

The inwardly rectifying K^+ current, I_{K1}, encoded by Kir2.x, stabilises the resting potential and is responsible for shaping the initial depolarisation and final repolarisation of the action potential.

The I_{K1} equation in our model was based on that of DiFrancesco and Noble [96] with parameters adapted to the experimental data. The 500-ms pulse in the voltage-clamp protocol was from the holding potential of -80 mV to voltages from -150 to -40 mV. Currents were normalised to the magnitude at -90 mV. Simulated results were similar to the experimental data (Figure 2.9).

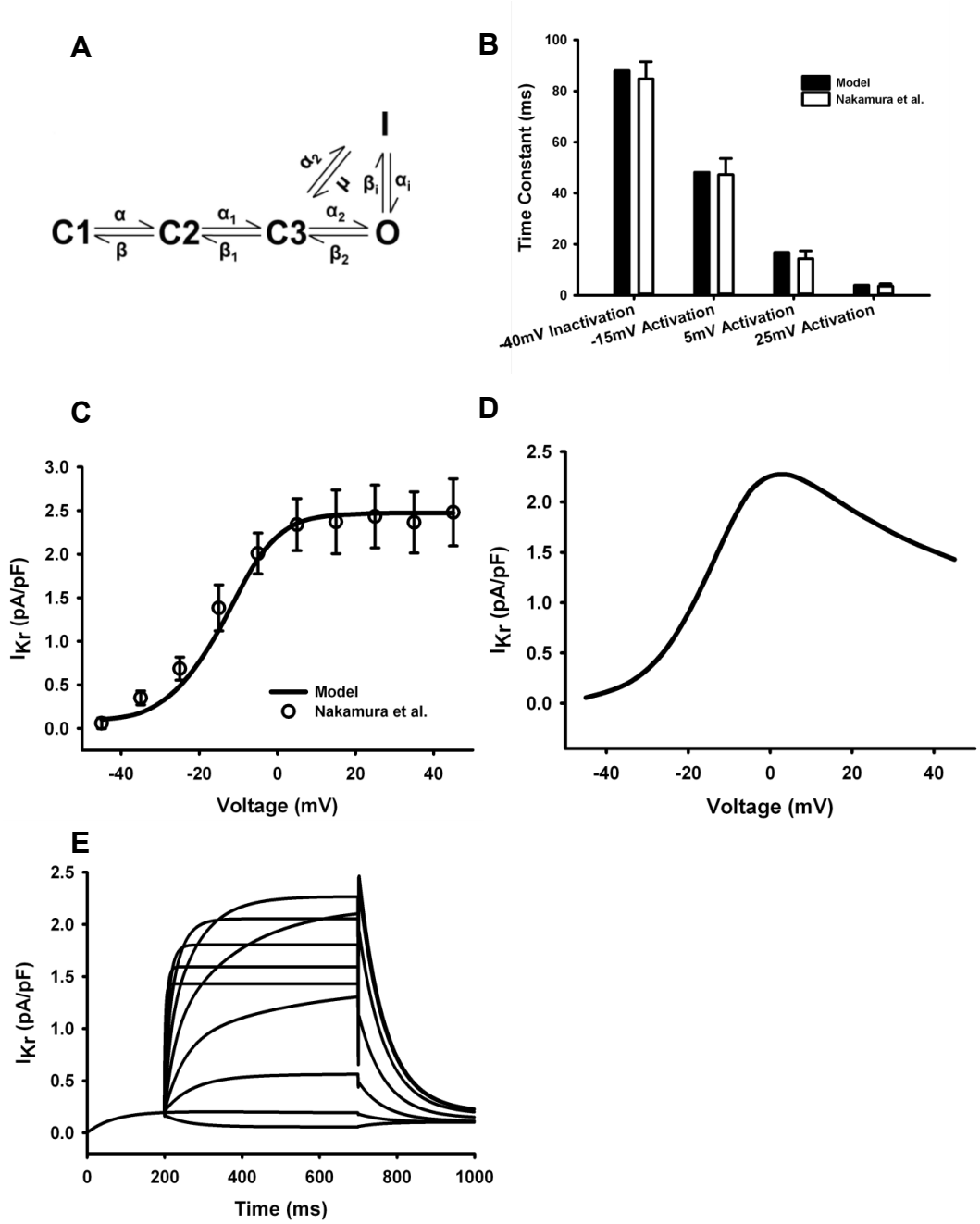

Figure 2.8 I_{Kr} in the atrial myocyte model and experiments. **A**: Five-state Markov chain model of I_{Kr}. **B**: Time constants for inactivation and activation. **C**: Tail I-V relationship. **D**: Steady-state I-V relationship. **E**: Current traces for the corresponding voltage clamp protocol. (Experimental data: Nakamura et al. [114])

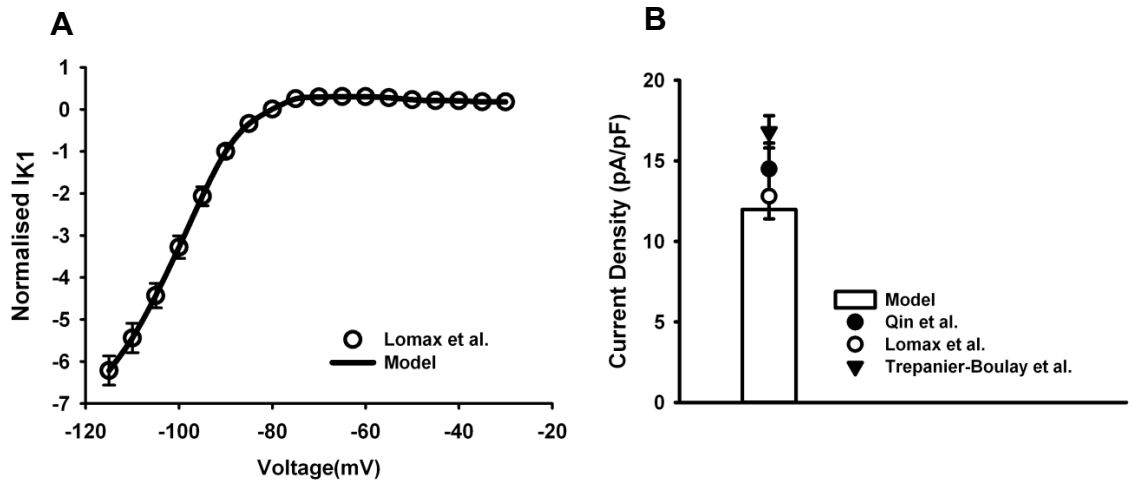

Figure 2.9 I_{K1} in the atrial myocyte model and experiments. **A**: I-V relationship for normalised I_{K1}. **B**: Current density of $I_{K1.}$ (Experimental data: Qin et al. [135], Lomax et al. [111], Trepanier-Boulay et al. [113])

2.3.9 Na^+-Ca^{2+} Exchanger Current, I_{NCX}

The Na^+-Ca^{2+} exchanger, encoded by the NCX family (NCX1, NCX2 and NCX3), is responsible for maintaining steady intracellular Ca^{2+} balance. It extrudes Ca^{2+} together with the Ca^{2+} pump. As a reversible transporter, it also mediates Ca^{2+} entry in parallel with LTCCs [144].

The protein ratio of NCX to SERCA was reported to be 1.99 and 1.65 in the rat ventricle and atrium, respectively [145]. Due to the lack of experimental results on NCX electrophysiological data for the mouse atria, the protein ratio was taken into consideration. The SERCA activity has been enhanced by increasing the maximum turnover rate and the affinity in the forward mode; therefore, the formulations for the NCX were kept unchanged from the model of Morotti et al. [106].

2.3.10 Na^+-K^+ Pump, I_{NaK}

The Na^+-K^+ pump is responsible for maintaining the Na^+ and K^+ gradients between the cytosol and extracellular medium, and plays an important role in the restoration of the resting potential, and the generation and propagation of APs [146].

In human atrial myocytes, the expression level of the Na^+/K^+ pump is moderately reduced compared to ventricle myocytes [119]. To adapt this change, the maximum rate for the Na^+/K^+ pump was decreased by 20% in the mouse atrial model, compared with the ventricular model, since there are no direct experimental data for I_{NaK} in mouse atria.

2.4 Modelling of Intracellular Ca^{2+} Handling

The intracellular Ca^{2+} handling in the mouse ventricular model is based on the framework developed by Shannon et al. [147]. For the mouse atrial model, this framework was also utilised with some modifications.

Similar to the model of Shannon et al. [147], the cell volume in our model was divided into four compartments (Figure 2.2B): the SR, the dyadic cleft, the SL and the bulk cytosol. Compared with ventricular cells, atrial cells usually have smaller size, higher percentage of cytosolic compartment, and lower percentage volume of other compartments. Thus, dimensions and parameters for the related structure in our model were modified accordingly (see Table 2.1).

During a Ca^{2+} release cycle, extracellular Ca^{2+} primarily fluxes via LTCCs into the dyadic cleft and the SL, which initiates CICR. As a result, Ca^{2+} in the cleft peaks at a high value and then diffuses into the cytosol through the SL compartment. The extruding of Ca^{2+} is predominately accomplished by SERCA (>80%), whilst the NCX and the Ca^{2+} pump contribute the rest of the Ca^{2+} removal, to a smaller extent [118].

2.4.1 Ryanodine Receptor, RyR

The formulations for RyR were based on the model of mouse ventricular myocyte [106], where EC_{50} of RyR was reduced by 10% to match the fractional Ca^{2+} release data from experiments (Figure 2.11E).

The RyR Markov chain model has four states (Figure 2.10A), with strong dependence of RyR gating upon dyadic Ca^{2+} concentration ($[Ca^{2+}]_{dyad}$). During a normal CICR, some RyR channels promptly open (O) and rapidly transit into the inactivated states (I) as Ca^{2+} diffuses out of the dyadic cleft (Figure 2.10B). These channels then become resting inactivated states (RI) and eventually return to the resting states (R) (Figure 2.10C). The rate of Ca^{2+} release from the SR was 5.2 mM/s with a Ca^{2+} leakage rate of 0.36 μM/s (Figure 2.10D).

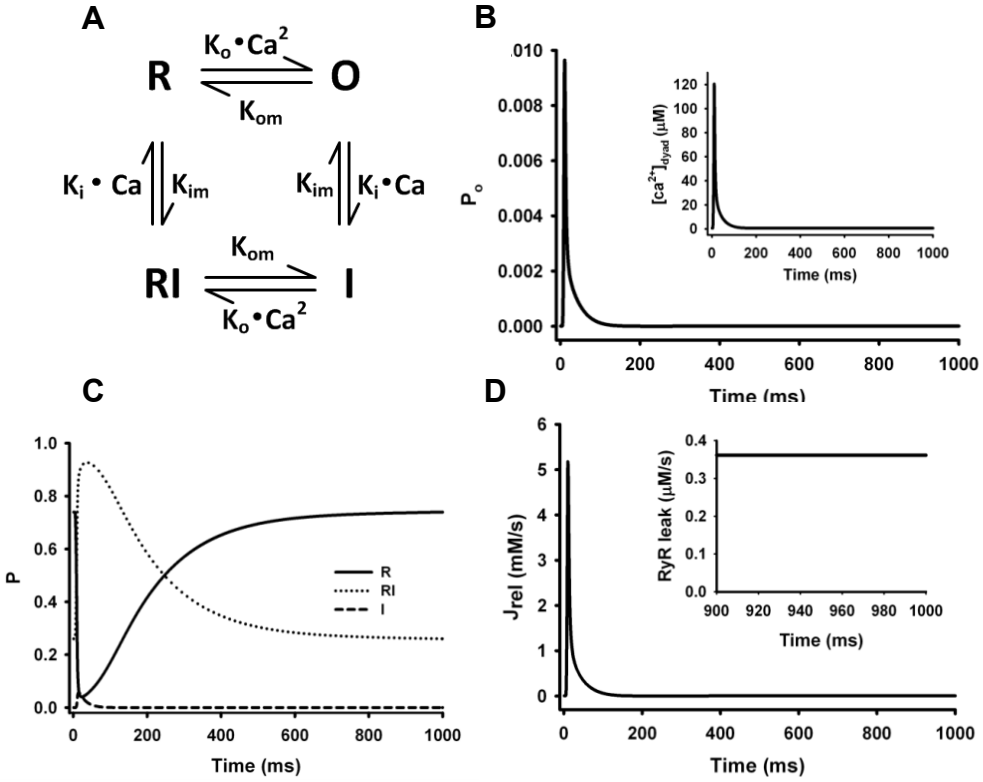

Figure 2.10 RyR in the mouse atrial model. **A**: Markov chain model of the RyR. **B**: Time-dependent profile of the channel open state with Ca transient in the dyadic cleft (inset). **C**: Channel profile of the resting (R), resting inactivated (RI) and inactivated (I) state during an AP. **D**: SR Ca release flux with RyR-dependent SR Ca leak (inset). All states were recorded under 1Hz pacing frequency.

2.4.2 Sarco/endoplasmic Reticulum Ca^{2+}-ATPase, SERCA

The SERCA resides in the SR and serves to uptake Ca^{2+} from the cytosol to the lumen of the SR and to cause muscle relaxation by lowering the $[Ca^{2+}]_i$ [148]. The uptake rate of SERCA is regulated by the protein PLB. When PLB is combined with SERCA, the uptake rate is decreased; when PLB is detached, the uptake rate is then increased [149].

The SERCA in our mouse atrial model was based on the model of Morotti et al. [106], where a few changes were made due to the regional differences observed from experiments. Compared to ventricular myocytes in many mammals, Ca^{2+} uptake by SERCA from cytosol is enhanced in atrial myocytes due to the higher expression of SERCA and lower expression of PLB [120, 150, 151]. Therefore, the SERCA activity was enhanced in our model by increasing the maximum turnover rate (V_{max}, by 65%) and the affinity in the forward mode (K_{mf}, by 13%). In addition, the total PLB concentration was reduced by 40%. Since there were no direct electrophysiological data on these parameters, all changes were estimated from the differences of the protein level, and parameters were optimised in order to reproduce the intracellular Ca^{2+} kinetics seen from experiments (Figure 2.11).

2.4.3 Intracellular Ca^{2+} Transient

The intracellular Ca^{2+} transient is a result affected by various factors in combination. To reproduce the dynamics of the $[Ca^{2+}]_i$ transient measured from experiments, several parameters were modified (as described previously): the results were in line with the experimental data.

Figure 2.11 shows the results of the $[Ca^{2+}]_i$ transient compared with experimental data at 1Hz pacing frequency. The diastolic $[Ca^{2+}]_i$ was 0.09μM in our model (Figure 2.11A). As suggested by Walden et al. [118], there was no apparent difference in the diastolic $[Ca^{2+}]_i$ between murine ventricular and atrial myocytes. The peak amplitude of the $[Ca^{2+}]_i$ transient was 2.3 times higher than the basal level (Figure 2.11A), and 37% smaller than the peak amplitude in the ventricular myocytes, which were consistent with

the experimental finding [118]. The time to peak of $[Ca^{2+}]_i$ transient and time constant for the decay phase were 22.2 ms and 111.0 ms, respectively (Figure 2.11C and D), while in the ventricular model they were 38.7 ms and 149.5 ms, respectively. The accelerated rate of decay phase in murine atrial myocytes has been reported by Walden et al. [118]. Although there is no direct evidence for the faster time to peak in the murine atria, a similar time shortening was found in human myocytes [152]. Moreover, the fractional SR Ca^{2+} release in our model was 48% (Figure 2.11 E), similar to most of the experimental data.

Ca^{2+} fluxes play a key role in the regulation of ECC [153, 154]. The mouse atrial model can closely resemble the experimental data of Ca^{2+} fluxes. Figure 2.12 shows the behaviour of major Ca^{2+} fluxes during a cardiac cycle. The fluxes of simulated SR Ca^{2+} release (J_{rel}) were smaller and much slower than those in ventricular myocytes (Figure 2.12B), which may be due to the structural differences between the two cell types and the smaller number of Ca^{2+} fluxes that induced Ca^{2+} release in the atrial myocyte. The peak value of J_{rel} is 2.0mM/s, which was similar to the experimental observation [155]. Ca^{2+} influx through the LTCC (J_{CaL}) was also smaller than that in the ventricular model (Figure 2.12D), and peaked at 0.35 mM/s, which was close to the experimental estimates of 0.30 mM/s [20]. Due to the lack of experimental data for Ca^{2+} fluxes through SERCA (J_{SERCA}) and NCX (J_{NCX}), we simply compared them in the atrial model with the ventricular model. J_{SERCA} and J_{NCX} both showed a lower magnitude in the atrial model than those in the ventricular model (Figure 2.12C and E). Ca^{2+} removal by the three systems in the atrial and ventricular models was also measured (Figure 2.12F). In the ventricular model, SERCA, NCX and the Ca pump contributed 82.5%, 15.9% and 1.6% of the overall Ca^{2+} removal, respectively. In the atrial model, the predominant removal mediator, SERCA, increased the contribution to 91.5%, with NCX significantly dropping to 7.2%. These results for Ca^{2+} removal were closely similar to the experimental observations in rat atrium (SERCA and NCX contributed 92.6% and 6.13% of the total Ca^{2+} removal) [118].

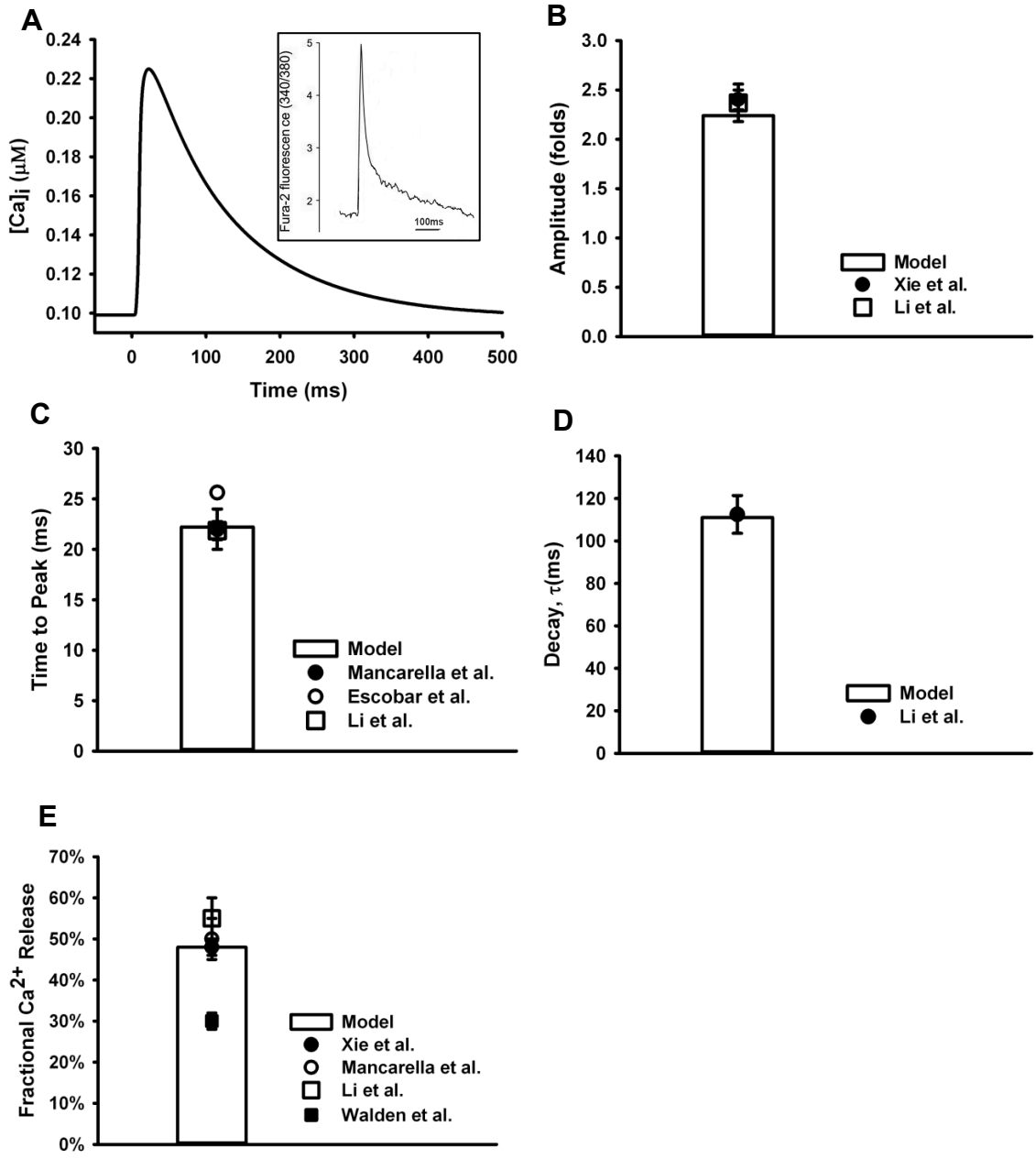

Figure 2.11 Intracellular Ca^{2+} transient in the atrial myocyte model and experiments. **A**: Time course of $[Ca^{2+}]_i$ transient under 1Hz pacing frequency. The inset shows the experimental trace of $[Ca^{2+}]_i$ which was recorded in mouse isolated right atrial myocytes loaded with fura 2-AM. Figure adapted from [108]. **B**: $[Ca^{2+}]_i$ amplitude. **C**: Time to the peak of $[Ca^{2+}]_i$. **D**: Time constant for the decay phase of $[Ca^{2+}]_i$. **E**: Fractional Ca^{2+} release. (Experimental data: Xie et al. [116], Li et al. [78], Mancarella et al. [108], Escobar et al. [156], Walden et al. [118])

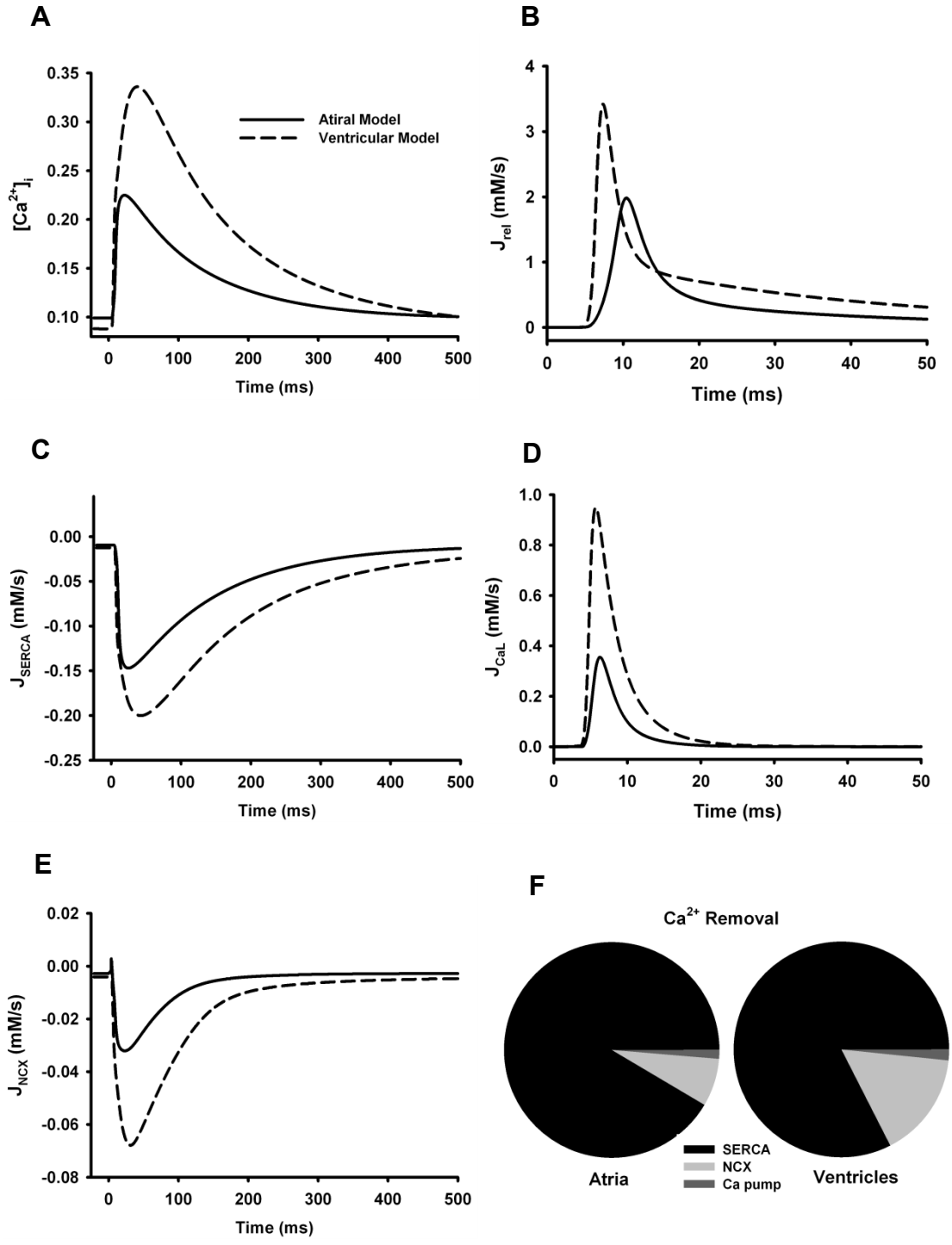

Figure 2.12 Comparison of Ca^{2+} fluxes during one cardiac cycle between the model of atrial and ventricular myocyte. **A**: $[Ca^{2+}]_i$ transients, **B**: Fluxes from the SR **C**: Fluxes from the SERCA, **D**: Fluxes from the LTCC. **E**: Fluxes from the NCX. **F**: Ca^{2+} removal contributed by SERCA, NCX and Ca pump.

2.5 Modelling of CaMKII Regulation

2.5.1 CaM, CaN and CaMKII Modules

The CaM, CaN and CaMKII modules were adapted from the model of Saucerman and Bers [157]. No modifications were made, since there were no available data on modulation for the mouse atrial myocyte.

As discussed in Chapter 1 (Section 1.3), CaM can bind four Ca ions: two to the C-terminal EF-hand with higher affinity and two to the N-terminal EF hand with lower affinity. This could be modelled as a sequential two-step process (Figure 2.13), where the associate and dissociate rate constants were in agreement with experimental studies [158]. The CaM buffer was also included with a 100-fold slower dissociation rate when in Ca-bound states than when Ca-free. It has been also reported that the Ca binding is $[Mg^{2+}]$ and $[K^{+}]$ dependent [159, 160]; therefore, the model also incorporates this condition.

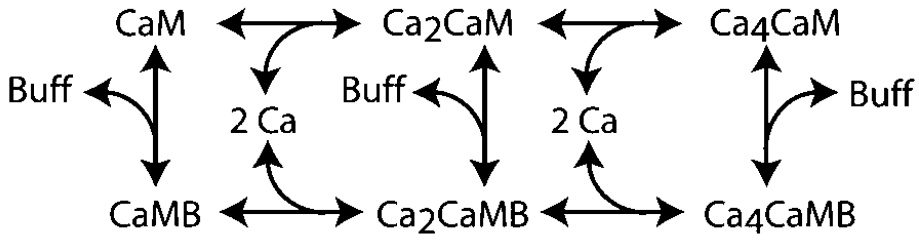

Figure 2.13 Reaction map for Ca binding to CaM along with binding of CaM buffers. Figure adapted from [157].

The module of CaN was modelled as a multistep binding model (Figure 2.14), where Ca_4CaMCaN exhibited 100% activity, whereas Ca_4CaN, CaMCaN, and Ca_2CaMCaN showed 10% activity. The model bound only the second pair of Ca ions to CaN, since the first two Ca sites were saturated even in the presence of strong Ca chelators [160].

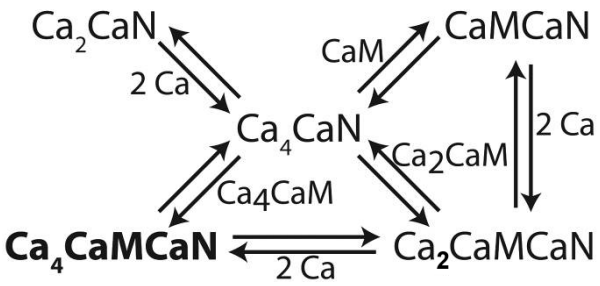

Figure 2.14 Reaction map for reversible binding of CaM, Ca_2CaM and Ca_4CaM to CaN. Figure adapted from [157].

CaMKII activation was modelled in such a way that Ca_2CaM bound CaMKII and then recruited additional Ca to form active Ca_4CaM/CaMKII, even though Ca_2CaM/CaMKII itself could exhibit <7% activity. Once activated, it was capable of auto-phosphorylation and was dephosphorylated by PP1 (Figure 2.15). The six modelled CaMKII states were: inactive (P_i); Ca_2CaM-bound (P_{b2}); Ca_4CaM-bound (P_b); Thr287P and Ca_4CaM-bound (P_t); Thr287P and Ca_2CaM-bound (P_{t2}); and Thr287P but CaM-autonomous (P_a). The active CaMKII states were P_b, P_t, P_{t2} and P_a.

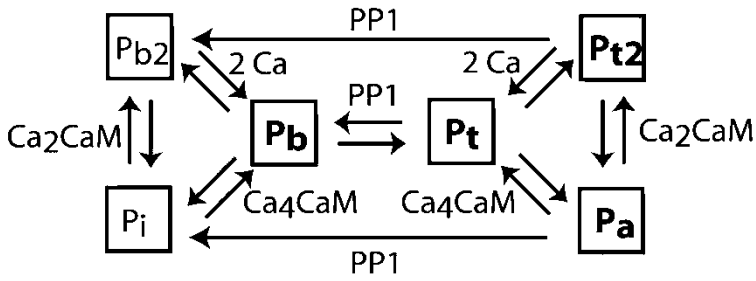

Figure 2.15 Reaction map for the activation of CaMKII. P_{b2} stands for inactivate Ca_2CaM-bound; P_b is the active Ca_4CaM-bound; P_i is the inactivate state; Pt is the auto-phosphorylation with Ca_4CaM trapped; P_{t2} is the active Ca_2CaM-bound; P_a is the auto-phosphorylated CaM-autonomous state. Figure adapted from [157].

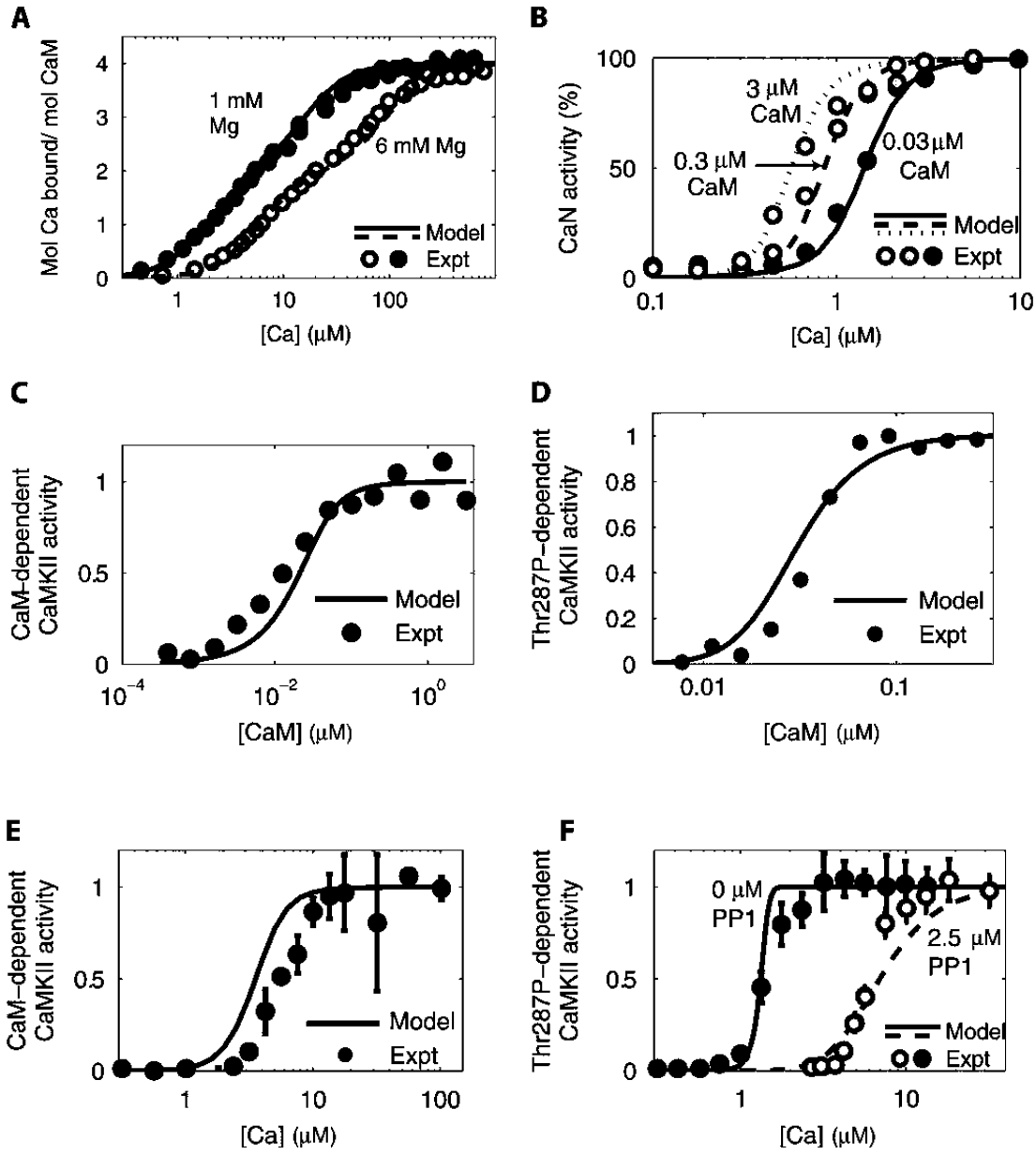

Figure 2.16 Validation of modules of CaM, CaN and CaMKII. **A**: Model-predicted Ca binding to CaM at 1 mM or 6 mM [Mg^{2+}] and 100 mM [K^{+}]. **B**: Predicted [Ca^{2+}] versus CaN activity for 0.03, 0.3 and 3μM CaM. **C** and **D**: Predicted [CaM] versus CaM-dependent CaMKII activity (**C**) and CaMKII-Thr287 activity (**D**). **E**: Predicted [Ca^{2+}] versus CaM-dependent CaMKII activity, compared with independent CaMKII. **F**: Predicted Thr287-dependent CaMKII activity for 0 or 2.5 μM [PP1]. Figures are reproduced from [157].

In Figure 2.16, predicted results were compared with experimental data to assess the models of CaM, CaN and CaMKII. Figure 2.16A shows the results of Ca binding to CaM with increasing [Ca^{2+}] under two different [Mg^{2+}], which agree with the experimental observations [160]. The simulated CaN activities with different [Ca^{2+}] for [CaM] of 0.03, 0.3, and 3μM are consistent with experimental data [160]. The CaM-dependent and Thr^{287}-autophosphorylation-dependent activities of CaMKII versus [CaM] are shown in Figure 2.16C and Figure 2.16D: they are also similar to the experimental observations [161]. The relationship between [Ca^{2+}] and CaM-dependent CaMKII activity is shown in Figure 2.16E and the relationship between [Ca^{2+}] and Thr^{287}-autophosphorylation-dependent CaMKII activity is presented in Figure 2.16F. In addition, the results of PP1-dependent dephosphorylation are presented in Figure 2.16F. These results shown are also consistent with experimental data [162].

2.5.2 CaMKII Phosphorylation on ECC Targets

2.5.2.1 LTCC Module

LTCCs can be phosphorylated by CaMKII at several sites, including Ser^{1512} and Ser^{1570} on the α subunit [163, 164], and Thr^{498} on the β_{2a} subunit [165], and can be dephosphorylated by PP1 [166]. As indicated in the model of Shannon et al. [147], assuming 90% of the cell membrane was dyadic cleft and the remaining 10% was SL, total [LTCC] was set to 28.3 μM and 84.6 nM in the dyadic cleft and SL, respectively [100].

Studies have demonstrated that LTCC is modulated via I_{CaL} facilitation upon phosphorylation, resulting in a larger peak current and slower inactivation of the channel kinetics [32], as well as a longer channel opening of LTCC at high activity gating modes (termed *mode 2*, whereas non-phosphorylated LTCC is termed *mode 1*) [33]. In order to model these effects, the seven-state Markov chain model of LTCC (Figure 2.4A) was divided into four sets with different channel kinetics: two for mode 1 in the dyadic cleft and SL, and an additional two for mode 2 in each compartment. The parameters in our

model were left unaltered from the ventricular model, where the maximum distribution of mode 2 was 10% [106].

The results of LTCC phosphorylation by CaMKII are shown in Figure 2.17. LTCC open probability for the two modes was assessed by the voltage clamp protocol, as shown in Figure 2.17A (inset). The peak channel open probability during 0mV voltage clamp was increased from ~0.05 in mode 1 to ~0.25 in mode 2 [33], with a relatively slower inactivation rate. The peak current density during 1Hz pacing frequency was increased from 10.7 pA/pF to 12.6 pA/pF, and the distribution of mode 2 LTCC showed a six-fold increase from CaMKII knockout condition to the control condition (Figure 2.17B).

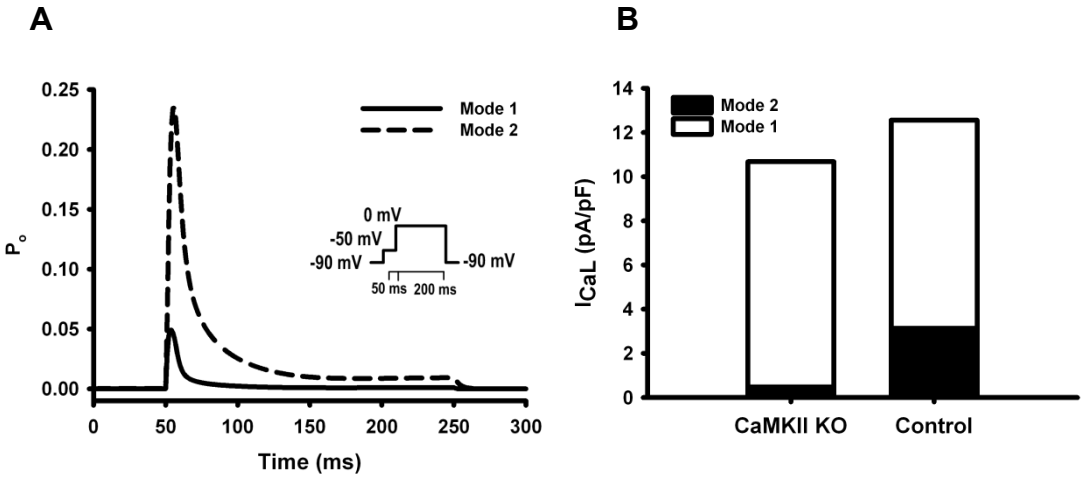

Figure 2.17 Effects of LTCC phosphorylation by CaMKII. **A**: Dynamic changes of LTCC open probability in mode 1 and mode 2 during voltage clamp. **B**: Comparison of I_{CaL} and distribution of mode 1 and mode 2 for CaMKII knockout and control condition.

2.5.2.2 RyR Module

Upon CaMKII phosphorylation, the sensitivity of RyRs for Ca^{2+} is enhanced [34]. Under basal conditions, ~15% of the phosphorylation site of Ser^{2815} is reported to be independent of CaMKII activity [167]. To reproduce these findings, EC_{50} of RyR (EC_{50SR}), the rate constant responsible for Ca^{2+}-dependent open probability (K_{oSR}) and the rate of SR leak (K_{leak}) were modified as functions of CaMKII-dependent phosphorylation [100]. The CaMKII-independent basal phosphorylation rate was

modelled as a process against PP1/PP2A dephosphorylation.

The phosphorylation effects on these parameters are summarised in Table 2.4. As compared with the control condition, CaMKII knockout (CaMKII-KO) revealed a slight increase in EC_{50} of the SR, a slight decrease in K_{leak}, and a half-fold reduction in K_{oSR}, whereas a 100% RyR phosphorylation by CaMKII showed a decrease in EC_{50} by 64% and significant 8-fold and 3-fold increases in K_{oSR} and K_{leak}, respectively.

	CaMKII-KO	**Max Phosphorylation**
EC_{50SR} (mM)	16% ↑	64% ↓
K_{oSR} (mM^{-2} ms^{-1})	50% ↓	800% ↑
K_{leak} (ms^{-1})	13% ↓	300% ↑

Table 2.4 Changes of parameters in the CaMKII knockout and full phosphorylation conditions as compared with control condition (1Hz pacing frequency).

2.5.2.3 PLB Module

PLB acts to negatively regulate the SERCA. Upon phosphorylation by CaMKII, the inhibitory action by PLB is relieved. Thus SERCA can freely uptake Ca^{2+} into the SR lumen during diastole [168]. To mimic the phosphorylation effects on SERCA, K_{mf} (forward mode rate) was modified as a function of CaMKII-dependent PLB phosphorylation. The maximum inhibitory effect in our mouse atrial model was decreased from 50% to 25%, as suggested by studies that the expression of PLB is lower in atria than that in ventricles [23, 50, 51].

2.6 Results

2.6.1 Mouse Action Potential

The simulated time course of the mouse atrial AP and major underlying currents are shown in Figure 2.18, together with the corresponding AP and currents in the mouse

ventricular AP [106]. The magnitudes of most currents in the mouse atrial myocyte were smaller than those in the ventricular myocyte (I_{Na}, I_{CaL}, I_{to}, I_{Kur}, I_{K1}, I_{NCX}, and I_{NaK}). The slower upstroke velocity in the atrial myocyte was attributable to the half-fold decrease in I_{Na}. The smaller Ca^{2+} entry through LTCC may be due to the smaller cleft space in the atrial myocyte [109]. Since total inward current was decreased, repolarising currents were reduced accordingly. I_{Kr} and I_{ss} in the model showed an increase in order to maintain a reasonable APD.

Figure 2.19 shows characteristics of simulated AP under 1Hz pacing frequency, compared with experimental data. The AP amplitude (APA) was 93 mV, slightly smaller than 100mV in the ventricular model. The maximal upstroke velocity (dV/dt_{max}) was 130 V/s in the atrial model, about a half-fold reduction from that in the ventricular model. There was no significant difference between the atrial and ventricular models for the resting potential (RP). APDs at 25%, 50%, 75% and 90% repolarisation were termed APD_{25}, APD_{50}, APD_{75} and APD_{90}, respectively. The APD_{90} and APD_{50} showed a wide range of experimental data, which may be due to different factors for the experiment, such as temperature, pacing frequency, species or method. Our model aimed to fit the experimental data at body temperature and to consider the relationship with the ventricular model. Knollmann et al. reported that APD_{90} in mouse atrial myocyte was shorter than that in ventricular myocyte [169]. Thus, taking these factors into account, the APD_{90} in our model was 26.0 ms, slightly shorter than 27.3 ms in ventricles. APD_{50} was 6 ms and 5.6 ms in the atrial and ventricular myocyte, respectively. Moreover, APD_{25}, APD_{50} and APD_{75} were normalised to APD_{90} to assess these APDs in the same cell. As shown in Figure 2.19, the above characteristics were all in agreement with experimental data.

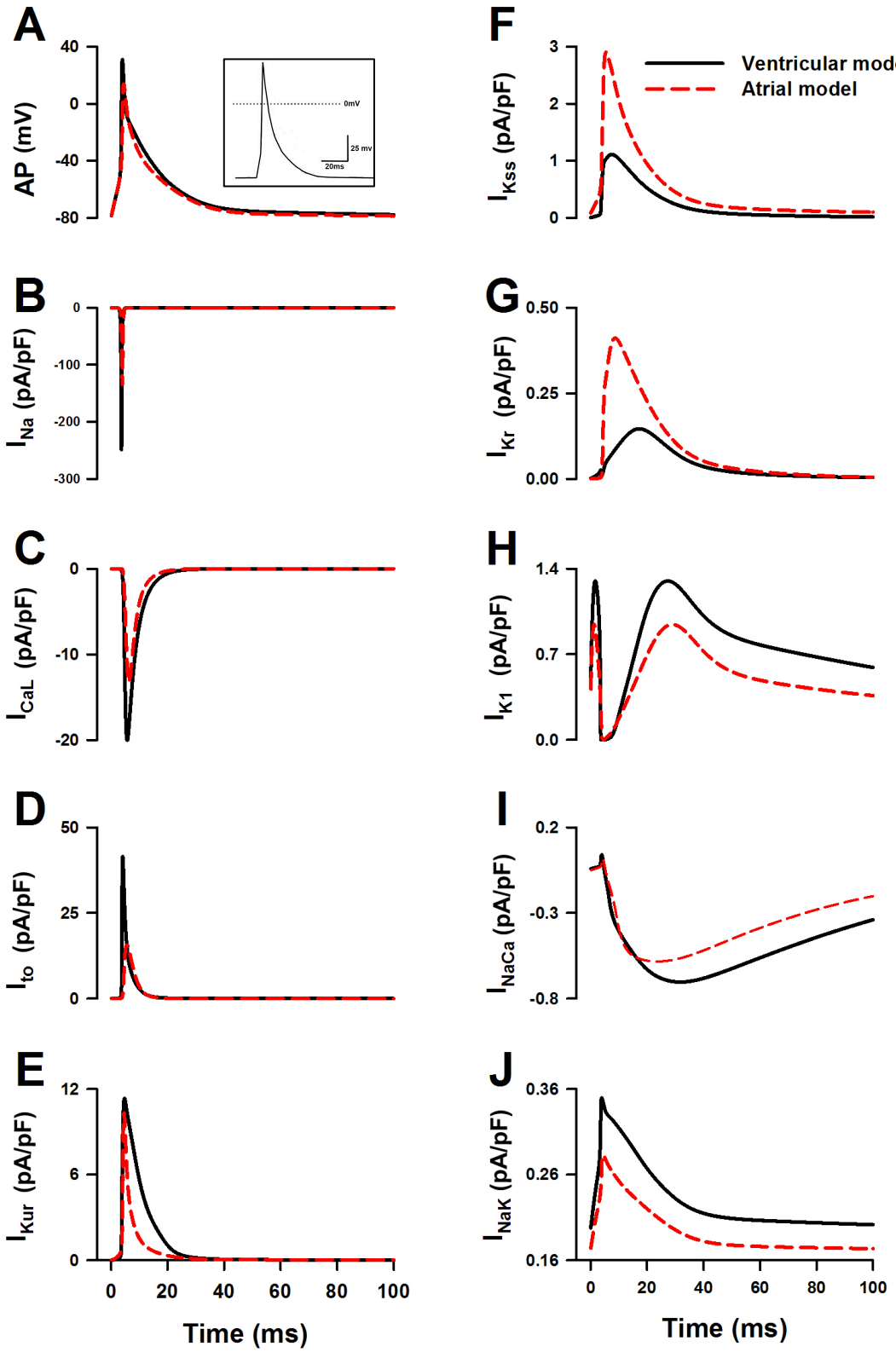

Figure 2.18 Mouse AP and major underlying currents at steady-state with 1Hz pacing frequency for ventricle (black) and atrium (red). The inset in panel A shows an experimental record of mouse atrial AP [111].

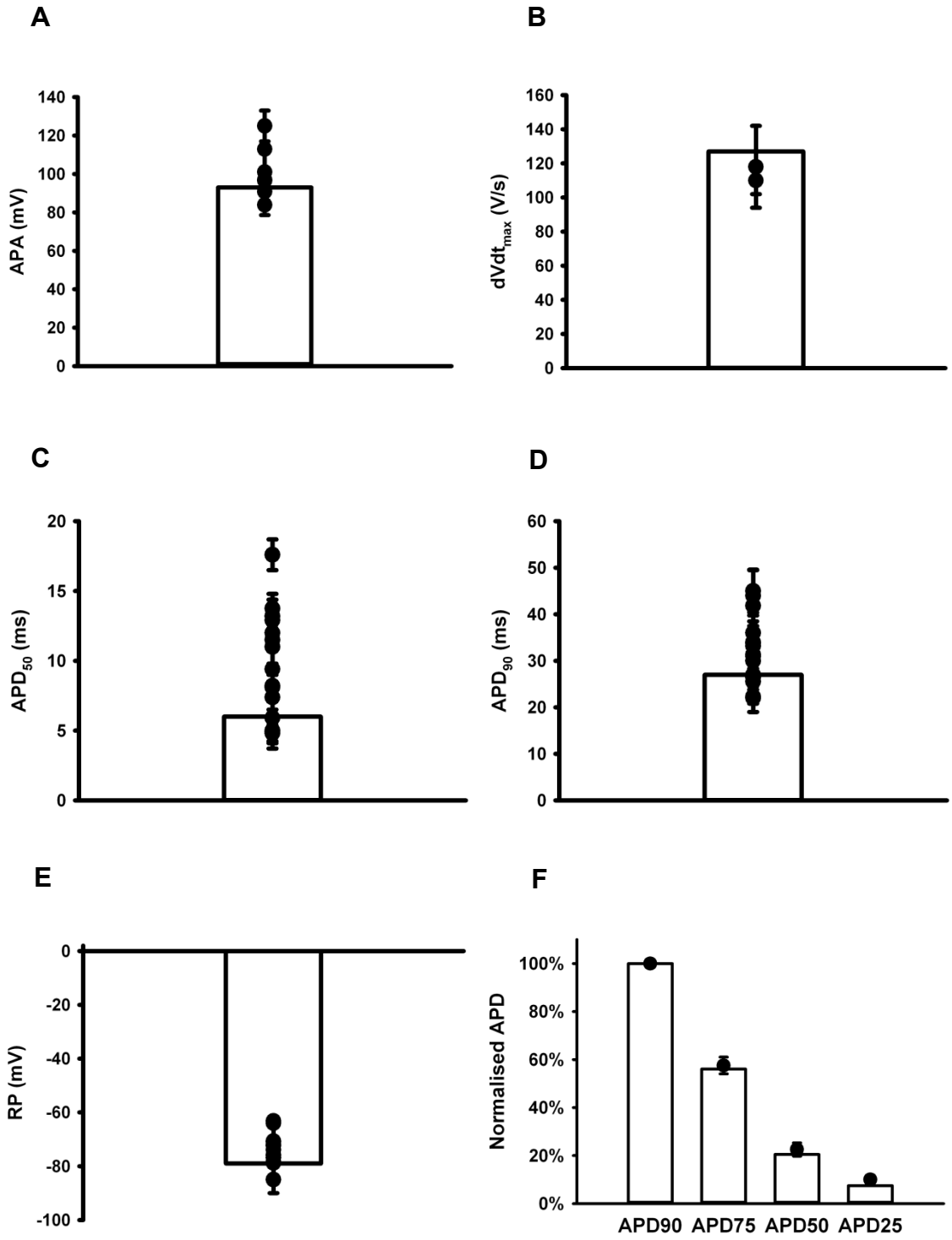

Figure 2.19 Comparison between simulated and experimental records of AP characteristics under room temperature. **A**: Action potential amplitude. **B**: Maximal upstroke velocity. **C**: APD_{90}. **D**: APD_{50}. **E**: Resting potential. **F**: APD_{25}, APD_{50} and APD_{75} that normalised to APD_{90} [170]. Experimental data are listed in Table 2.5.

Ref	BCL (ms)	APA (mV)	RP (mV)	APD_{50} (ms)	APD_{90} (ms)
Room Temperature					
Lemoine [127]	500			12	85±2
Qin [135]	150		-78.3±1.8	12.9±1.1	29.7±2.9
Lomax [111]	120		-72.4±1.5	10.97±1.77	44.03±5.49
Xu [133]	500	125±8	-64±1	5.0±0.9	27±8
Trepanier-Boulay [113]		96.9	-73.9±1.1	4.81±0.57	22.34±1.45
Hu [140]			-63.2±1.1		19.00±1.89 (APD80)
Reil [171]			-70.9±0.9		24.8±7.3 (APD70)
Lomax [172]			-70.7±7.9	8.1±1.6	33.2±5.3
Hirose [13]	150			13.51±1.72 (APD80)	
Hua [173]	150		-76.9±0.2	8.2±0.9	45±4.6
Body Temperature					
Xie [116]	200			4.91±1.2	36.06±1.5
Nygren [14]	130				13.75±0.63 (APD70)
Koh [174]	1000	90.8±4.6	-78.8±1.6		90.4±21.8
Verheule [175]	150	97.07±3.71	-76.83±1.38		41.84±2.08
Saegusa [176]	200				25.56
Bagwe [177]	200	101±11	-85±5	11.5±3.3	34±1.1
Knollmann [169]	130			9.4±0.4	31±1.7
Odening [178]					27±8
Nakamura [114]	300	112.9±1.9	-82.0±0.8	17.6±1.1	69.0±4.5
Glukhov [179]	200				33.75±1.89
Doutova [180]	125			5.9±0.3	22±0.5
Choi [181]	150				33.0±8.4 (APD80)
Xiao [131]	100	96.5±3.1	-76.1±0.61	41.5±3.0	120±7.1
Chelu [182]	200			13.2±0.5	24±1 (APD80)
King [110]	125	83.92±5.3	75.8±1.4	7.38	26.42±1.9
Faggioni [15]	100				31.33±3.6

Table 2.5 Experimental data for the basic cycle length (BCL), action potential amplitude (APA), resting potential (RP), APD_{50} and APD_{90} under room and body temperature in the mouse atrial myocyte.

2.6.2 Frequency Dependence

The frequency dependence of APD was measured at different stimulation frequencies (Figure 2.20). APD_{90} was decreased from 26ms (1Hz frequency) with increasing pacing frequency and gradually approached 21ms (>15Hz) (Figure 2.20A), which was consistent with experimental data of mouse atrium [174]. APD_{25} and APD_{50}, however, were slightly prolonged with increasing pacing frequency. APD_{75} was barely changed when pacing frequency was larger than 1Hz (Figure 2.20A). These tendencies were similar to the observations from experiments in rat atrium [170].

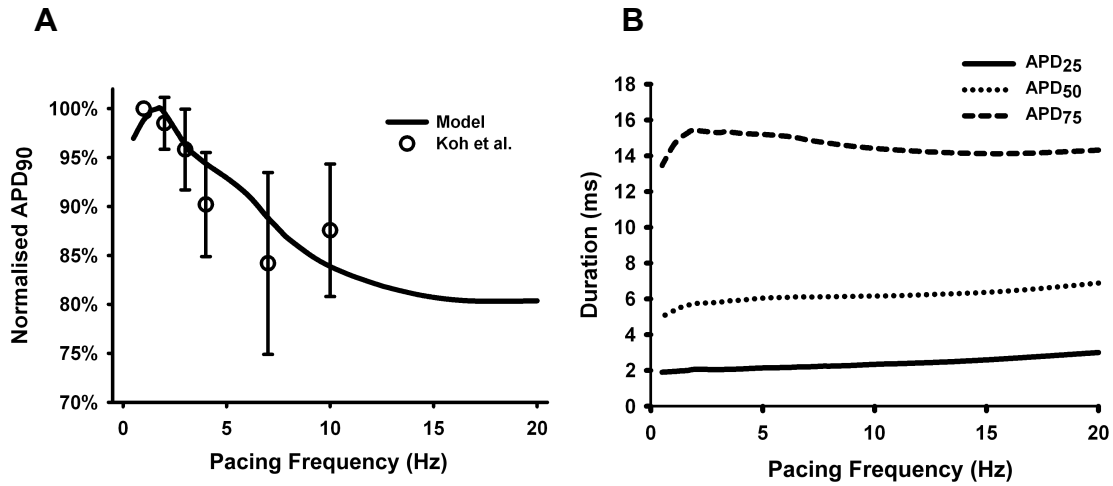

Figure 2.20 Frequency dependence of APDs. **A**: APD_{90} versus pacing frequency. APD_{90} is normalised to the value at 1Hz rate. **B**: Frequency dependence of APD_{25}, APD_{50} and APD_{75}.

Since there were no available data on other frequency-dependent profiles for the mouse atria, comparisons between the atrial and ventricular models [106] were made. As shown in Figure 2.21, the atrial model reveals a moderate change in diastolic $[Ca^{2+}]_i$ and maximal amplitude, compared with the ventricular model. This may be due to the fact that less expression of PLB allows enhanced SERCA activity that uptakes Ca^{2+} effectively from cytosol (Figure 2.21A and B). The intracellular sodium concentration ($[Na^+]_i$) showed similar frequency-dependence, apart from the amplitude difference caused by the reduction of I_{NaK} in the atrial myocyte (Figure 2.21D).

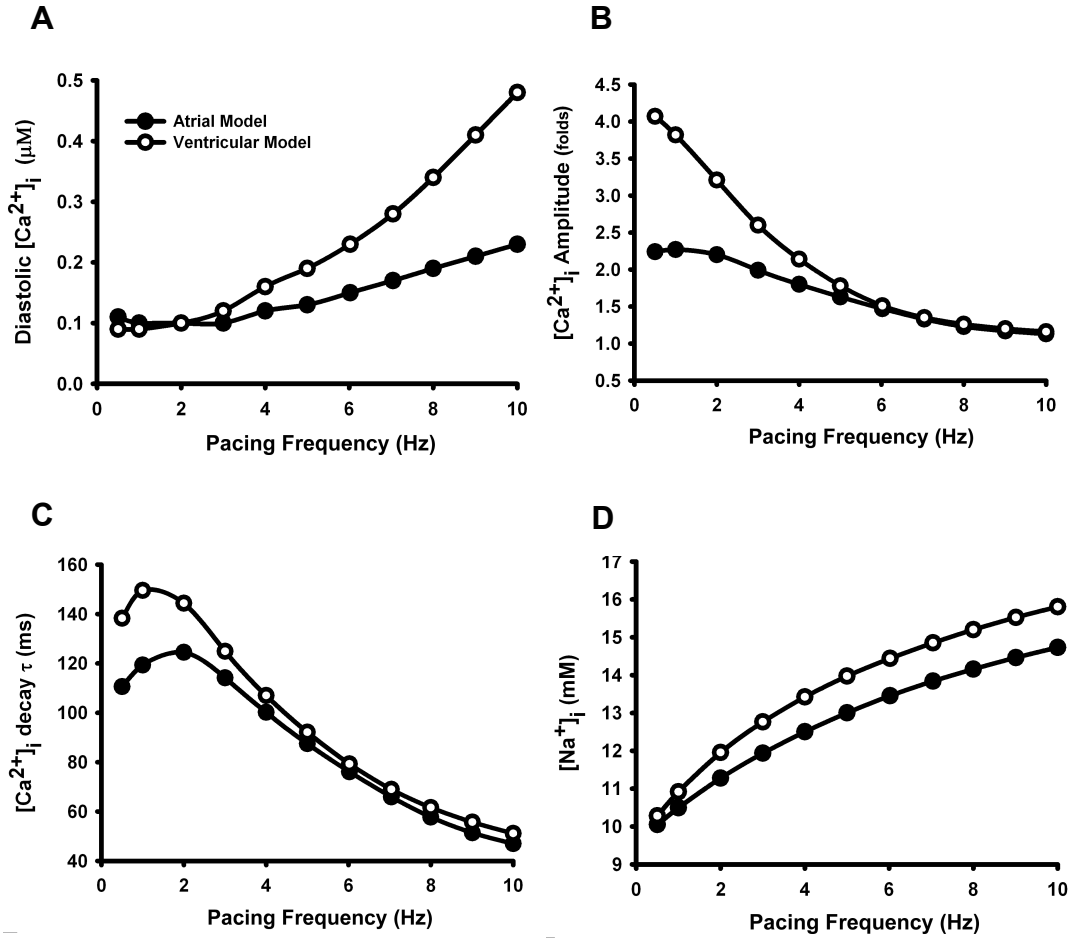

Figure 2.21 Comparison of frequency-dependent intracellular Ca^{2+} and Na^{+} between atrial and ventricular models. **A**: Diastolic $[Ca^{2+}]_i$. **B**: $[Ca^{2+}]_i$ amplitude (peak systolic $[Ca^{2+}]_i$ over diastolic $[Ca^{2+}]_i$). **C**: Time constant for the decay phase of $[Ca^{2+}]_i$. **D**: Steady-state intracellular $[Na^{+}]$ during diastole.

Interestingly, the time constant for the $[Ca^{2+}]_i$ decay phase increased at pacing frequencies less than 1-2Hz and then decreased monotonically for frequencies above 1-2Hz. The $[Ca^{2+}]_i$ decay was mainly determined by SERCA and NCX. With increasing pacing frequency, SERCA activity was enhanced leading to more rapid decay, while NCX was weakened leading to prolongation of the decay (Figure 2.22). Therefore, with increasing pacing frequency, there must exist a certain pacing frequency at which SERCA takes over the major influence on the decay rate of $[Ca^{2+}]_i$.

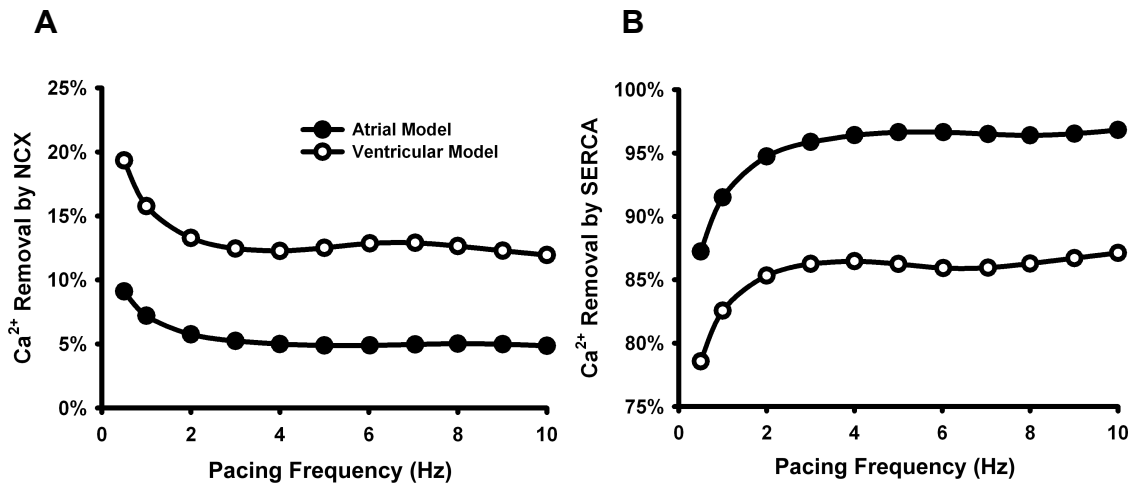

Figure 2.22 Frequency-dependent Ca^{2+} removal activity by NCX (A) and SERCA (B). The percentage indicates the Ca^{2+} removal by NCX (A) or SERCA (B) to the overall Ca^{2+} during diastole.

2.6.3 CaMKII-mediated Phosphorylation

CaMKII-mediated phosphorylation levels (percentage of total phosphorylated substrates) increase with higher pacing frequency, although levels and kinetics are quantitatively distinct. Figure 2.23 shows the time course of CaMKII phosphorylation profiles during stimulation at low (1Hz) and higher (4Hz) frequency. When initially pacing at 1Hz and switching to 4Hz at 5s in the atrial model, LTCC exhibited moderate (~60%) to high (88%) phosphorylation activity within a few beats, whereas RyR and PLB took more beats to achieve a steady level of phosphorylation. RyR phosphorylation level was increased from ~20% to 31% and the level in PLB was increased from ~1.0% to 2.8%.

Compared with ventricular profiles at 4Hz pacing frequency, the PLB phosphorylation level in the atrial model was relatively larger, while CaMKII phosphorylation of LTCC and RyR revealed similar levels. The frequency-dependent phosphorylations for LTCC, RyR and PLB are shown in Figure 2.24. There were no significant differences for the phosphorylation of LTCC and RyR between the two cell types. Phosphorylation of PLB in the atrial model, however, exhibited a higher level of phosphorylation as compared with the ventricular model: this is because a lesser amount of PLB was expressed in the atrial model. Although PLB showed a higher percentage of

phosphorylation, its overall inhibitory effect on SERCA was actually weakened because of the reduced PLB, as compared with that in ventricular myocyte model.

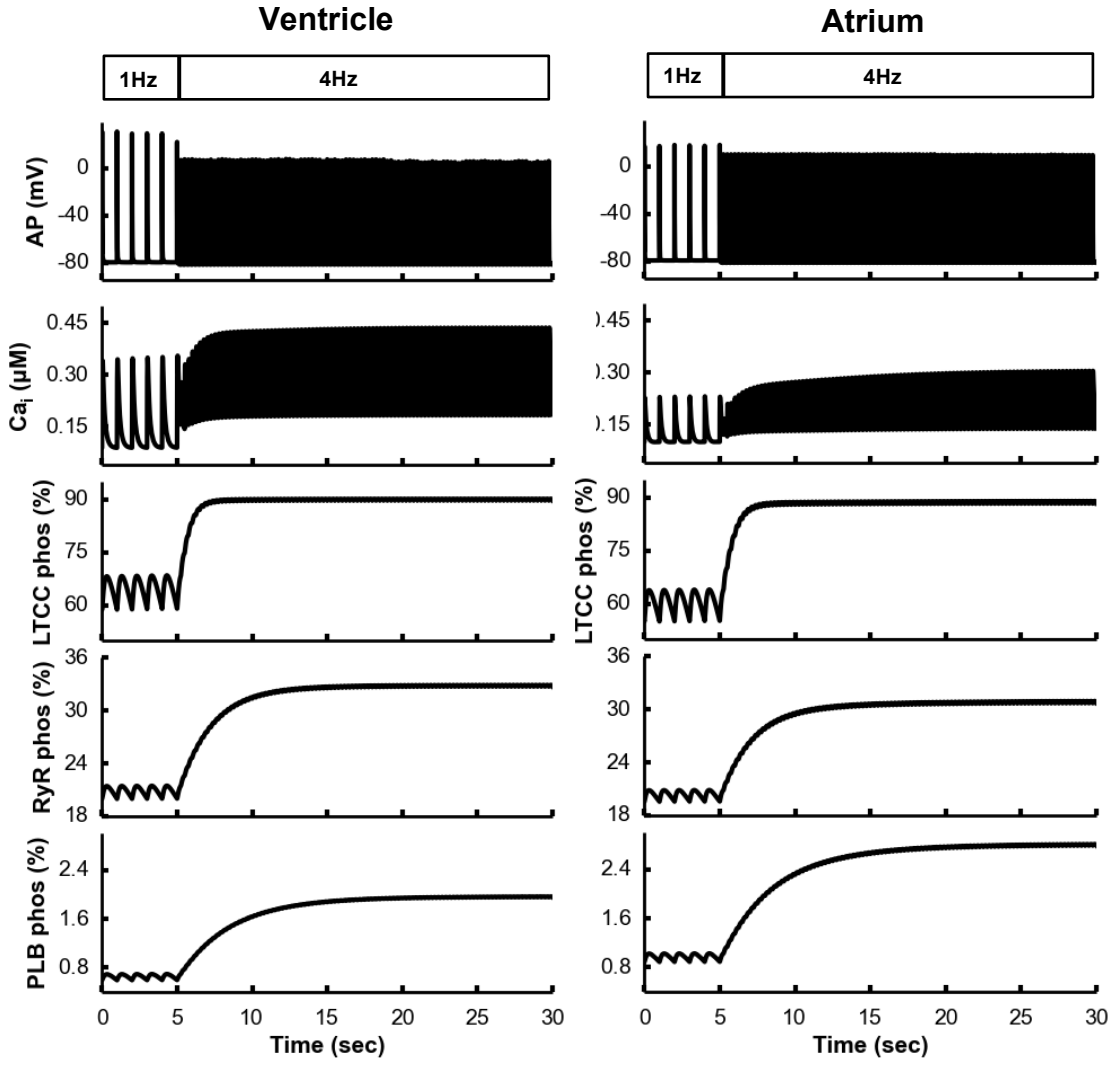

Figure 2.23 Time course of CaMKII phosphorylation in atrial (right panels) and ventricular models (left panels). The model was paced to steady state at 1Hz and switched to 4Hz at 5s.

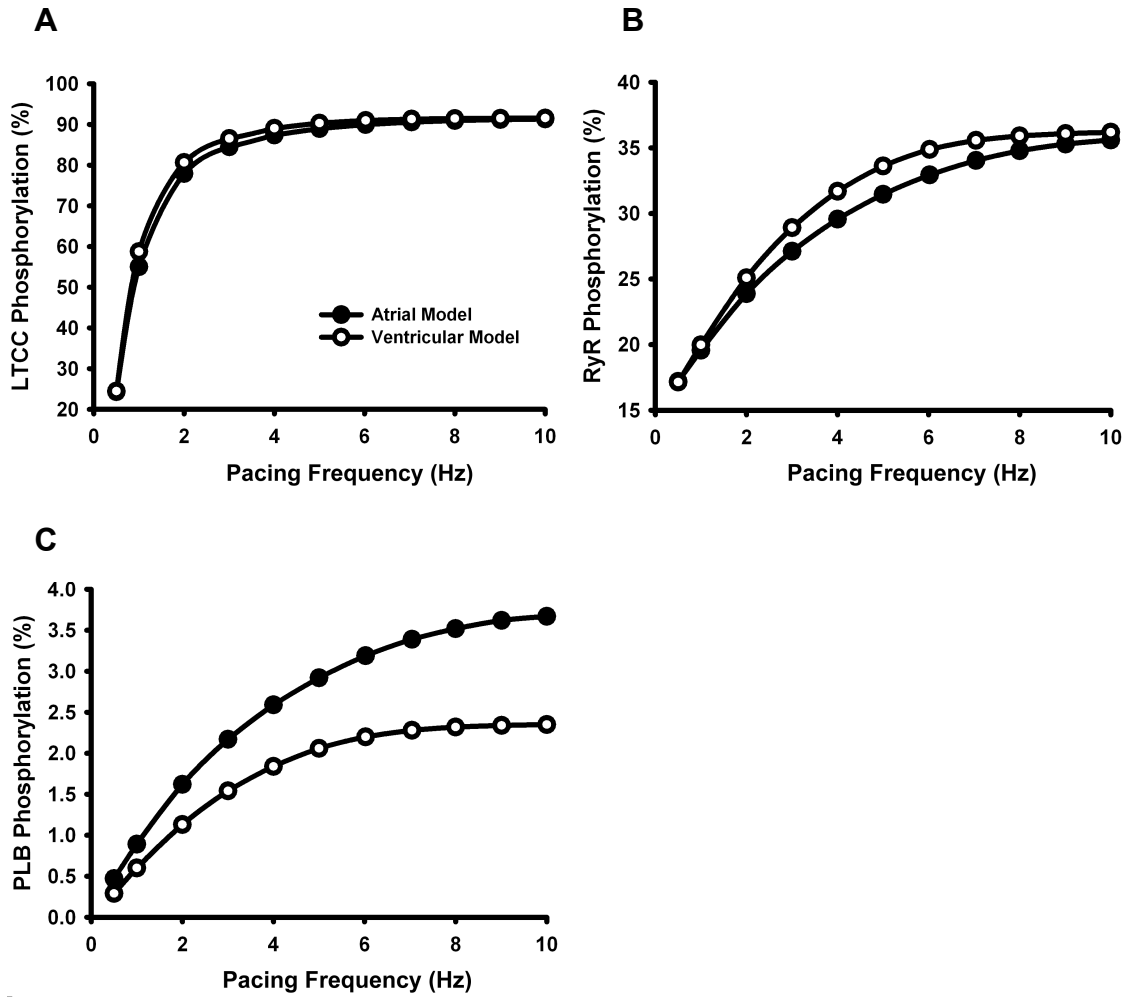

Figure 2.24 Comparison of frequency-dependent CaMKII phosphorylation for atrial and ventricular models. Phosphorylation levels in LTCC (**A**), RyR (**B**), and PLB (**C**).

It has been hypothesised that CaMKII participates in frequency-dependent acceleration of relaxation (FDAR) [56, 183-185]. FDAR is an intrinsic physiological mechanism that allows more rapid ventricular diastolic filling at higher heart rates. To test if our model is able to reproduce this effect, a similar pacing protocol as above was set. FDAR was quantified as the time constant of $[Ca^{2+}]_i$ during the decay phase (τ_{decay}). Specifically, during a 30s stimulation from 1Hz switching to 4Hz, time constants for each beat were recorded and compared with the CaMKII knockout model. In addition, the ventricular model was also tested and all values of τ_{decay} were normalised to the one at 1Hz pacing frequency for comparison (Figure 2.25).

Results in Figure 2.25 show that both atrial and ventricular models exhibited rapid FDAR adaptation from pacing frequency of 1Hz to 4Hz, where τ_{decay} reached steady state within 3s. However, the atrial model without CaMKII showed a slow FDAR, where a longer time (>10s) was needed for τ_{decay} to reach the steady state.

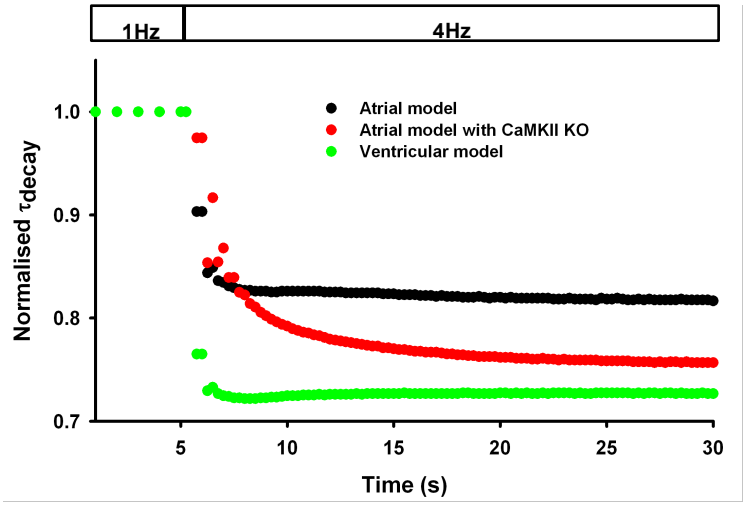

Figure 2.25 CaMKII-mediated enhancement of FDAR. Time constants of $[Ca^{2+}]_i$ during decay phase (τ_{decay}) were normalised to the value at 1Hz pacing frequency. Models were paced to steady state at 1Hz and switched to 4Hz at 5s.

2.7 Summary

A new biophysically detailed model for the mouse atrial cell has been developed. The model was primarily based on the model of Morotti et al. [106]. Three potassium currents were developed using Markov chain formulism (I_{to}, I_{Kur} and I_{Kr}); cell geometry and other membrane currents were updated (I_{Na}, I_{NaL}, I_{CaL}, I_{ss}, I_{K1}, I_{pCa}, I_{NCX} and I_{NaK}); intracellular Ca^{2+} handling was modified (RyR, SERCA); and the CaMKII phosphorylation module was adjusted. All changes were made based on the experimental data. The model was validated by its ability to reproduce the morphology of APs, characteristics of Ca^{2+} transients, frequency-dependence and FDAR adaptation that were similar to the observations from experiments.

Chapter 3 - Proarrhythmic Effects of Overexpression of CaMKII

3.1 Introduction

CaMKII is a multifunctional protein kinase expressed extensively in the heart. It can phosphorylate and alter the function of many substrates in atrial myocytes [25]. CaMKII phosphorylation of LTCC promotes I_{CaL} facilitation, which results in a larger current density, slower kinetics of channel inactivation [32], and shift to high-activity mode-2 gating [33]. CaMKII phosphorylation of RyR can enhance sensitising to Ca^{2+} [34]. CaMKII phosphorylation of PLB is able to increase sensitivity for Ca^{2+} of SERCA [37]. Evidence has shown that CaMKII phosphorylation may also regulate other membrane currents (I_{Na}, I_{NaL}, I_{Kur}, I_{to}, I_{K1}, and I_{NCX}) [38-40, 186]. These regulations ensure an effective adaptation to increased heart rate.

Dysregulation of CaMKII could be associated with cardiac abnormalities. CaMKII blockade and genetic inhibition of RyR Ser^{2814} phosphorylation have been proved to prevent ventricular tachycardia induction [187]. Excessive CaMKII activity has been associated with sinus node disease due to Ca^{2+} overload which induces increased reactive oxygen species production and causes SAN cell damage or death [188]. CaMKII protein expression and activity are also linked to atrial fibrillation (AF). Hyperactivities of CaMKII were observed in dogs with pacing-induced atrial tachycardia remodelling [189], goats with long-standing AF [190], and patients with chronic AF [191, 192].

Based on the developed mouse atrial model as described in Chapter 2, models with acute and chronic CaMKII overexpression (CaMKII-OE) were developed. We aimed to examine how CaMKII-OE affects individual phosphorylation targets, AP, and Ca^{2+} handling. It has been reported that elevated $[Na^+]_i$ may result in $[Ca^{2+}]_i$ overload in heart failure and further activate CaMKII to enhance target phosphorylation, thus creating a CaMKII-Na^+-Ca^{2+}-CaMKII feedback [193]. We simulated and analysed the fast pacing induced AF, and the mechanisms of CaMKII-Na^+-Ca^{2+}-CaMKII feedback and its impact

on AP abnormalities.

3.2 Development of CaMKII-OE Model

To model the effects of overexpression of CaMKII, several modifications were made to the newly developed atrial mouse model (WT model). These changes are summarised in Table 3.1. Ca^{2+} handling units (LTCC, RyR and SERCA) were not altered since they are able to respond dynamically to the increase in total CaMKII ($CaMKII_{tot}$). The $CaMKII_{tot}$ was increased six-fold. A similar effect was implemented in a CaMKII-OE model of the ventricular myocyte [106].

Targets	Changes
$CaMKII_{tot}$	Six-fold increase in the total CaMKII.
I_{Na}	The steady-state inactivation curve was shifted by 3.25mV to more negative voltages.
I_{NaL}	Inactivation curve was shifted by 6.8mV to more positive voltages.
I_{to}	Rate constant (K_{f_to}) was increased five-fold.
I_{K1}	Current density was decreased by 40%.
I_{NCX}	Current density was increased by 30%.

Table 3.1 Changes of parameters in the CaMKII-OE model.

3.2.1 Fast Na^+ Currents, I_{Na}

Studies have shown that CaMKII phosphorylation of Na channels results in a slowed recovery from inactivation [38, 39]. To mimic CaMKII-OE effects on I_{Na}, the steady-state inactivation curve was shifted by 3.25mV to more negative voltages [106]. Figure 3.1A illustrates the steady-state activation and inactivation curves. CaMKII-OE and WT models shared the same activation kinetics except for that the inactivation curve for the CaMKII-OE model was shifted to more negative potentials. Figure 3.1B shows

the peak current density for I_{Na} during an AP at 1Hz pacing frequency. Notably, although the parameter for the conductance of I_{Na} was not altered in the CaMKII-OE model, the peak current density was significantly reduced, which was attributable to the slowed inactivation decreasing I_{Na} availability [194].

To evaluate the effect of CaMKII-OE modulated I_{Na} on AP, the CaMKII-OE model was further investigated in such a way that CaMKII only phosphorylated I_{Na}, eliminating phosphorylation effects for all other targets. As shown in Figure 3.1C and D, dV/dt_{max} and amplitude decreased by 28% and 9%, respectively; APD_{50} and APD_{90}.increased by 21% and 4%, respectively.

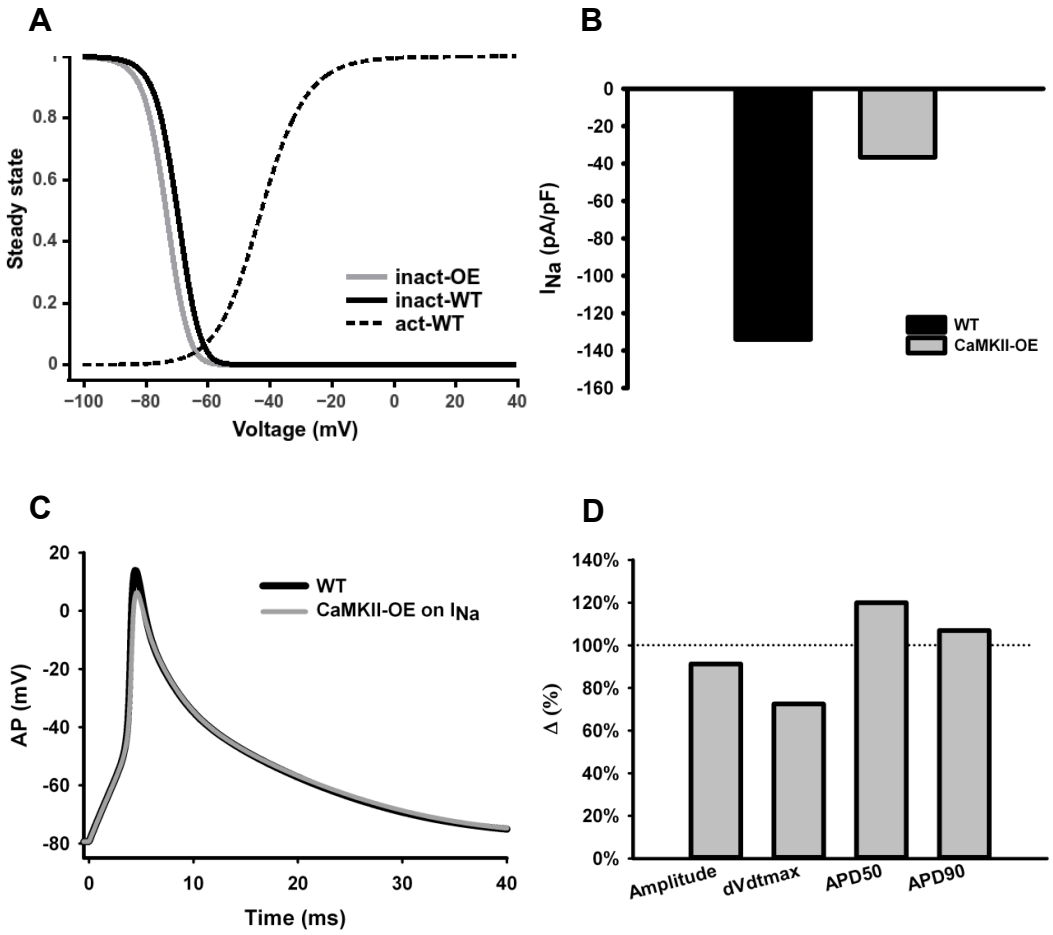

Figure 3.1 Influence of CaMKII-OE on I_{Na}. **A**: Steady-state activation curve for WT and inactivation curves in WT and CaMKII-OE models. **B**: Peak I_{Na} during a normal AP at 1Hz pacing frequency. **C**: APs in the conditions of WT and CaMKII-OE that simply regulated I_{Na}. **D**: Changes in AP profiles for the CaMKII-OE where I_{Na} was the only target.

3.2.2 Late Na^+ Currents, I_{NaL}

Experimental studies on CaMKII phosphorylation of late Na^+ channel have shown that CaMKII increases the current density of I_{NaL} [188] and slows the decay phase, and shifts steady-state inactivation to more positive voltages [39]. In our CaMKII-OE model, this was achieved by shifting the inactivation curve by 6.8mV to more positive potentials [188] (Figure 3.2A). The resultant peak current density of I_{NaL} during an AP was doubled compared with the WT model (Figure 3.2B). The individual role of phosphorylation on I_{NaL} under CaMKII-OE in shaping AP was investigated. As shown in Figure 3.2C and D, APD_{50} and systolic $[Ca^{2+}]_i$ were slightly augmented, whereas other profiles of AP and $[Na^+]_i$ were not noticeably changed due to the small current density of I_{NaL} compared with other currents.

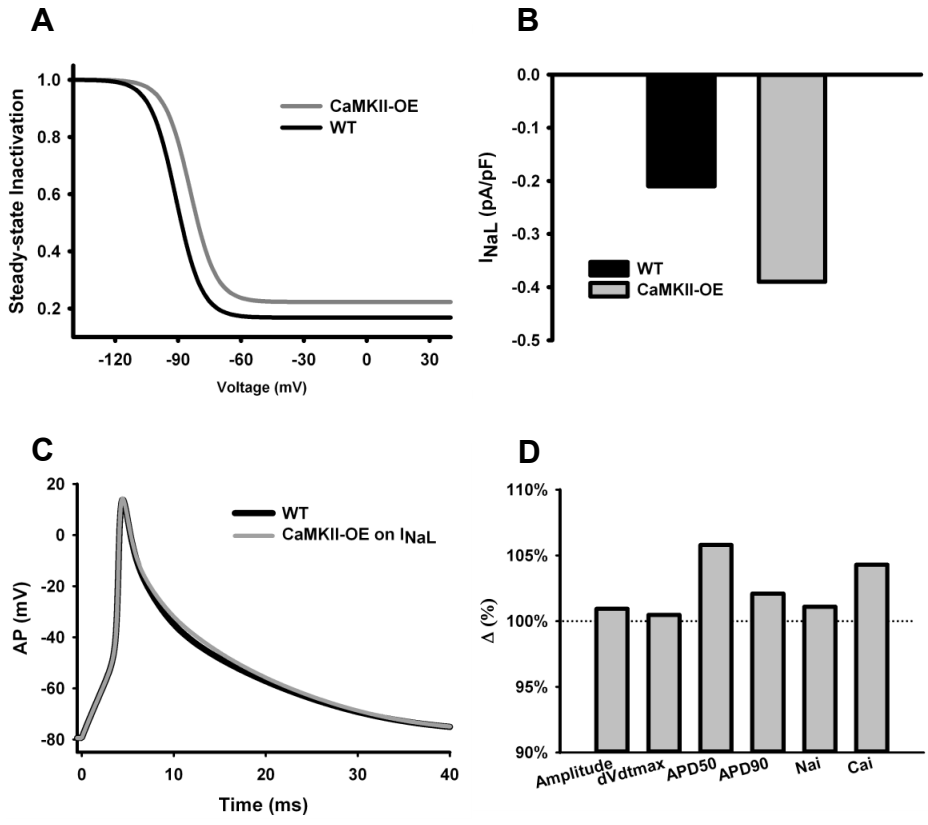

Figure 3.2 Influence of CaMKII-OE on I_{NaL}. **A**: Steady-state inactivation curves for CaMKII-OE and WT. **B**: Peak I_{NaL} during a normal AP at 1Hz pacing frequency. **C**: APs in WT and CaMKII-OE which regulated only I_{NaL}. **D**: Changes in AP profiles, $[Na^+]_i$ and systolic $[Ca^{2+}]_i$ for the CaMKII-OE that regulated only I_{Na}.

3.2.3 Transient Outward K^+ Current, I_{to}

Evidence has been provided that CaMKII phosphorylation of I_{to} results in an accelerated recovery from inactivation in the presence of CaMKII-OE [40]. In the CaMKII-OE model, the rate constant (K_{f_to}) governing transition rate from close and open states to inactivated states of I_{to} was increased five-fold to reproduce the kinetics seen from experiments [40].

Figure 3.3 illustrates the results of I_{to} kinetics in the CaMKII-OE model compared with WT. The curve of recovery from inactivation was determined by applying two 500-ms pulses to +35mV from a holding potential of -75mV (Figure 3.3A). The first pulse (P1) was followed by the second pulse (P2) after an interstimulus interval of 0-500ms, in 25ms increments. The peak amplitudes after applying P2 were recorded and normalised to their maximum value. Compared with the WT model, I_{to} recovery from inactivation was much faster in the CaMKII-OE model, which agreed with the observation from experiment [40].

To plot the steady-state inactivation curve for I_{to}, a two-pulse of 500ms protocol was applied. The first was from the holding potential of -75 mV to potentials between -105 mV and +35mV in 10-mV increments; the second was from the holding potential of -75 mV to potentials between -105 mV and +50mV. The peak amplitudes after applying the second stimulus were recorded and normalised to their maximum value. As shown in Figure 3.3B, the steady-state inactivation curve was shifted to the negative potentials.

Figure 3.3C shows the I-V relationship in both models, where I_{to} revealed much smaller current density in the CaMKII-OE model for each testing voltage, which was in good agreement with experimental findings [40]. Figure 3.3D shows the peak current density of I_{to} during an AP. There was a significant reduction of I_{to} in the CaMKII-OE model, compared with the WT model.

Simulations that solely incorporated I_{to} phosphorylation under CaMKII-OE were performed. As shown in Figure 3.3E and F, APD_{50} was significantly prolonged. APD_{90} and systolic $[Ca^{2+}]_i$ also exhibited mild increases. No marked changes were observed in

amplitude, dV/dt_{max} and $[Na^+]_i$.

3.2.4 Inward Rectifying K^+ Current, I_{K1}

A reduction in amplitude of inward rectifier K^+ current (I_{K1}) has been observed in a mouse transgenic study of CaMKII-OE [40]. Accordingly, in our CaMKII-OE model, the maximum conductance of I_{K1} was decreased by 40%. As shown in Figure 3.4, the WT model with I_{K1} decreasing by 40% resulted in a marked increase of APD_{90}, whereas other AP profiles were hardly altrered.

3.2.5 Na^+-Ca^{2+} Exchanger Current, I_{NCX}

Transgenic mouse study has estimated that overexpression of CaMKII promoted the function of NCX by 30% [35]. In order to account for this increase, a scale factor for NCX maximum current in the CaMKII-OE model was introduced (130%). Individual phosphorylation of I_{NCX} in the CaMKII-OE model at 1Hz pacing frequency exerted no changes to the AP morphology, whereas $[Ca^{2+}]_i$ transients were distinct with that in the WT model. As shown in Figure 3.5, both diastolic and systolic $[Ca^{2+}]_i$ levels were decreased, with an approximately 30% reduction in the peak $[Ca^{2+}]_i$.The time to peak and time constant for the decay phase were prolonged. The enhancement of I_{NCX} limited the amount of Ca^{2+} in the dyadic cleft and SL, which in turn reduced the CICR, leading to decreased Ca^{2+} levels in all compartments.

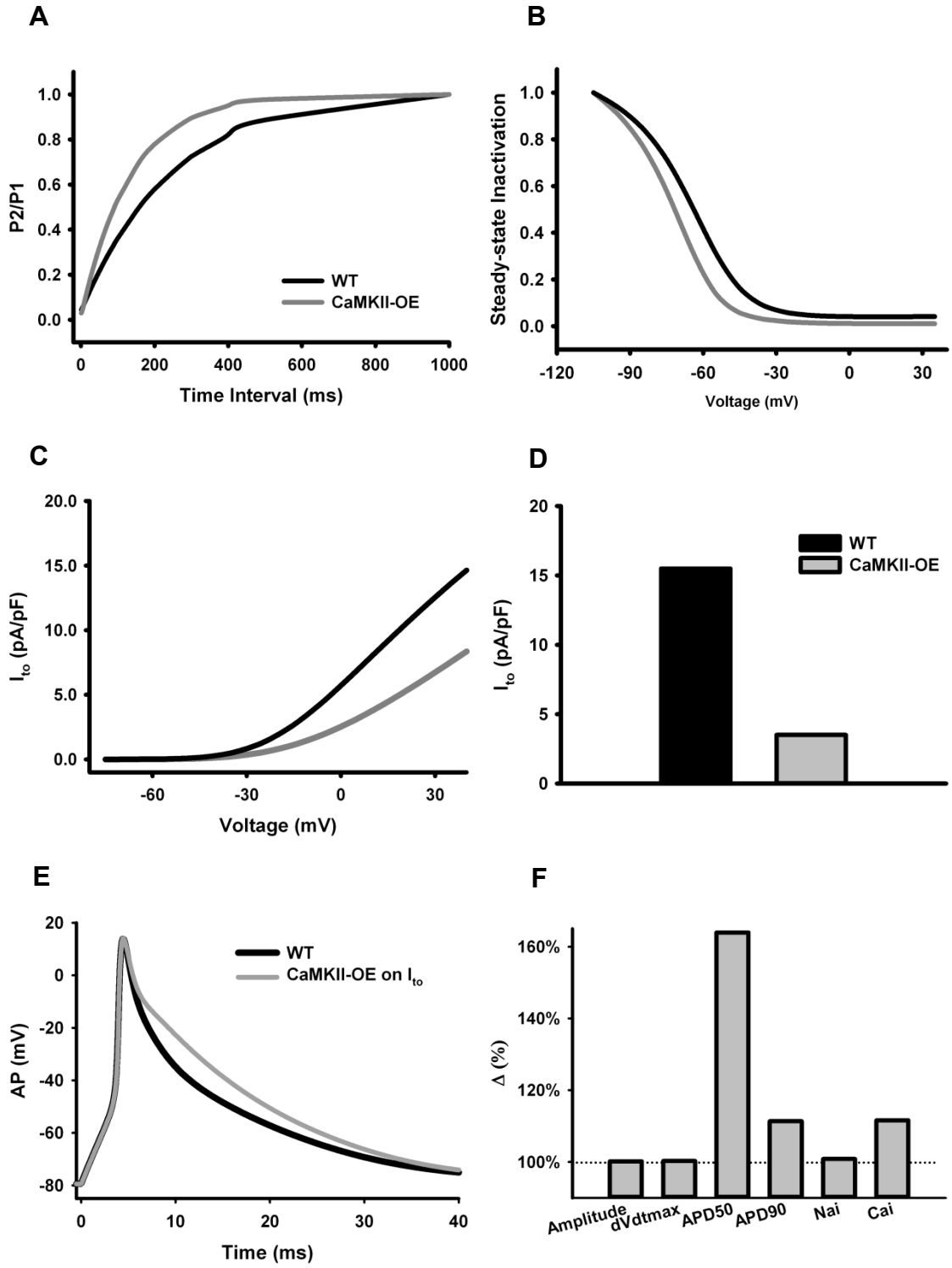

Figure 3.3 Kinetics of I_{to} in the WT and CaMKII-OE models. **A**: Recovery from inactivation curve. **B**: Steady state inactivation. **C**: I-V relationship. **D**: Peak current density. **E** and **F**: Simulations that considered only I_{to} phosphorylation in the CaMKII-OE model. E: APs in WT and CaMKII-OE. F: Changes in AP profiles, $[Na^+]_i$ and systolic $[Ca^{2+}]_i$.

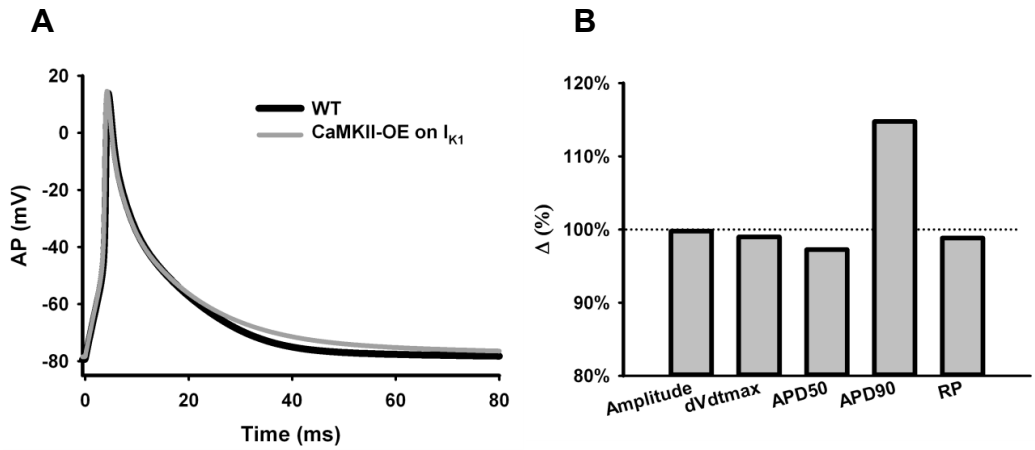

Figure 3.4 Simulations that considered only I_{K1} phosphorylation in the CaMKII-OE model. **A**: APs in WT and CaMKII-OE. **B**: Changes in AP profiles.

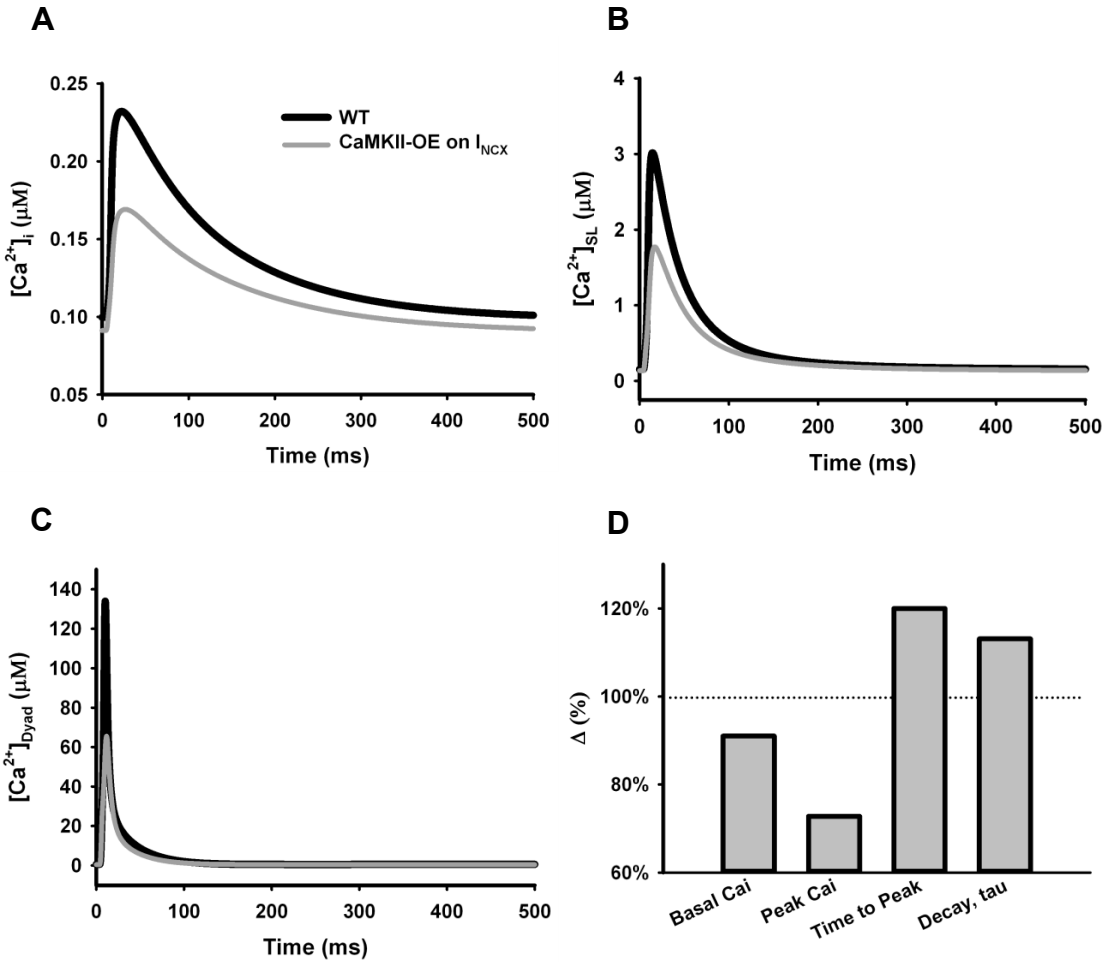

Figure 3.5 Simulations that considered only I_{NCX} phosphorylation in the CaMKII-OE model. **A-C**: Ca^{2+} transients in WT and CaMKII-OE in cytosol (**A**), SL (**B**) and dyad cleft (**C**). **D**: Changes in profiles of $[Ca^{2+}]_i$ transients.

3.3 Proarrhythmic Effects of Chronic CaMKII-OE

Chronic effects were simulated by integrating CaMKII-dependent alterations of I_{NaL}, I_{to}, I_{K1} and I_{NCX} into the WT model. These changes have been identified in studies of chronic CaMKII-OE mice [35, 40, 195].

3.3.1 Effects of Chronic CaMKII-OE on AP

The AP in the chronic CaMKII-OE model was dramatically changed (Figure 3.6A). All tested APDs showed a significant prolongation in the CaMKII-OE model, while a slight decrease occurred in the CaMKII-KO model (Figure 3.6B). The AP in the CaMKII-OE model showed a slightly reduced maximal upstroke velocity from 140V/s to 118V/s, a RP that shifted from -79mV to -77mV and a decreased APA from 94mV to 90mV (Figure 3.6C-E). No significant differences were found in these AP profiles in the CaMKII-KO model. The prolonged APD in the CaMKII-OE model was consistent with the reductions in I_{to} and I_{K1}, and the increase in I_{NaL}, as they were all expected to prolong APDs.

3.3.2 Effects of Chronic CaMKII-OE on Ca^{2+} Handling

The Ca^{2+} transient in the chronic CaMKII-OE model was distinct from that in the WT model (Figure 3.7), featuring a short amplitude with lower diastolic $[Ca^{2+}]_i$ level (Figure 3.7A). There was a slight increase of 5ms in the time to peak and a marked prolongation of 40ms in the time constant for the decay phase of Ca^{2+} transient in the CaMKII-OE model, compared with WT (Figure 3.7B). Additionally, the SR content in the CaMKII-OE model was significantly reduced by about a half (Figure 3.7C), while the SR fractional release was increased by one third (Figure 3.7D). Maier et al. [35] reported that the diastolic $[Ca^{2+}]_i$ level in the CaMKII-OE transgenic mouse ventricules was decreased. They also found reductions in SERCA, RyR and PLB, and an increase in NCX expression. These changes resulted in enhanced Ca^{2+} release from SR, but less (and

slowed) Ca^{2+} uptake from cytosol, which may account for the slowed kinetics of $[Ca^{2+}]_i$ and reduced SR content. Moreover, the CaMKII-OE model exhibited negative frequency dependence (values were decreasing with higher pacing frequencies) in $\Delta[Ca^{2+}]_i$ and a decline rate of $[Ca^{2+}]_i$ (Figure 3.7E and F), similar to the result reported in ventricular myocytes in CaMKII-OE transgenic mice [35].

3.3.3 Effects of Chronic CaMKII-OE on ECC Phosphorylation

In the chronic CaMKII-OE model, CaMKII phosphorylation of LTCC, RyR and PLB increased with higher pacing frequencies, although phosphorylation levels and kinetics were quantitatively different from those in the WT model. LTCCs exhibited markedly high phosphorylation at all frequencies and saturated at lower frequencies (Figure 3.8A). RyR phosphorylation also showed high levels, with ~3-fold increase at all frequencies (Figure 3.8B). PLB phosphorylation level in the CaMKII-OE model was increased from ~10% to ~60% with increasing pacing frequencies from 1Hz to 5Hz, while in the WT model the level remained ~1% at all frequencies (Figure 3.8C).

3.3.4 Effects of Chronic CaMKII-OE on FDAR

To examine the effects of chronic CaMKII-OE on FDAR, a protocol switch from 1Hz to 4Hz was used. FDAR was quantified as the time constant of $[Ca^{2+}]_i$ during the decay phase. As shown in Figure 3.9, in contrast to CaMKII-KO model that took a longer time for τ_{decay} to reach a steady state, both WT and CaMKII-OE models exhibited rapid FDAR adaptation from pacing frequency of 1Hz to 4Hz, where τ_{decay} reached steady state within 3s. Therefore, in the present study, FDAR was demonstrable under both WT and CaMKII-OE conditions, suggesting that CaMKII levels do not greatly alter FDAR. These results agreed with the experimental observations [35].

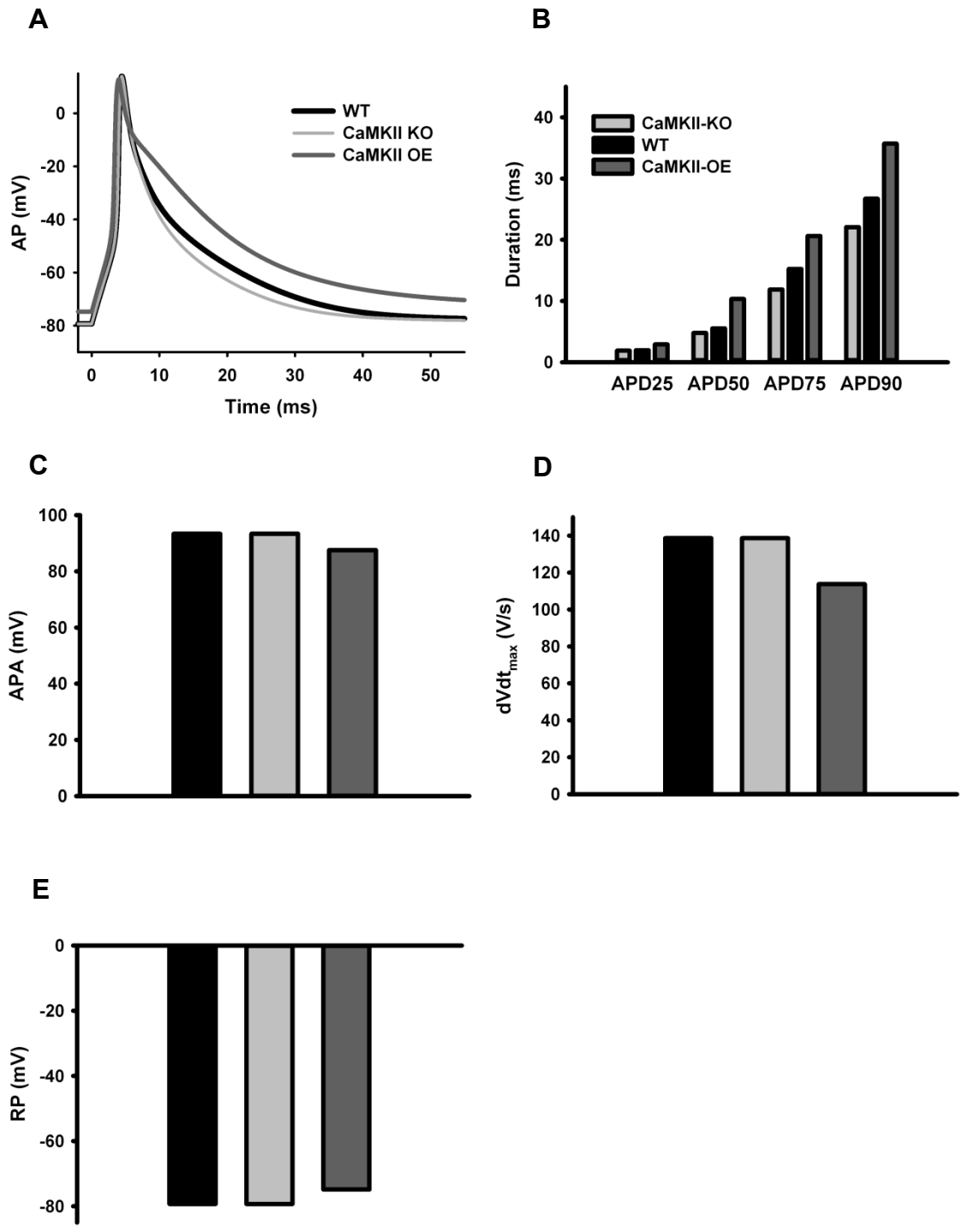

Figure 3.6 AP profiles in WT, CaMKII-KO and CaMKII-OE models at 1Hz pacing frequency, illustrating the shapes of AP (**A**), APDs (**B**), APA (**C**), dV/dt_{max} (**D**), and RP (**E**).

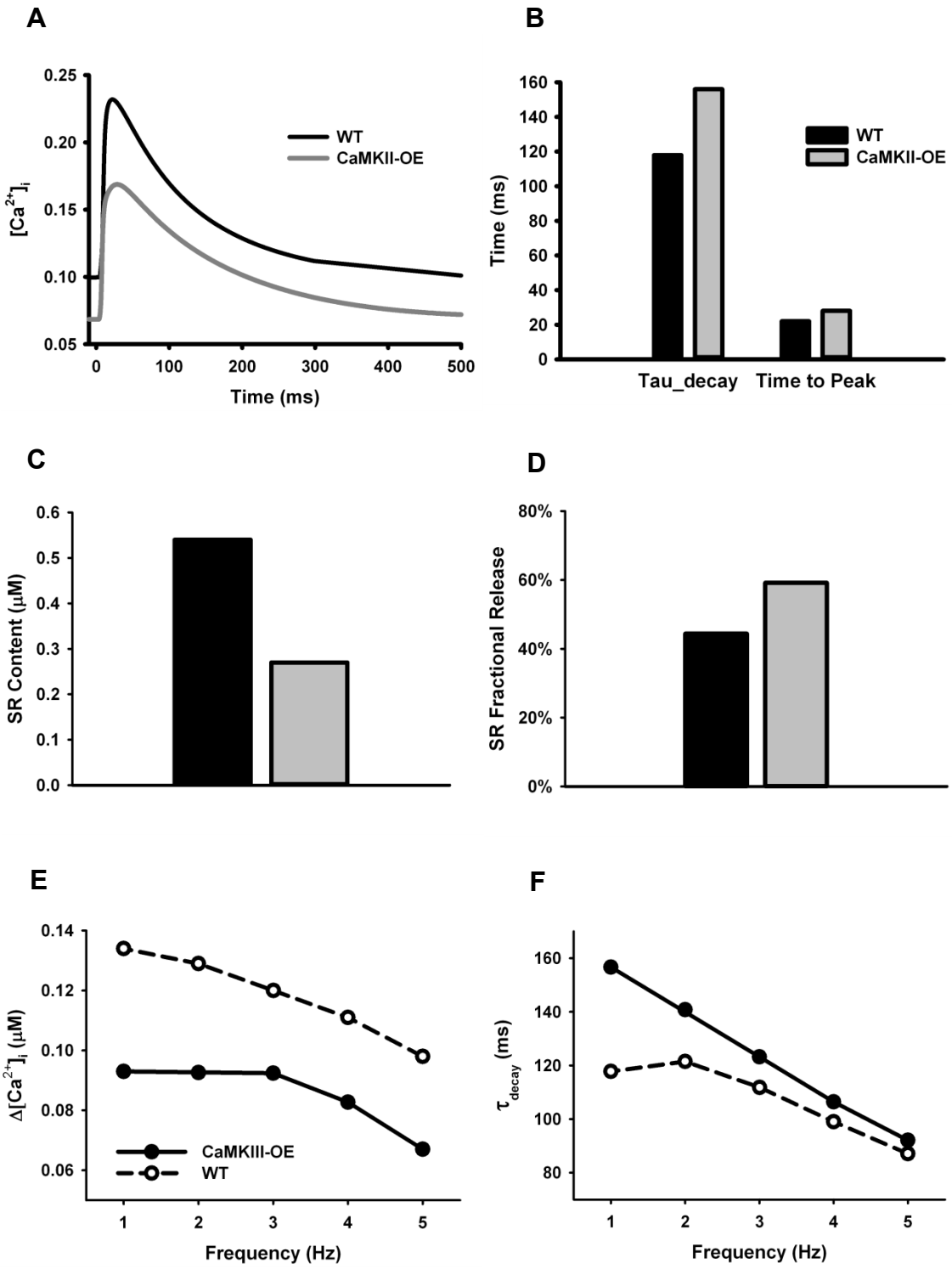

Figure 3.7 Ca^{2+} transients in the WT and CaMKII-OE models. A-D: Pacing frequencies at 1Hz. **A**: Waveforms of Ca^{2+} transient. **B**: Time constants and times to peak for Ca^{2+} transient. **C**: SR content. **D**: SR fractional release. **E**: Frequency-dependent $\Delta[Ca^{2+}]_i$. **F**: Frequency-dependent time constants of $[Ca^{2+}]_i$ decay phase.

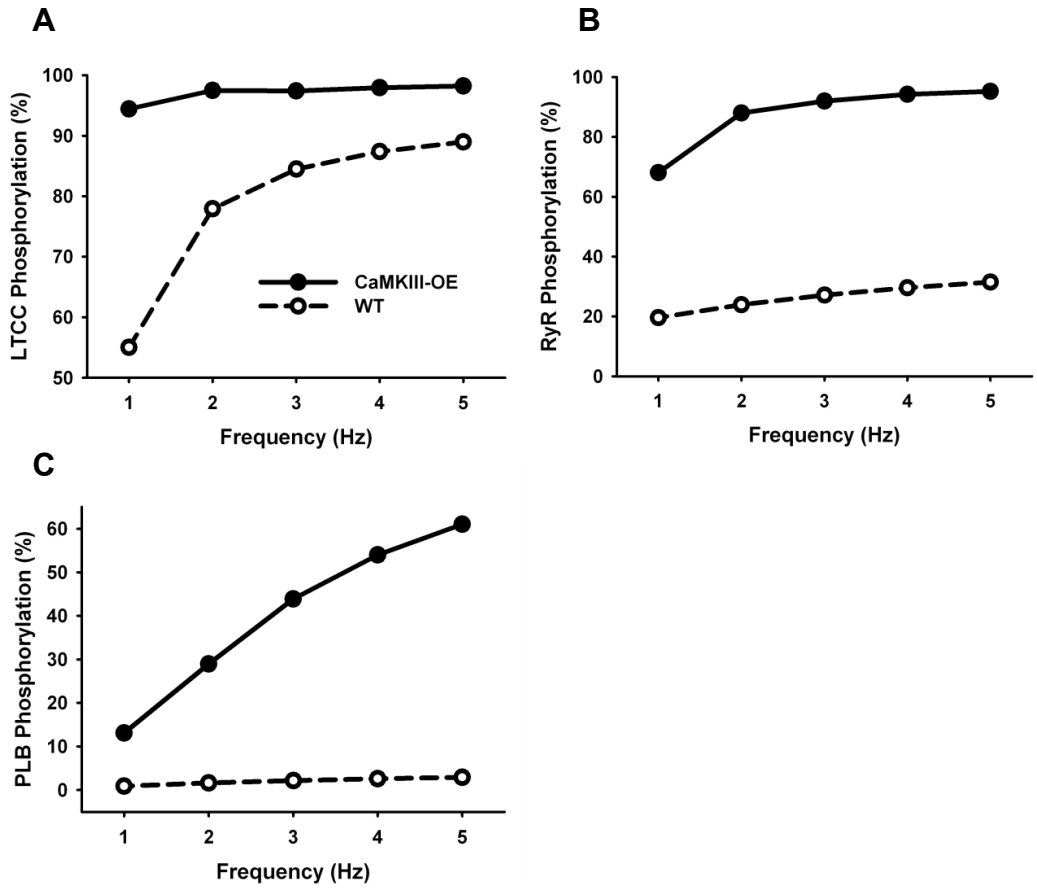

Figure 3.8 Comparison of frequency-dependence of CaMKII phosphorylation between WT and CaMKII-OE models. **A**: LTCC phosphorylation. **B**: RyR phosphorylation. **C**: PLB phosphorylation.

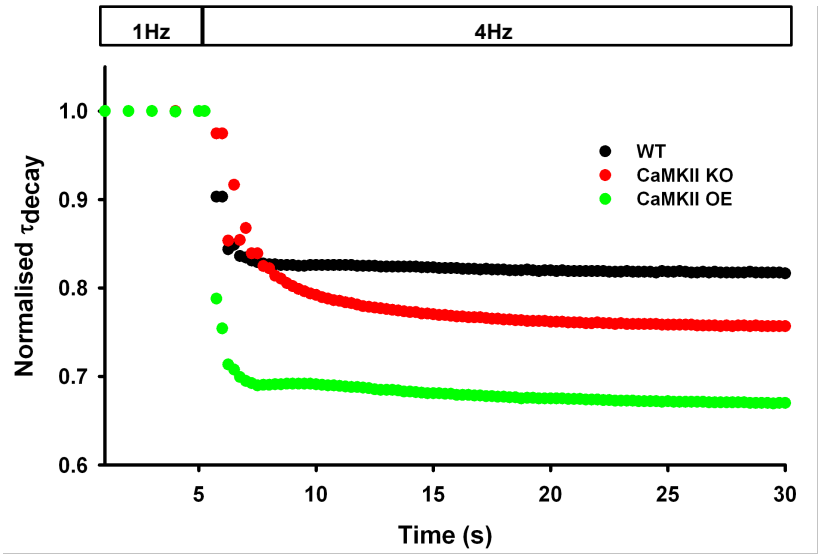

Figure 3.9 Enhancement of FDAR in CaMKII-OE model. Time constants of $[Ca^{2+}]_i$ during decay phase (τ_{decay}) were normalised to the value at 1Hz pacing frequency. Models were paced to steady state at 1Hz and switched to 4Hz at 5s.

3.3.5 Increased susceptibility to Pacing-induced AF

In our chronic CaMKII-OE model, although profiles of AP were significantly altered, abnormal depolarisations during steady pacing were not observed. To investigate further the effects of chronic CaMKII-OE, a burst pacing protocol was applied. The frequency was initially set at 1Hz, followed by a burst rate of 10Hz for 12s, and then a frequency of 1Hz resumed.

First, a comparison between the CaMKII-KO and WT model was performed (Figure 3.10). Both models showed a ~5% increase in $[Na^+]_i$ after the burst pacing, due to an increase in time-averaged Na influx via I_{Na}. The burst pacing caused little change in AP morphology in the CaMKII-KO model, but did increase the amplitude of $[Ca^{2+}]_i$ transients when the rate was set back to 1Hz. Given sufficient time with 1Hz pacing, $[Na^+]_i$ and $[Ca^{2+}]_i$ eventually recovered to the levels before burst pacing. The WT model, however, showed different results. Although a few DADs were found after the burst pacing, $[Ca^{2+}]_i$ soon recovered to normal transient, implying a faster rate adaptation.

During the burst pacing in the WT model, the elevated $[Na^+]_i$ decreased NCX-mediated Ca^{2+} extrusion, and thus increased Ca^{2+}-dependent CaMKII activity and target phosphorylation: this ensured CICR at fast pacing frequency. Since there was no CaMKII regulation in the CaMKII-KO model, LTCC, RyR and SERCA were less active than those in the WT model, resulting in a depressed Ca^{2+} release from SR and thus a high level of luminal Ca^{2+} ($[Ca^{2+}]_{SR}$). Therefore, after the rate was back to 1Hz, the high level of $[Ca^{2+}]_{SR}$ caused the initial boost of Ca^{2+} transients.

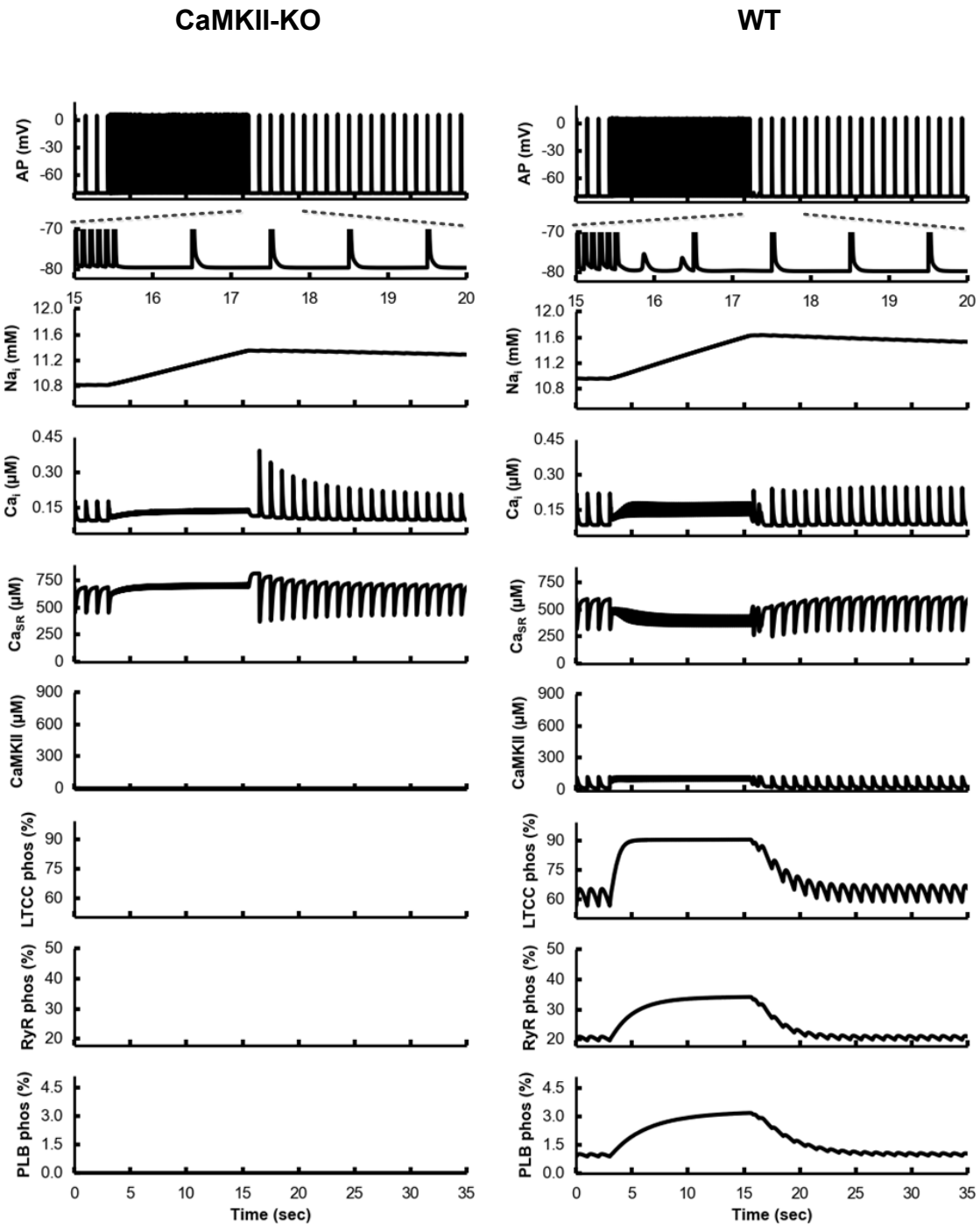

Figure 3.10 Burst-pacing protocol to induce DADs. Left panels are in the CaMKII-KO model. Right panels are in the WT model. The frequency was initially set at 1Hz, followed by a burst rate of 10Hz for 12s, and a frequency of 1Hz resumed. Dashed lines in panels in the second row indicate the enlarged area of APs. Concentrations of $[Na^+]_i$, $[Ca^{2+}]_i$, $[Ca^{2+}]_{SR}$, and CaMKII are shown in the middle panels. Phosphorylation levels of LTCC, RyR and PLB are shown in the bottom panels.

Next, the burst pacing protocol was applied to the CaMKII-OE model (Figure 3.11). Spontaneous Ca^{2+} release events were observed after the burst pacing. These sustained DADs exhibited different amplitudes that gradually fall and rise. During the burst pacing, $[Na^+]_i$ was slightly increased from 13.4 mM to 13.8 mM. CaMKII showed enhanced activity where LTCC and RyR achieved 100% phosphorylation and PLB increased from 13% to 40% phosphorylation. As discussed before, the increase in I_{NaL} and I_{NCX} contributed to the elevation of $[Na^+]_i$, leading to Ca^{2+} overload in the chronic CaMKII-OE model. The increase in CaMKII activity arising from increased $[Na^+]_i$ during burst pacing contributed to enhanced RyR open probabilities and to worsening of the Ca^{2+} overload, which in turn induced AP abnormalities. The spontaneous Ca^{2+} release further augmented Ca^{2+}-dependent CaMKII activity, leading to the enhancement of SERCA functionality and consequent increase in $[Ca^{2+}]_{SR}$ and decrease in $[Ca^{2+}]_{dyad}$, which in turn reduced CaMKII activity. When the difference between $[Ca^{2+}]_{SR}$ and $[Ca^{2+}]_{dyad}$ is large enough, more Ca^{2+} is released from RyRs, resulting in the increase in CaMKII activity. This CaMKII-Ca^{2+}-CaMKII interactions may account for the periodical fall and rise in the amplitude of DADs.

To investigate the role of $[Na^+]_i$ in these disturbances, the same burst pacing protocol with clamped $[Na^+]_i$ was performed (Figure 3.12). When $[Na^+]_i$ was clamped to the initial level before burst pacing (13.5mM), DADs were still observed, although the amplitude was to a lesser extent and all DADs were eventually abolished, as CaMKII activity soon recovered to the initial level. When $[Na^+]_i$ was clamped to the WT level (11mM), DADs were eliminated, despite that the maximum phosphorylation levels of LTCC, RyR and PLB remained the same. We also checked the high level $[Na^+]_i$ clamping (15mM), and found sustained DADs after the burst pacing. These results revealed that $[Na^+]_i$ plays an important role in putative cellular mechanisms of arrhythmogenesis.

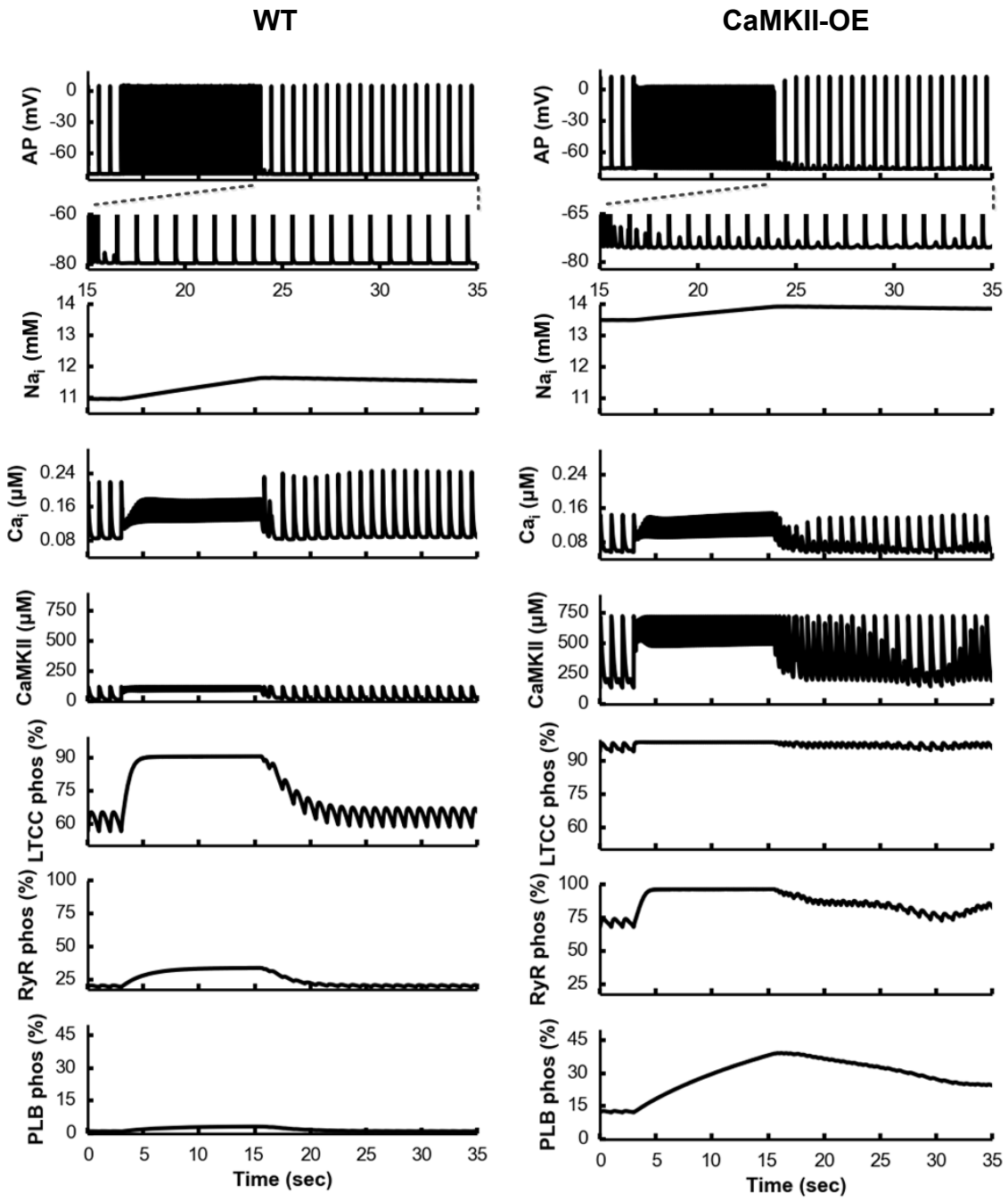

Figure 3.11 Burst-pacing protocol to induce DADs. Left panels are in the WT model. Right panels are in the CaMKII-OE model.

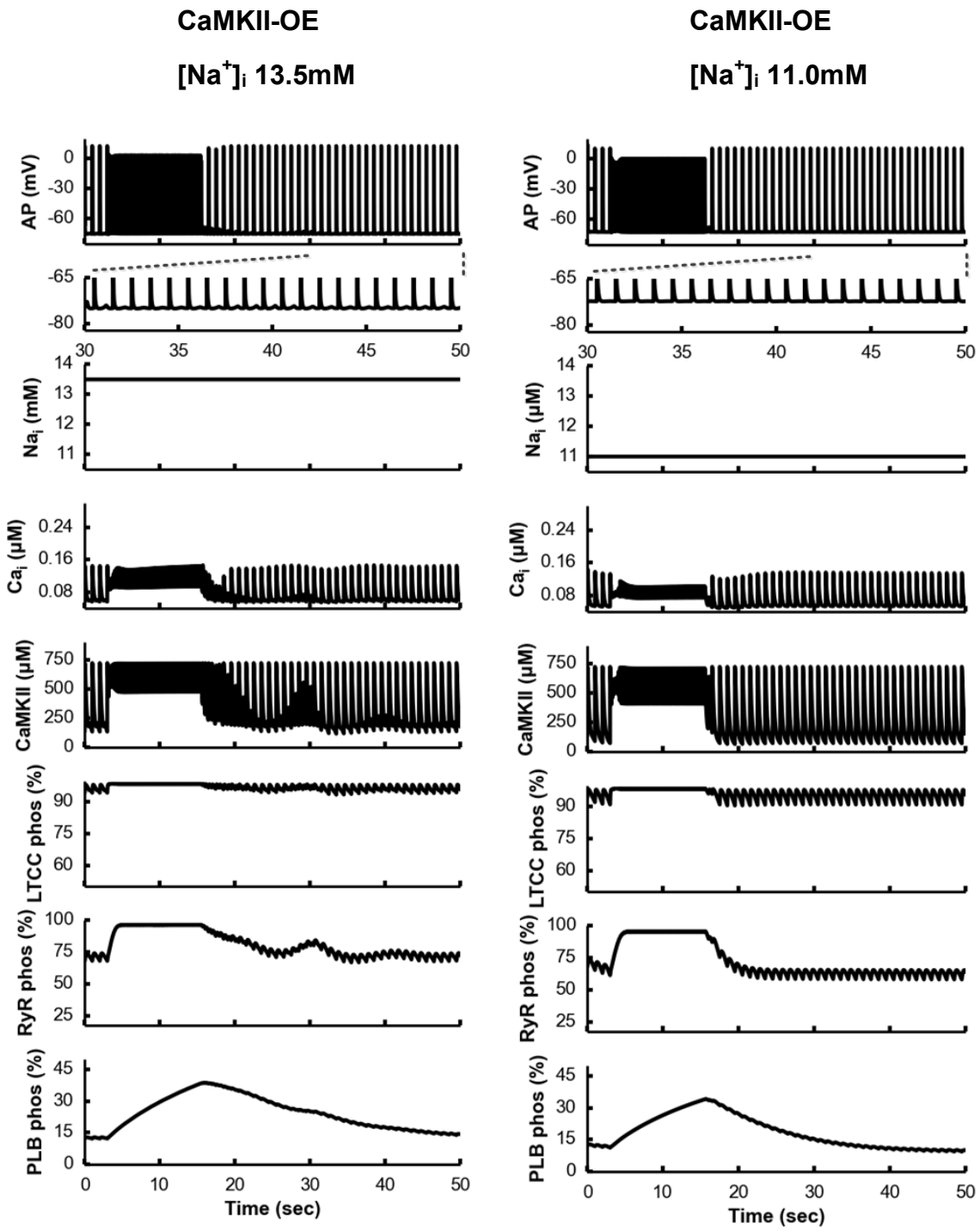

Figure 3.12 Burst-pacing protocol to induce DADs. Left panels are in the CaMKII-OE model with $[Na^+]_i$ clamped to 13.5mM. Right panels are in the CaMKII-OE model with $[Na^+]_i$ clamped to 11.0mM.

To investigate the influence of target phosphorylation on AP abnormalities, the burst pacing protocol with phosphorylation clamping was applied. As shown in Figure 3.13, when the phosphorylation of RyR was clamped at steady-state level in the CaMKII-OE model (~75%), sustained DADs were observed, although the amplitude was to a lesser extent. When the phosphorylation of RyR was clamped at WT level (~20%), DADs were abolished. We also tested LTCC and PLB using the same protocol with phosphorylation clamped at their WT level, and found DADs were not eliminated, suggesting that RyR phosphorylation level plays a more important role in proarrhythmic effects of CaMKII-OE.

We also examined the contribution of $[Na^+]_i$ and RyR phosphorylation to the formation of DADs by using a double clamping protocol. When clamping $[Na^+]_i$ at a high level of 15mM and RyR phosphorylation at a low level of 20%, no DADs were detected after the burst pacing. When clamping $[Na^+]_i$ at a low level of 11mM and RyR phosphorylation at a high level of 100%, a few DADs were observed after the burst pacing, but soon eliminated.

These simulations support the notion of a synergistic interaction between perturbed Na^+ fluxes and CaMKII-dependent RyR phosphorylation. The elevated $[Na^+]_i$ limited Ca^{2+} extrusion via NCX thus increases Ca^{2+}-dependent CaMKII activity and DAD occurrence. RyR hyperphosphorylation was also critical for the spontaneous release, even though SR Ca^{2+} load was reduced in CaMKII-OE, as it increases the open probability of SR. Therefore, to induce DADs in the CaMKII-OE model, both elevated $[Na^+]_i$ and hyperphosphorylated RyR were required.

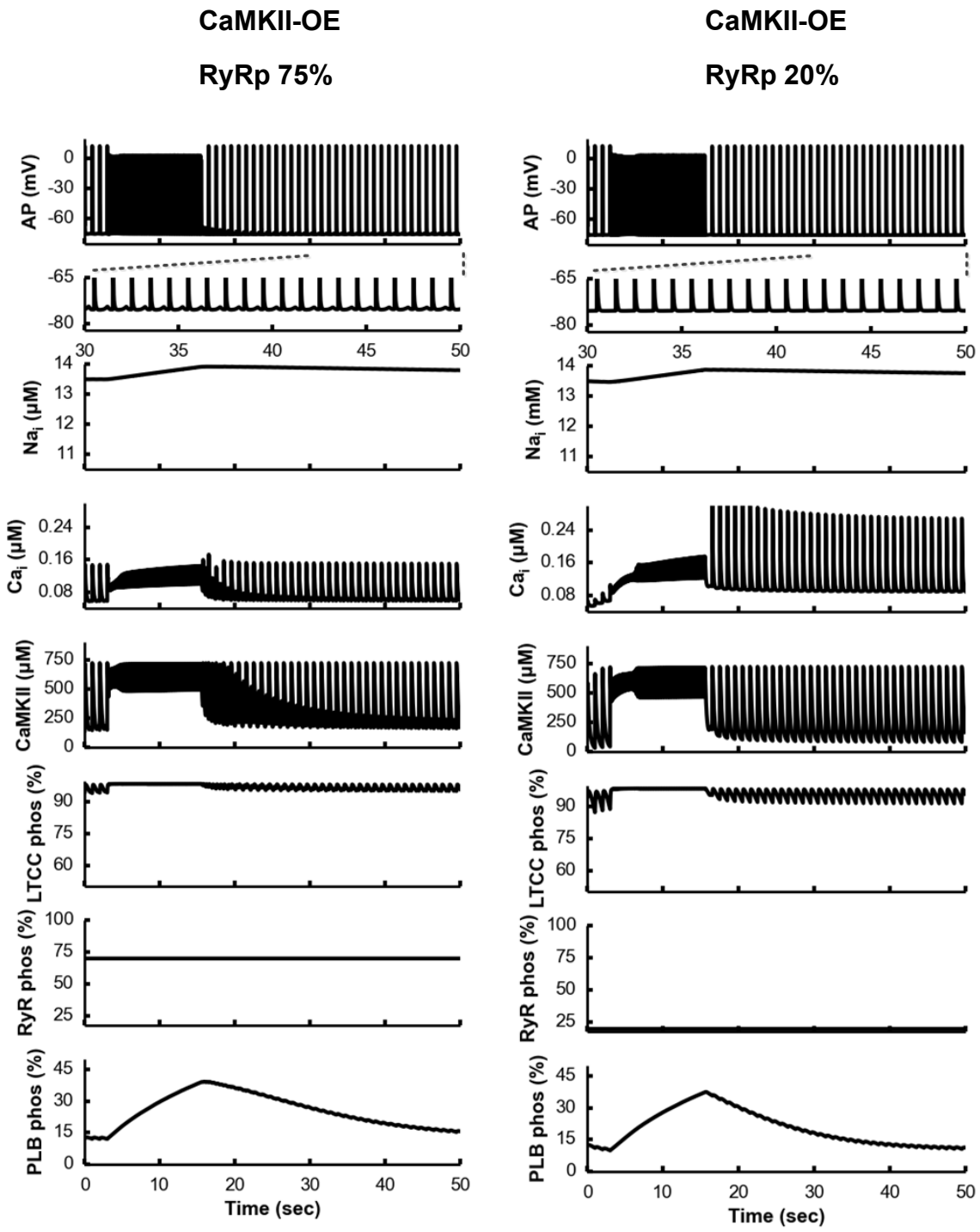

Figure 3.13 Burst-pacing protocol to induce DADs. Left panels are in the CaMKII-OE model with RyR phosphorylation clamped to 75%. Right panels are in the CaMKII-OE model with RyR phosphorylation clamped to 20%.

3.4 Proarrhythmic Effects of Acute CaMKII-OE

Acute effects were investigated by applying CaMKII-dependent alterations of I_{Na}, I_{NaL}, and I_{to}. These changes have been identified in studies of acute CaMKII-OE mice [38-40]. In addition, I_{NaK} was reduced by 10% in the acute CaMKII-OE model, as suggested in the ventricular CaMKII-OE study [106].

In the chronic CaMKII-OE model, CaMKII effects on I_{NaL} and I_{Nab} were modelled without dynamic modulation and simply turned on during CaMKII-OE simulations. To reflect dynamic changes of CaMKII-dependent $[Na^+]_i$ for the acute CaMKII-OE model, alteration of Na^+ fluxes was further developed. The increases in I_{NaL} and I_{Nab} were reimplemented as functions of CaMKII-dependent phosphorylation using the RyR module formulations, since there are no data on the kinetics of CaMKII-mediated phosphorylation and dephosphorylation of Na^+ channels. Thus, the effect of CaMKII-Na^+-Ca^{2+}-CaMKII positive feedback was modelled in an open-loop manner.

To investigate proarrhythmic effects of acute CaMKII-OE, the WT model was paced at 1Hz for 5s, followed by a sudden increase of total dyadic CaMKII. Simulations were carried out with or without CaMKII-Na^+-Ca^{2+}-CaMKII positive feedback to assess its impact on arrhythmogenesis (Figure 3.14). Our results show that the acute CaMKII-OE was able to induce DADs, irrespective of whether or not CaMKII-Na^+-Ca^{2+}-CaMKII positive feedback. In the presence of CaMKII-Na^+-Ca^{2+}-CaMKII positive feedback, the induced DADs have larger amplitude and are more sustainable. One striking feature induced by the feedback was that $[Na^+]_i$ increases faster and higher than that in the simulation without feedback loop. Thus, the CaMKII and phosphorylation activities were constantly at a higher level with the feedback loop, rather than periodical rise and fall without feedback loop.

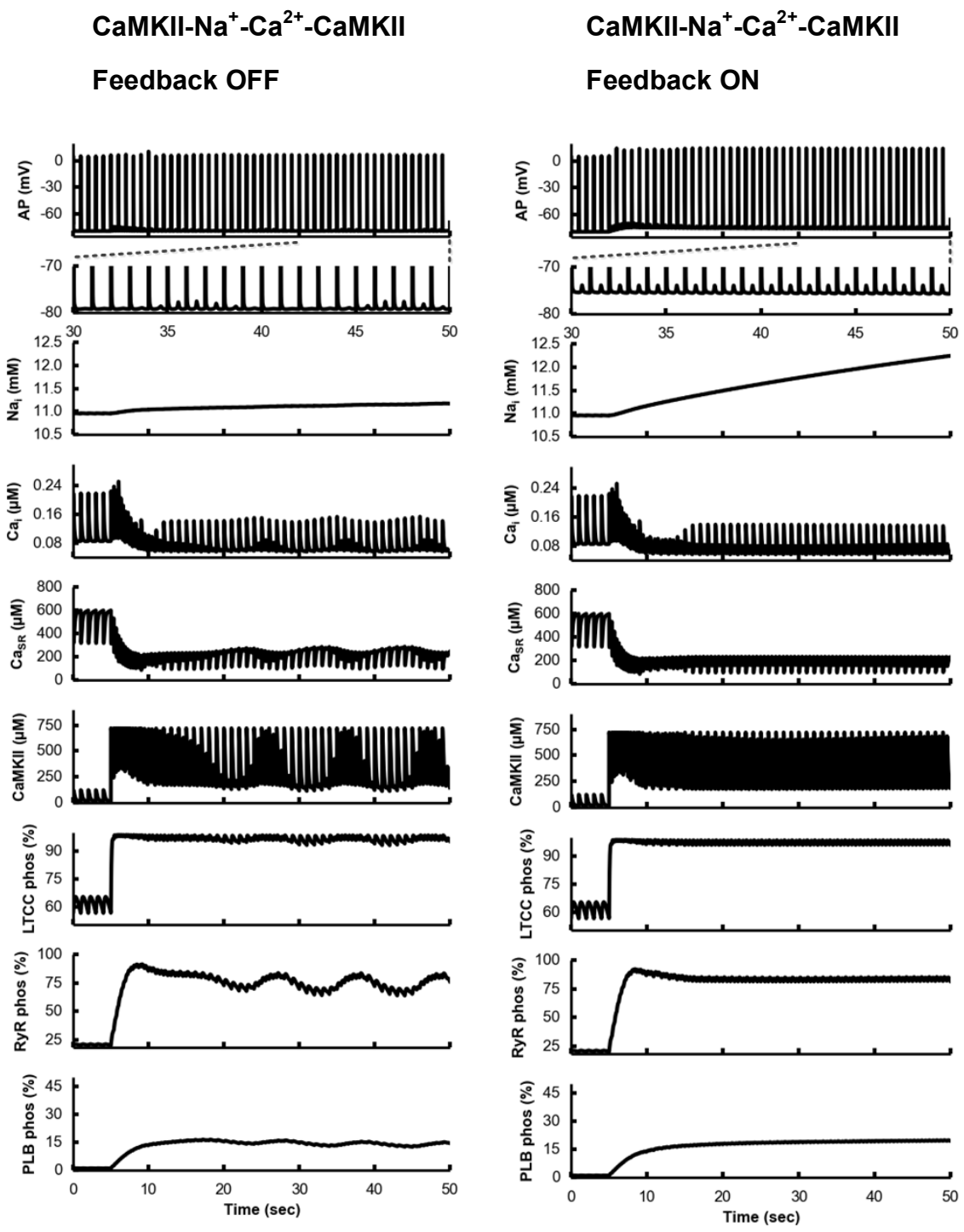

Figure 3.14 CaMKII-Na^+-Ca^{2+}-CaMKII feedback in acute CaMKII-OE model. Left panels were simulated without CaMKII-Na^+-Ca^{2+}-CaMKII feedback. Right panels were simulated with the feedback.

These results suggest that CaMKII-Na^+-Ca^{2+}-CaMKII positive feedback contributed to the augment of the Ca^{2+} and Na^+ overload, leading to enhanced spontaneous Ca^{2+} release events and AP abnormalities. As summarised in Figure 3.15, hyperphosphorylation arising from CaMKII-OE not only increased $[Ca^{2+}]_i$ via LTCC, RyR and PLB phosphorylation, but also increased $[Na^+]_i$ via phosphorylation on Na channels, which limited Ca^{2+} extrusion by NCX and in turn worsened $[Ca^{2+}]_i$ overload and CaMKII-OE.

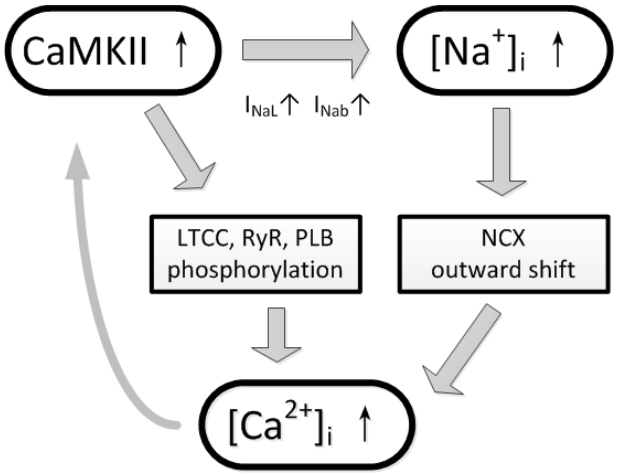

Figure 3.15 Schematic diagram of CaMKII-Na^+-Ca^{2+}-CaMKII positive feedback.

3.5 Summary

In this chapter, the effects of CaMKII-OE on individual phosphorylation substrate were introduced. Upon phosphorylation, I_{Na} showed a slowed recovery from inactivation; I_{NaL} exhibited shifted inactivation curve to more positive voltages; I_{to} exerted increased recovery rate from inactivation; current magnitude increase occurred in I_{NCX}, whereas I_{K1} and I_{NAK} were reduced.

Effects of chronic CaMKII-OE on AP and ECC were examined. Under the steady state pacing condition, no AP abnormalities were found, although APD was markedly prolonged. $[Ca^{2+}]_i$ transient showed a smaller amplitude with lower diastolic $[Ca^{2+}]_i$ level.

Phosphorylation of LTCCs, RyRs and PLB showed a significant increase under the CaMKII-OE condition. Our results also showed that CaMKII levels do not greatly alter FDAR.

Proarrhythmic effects of CaMKII-OE were investigated considering chronic and acute effects. Under the chronic CaMKII-OE condition, DADs could only be induced with elevated $[Na^+]_i$ and hyperphosphorylated RyR. The increase in $[Na^+]_i$ could be achieved by clamping to a high level or accumulation through fast pacing. Under the acute CaMKII-OE condition, DADs could be easily induced when total CaMKII increased to a high level.

To further study the acute CaMKII-OE effects in arrhythmogenesis, a CaMKII-Na^+-Ca^{2+}-CaMKII positive feedback loop was incorporated. The accumulation of $[Na^+]_i$ was faster and higher with the feedback loop, and resulted in NCX outward shift and consequent increase in $[Ca^{2+}]_i$, thus augmenting the overload of CaMKII and $[Na^+]_i$ DADs induced in the CaMKII-OE with feedback loop were more sustainable with relatively higher amplitude.

Chapter 4 – Role of β-adrenergic Stimulation in Arrhythmogenesis

4.1 Introduction

Stimulation of cardiac β-adrenergic receptors (β-AR) induces positive inotropic and chronotropic effects on the cardiac muscle, leading to increased heart rate and blood pressure. However, excessive sympathetic nervous system activity may stimulate apoptosis of cardiac myocytes, contributing to the progression of myocardial failure [196-198].

Mathematical modelling of the β-adrenergic signalling system is a supplementary tool for understanding its functions in the heart. The pioneering model for the β-adrenergic signalling system in rat ventricular myocytes was developed by Saucerman et al. [199]. The model not only reproduced the dynamics of cAMP and PKA, but also included PLB and LTCC, two major PKA targets. A similar model for rabbit ventricular myocytes was developed, which incorporated new PKA targets: RyR, TnI, and I_{Ks} [200]. The model was then updated for guinea pig ventricular myocytes [201]. A more recent model was developed by Bondarenko [202], which includes both biochemical and electrophysiological aspects, as well as a compartmentalisation of the β-adrenergic signalling system.

In this chapter, a mathematical model of β-adrenergic signalling system for mouse atrial myocytes and their physiological and pathological roles in cellular functions are described. Modules of β-adrenergic activation and PKA phosphorylation of ECC targets were primarily based on the mouse ventricular model of Morotti et al. [106], with some modifications based on regional differences between atria and ventricles. In addition, synergy between CaMKII substrates and β-adrenergic signalling in regulation of cardiac myocyte Ca^{2+} handling were simulated and investigated.

4.3 Development of Phosphorylation Effects on PKA Targets

Due to lack of experimental data for mouse atrial myocytes, modules of the β-adrenergic signalling pathway, including β-AR, AC, cAMP, PKA and PP1/inhibitor-1 (I-1), were left unaltered from the parent model of mouse ventricular myocytes [106], except that the total β-AR was increased by 60% to reproduce the kinetics of cAMP accumulation in response to isoproterenol (ISO) observed in an experimental study on rat atrium [203]. ISO was introduced in our model as the ligand of β-AR with concentrations in the range from 0.001 μM to 100 μM.

cAMP is a second messenger responsible for intracellular signal transduction. In the β-adrenergic signalling system, cAMP is one of the major signalling molecules, whose concentration is determined by the balance between cAMP production by AC and cAMP degradation by phosphodiesterases. Stimulation of the β-adrenergic signalling system results in an increase in cAMP production as well as cAMP degradation. Figure 4.1A shows the experimental time course of cAMP obtained upon stimulation with 100nM ISO. Figure 4.1B shows the dependence of cAMP accumulation over a wide range of ISO concentration. Both simulated results showed good consistencies with experimental observations.

PKA is a family of enzymes whose activity depends on intracellular levels of cAMP. Upon stimulation of the β-adrenergic signalling system, PKA is capable of phosphorylating a wide range of target proteins, exerting positive inotropic and chronotropic effects on the myocardium. Figure 4.1C shows time-dependent PKA dynamics in our model upon application of 1μM ISO. Figure 4.1D shows concentration dependence of PKA activation to a wide range of ISO concentration. Both time- and ISO-dependent PKA activity showed good agreements with the experimental data.

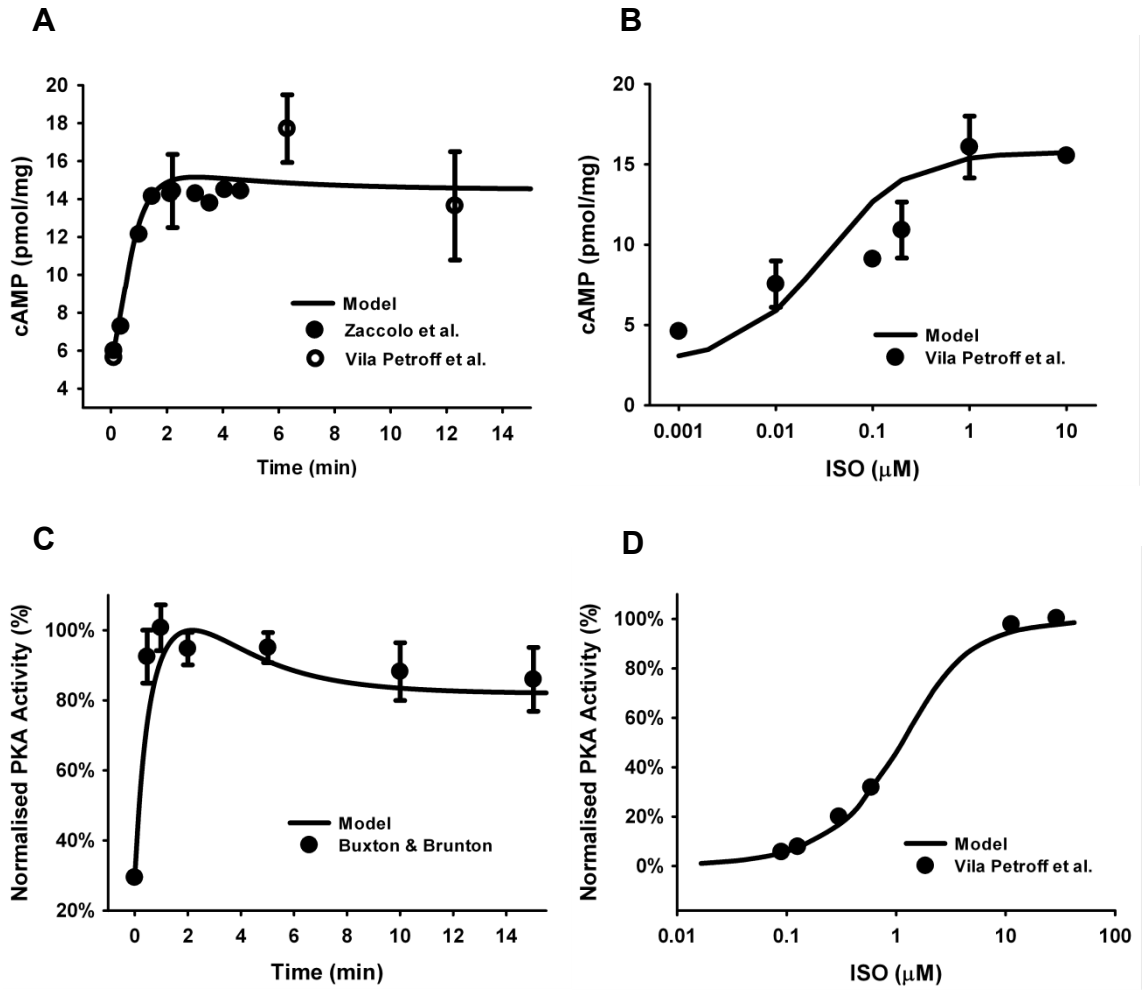

Figure 4.1 cAMP and PKA dynamics. **A**: Time course of cAMP upon stimulation with 100nM ISO. **B**: ISO-dependent cAMP accumulation. **C**: Time course of PKA activity upon stimulation with 1μM ISO. **D**: ISO-dependent PKA activity. (Experimental data: Zaccolo et al. [203], Vila Petroff et al. [204], Buxton & Brunton [205])

4.3.1 L-type Ca^{2+} Channel, LTCC

PKA can phosphorylate the α_{1C} and β_{2a} subunits of LTCCs: phosphorylation at α_{1C} sites increases channel open probability, and phosphorylation at β_{2a} sites increases channel availability [200]. The distribution of LTCC gating in mode 2 was also shown to be enhanced [206].

In our model, the effects of PKA-dependent phosphorylation at β_{2a} subunits were implemented by multiplying I_{CaL} by a factor f_{avail} that was positively correlated with

β_{2a}-phosphorylation level. PKA-dependent shifting of channels gating to mode 2 was implemented as a function of α_{1C} phosphorylation with 15% maximum distribution of mode 2 [100].

Figure 4.2 shows the effects of PKA-dependent phosphorylation on LTCCs. Upon β-adrenergic stimulation with 100nM ISO, I_{CaL} was significantly increased (from ~12pA/pF to ~20pA/pF), and the contribution to the total I_{CaL} by gating mode 2 was relatively larger than that in the control condition (Figure 4.2A). We also simulated ISO-dependent magnitudes of I_{CaL}; the result of the simulation for the total I_{CaL} was close to the experimental data (Figure 4.2B).

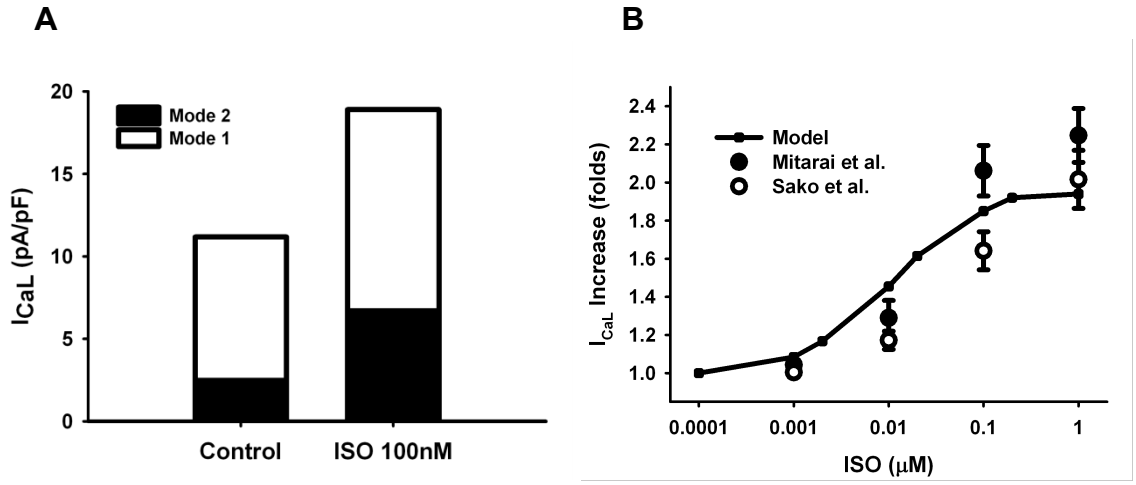

Figure 4.2 Effects of PKA-dependent phosphorylation on LTCCs. **A**: Comparison of contribution to the total I_{CaL} of the two gating modes between control condition and application of 100nM ISO. **B**: ISO-dependent peak I_{CaL} to a wide range of ISO concentration. (Experimental data: Sako et al. [207], Mitarai et al. [208])

4.3.2 Ryanodine Receptor, RyR

Similar to CaMKII phosphorylation, PKA phosphorylation has been shown to increase RyR open probability and channel Ca^{2+}-sensitivity [34, 54]. In our model, this was implemented by increasing the rate constants (K_{oSR}) as a linear function of PKA-dependent phosphorylation. The simulated results are shown in Figure 4.3. Upon stimulation with 100nM ISO, RyR phosphorylation activity became saturated after 80s and the maximum level of RyR phosphorylation could be achieved was ~48% when ISO was larger than 0.1 μM.

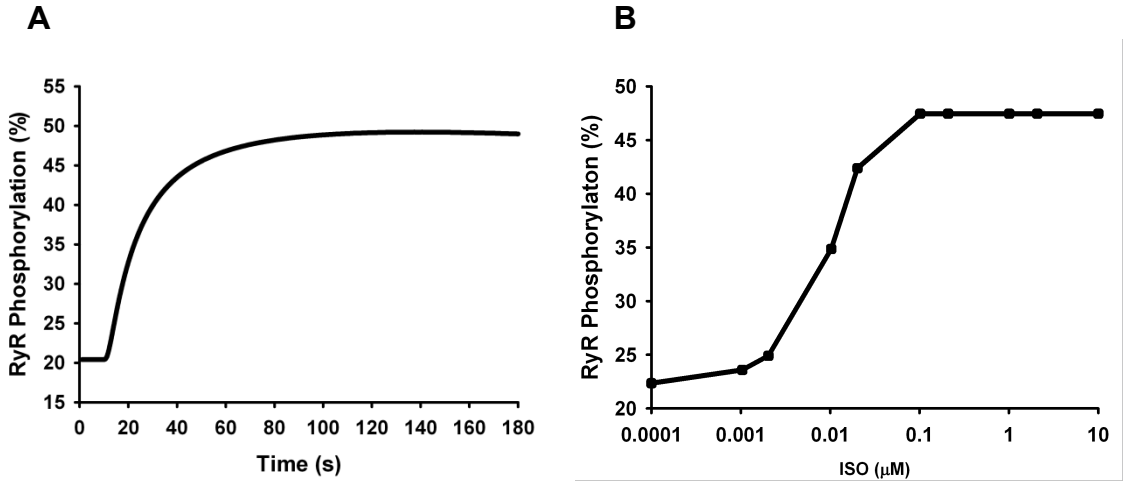

Figure 4.3 Simulated time- and ISO-dependent RyR phosphorylation by PKA. **A**: Time course of RyR phosphorylation activity upon stimulation with 0.1μM ISO. **B**: ISO-dependent RyR phosphorylation activity.

4.3.3 Phospholamban, PLB

PKA and CaMKII phosphorylations on PLB are functionally similar, in spite of having different phosphorylation sites. The phosphorylation could markedly reduce SERCA forward mode K_{mf} by ~50% at maximum [37], leading to increased pumping rate of Ca^{2+} from the cytosol into the SR through SERCA. Studies demonstrated that phosphorylation at Ser^{16} by PKA (without the site Thr^{17} phosphorylated by CaMKII) is sufficient for mediating full responses to β-adrenergic stimulation, and therefore K_{mf} is eventually

determined by the maximal effect exerted by either PKA or CaMKII phosphorylation.

Figure 4.4 shows time- and ISO-dependent PLB phosphorylation by PKA in the simulation and in experiments. The simulated time course of PLB phosphorylation upon β-adrenergic stimulation with 1μM ISO reached its maximal activity rapidly within one minute, which well reproduced the experimental findings (Figure 4.4A). PLB phosphorylation over a wide range of ISO concentration was also in good agreement with the experimental data (Figure 4.4B).

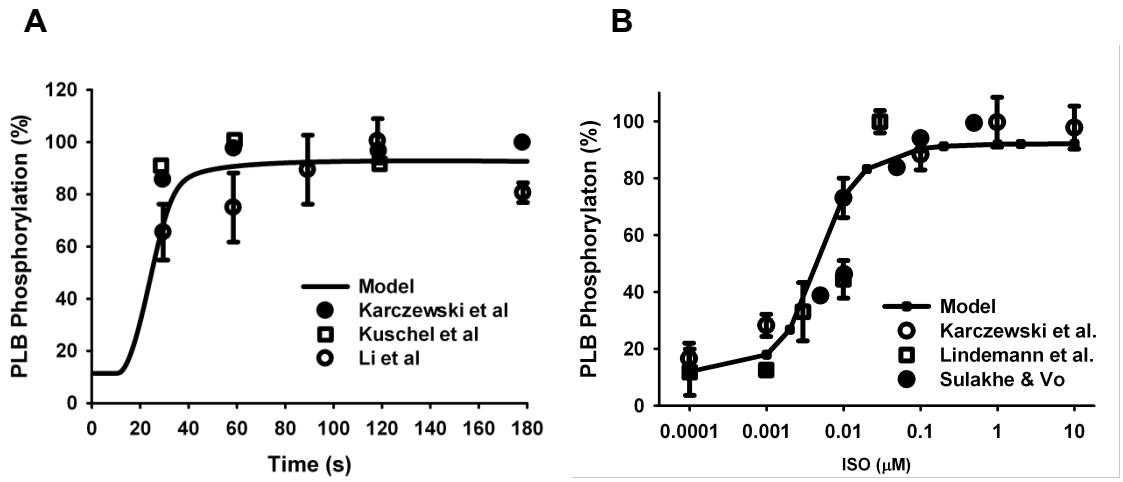

Figure 4.4 Simulated time- and ISO-dependent PLB phosphorylation by PKA. **A**: Time course of PLB phosphorylation activity upon stimulation with 1μM ISO at 10s. **B**: ISO-dependent PLB phosphorylation activity. The experimental data were from studies of mouse ventricular myocytes. (Experimental data: Karczewski et al. [209], Kuschel et al. [210], Li et al. [211], Lindemann et al. [212], Sulakhe & Vo [213])

4.3.4 Troponin I, TnI

TnI is a part of the troponin complex, binding to actin in thin myofilaments to hold the actin-tropomyosin complex in place. PKA phosphorylation on TnI results in an increase in the Ca^{2+} unbinding rate, accelerating in the rate of muscle relaxation [59, 60]. The phosphorylation effect was implemented in our model by increasing the dissociation rate K_d of TnC for Ca^{2+}.

Figure 4.5 shows the simulated time- and ISO-dependent TnI phosphorylation by PKA. The simulation well reproduced the experimental time course of TnI phosphorylation after β-adrenergic stimulation with 1μM ISO (Figure 4.5A). The ISO-dependent phosphorylation level of TnI was also consistent with experimental data. The phosphorylation level showed a significant increase at low concentrations of ISO, and TnI was completely phosphorylated at ISO of 0.1 μM.

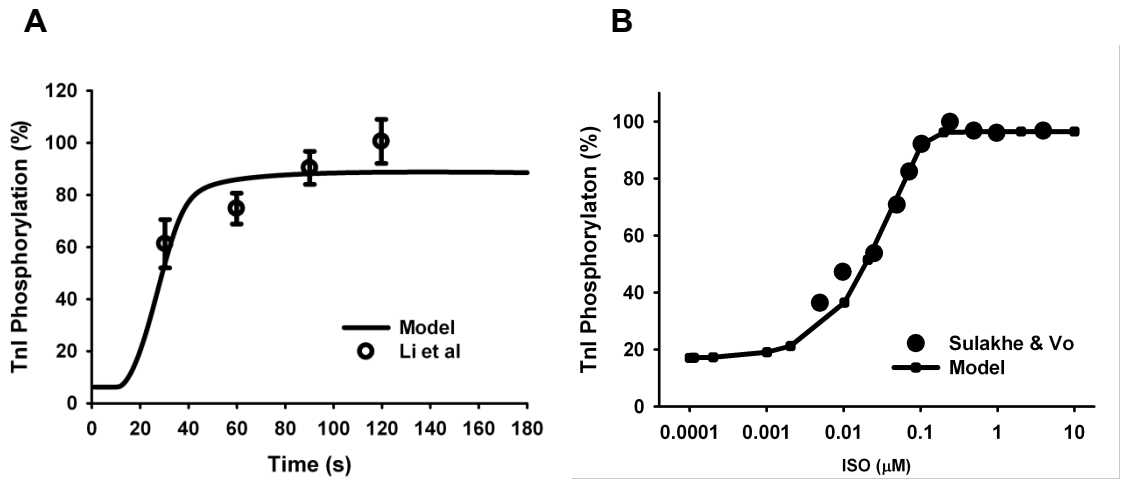

Figure 4.5 Simulated time- and ISO-dependent TnI phosphorylation by PKA. **A**: Time course of TnI phosphorylation activity upon stimulation with 1μM ISO at 10s. **B**: ISO-dependent TnI phosphorylation activity. (Experimental data: Li et al. [211], Sulakhe & Vo [213])

4.3.5 Ultrarapidly Activating Delayed Rectifying K^+ Current (I_{Kur})

PKA phosphorylation on I_{Kur} has been shown to increase its current density in human atrial myocytes [67], which was implemented in our model by multiplying I_{Kur} by f_{avail_Kur}, a factor positively correlated with the PKA phosphorylation level. Figure 4.6A shows the time course of I_{Kur} activation upon β-adrenergic stimulation with 1μM ISO, where I_{Kur} was saturated after 50s exposure to ISO. Figure 4.6B shows the increase in I_{Kur} at different concentrations of ISO, where the current amplitude was saturated at 0.1 μM ISO. The ISO-dependency well reproduced experimental observations.

4.3.6 Na^+-K^+ Pump, I_{NaK}

PLM is an inhibitory substrate that negatively regulates I_{NaK}. Upon stimulation with ISO, PKA phosphorylation on PLM results in an increase in I_{NaK}: thus $[Na^+]_i$ is decreased [63]. In our model, the effect of PKA phosphorylation on PLM was implemented by reducing the parameter K_{mNaip} to increase the NKA affinity for Na^+. Figure 4.7A shows the time course of a relative decrease in $[Na^+]_i$ after application of 1μM ISO, where the maximal decrease in $[Na^+]_i$ occurred after 250s. Figure 4.7B shows the ISO-dependence of the relative increase in I_{NaK}, similar to the experimental data.

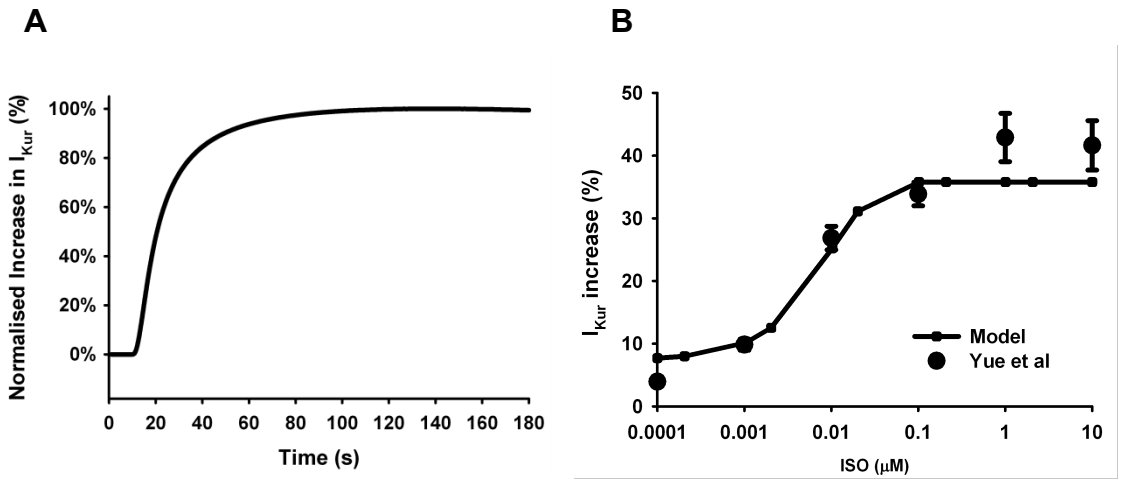

Figure 4.6 Simulated time- and ISO-dependent I_{Kur} phosphorylation by PKA. **A**: Time course of normalised increase in I_{Kur} upon stimulation with 1μM ISO at 10s. **B**: ISO-dependent increase in I_{Kur} upon stimulation with a wide range of ISO. Experimental data were from the study on canine ventricular myocytes. (Experimental data: Yue et al. [214])

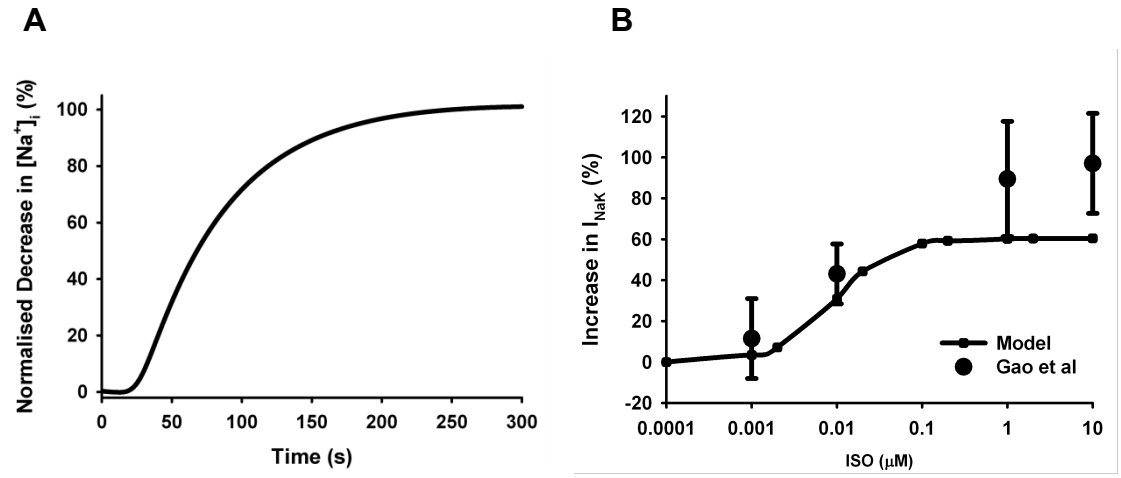

Figure 4.7 Effects of β-adrenergic stimulation on the Na^+-K^+ pump. **A**: Simulated time course of a relative decrease in $[Na^+]_i$ upon application of 1μM ISO at 10s. **B**: ISO-dependent increase in INaK upon stimulation with different concentrations of ISO. Experimental data were from the study on guinea pig ventricular myocytes. (Experimental data: Gao et al. [215])

4.4 Results

4.4.1 Effects of the β-adrenergic Signalling System on Action Potential

It has been demonstrated that β-adrenergic stimulation affects AP shape and moderately prolongs APD [216, 217]. To test if our model could reproduce these effects, it was run without and with 100nM ISO at a pacing frequency of 1Hz. As shown in Figure 4.8A and B, APD prolongation occurred at different levels of repolarisation. APD_{50} was significantly increased by 70%, while APD_{25}, APD_{75} and APD_{90} were increased by 50%, 30% and 12%, respectively. The prolongation in APD was largely attributable to the significant increase in I_{CaL} during β-adrenergic stimulation.

The simulation results showed that the prolongations of APD_{90} and APD_{50} stimulated with 100nM ISO were rate dependent (Figure 4.8C and D). The prolongations of APD_{50} were more prominent than those of APD_{90} at all tested frequencies, which was also reported in some experimental studies on mouse ventricular myocytes [216, 217]. This may be due to the fact that the increase in I_{Kur} partially counteracts the prolongation effects caused by the increase in I_{CaL} at late repolarisation phase. We have also simulated the effects of ISO on APA at frequencies ranging from 1Hz to 5 Hz. APA showed a slight increase upon exposure to 100nM ISO at all frequencies, due to the increase in I_{CaL} (Figure 4.8E).

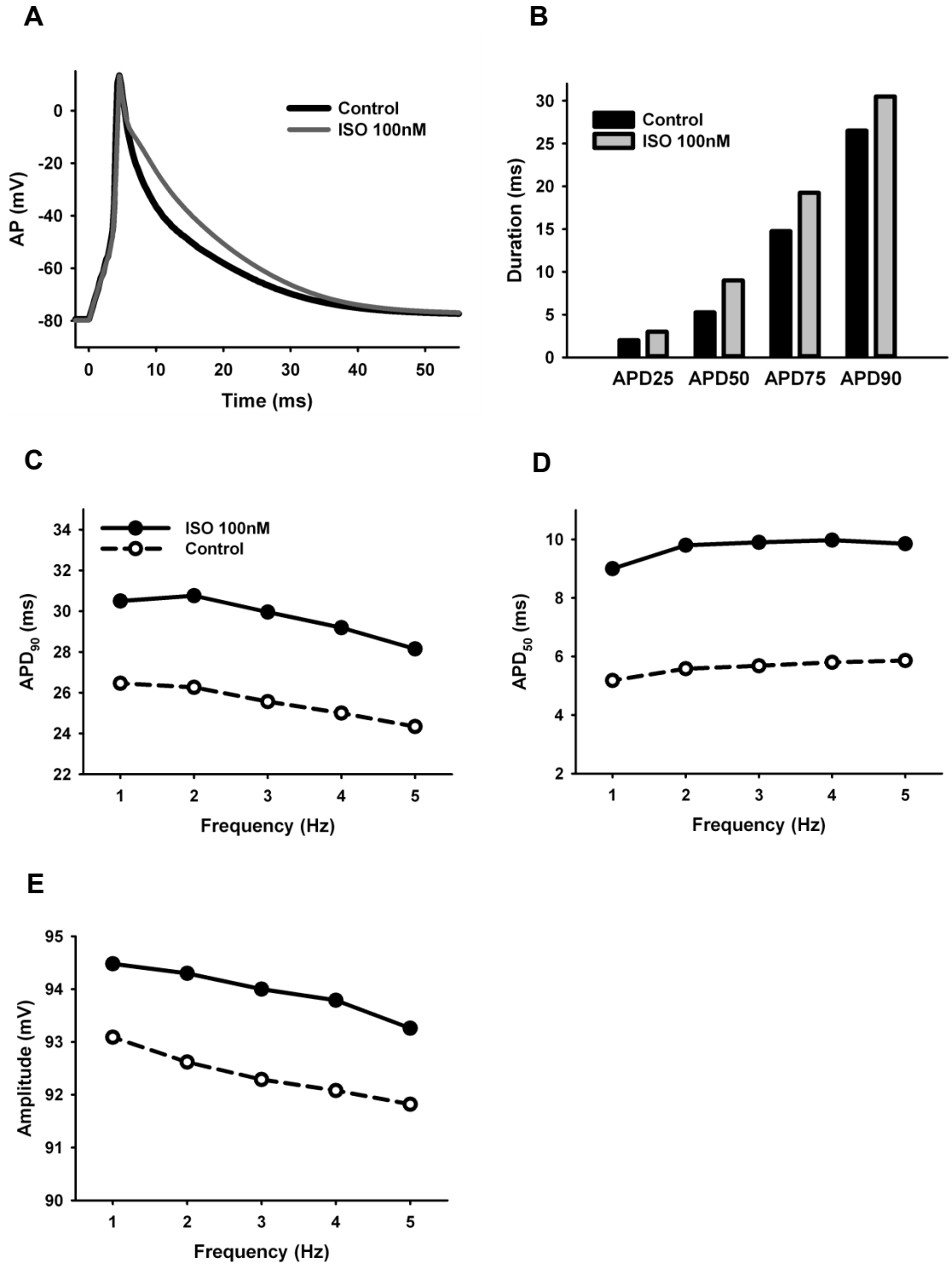

Figure 4.8 Changes in AP profiles after application of 100nM ISO. **A**: Time course of APs during 1Hz pacing frequency. **B**: APD_{25}, APD_{50}, APD_{75}, and APD_{90} during 1Hz pacing frequency. **C-E**: Frequency-dependent APD_{90} (**C**), APD_{50} (**D**), APA (**E**).

4.4.2 Effects of the β-adrenergic Signalling System on Ca^{2+} Dynamics

Our mouse atrial myocyte model showed that the $[Ca^{2+}]_i$ transient of mouse atrial myocytes was significantly increased (~two folds) upon β-adrenergic stimulation, which is consistent with experimental studies where a two-fold increase in $[Ca^{2+}]_i$ transients upon β-adrenergic stimulation was observed [218]. Figure 4.9A shows simulated $[Ca^{2+}]_i$ transients, in the presence/absence of 100n M ISO at 1Hz pacing frequency. The amplitude of $[Ca^{2+}]_i$ transients was increased from 0.22μM to 0.39μM after application of 100nM ISO. The time to peak was slightly shortened, whereas the time constant for the decay of $[Ca^{2+}]_i$ was moderately increased during β-adrenergic stimulation (Figure 4.9B). The SR content was increased from 0.54μM to 0.68 μM, and the SR fraction release was increased from 44.4% to 55.8% (Figure 4.9C and D).

Rate-dependence of $[Ca^{2+}]_i$ transients was also simulated without and with ISO of 100nM at pacing frequencies from 1Hz to 5Hz. Frequency dependence of the diastolic and systolic $[Ca^{2+}]_i$ showed an increase in their magnitudes (Figure 4.9E). Time constants for the decay of $[Ca^{2+}]_i$ transients demonstrated a decline tendency with increasing pacing frequency after stimulation of 100nM ISO. Time constants in the presence of ISO were smaller than those in the control condition, except for the point at frequency of 1Hz. The faster decay of [Ca2+]i transient can be explained by the fact that enhanced activity of SERCA with ISO contributed more to the $[Ca^{2+}]_i$ decay than NCX at all frequencies. However, in the control condition, NCX took more contributions to the decay of $[Ca^{2+}]_i$ than SERCA at 1Hz pacing frequency and was overtaken by SERCA when the rate was larger than 2Hz.

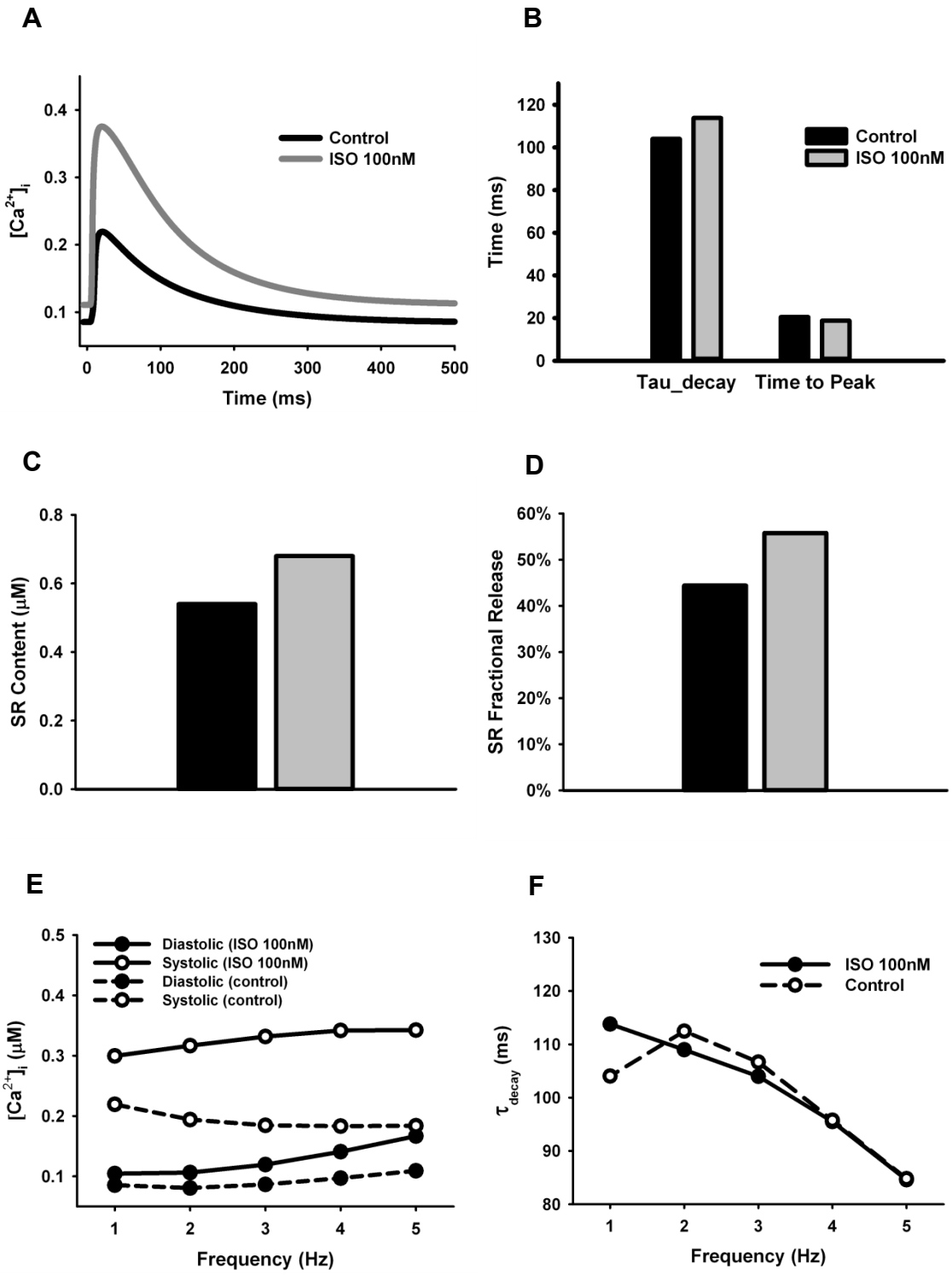

Figure 4.9 Simulated $[Ca^{2+}]_i$ transients and their characteristics for control conditions and upon application of 100nM ISO. A-D**:** Pacing frequency was set to 1Hz. **A**: Time course of $[Ca^{2+}]_i$ transients. **B**: Time constants of $[Ca^{2+}]_i$ decay and time to peak. **C**: SR content. **D**: SR fractional release. **E**: Diastolic and systolic $[Ca^{2+}]_i$ magnitudes as functions of pacing frequency. **F**: Time constants for the decay of $[Ca^{2+}]_i$.

4.5 Synergy between CaMKII and PKA Phosphorylation in Regulation of ECC

CaMKII activity responds to the frequency and magnitude of Ca^{2+} signals, both of which are increased by β-adrenergic stimulation in the heart [219]. β-adrenergic stimulation, results in increased Ca^{2+} entry via LTCC and SR Ca^{2+} release through RyR, which is expected to augment $[Ca^{2+}]_{dyad}$ beyond the low level maintained during normal beat-to-beat Ca^{2+} transients. This could promote CaMKII activation.

To test whether β-adrenergic signalling through PKA enhances CaMKII activity, we performed simulations with/without CaMKII phosphorylation (control VS CaMKII-KO model) in the presence/absence of ISO. As shown in Figure 4.10A, ISO significantly enhanced Ca^{2+} transients during β-adrenergic stimulation. In the CaMKII-KO model, however, the ISO response was partially diminished. The change in Ca^{2+} transients from CaMKII-KO to control with ISO models ($\Delta[Ca^{2+}]_i$ of 180 nM) was larger than the sum of Ca^{2+} transient increases from the CaMKII-KO model to control condition ($\Delta[Ca^{2+}]_i$ of 15 nM) and CaMKII-KO with ISO model ($\Delta[Ca^{2+}]_i$ of 150 nM).

In addition to the Ca^{2+} transients, the average dyadic CaMKII activity was also evaluated (Figure 4.10B). Similar to the Ca^{2+} transients, the increase from control condition for the average dyadic CaMKII activity in the CaMKII-OE model with 100nM ISO was larger than the sum of it with CaMKII-OE and with 100nM ISO, suggesting that through PKA enhancement of Ca^{2+} fluxes, CaMKII activity was promoted, which was further potentiated by CaMKII-OE. These results predicted synergy between PKA and CaMKII in the β-adrenergic response.

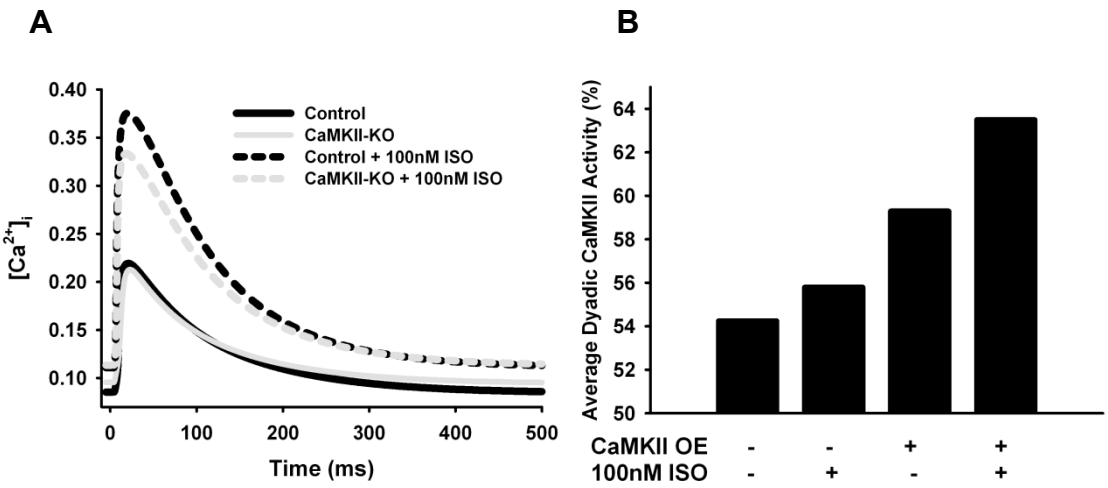

Figure 4.10 Synergy between CaMKII and PKA substrates. **A**: $[Ca^{2+}]_i$ transients without and with CaMKII upon stimulation of 100nM ISO compared with control condition. **B**: Analysis of individual target contributions to enhanced CaMKII activity.

4.6 Proarrhythmic Effects of β-adrenergic Stimulation

Hyperactivity of CaMKII is suggested to be proarrhythmogenic, as discussed in Chapter 3. Due to the synergy between CaMKII and PKA phosphorylation on ECC, we hypothesised that β-adrenergic activation may promote arrhythmia in the CaMKII-OE model through PKA-mediated increases in cellular Ca^{2+} load. To test this hypothesis in the model, we conducted simulations upon β-adrenergic activation with 100nM ISO in the CaMKII-OE model and control condition (Figure 4.11).

Following the application of 100 nM ISO at 5s, PKA-mediated phosphorylation activities were gradually increased in both models: RyR phosphorylation revealed a dramatic increase of 8-folds while LTCC and PLB phosphorylation showed a two-fold increase. In the control condition, CaMKII activities showed little change after application of ISO, whilst activities in the CaMKII-OE model exhibited a marked increase in PLB and a slight increase in RyR.

In the control model, DADs were not found, regardless of whether ISO was applied. The peak Ca^{2+} transients was gradually increased from 0.2 μM to 0.4 μM, whereas $[Na^{+}]_i$ was gradually decreased from 11 mM to 10 mM. In the CaMKII-OE model after

exposure to 100nM ISO, alternans of $[Ca^{2+}]_i$ and sustained DADs were observed. $[Na^+]_i$ was decreased from 13.5 mM to 12.1 mM at 50s, and continued falling to reach a steady level of 10 mM. The SR content was markedly decreased in the CaMKII-OE model and was further reduced after the application of ISO, due to enhanced SR release events.

Notably, DADs were not eliminated even when $[Na^+]_i$ was decreased to 10 mM after 100s. In contrast, at such low level $[Na^+]_i$, the chronic CaMKII-OE model was not able to induce DADs (as described in Chapter 3). We then clamped $[Na^+]_i$ to examine whether DADs induced by the CaMKII-OE model with β-adrenergic stimulation were independent of $[Na^+]_i$ (Figure 4.12). When $[Na^+]_i$ was clamped at a low concentration of 8 mM, DADs were abolished, with lowered phosphorylation activities in RyR and PLB. When $[Na^+]_i$ was clamped at a high concentration of 15 mM, CaMKII activity was significantly increased, accompanied by enhanced SR spontaneous release events leading to worsening of the abnormalities. Therefore, $[Na^+]_i$ is an important factor in inducing DADs in the CaMKII-OE model with β-adrenergic stimulation.

During β-adrenergic stimulation, PKA-mediated phosphorylation at LTCC increased channel open probability and channel availability, leading to a significant increase in Ca^{2+} influx, followed by the boost in CaMKII activation and enhancement of RyR sensitivity to Ca^{2+}, which resulted in promoted spontaneous Ca^{2+} release events. Overload of $[Na^+]_i$ caused outward shifting of NCX, leading to decreased Ca^{2+} efflux through NCX, thus promoting the overload of Ca^{2+}. Therefore, this positive feedback contributed to the increased DADs in the CaMKII-OE model with β-adrenergic stimulation.

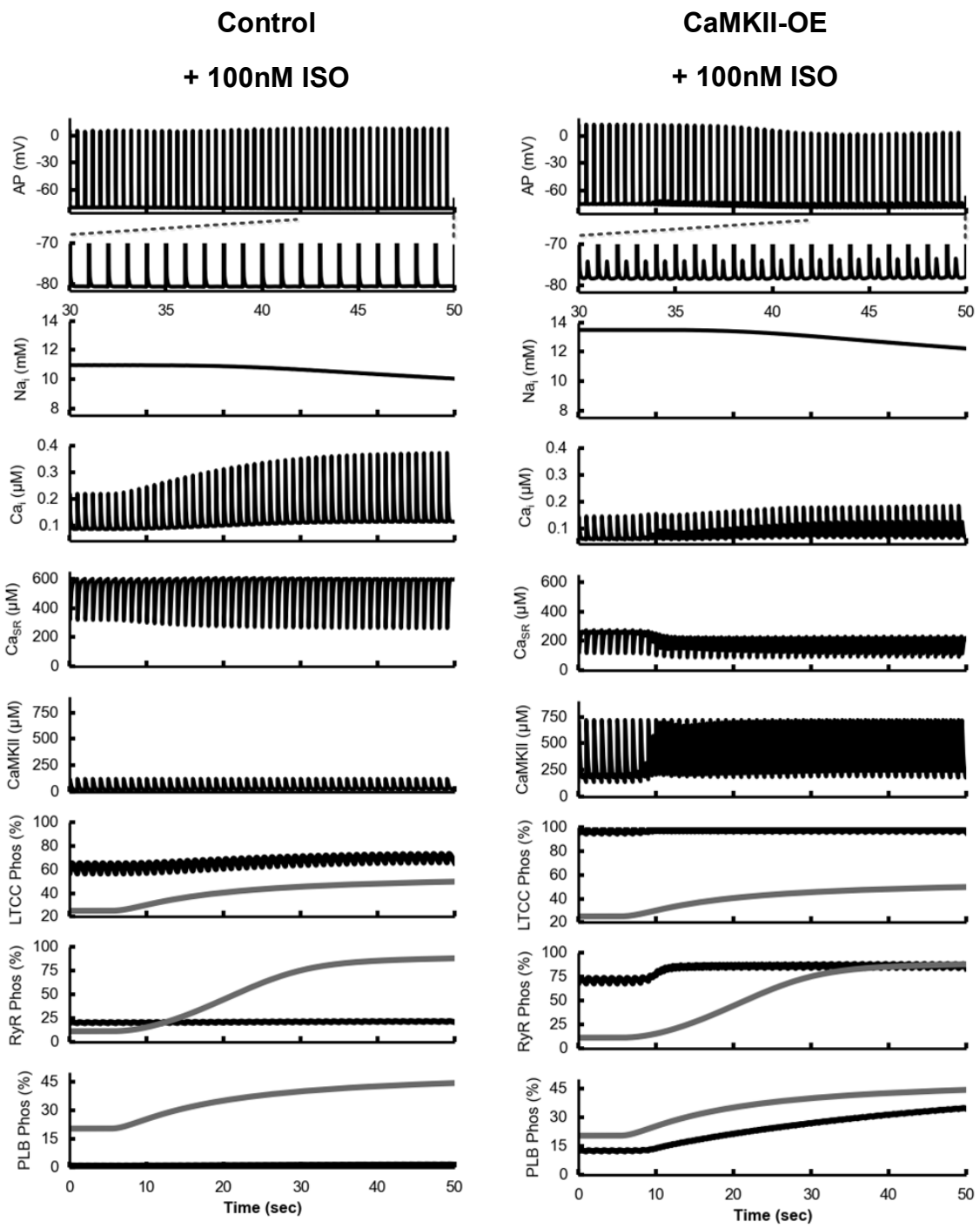

Figure 4.11 Effects of β-adrenergic stimulation in the CaMKII-OE model and control condition. ISO is applied at 5s. Simulations were taken at 1Hz pacing frequency. Dashed lines in panels in the second row indicate the enlarged area of APs. Concentrations of $[Na^+]_i$, $[Ca^{2+}]_i$, $[Ca^{2+}]_{SR}$, and CaMKII are shown in the middle panels. The three bottom panels show phosphorylation activities for LTCC, RyR and PLB, where the black line is CaMKII-mediated phosphorylation and the grey line is PKA-mediated phosphorylation.

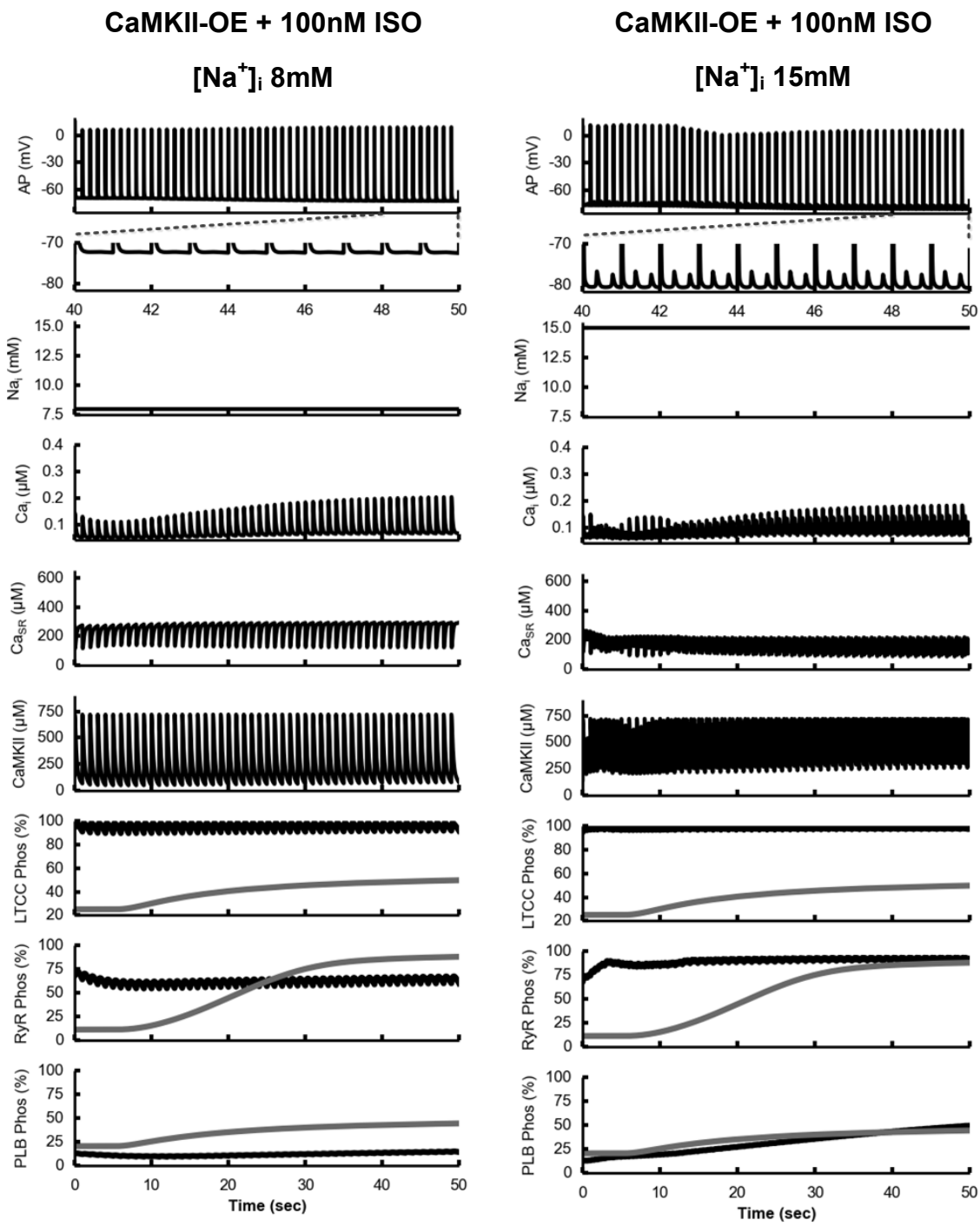

Figure 4.12 Effects of β-adrenergic stimulation in the CaMKII-OE model with clamped $[Na^+]_i$. The three bottom panels show phosphorylation activities for LTCC, RyR and PLB, where the black line is CaMKII-mediated phosphorylation and the grey line is PKA-mediated phosphorylation. ISO is applied at 5s. Simulations were taken at 1Hz pacing frequency.

4.7 Summary

In this chapter, the effects of β-adrenergic stimulation on individual PKA phosphorylation targets were described and simulated. PKA phosphorylation showed increased channel open probability and availability in LTCC, enhanced open probability and channel sensitivity in RyR, increased uptake rate from cytosol in SERCA, increased Ca^{2+} unbinding rate in TnI and increased current density in I_{Kur} and I_{Na}.

We evaluated the effects of β-adrenergic stimulation on AP profiles at different pacing frequencies. APD showed prolongation at different levels of repolarisation, where APD_{50} revealed a two-fold increase, due to the increase in I_{CaL} during β-adrenergic stimulation. In addition, we investigated the effects on Ca^{2+} transients in the control condition. The total Ca^{2+} transient amplitude was significantly increased by ~two folds upon ISO treatment, along with increases in SR content and fractional release.

We tested the impact of β-adrenergic stimulation on a Ca^{2+}-CaMKII-Ca^{2+} feedback loop. Upon application of ISO, the average dyadic CaMKII activity showed an increase of ~2% in the control condition, but a significant increase of ~20% in the CaMKII-OE model. PKA enhancement of Ca^{2+} fluxes resulted in an increase in CaMKII activity, which was further potentiated by CaMKII-OE, suggesting synergy between PKA and CaMKII in the β-adrenergic response.

Abnormal APs were not observed in the control condition with ISO exposure or in the steady state CaMKII-OE model. When the CaMKII-OE model was treated with β-adrenergic stimulation, sustained DADs were recorded. These abnormalities in AP could be eliminated by reducing $[Na^+]_i$ or augmented by increasing $[Na^+]_i$.

Chapter 5 – Role of IP_3 Signalling in Arrhythmogenesis

5.1 Introduction

IP_3 is a common secondary messenger which controls various functions in many eukaryotic cells. It is produced by the PLC signalling pathway in response to GPCRs stimulation and is able to induce Ca^{2+} release from endogenous stores through IP_3Rs. Evidence accumulated over the past decade suggests that IP_3R-mediated Ca^{2+} release is a major factor that affects the modulation of ECC in atrial tissue as well as the generation of arrhythmias. Atrial myocytes express type-2 IP_3Rs at a level that is 6 to 10 times higher than ventricular myocytes [220, 221]. IP_3-dependent Ca^{2+} release in atrial myocytes was shown to improve Ca^{2+} spark frequency and twitch $[Ca^{2+}]_i$ transient amplitude, and thus may exert a positive inotropic function [220, 222].

The relationship between IP_3-dependent Ca^{2+} signalling and cardiac arrhythmias has been noted by many researchers. Cardiac arrhythmias are suggested to cause ischemia and reperfusion injury, inflammatory processes, and even cardiac failures [221, 223]. IP_3Rs are upregulated in heart failure [224] and AF [71]. In atrial myocytes, IP_3 caused spontaneous $[Ca^{2+}]_i$ transients, Ca^{2+} waves, and Ca^{2+} alternans, and facilitated the generation of EADs and DADs [221], which may lead to cardiac arrhythmias [225]. It should be noted that these effects were absent in ventricular myocytes [226].

To study the role of IP_3-dependent Ca^{2+} release in myocytes at the cellular level, we incorporated the model of the IP_3 production and degradation signal transduction system established by Cooling et al. [227]. We also developed a type-2 IP_3R model based on the previously published model of IP_3R [228]. The integrated model of mouse atrial myocytes was able to reproduce the positive inotropic function as well as the proarrhythmic effects.

5.2 The Model of the IP_3 Signal Transduction System

The biochemical processes of the IP_3 production system constitute only a small proportion of the activities in a cell, although many players and diverse interactions are involved. Cooling et al. [227] developed the first mathematical model of the IP_3 production and degradation signal transduction system in the mouse atrial myocyte. The model consists of three modules: GPCR cycling, PLC_β cycling, and the IP_3 production and degradation process.

The full reaction scheme are shown in Figure 5.1A for this model. In the reaction, the extracellular ligand, which is the L part as shown in the figure, binds to receptors (R in the figure). Then, it is precoupled with $G_\alpha GDP$ (G_d, yielding R_{lg}) or not (R_l). Fully activated receptors (R_{lg}) release $G_\alpha GTP$ (G_t), which, along with Ca^{2+}, activates PLC_β (P). In the unstimulated state, PLC_β-Ca^{2+} (P_c) hydrolyses PIP_2 to produce IP_3 via reaction R14. When stimulated, PLC_β-Ca^{2+}-$G_\alpha GTP$ (P_{cg}) hydrolyses PIP_2 at a faster rate via reaction R15. Free IP_3 is then degraded via reaction R16.

Time- and dose-dependent IP_3 transients are shown in Figure 5.1B and C. The simulated time course of IP_3 transients well reproduced experimental observations [229] upon application of 100 nM ET-1. Compared with beat-to-beat Ca^{2+} transients, IP_3 transients had relatively slow kinetics. The time to peak is ~450s and the time for full decay may be more than one hour. The model also closely matches experimental observations for the concentration of IP_3 upon stimulation by a wide range of concentrations of ET-1.

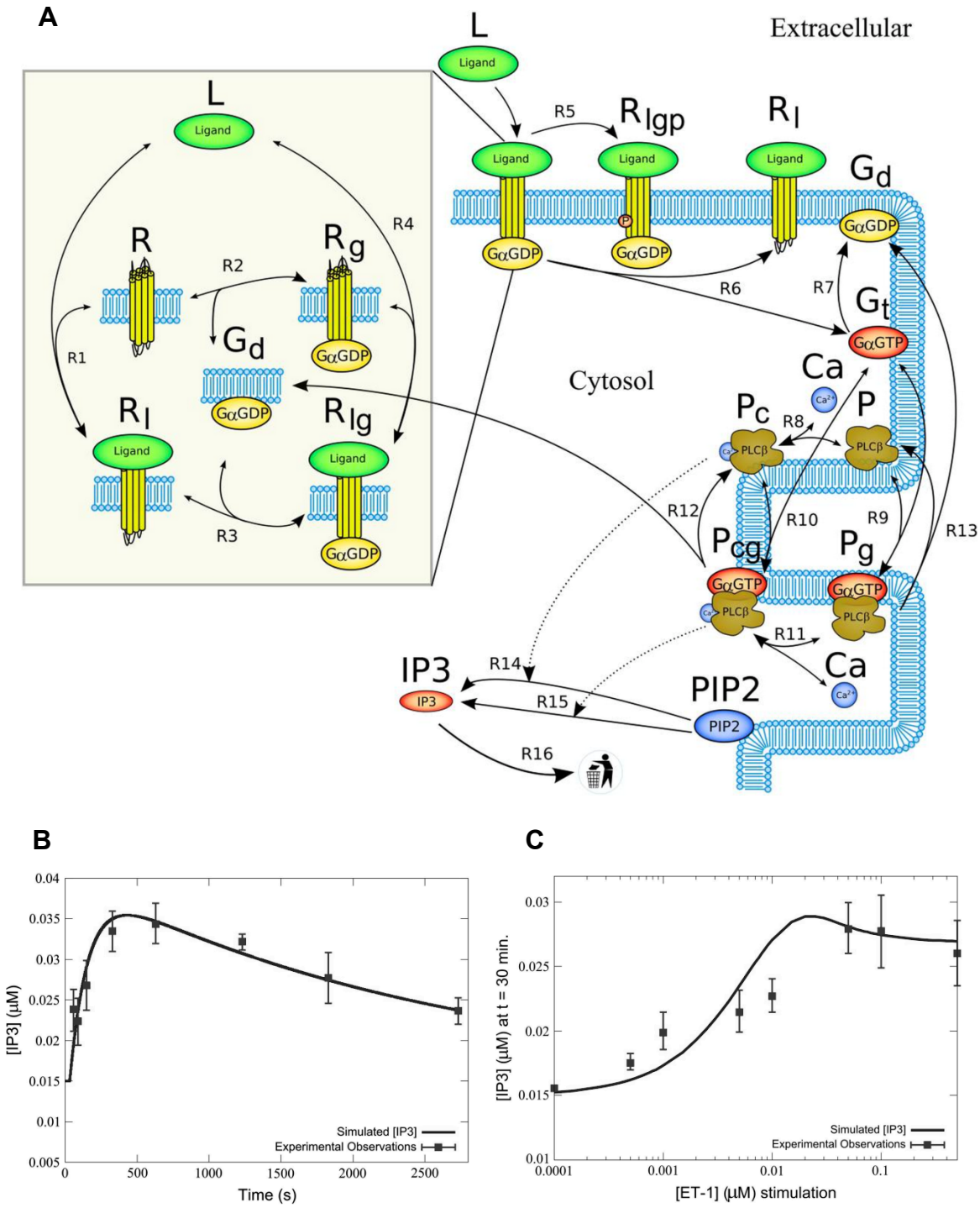

Figure 5.1 Model of IP_3 production and degradation signal transduction system in the mouse atrial myocyte. **A**: Reaction scheme of the IP_3 production system. **B**: IP_3 transient curve on ET-1 stimulation. **C**: IP_3 dose-dependent curve on ET-1 stimulation. Figures reproduced from [227].

5.3 Development of IP_3-induced Ca^{2+} Release Module

5.3.1 Development of IP_3 Receptor Model

In many cell types, IP_3R acts as release channel for ligand-gated Ca^{2+} on SR or endoplasmic reticulum. It has a major role in $[Ca^{2+}]_i$ dynamics, which in turn is involved in many cellular processes such as muscle contraction. IP_3R is activated and opened by both IP_3 and Ca^{2+}. Ca^{2+} can also become the inhibitor of IP_3R. Upon activation, IP_3Rs can release Ca^{2+} from the SR lumen to the cytosol. They are known to be responsible for the CICR, in addition to RyRs [230].

Expression of IP_3Rs in atrial myocytes has been shown at mRNA and protein levels in many species. According to papers, these species include mouse, rabbit, rat and human [71, 78, 220, 231]. Given that type-2 IP_3Rs are predominant in mouse myocytes and that they are expressed at 6- to 10-fold higher levels in atria than ventricles [220, 221], we developed a type-2 IP_3R based on the model of Doi et al. [228], which was then incorporated into our mouse atrial model.

The IP_3R model of Doi et al. [228] was originally used to study the model for Ca^{2+} in the cerebellar Purkinje cell spine, which is shown in Figure 5.2. In their model, the receptors are required to bind with both IP_3 and Ca^{2+} so that it provides Ca^{2+} flux from SR lumen to cytosol. Also, the IP_3R has shown seven states in their model. In our model, all formulations were reparameterised to reproduce type-2 IP_3R kinetics. The fitting results presented in Figure 5.3 show that the simulations of IP_3R open probability in our model well reproduced experimental observations. Open probability increased with rising IP_3 concentration ($[IP_3]$) when $[Ca^{2+}]_i$ fixed to 0.25 μM, and was saturated when IP_3 was larger than 10μM. When $[IP_3]$ was fixed, however, open probability was first increased as $[Ca^{2+}]_i$ rose to ~0.2μM and gradually declined as $[Ca^{2+}]_i$ became even larger.

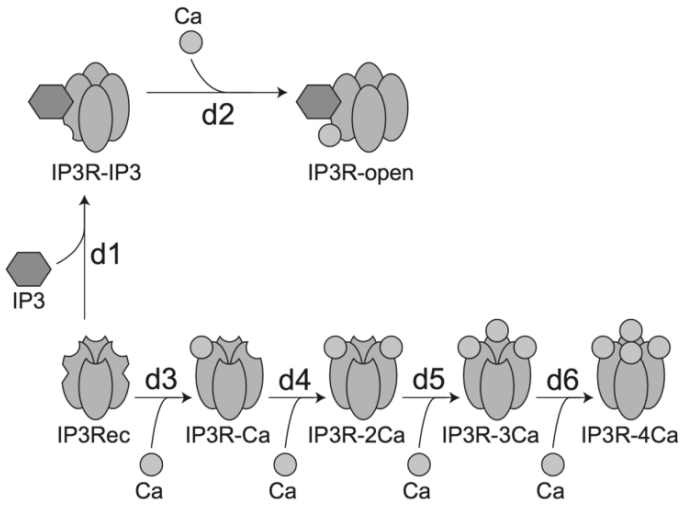

Figure 5.2 Schematic plot of the states and transitions of the IP_3R models. Figure adapted from [228].

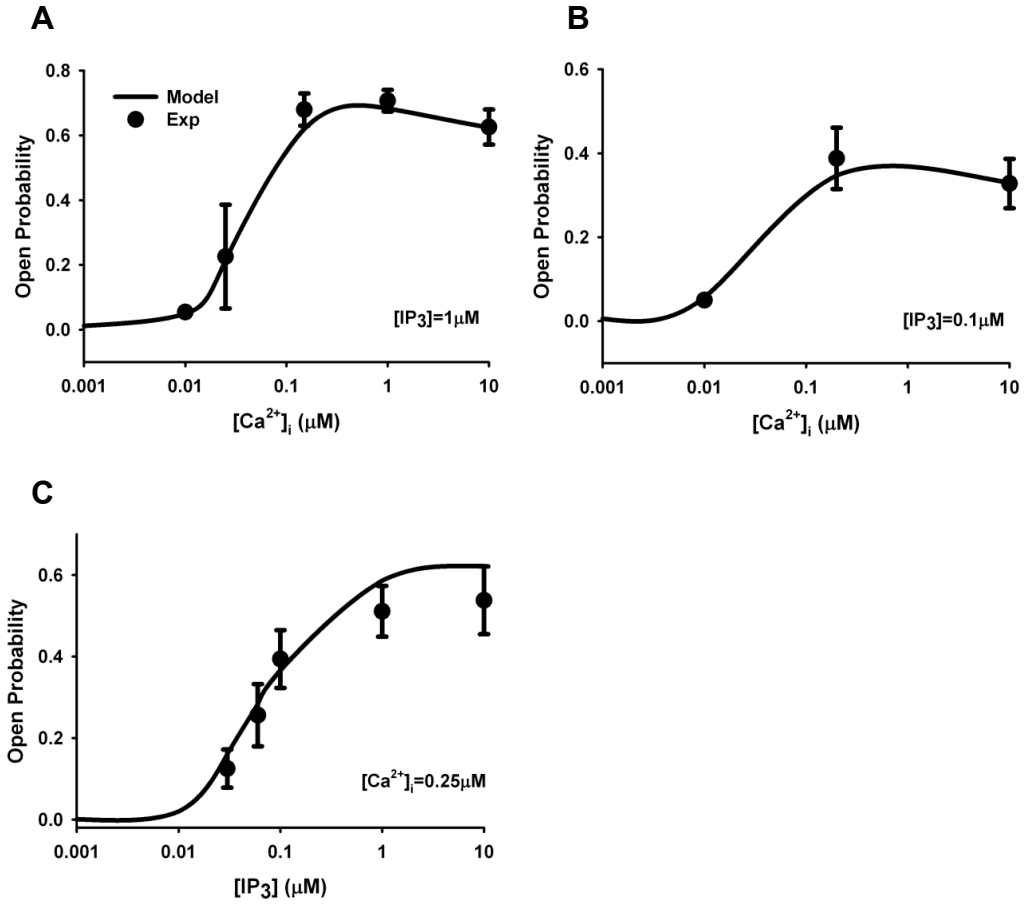

Figure 5.3 Dose-dependent open probability for the IP_3R in the simulation and experiments. **A**: $[Ca^{2+}]_i$ dependent open probability of IP_3R when IP_3 was set to 1μM. **B**: $[Ca^{2+}]_i$ dependent open probability of IP_3R when IP_3 was set to 1μM. **C**: IP_3-dependent open probability when $[Ca^{2+}]_I$ was set to 0.25μM (Experimental data: Ramos-Franco et al. [232])

5.3.2 Incorporation of IP_3 Receptor into the Atrial Model

ECC relies principally on CICR through type 2 RyRs. Direct comparison of the expression of RyRs and IP_3Rs in cardiac myocytes revealed that IP_3R mRNA levels are approximately 50-fold lower than those of the cardiac RyR mRNA [75]. Thus, compared with CICR through RyRs, the IP_3-induced Ca^{2+} release was slow and small. It has been suggested that IP_3R activity increases $[Ca^{2+}]_i$ in the vicinity of RyRs and thus facilitates CICR during ECC in adult cat atrial myocytes [226] and that IP_3-dependent Ca^{2+} release has a positive inotropic effect on ECC by facilitating Ca^{2+} release through RyR clusters in rabbit ventricle myocytes [231]. Furthermore, there is evidence that Ca^{2+} leak through IP_3Rs is present at sites where RyRs are located, and that this Ca^{2+} leak can modulate RyR Ca^{2+} release events [233]. Recent studies have also revealed that IP_3R Ca^{2+} release flux is part of SR-Ca^{2+} leak and facilitates SR-Ca^{2+} spark probability [234]. Taken together, the integral SR Ca^{2+} leak was implemented in our model as follows:

$$J_{SRleak} = (k_{leak} + k_{\text{leak\_IP3}} \times \text{O}_{\text{IP3}})(\text{Ca}_{\text{SR}} - \text{Ca}_{dyad}) \qquad (5.1)$$

where O_{IP3} is the open probability for IP_3Rs, and k_{leak_IP3} is the scale factor for IP_3R open probability. The SR release was reimplemented by multiplying the rate constants (K_{oSR}) by a factor k_{IP3}. This is formulated as follows:

$$k_{\text{IP3}} = O_{IP3} \times 12.0 \qquad (5.2)$$

In this way, the SR sensitivity is regulated as a function of IP_3R open probability. In addition, the average diffusion rate from SL to cytosol was also modified by multiplying the k_{IP3}, as it is suggested that IP_3 agonist promotes the response of the central SR release [222].

To generate sustained increases in Ca^{2+} transients, both SR Ca^{2+} load and Ca^{2+} release have to be increased. The balance between Ca^{2+} uptake into the SR and the Ca^{2+} release or the SR leak determined the SR Ca^{2+} load. Studies have shown that enhancement of SR Ca^{2+} release without increasing the uptake in parallel is not sufficient to generate sustained increases for Ca^{2+} transients [154, 235]. The reason is that, Ca^{2+}

released from SR have extruded from the cell and reduce the SR Ca^{2+} load. Thus, the steep dependence of release on SR load have limited SR Ca^{2+} release [236]. Therefore, a similar result should be expected when $[IP_3]$ is elevated. The larger Ca^{2+} transients result in a net loss of Ca^{2+} from the cell via the NCX, which in turn reduces SR Ca^{2+} load. Moreover, it has also limits the amplitude of Ca^{2+} transient. However, this is not what is observed experimentally. Exposure of cardiac myocytes to IP_3 agonists causes a sustained increase in global Ca^{2+} transients [226, 237, 238], with SR Ca^{2+} load being unchanged, or even tending to decrease [238]. Moreover, studies have also shown that IP_3 agonist, ET-1, increases the reverse mode of NCX [239, 240]. Therefore, to generate sustained increases of Ca^{2+} transients as seen experimentally, the saturation factor k_{sat} for NCX was modified by multiplying by a factor k_{sat_IP3} (ranging from 1.0 to 1.5): k_{sat_IP3} is positively correlated with $[IP_3]$. Thus, the Ca^{2+}-efflux mode of NCX is depressed with an increasing concentration of IP_3. The formulation is as follows:

$$k_{sat\_IP3} = 1.5 - \frac{1}{2 \times (1 + e^{([IP_3]-0.02186)/0.001317})} \tag{5.3}$$

5.5 Effects of IP_3-induced Ca^{2+} Release on ECC

To assess the effects of IP_3-induced Ca^{2+} release under the control condition, comparison between the control condition and IP_3R knockout (IP_3R-KO) was simulated. As shown in Figure 5.4, the amplitude of $[Ca^{2+}]_i$ transient was reduced by 21% in the IP_3R-KO model compared with the control condition, which was in agreement with experimental data [78]. The fractional SR Ca^{2+} release was unaltered in the IP_3R-KO model, which was in line with experimental observations [78]. Profiles of AP did not differ significantly between control and IP_3R-KO models. These results suggested that under basal conditions the absence of IP_3R had little effect on ECC.

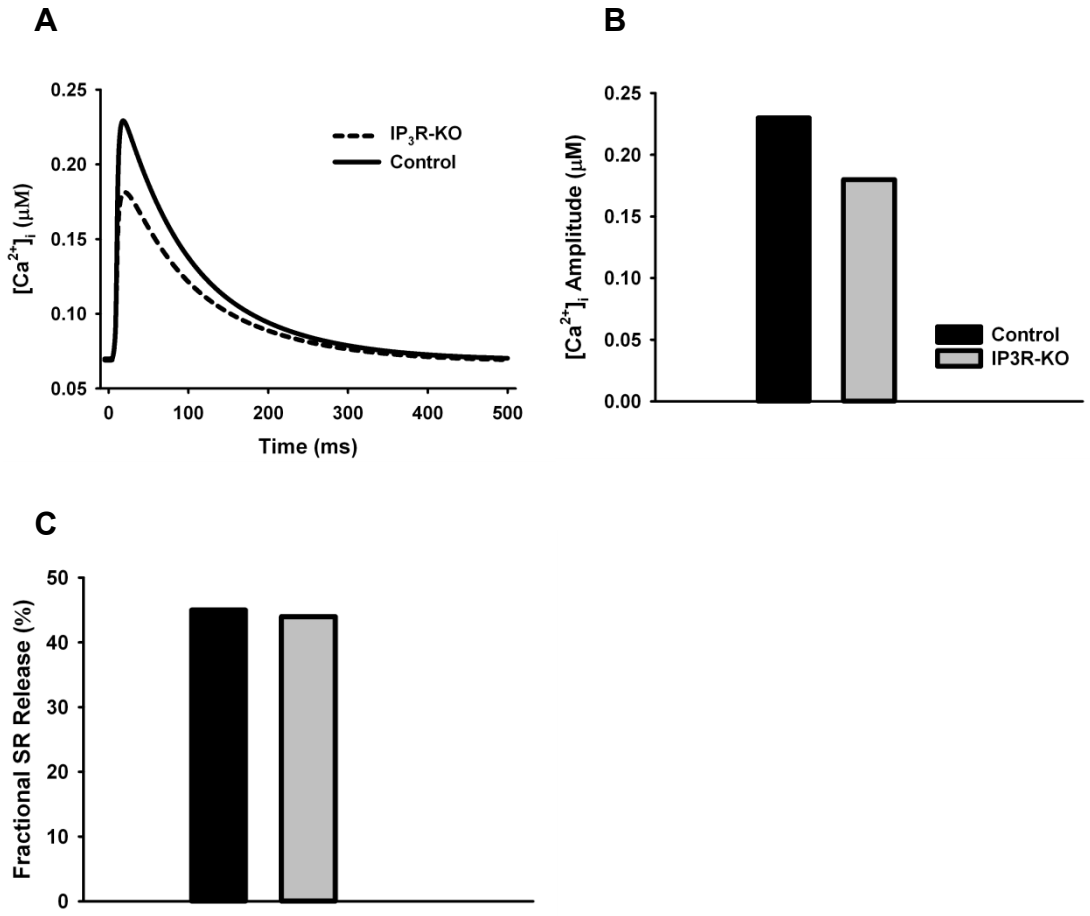

Figure 5.4 Comparison of Ca^{2+} transients between IP_3R-KO and control conditions under 1Hz pacing frequency. **A**: Time course of $[Ca^{2+}]_i$ transients. **B**: $[Ca^{2+}]_i$ transients amplitude. **C**: Fractional SR Ca^{2+} release.

ET-1 has been shown to increase $[IP_3]$ in atrial cells and to cause IP_3-dependent Ca^{2+} release. Experiments have demonstrated that IP_3-induced Ca^{2+} release may lead to arrhythmogenic alteration in atrial Ca^{2+} homeostasis. To further test the effects of IP_3-induced Ca^{2+} release on ECC, the atrial model with IP_3R upon exposure to 100nM ET-1 was simulated. As shown in Figure 5.5, $[IP_3]$ was gradually increased from the basal level of 0.015μM to the peak level of 0.035μM after the application of 100nM ET-1, and resulted in the increase in IP_3R open probability, which in turn enhanced the RyR open probability leading to abnormalities. Irregular spontaneous Ca^{2+} release and DADs occurred when $[IP_3]$ was elevated to 0.023 μM. The amplitude of $[Ca^{2+}]_i$ transient

was increased by 40%, which was close to the experimental measurement of 35±6% [78].

Notably, when $[IP_3]$ was lower than 0.023 μM, ET-1 was able to exert positive inotropic effects on $[Ca^{2+}]_i$ transients, where systolic $[Ca^{2+}]_i$ was markedly increased and no abnormalities in APs were observed. To compare the positive inotropic effects caused by IP_3 and ISO, simulations with exposure to $[IP_3]$ fixed at 0.023 μM and to 100nM ISO were performed. The diastolic $[Ca^{2+}]_i$ was increased to 0.39 μM and 0.36 μM after applying ISO and IP_3, respectively. The SR content was increased by 15% after ISO stimulation and unchanged after IP_3 stimulation. The most significant difference was the change in I_{CaL}, where a more than two-fold increase occurred when ISO was applied, while I_{CaL} was unaltered after exposure to IP_3 (Figure 5.6A). The current density of I_{NCX} was increased by 25% in the model with ISO. In contrast, it was decreased by 23% in the model with IP_3 (Figure 5.6B). Both showed a significant increase in SR release rate and a marked increase in SERCA uptake rate, but with slightly different extent (Figure 5.6C and D). Applying IP_3 caused a 15% increase in the SR leak while no significant changes occurred in the model with ISO (Figure 5.6E). $[Na^+]_i$ was decreased by 20% after exposure to ISO and unaltered after exposure to IP_3. These results implied that positive inotropic effects by IP_3 and ISO are exerted with different mechanisms. ISO stimulation, featuring an increased SR content, primarily depends on the significant increase in I_{CaL} that arises from PKA phosphorylation: thus, I_{NCX} is accordingly increased to extrude excess Ca^{2+}. IP_3 stimulation, however, achieves the increased amplitude of $[Ca^{2+}]_i$ by enhanced SR release, strengthened SERCA uptake and reduced activity of NCX: thus, the SR content remains unchanged.

IP_3-induced DADs may be due to Ca^{2+} overload caused by enhancement of SR release. Upon stimulation of ET-1, IP_3 increases the open probability of IP_3R and the sensitivity of RyR, resulting in a marked increase in SR release. The lowered activity of NCX, which extrudes less Ca^{2+} from the cell, further increases the Ca^{2+} overload and triggers spontaneous Ca^{2+} release.

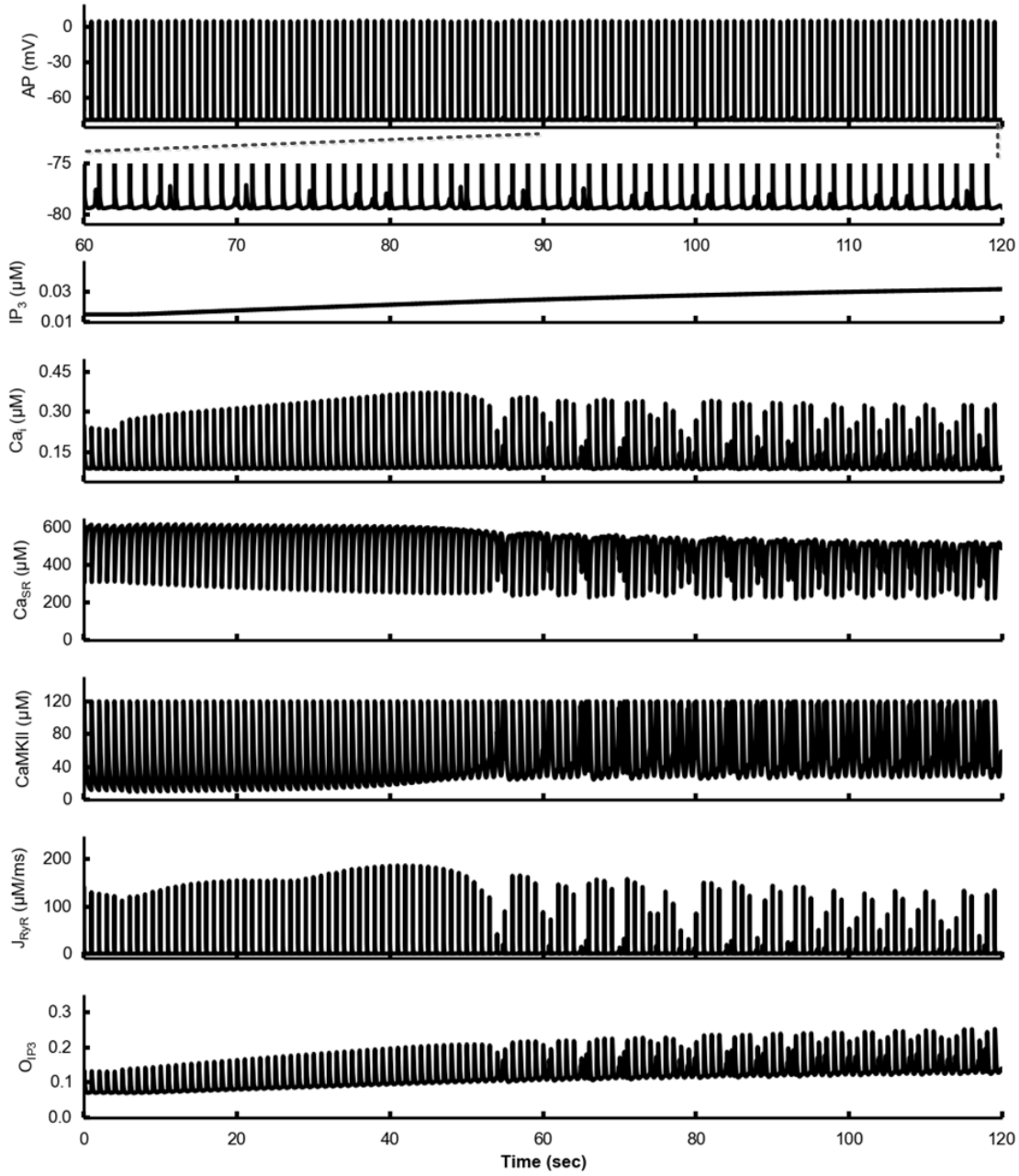

Figure 5.5 Effects of ET-1 on ECC in the model of atrial myocytes. The model was pacing at 1Hz rate. 100nM ET-1 was applied at 5s.

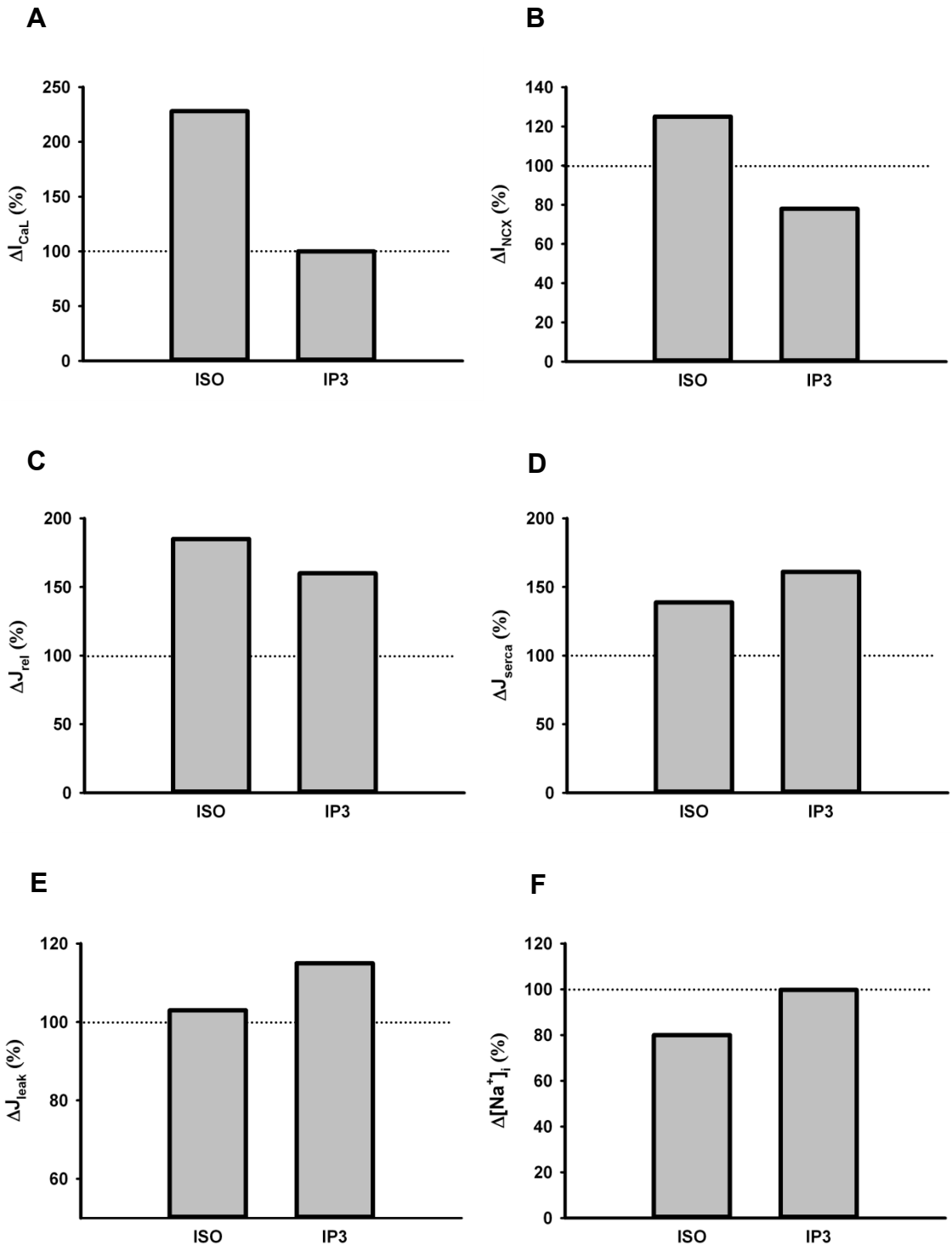

Figure 5.6 Comparison of underlying changes to control condition between ISO- and IP_3-induced positive inotropic effects.

To examine the effects of IP_3-induced Ca^{2+} release in the CaMKII-OE model, a simulation with 100nM ET-1 in the chronic CaMKII-OE model was performed. As expected, sustained DADs were observed after 65s (Figure 5.7). The amplitudes of the DADs were relatively larger than those in the control condition with ET-1 stimulation, suggesting an enhanced Ca^{2+} overload, which could be attributable to the Ca^{2+}-CaMKII-Ca^{2+} positive feedback. IP_3 caused the enhancement of SR release and the reduction of I_{NCX}, leading to the Ca^{2+} overload, which in turn increased the activities of CaMKII-dependent phosphorylation. PLB showed a two-fold increase in its CaMKII phosphorylation, and LTCC phosphorylation revealed a subtle change as it had reached almost 100% activity before applying ET-1. RyR phosphorylation activity was increased from the initial 73% to 88%, causing SR to be more prone to release Ca^{2+}.

To test the hypothesis that CaMKII plays a crucial role in IP_3-induced arrhythmia, the CaMKII-KO model with stimulation of 100nM ET-1 was simulated (Figure 5.8). In this scenario, increased [IP_3] caused a significant increase in the amplitude of $[Ca^{2+}]_i$ transient, but DADs were not induced. Without CaMKII phosphorylation, the sensitivity to Ca^{2+} for RyR was not altered; even more Ca^{2+} leaked into the dyadic space, thus eliminating spontaneous Ca^{2+} release events.

We next tested whether $[Na^+]_i$ contributes to the IP_3-induced DADs. Simulations with exposure to 100nM ET-1 were carried out under two different $[Na^+]_i$. Figure 5.9 shows the time course after 50s for the two simulations. As expected, the low $[Na^+]_i$ did not induce DADs, while the high $[Na^+]_i$ exhibited hyperactivity of spontaneous SR Ca^{2+} release and sustained DADs. Higher $[Na^+]_i$ was able to further decrease the NCX activity, which had already been depressed by IP_3 stimulation, and resulted in the increase of Ca^{2+} overload. In addition, Ca^{2+}-CaMKII-Ca^{2+} positive feedback contributed to the worsening of the overload and triggered spontaneous Ca^{2+} release events and DADs. In contrast, lower $[Na^+]_i$ eliminated the abnormalities by enhancing the NCX forward mode, extruding excess Ca^{2+} from the cell and thus maintaining lower CaMKII activity and normal Ca^{2+} handling.

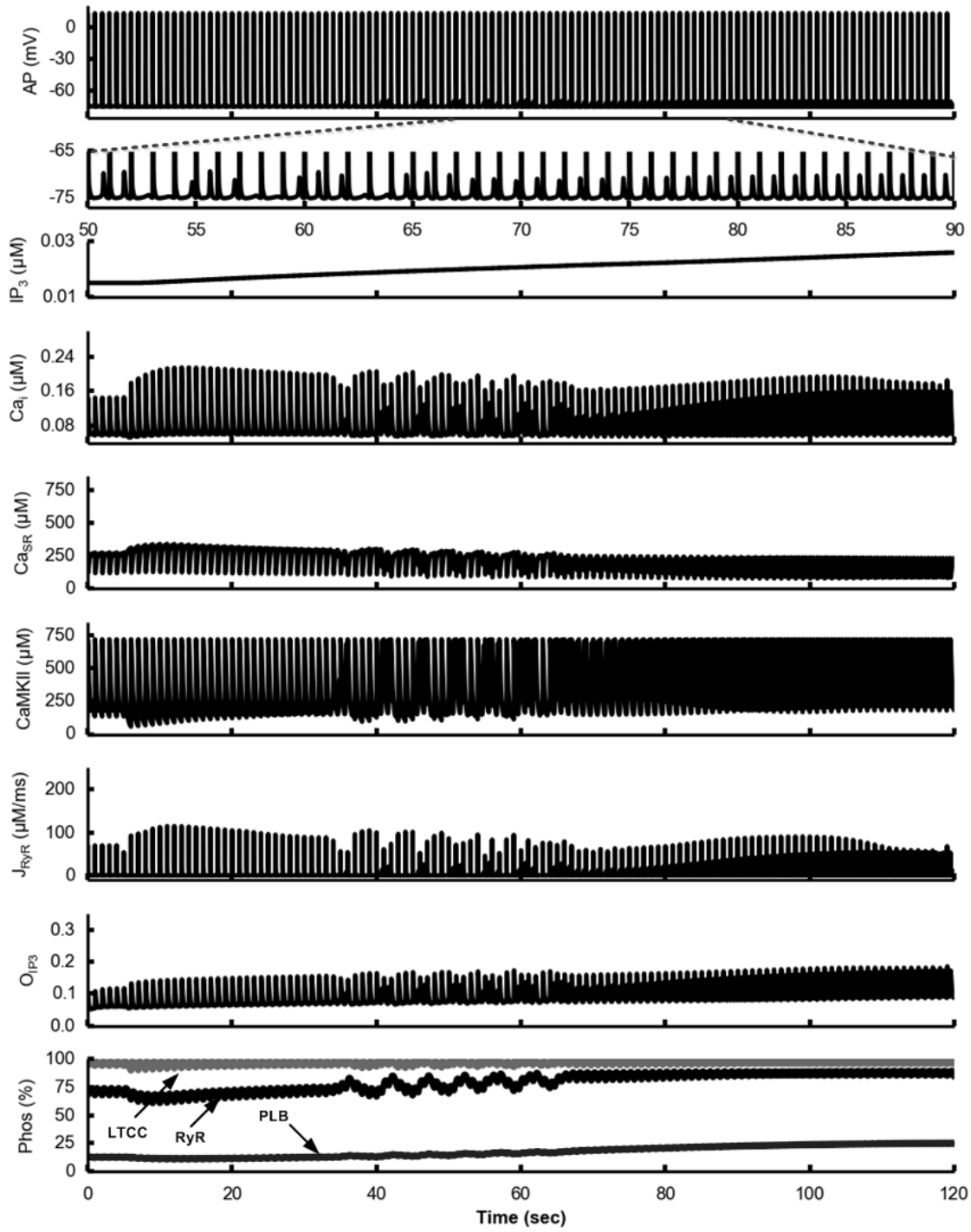

Figure 5.7 Effects of ET-1 on ECC in the chronic CaMKII-OE model of atrial myocytes. The model was pacing at 1Hz rate. 100nM ET-1 was applied at 5s.

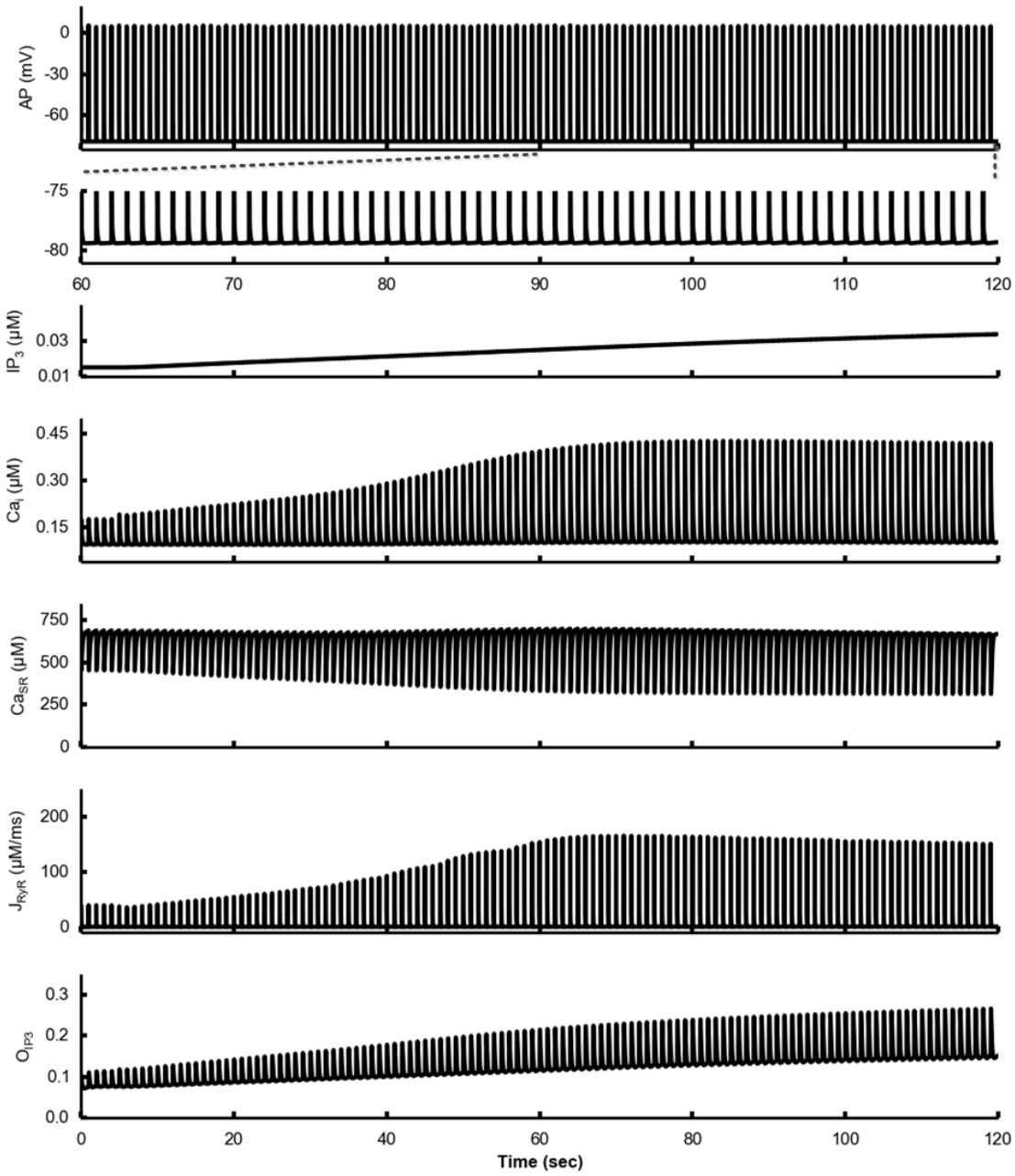

Figure 5.8 Effects of ET-1 on ECC in the chronic CaMKII-KO model of atrial myocytes. The model was pacing at 1Hz rate. 100nM ET-1 was applied at 5s.

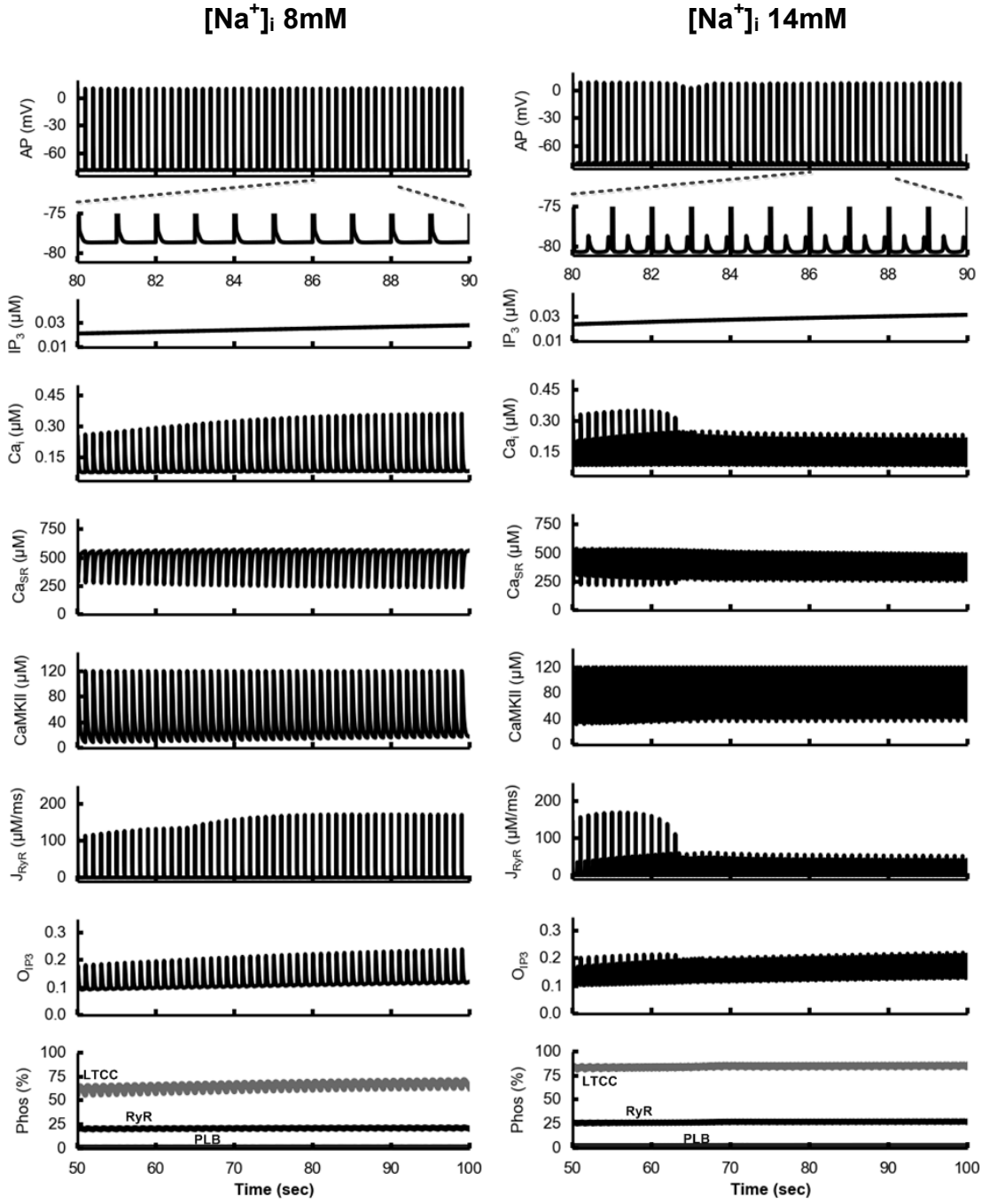

Figure 5.9 Effects of stimulation of 100nM ET-1 with clamped $[Na^+]_i$. $[Na^+]_i$ was set at 8mM for the left panels and 14mM for the right panels. ET-1 was applied at 10s. Pacing frequency was set to 1Hz.

Chapter 6 - Discussion and Conclusion

6.1 New Model Development

Mice and rats are the most commonly used mammals in research. They make up 90% of research animals [241]. A number of computational models have been developed for mouse SAN and ventricles [101, 102, 104-106]; however, models for mouse atrial myocytes are not currently available. Therefore, the aim of this study was to develop a biophysically detailed model of the isolated mouse atrial myocyte and to study the cellular proarrhythmic mechanisms.

The model of single mouse atrial myocyte is based on the model for mouse ventricular myocyte developed by Morotti et al. [106], but with a number of updates and modifications according to available experimental data. The model consists of electrophysiologically based membrane currents, dynamic Ca^{2+} handling, activation of CaMKII with phosphorylation of ECC targets, and PKA phosphorylation upon β-adrenergic activation. The model also incorporates the IP_3 production system and IP_3R into the ECC for the first time.

The model was validated by the ability to reproduce the profiles of APs and Ca^{2+} handling that are similar to experimental observations. Quantitative validations were carried out by comparing simulated APA, RP, APD, dV/dt_{max} and $[Ca^{2+}]_i$ transients with those measured from experiments. Moreover, APD rate-dependency was also performed for further validation.

6.1.1 Formalisms of the Model

Wherever possible, ion channels were modelled using Markov chain formalisms rather than HH formulations. We replaced the HH formulations for I_{to}, I_{Kr} and I_{Kur} in the parent model with Markov chain versions. Although the process of parameter fitting is usually more complicated and the running process of simulation takes more time to solve the

additional differential equations, Markov models benefit from the ability to represent complex interactions between different states, and from being closely related to the underlying structure and conformation of the ion channel proteins. This would be an advantage for the study of drug binding or genetic defects that result in altered channel function to the pathological phenotype, making this model a useful platform for a wide scope of application for further studies.

6.1.2 Action Potentials

The morphology of the simulated AP in our atrial myocyte was relatively short, similar to the report that mouse AP is quite different from the one in human, dog, pig or other species. [242]. According to scientific study, the key reason of generating the short mouse AP is because of the relative magnitude of the currents present. Large amount of K^+ currents have been found in mouse myocytes, which ensure rapid repolarisation. In our model, APD_{90} was shorter than that in the ventricular model [106], which was in agreement with experimental observation [169].

The atrial AP is shown in a triangular wave shape, which is common for most of the mammalian species. [243]. Our atrial model is able to reproduce this triangular atrial AP wave shape. On the other way around, the atrial mouse AP was longer during the early repolarisation phase (APD_{25}), compared with that in the ventricle. Our model suggests that it is likely to be the result of reduced current density of I_{to} in atrial, compared with left ventricular, myocytes.

6.1.3 Ca^{2+} Handling

ECC is governed by a mechanism termed *Ca^{2+}-induced Ca^{2+} release* [25]. The influx of Ca^{2+} via LTCC (Cav1.2) triggers the RyR to release a much greater Ca^{2+} from the SR [244]. The amplitude and kinetics of these Ca^{2+} fluxes are tightly regulated in cardiac myocytes in order to ensure physiological modulation of contractility.

Ca^{2+} handling in mice features extremely fast mechanisms [20]. Unlike that in other

mammals with longer APDs, the percentage of the Ca^{2+} release from intracellular stores in a systolic Ca^{2+} transient is much higher in mouse myocytes, while the Ca^{2+} influx via LTCC is less needed. Due to the relatively short APD of mouse myocytes, the Ca^{2+} removal during diastole is also fast to ensure a sufficient refilling for the ventricles.

Compared with the ventricular model of the mouse myocyte [103, 106], our atrial model exhibits less current density of I_{CaL} and I_{NCX}, suggesting that less Ca^{2+} influx is required for a normal ECC and thus less Ca^{2+} needs to be extruded. Consequently, Ca^{2+} transients in mouse atrial myocytes depend further on internal Ca^{2+} stores, making the rates of Ca^{2+} transients achieving the peak and pumping back from cytosol even faster than those in ventricular myocytes. This is in line with the observations from experiment on rats that time to peak and decay of Ca^{2+} transients are faster in atria than in ventricles [156]. Proportions that contribute to the Ca^{2+} removal by the known mechanisms (SERCA, NCX and Ca^{2+} pump) also showed a difference between the two types of models, where the contribution made by SERCA to the decay of the systolic Ca^{2+} transient was far greater in the atria. This is also in agreement with the experimental measures [118].

6.1.4 CaMKII Phosphorylation in the Regulation of ECC

Due to the limited kinetic data regarding CaMKII phosphorylation on atrial substrates, the CaMKII module in our atrial model is primarily based on the previously published model of mouse ventricles [106]. Studies have shown that CaMKII can phosphorylate the α_{1C} and the β_{2a} subunits of the LTCC [165]. Our model is able to reproduce the quick CaMKII-dependent I_{CaL} facilitation as suggested by a number of experiments [56, 183]. RyRs control Ca^{2+} release from the SR during systole and it is activated by $[Ca^{2+}]_{dyad.}$ The sensitivity of RyRs for Ca^{2+} is enhanced by CaMKII phosphorylation [34]. The SR leak and the open probability of RyR are shown to be increased during CaMKII phosphorylation [182]. Our model is able to mimic these effects by implementing the CaMKII-dependent factor of SR sensitivity and the factor of SR leak. PLB resides in the

SR membrane and negatively regulates the SERCA pump. PLB phosphorylation relieves the inhibitory effects, allowing SERCA to more freely uptake Ca^{2+} from cytosol. Our simulation shows a slow kinetics of PLB phosphorylation, which is observed experimentally [183]. Compared with the ventricular model, our atrial model shows relatively smaller inhibitory effects of PLB phosphorylation, due to the fact that expression of PLB in murine atrial tissue is half of that in ventricular tissue [151].

Although excessive CaMKII activity is associated with arrhythmias, physiologic CaMKII activity may take an important role in maintaining normal cardiac function and heart rhythm. CaMKII-KO model shows little changes in the $\Delta[Ca^{2+}]_i$ and APD under steady state pacing. CaMKII on FDAR show that CaMKII-KO slows FDAR, while in contrast, both WT and CaMKII-OE exhibit fast adaptation to a sudden increased pacing frequency. Moreover, β-adrenergic stimulation shows that CaMKII-KO reduced the amplitude of $\Delta[Ca^{2+}]_i$ in response to ISO application as compared to WT. The experimental study using CaMKII-KO mouse also showed that CaMKII is required for heart rate increases by ISO stimulation or in response to a physiological fight or flight mechanism [245]. Taken together, our study support the view that CaMKII is not required to maintain basal heart rates but plays an important role in adaptation to the sustained heart rate increases during physiological stress.

6.1.5 Effects of β-adrenergic Stimulation on ECC

Our model of the mouse atrial myocyte with β-adrenergic stimulation is able to reproduce PKA-mediate modulation on ECC targets. LTCC phosphorylation shows an enhanced open probability and increased distribution of gating in mode 2, similar to the experimental observations [200, 206]. PKA phosphorylation also shows enhanced open probability and channel sensitivity in RyR, increased uptake rate from cytosol in SERCA, increased Ca^{2+} unbinding rate in TnI and increased current density in I_{Kur} and I_{Na}. In addition, the model can also show the reduction of $[Na^{+}]_i$ concentration upon exposure to

ISO [246].

Our model of the β-adrenergic signalling system in mouse atrial myocytes can also reflect the prolongation of APD. Upon β-adrenergic stimulation, the major effect on APD_{25} and APD_{50} comes from an increase in the I_{CaL}, while APD_{75} and APD_{90} show moderate increase due to an increase in I_{Kur}. The total result of interaction is the moderate prolongation of APD. It is previously proven by researchers that similar phenomenon have been found in rat ventricular cells. [199]. However the major contributing currents and APD prolongation mechanism were not studied.

According to the study, activation of the β-adrenergic signalling system significantly increases the magnitude of $[Ca^{2+}]_i$ transients [218]. Although it is obvious that phosphorylation of PLB increases the uptake rate of Ca^{2+} into the SR upon β-adrenergic stimulation [20], however, it has also been proven that this increase is not only caused by PLB phosphorylation. Recently Eisner et al. [247] analysed the main reason for cardiac positive inotropic effects upon β-adrenergic stimulation. According to their study, there are four main factors - RyR, SERCA, LTCC and troponin, affected by stimulation. Their analysis has shown that the main factors among them which causes the positive cardiac inotropy is LTCC. In our model, stimulation of the β-adrenergic signalling system increases I_{CaL} by about two-fold compared to the control condition. This has almost doubles Ca^{2+} influx into the myocyte, while Ca^{2+} extrusion from the myocyte, predominantly by the NCX, does not increase to the same degree. Therefore, our results are in agreement with the view by Eisner et al. that LTCC is the crucial factor for cardiac inotropy in mouse atrial myocytes.

6.1.6 Effects of IP_3 Signalling in ECC

In atrial myocytes, the role of cytosolic $[IP_3]$ has been reported for the modulation of cytosolic Ca^{2+} transients in a variety of animals [226, 231, 248-250]. IP_3R channel activity, with type-2 IP_3Rs as the most prevalent isoform in cardiac myocytes, depends on $[IP_3]$ and $[Ca^{2+}]_i$ [70, 231]. There is evidence that atrial myocytes express functional

IP_3Rs at higher densities than ventricular myocytes [222, 226]. Our mouse atrial model is the first to incorporate the IP_3 signalling system, and is able to reproduce the inotropic effects. Compared with control conditions (with basal $[IP_3]$ of 0.015μM), the IP_3R-KO model shows a slight decrease in $[Ca^{2+}]_i$ amplitude and unaltered SR content. APs are not significantly changed between control and IP_3R-KO models. These results suggested that under basal conditions the absence of IP_3R had little effect on ECC, which is consistent with experimental findings [78]. Our model also predicted the difference in exerting inotropic effects between β-adrenergic and IP_3 signalling pathways. Upon ET-1 stimulation, enhancement of RyR and reduced activity of NCX are the main factors that contribute to the increased $[Ca^{2+}]_i$ amplitude, whereas the significant increase of I_{CaL} is primarily responsible for the inotropy by β-adrenergic stimulation.

6.2 Cellular Proarrhythmic Mechanisms Underlying Atrial Fibrillation

AF is the top sustained cardiac arrhythmia which poses lifelong risks for human health [251]. It was believed that impaired $[Ca^{2+}]_i$ handling contributed to atrial mechanical dysfunction [252]. The main two causes for AF at the organ level mainly consist of ectopic and re-entry activities. Risk factors such as age and cardiovascular diseases such as heart failure could lead to specific structural and electrical substrates, and thus increase the possibility to trigger AF. Moreover, cardiovascular diseases are also believed to increase the susceptibility to AF.

Reentry requires a susceptible substrate as well as a trigger, usually provided by an ectopic beat. According to the leading-circle concept, reentry results from a balance between tissue refractoriness and conduction speed [253]. Ectopic activity may contribute to AF initiation by acting as a trigger of reentry. Ectopic activity is caused by abnormal spontaneous depolarisations termed *EADs* or *DADs*. It has been reported that excessive AP prolongations with re-activation of the I_{CaL} or I_{NaL} contribute to the development of EADs in isolated canine right atria [254]. DADs result from spontaneous diastolic SR Ca^{2+} releases, typically caused by either SR Ca^{2+} overload or dysfunction of

the SR Ca^{2+} release channels. They manifest as individual, or a series of, small-amplitude membrane oscillations that could eventually lead to full APs.

We have developed a new computational model of a mouse atrial myocyte with biochemical detailed modules of CaMKII-dependent regulation, β-adrenergic stimulation and the IP_3 signalling system, aiming to analyse potentially arrhythmogenic effects induced by each module. Our simulations on single cells were primarily focused on the investigation of mechanisms underlying triggered activities and predict that enhanced RyR activity and elevation of $[Na^+]_i$ are the main determinants of DAD induction. EADs were not observed in our model, even during adrenergic stimulation. The reasons may be as follows: 1) EADs occur when an abnormal depolarisation starts during phase 2 or 3 of AP. However, AP in the mouse atrial myocyte has a very short early repolarisation phase and total duration; thus, by the time spontaneous SR Ca^{2+} release occurs, AP has already repolarised to resting level. 2) EADs occur in the presence of APD prolongation [127]. However, APD prolongations in our studies were insufficient, whether induced by CaMKII-OE with β-adrenergic stimulation or exposure to ET-1 together with ISO. 3) In some studies of larger animals, EADs are not induced using the similar deterministic formalisms of CaMKII and PKA phosphorylation modules [100], while stochastic models of LTCC model gating can trigger EADs [255]. This may suggest that EAD formation via CaMKII is sensitive to stochasticity.

6.2.1 Role of CaMKII and $[Na^+]_i$ in Arrhythmogenesis

CaMKII can phosphorylate multiple substrates and regulate many aspects of cellular functions in cardiac myocytes. However, hyperactivity of CaMKII in the myocyte may promote triggered activities leading to AF [182]. We assessed the effects of CaMKII-OE in chronic and acute models. In the simulation of chronic CaMKII-OE, DADs are not observed under steady state, although APD and CaMKII-mediated phosphorylation of LTCC, RyR and PLB have been markedly increased. The compensatory increase in NCX in CaMKII-OE myocytes, promoting extrusion of excess Ca^{2+}, may counteract the effects

of augmented SR Ca^{2+} release. Simulation with fast pacing protocol was performed, since activities of CaMKII phosphorylation exhibit rate-dependent increases [35]. As expected, DADs can be induced by the fast pacing frequency in the chronic CaMKII-OE model, due to enhanced RyR activity regulated by the increased activity of CaMKII. Clamping the phosphorylation of RyR at WT level may abolish DADs that are induced by the above fast pacing protocol. However, clamping the phosphorylation of LTCC or PLB cannot eliminate DADs. This implies the importance of RyR phosphorylation in arrhythmogenesis, as suggested in the study that mice with a gain-of-function mutation in RyR exhibit an increased susceptibility to pacing-induced AF [182]. Genetic and pharmacological inhibition of CaMKII phosphorylation of RyR reduced the inducibility of AF in mice, showing that hyperphosphorylation of the RyR might play a central role in AF pathogenesis [182]. When the CaMKII level acutely changes to overexpressed, the model also predicts the induction of DADs, and the amplitude of the induced DAD oscillates up and down. These DADs that arise from acute CaMKII-OE become augmented when the CaMKII-Ca^{2+}-Na^{+}-CaMKII feedback loop is incorporated, suggesting a synergistic interaction between perturbed Na^{+} loading and CaMKII.

CaMKII-dependent $[Na^{+}]_i$ elevation has been associated with diastolic dysfunction and arrhythmias in CaMKII-OE mice [256]. These events were thought to result from reduced forward- and increased reverse-mode in NCX, which facilitated Ca^{2+} overload and spontaneous SR Ca^{2+} release, thus causing DADs. These proarrhythmic effects could be abolished by application of the potent Na^{+} channel blocker tetrodotoxin, thus supporting Na^{+} channel-dependent effects on DAD induction. An increase in $[Na^{+}]_i$ exerts a positive inotropic effect by increasing the SR Ca^{2+} load through CaMKII phosphorylation modulations, thus enhancing cardiac contractility. It has been also proposed that the alteration underlying arrhythmias induced by ouabain (a NKA inhibitor) is at the level of the RyR, rather than the SR Ca^{2+} load [257]. Studies have showed that ouabain increased the activity of CaMKII and that ouabain-induced spontaneous contractile activity and Ca^{2+} waves were significantly reduced by CaMKII inhibition [258]. CaMKII-OE has been demonstrated to exacerbate ouabain-induced spontaneous

contractile activity [258], in line with our simulation results that CaMKII-OE with high $[Na^+]_i$ rather than low $[Na^+]_i$ exhibits DADs. This supports the concept that Na^+-induced Ca^{2+} overload increases CaMKII activation, thus forming an arrhythmogenic positive feedback loop of increasing CaMKII activity, $[Na^+]_i$, and $[Ca^{2+}]_i$.

6.2.2 Role of β-adrenergic Stimulation in Arrhythmogenesis

During β-adrenergic stimulation, PKA-mediated phosphorylation at LTCC increases channel open probability and channel availability, leading to a significant increase in Ca^{2+} influx, followed by a boost of CaMKII activation and an enhancement of RyR sensitivity, which promotes SR Ca^{2+} release. In the control condition, the β-adrenergic stimulation does not induce DADs, because reduced $[Na^+]_i$ arising from NKA phosphorylation promotes the forward mode of NCX and thus relieves Ca^{2+} overload. The overall RyR phosphorylation by PKA and CaMKII is insufficient to cause hypersensitivity of RyR leading to spontaneous Ca^{2+} release. In the CaMKII-OE model with β-adrenergic stimulation, however, sustained DADs are easily induced, even without applying the fast pacing protocol. CaMKII hyperactivity in the CaMKII-OE model becomes exacerbated as Ca^{2+} influx is increased two-fold through PKA-mediated LTCC. The overall high level of phosphorylation of RyR enhances the sensitivity of RyR, resulting in the spontaneous SR Ca^{2+} release.

The effect of Na^+ loading to fuel CaMKII-Na^+-Ca^{2+}-CaMKII feedback is even more striking upon stimulation of ISO. In this context, Na^+ overload and PKA activation synergise to enhance Ca^{2+} cycling and reinforce the arrhythmogenic positive feedback leading to ever-increasing CaMKII activation. As previously demonstrated [100], RyR phosphorylation is primarily responsible for the occurrence of DADs, as preventing CaMKII effects at RyRs limits the arrhythmogenic events. We also showed that ISO-induced DADs could be prevented by reducing $[Na^+]_i$, or facilitated by increasing it. Consistent with our model predictions, β-adrenergic stimulation of myocytes isolated from mice overexpressing CaMKII increased the number of DADs [259]. DADs and

triggered activity were largely prevented in these failing mouse myocytes with application of either I_{NaL} or CaMKII inhibitor [260].

6.2.3 Role of IP_3 signalling in Arrhythmogenesis

Studies have shown that IP_3-induced Ca^{2+} release may lead to arrhythmogenic alterations in atrial Ca^{2+} handling. Patients with chronic AF demonstrate an upregulated expression of IP_3R in atrial tissue [71]. In cat atrial myocytes, ET-1 can induce Ca^{2+} alternans [226], which may degenerate into arrhythmogenic Ca^{2+} waves [261]. Furthermore, ET-1 can also induce spontaneous Ca^{2+} release events during diastole in rabbit, cat, rat and mouse atrial myocytes. These spontaneous signals ranged from Ca^{2+} puff events and Ca^{2+} waves to extra AP-derived global Ca^{2+} transients [221, 222, 226, 237, 238]. Similarly, in the human atrial myocardium, ET-1 can also induce arrhythmic extra contractions mediated by activation of PLC and IP_3Rs [262] and, in isolated human atrial myocytes, IP_3 agonist increases the frequency of spontaneous Ca^{2+} sparks without altering SR Ca^{2+} load [83].

Our mouse atrial model with the IP_3 signalling system reproduces well the positive inotropic effects and induction of DADs after exposure to ET-1. However, results from the simulation suggest that IP_3-induced SR Ca^{2+} release via IP_3R is small and slow, and thus insufficient to generate DADs. Moreover, it is not sufficient to enhance the overall SR Ca^{2+} release alone to achieve a sustained increase in the Ca^{2+} transient. We hypothesised that Ca^{2+} removal should also be altered, in which NCX forward mode is depressed. This can be explained as PLC-mediated NCX modulation, as suggested experimentally [239, 240]. We conclude that the induction of DADs by ET-1 is primarily attributable to the enhanced sensitivity of RyR arising from nearby activation of IP_3R. In rat atrial myocytes, some IP_3Rs and RyRs are colocalised in the SL area, making it possible that activation of IP_3Rs will facilitate RyR opening. The resultant Ca^{2+} signal would then activate the nearby NCX, thus generating a depolarising current. Furthermore, in the human atrial myocardium, inhibition of RyRs suppressed ET-1-induced arrhythmias, suggesting that the relatively few IP_3Rs in the atrium can cause a large Ca^{2+}

release due to amplification from nearby RyRs, and thereby induce NCX-triggered arrhythmias. Since IP_3-induced arrhythmogenesis is eventually accomplished by enhanced RyR activity, we predict that CaMKII-OE or high $[Na^+]_i$ will further augment RyR activity leading to enhanced Ca^{2+} overload and DADs, while CaMKII-KO or low$[Na^+]_i$ will abolish the spontaneous Ca^{2+} release events.

6.3 Limitations

Although the presented model was extensively verified by the available experimental data and reproduced most effects that result from stimulation of CaMKII-OE, β-adrenergic stimulation and the IP_3 signalling system, there are some limitations. First, some of the experimental data used to validate the developed model were obtained from other regions of the heart or species, such as mouse ventricles, rats, rabbits and canines. Second, the accuracy of model parameters is subject to the accuracy of biochemical experiments, which can vary over an order of magnitude. Third, some model parameters are numerically optimised to fit the experimental data in the absent of direct experimental data. Finally, a fourth limitation lies in the cellular structure of the model. Mouse atrial myocytes lack a prominent transverse tubular system, which establishes the tight coupling of the SR to SL in ventricular myocytes, enabling a virtually uniform Ca^{2+} release throughout the myocyte. Since the Ca^{2+} handling in our atrial model is based on the framework of ventricular myocytes [147], Ca^{2+} fluxes from SL to cytosol are not considered to be attenuated. Dividing the bulk cytosol into several compartments is a better implementation and can mimic the effect that ECC is initiated around the periphery of the cells and then propagates into the centre of the cells with decreasing amplitude.

6.4 Conclusion

We have developed a novel biophysically and biochemically detailed mathematical model of a mouse atrial myocyte, which includes intracellular Ca^{2+} handling, CaMKII

and β-adrenergic regulation of ECC, and the IP_3 signalling system. Our results support experimental findings of a synergistic interaction between perturbed Na^+ fluxes and CaMKII activity, and predict that enhanced RyR activity during IP_3-induced Ca^{2+} release is the major cause of the arrhythmogenesis in IP_3 signalling. The model presented in this thesis provides a powerful computational tool for investigating the specific mechanisms of atrial arrhythmias and may develop enhanced treatment options for atrial disorders.

References

1. H. Gray, W.L., *Anatomy of the human body. 20 ed*. 1918, Philadelphia: Lea & Febiger.

2. Fagan, T., *Cardiovascular System. Second edition.* Vol. Elsevier. 2002.

3. Wessels, A. and D. Sedmera, *Developmental anatomy of the heart: a tale of mice and man.* Physiol Genomics, 2003. **15**(3): p. 165-76.

4. Courneya, C.A.M. and M.J. Parker, *Cardiovascular Physiology: A Clinical Approach*. 2011: Wolters Kluwer/Lippincott Williams & Wilkins Health.

5. Rosen, M., *Cardiac electrophysiology: a textbook.* 1990, New York: Futura Publishing Co.

6. *Heart and ECG*. Available from: http://toxsci.oxfordjournals.org/content/121/1/11/F2.large.jpg.

7. *Cardiac Cycle*. Available from: http://www.zuniv.net/physiology/book/images/10-1.jpg.

8. *Cadiac muscle fibres*. Available from: http://www.histology-world.com/photomicrographs/cardiacmuscle1label.jpg.

9. Xu, F., et al., *Disruption of a mitochondrial RNA-binding protein gene results in decreased cytochrome b expression and a marked reduction in ubiquinol-cytochrome c reductase activity in mouse heart mitochondria.* Biochem J, 2008. **416**(1): p. 15-26.

10. *Cell Membrane.*

11. Nedovic, V. and R. Willaert, *Applications of Cell Immobilisation Biotechnology*. 2006: Springer Netherlands.

12. Katz, A., *Physiology of the Heart, 5th Revised edn.* 2010: Lippincott Williams and Wilkins.

13. Hirose, M., et al., *Diacylglycerol kinase zeta inhibits G(alpha)q-induced atrial remodeling in transgenic mice.* Heart Rhythm, 2009. **6**(1): p. 78-84.

14. Nygren, A., A.E. Lomax, and W.R. Giles, *Heterogeneity of action potential durations in isolated mouse left and right atria recorded using voltage-sensitive dye*

mapping. Am J Physiol Heart Circ Physiol, 2004. **287**(6): p. H2634-43.

15. Faggioni, M., et al., *Suppression of spontaneous ca elevations prevents atrial fibrillation in calsequestrin 2-null hearts.* Circ Arrhythm Electrophysiol, 2014. **7**(2): p. 313-20.

16. B Alberts, A.J., J Lewis, *Molecular Biology of the Cell. 4th edition.* 2002, New York: Garland Science.

17. Walker, C.A. and F.G. Spinale, *The structure and function of the cardiac myocyte: a review of fundamental concepts.* J Thorac Cardiovasc Surg, 1999. **118**(2): p. 375-82.

18. J. Malmivuo, R.P., *Bioelectromagnetism*. 1995, Oxford: Oxford university press.

19. Sutko, J.L. and J.T. Willerson, *Ryanodine alteration of the contractile state of rat ventricular myocardium. Comparison with dog, cat, and rabbit ventricular tissues.* Circ Res, 1980. **46**(3): p. 332-43.

20. Bers, D.M., *Excitation-contraction coupling and cardiac contractile force. second ed.* 2001, Boston: Kluwer academic publishers.

21. Mitchell, R.D., H.K. Simmerman, and L.R. Jones, *Ca2+ binding effects on protein conformation and protein interactions of canine cardiac calsequestrin.* J Biol Chem, 1988. **263**(3): p. 1376-81.

22. Viatchenko-Karpinski, S., et al., *Abnormal calcium signaling and sudden cardiac death associated with mutation of calsequestrin.* Circ Res, 2004. **94**(4): p. 471-7.

23. Terentyev, D., et al., *Calsequestrin determines the functional size and stability of cardiac intracellular calcium stores: Mechanism for hereditary arrhythmia.* Proc Natl Acad Sci U S A, 2003. **100**(20): p. 11759-64.

24. Song, Q., et al., *Differential integration of Ca2+-calmodulin signal in intact ventricular myocytes at low and high affinity Ca2+-calmodulin targets.* J Biol Chem, 2008. **283**(46): p. 31531-40.

25. Bers, D.M., *Cardiac excitation-contraction coupling.* Nature, 2002. **415**(6868): p. 198-205.

26. Cheung, W.Y., *Cyclic 3',5'-nucleotide phosphodiesterase. Demonstration of an activator.* Biochem Biophys Res Commun, 1970. **38**(3): p. 533-8.

27. Tadross, M.R., I.E. Dick, and D.T. Yue, *Mechanism of local and global Ca2+ sensing by calmodulin in complex with a Ca2+ channel.* Cell, 2008. **133**(7): p. 1228-40.

28. Maier, L.S. and D.M. Bers, *Calcium, calmodulin, and calcium-calmodulin kinase II: heartbeat to heartbeat and beyond.* J Mol Cell Cardiol, 2002. **34**(8): p. 919-39.

29. Jeremy M. Berg, J.L.T., L. Stryer, *Biochemistry. Seventh Edition.* 2012, New York: W. H. Freeman.

30. Strack, S., et al., *Differential inactivation of postsynaptic density-associated and soluble Ca2+/calmodulin-dependent protein kinase II by protein phosphatases 1 and 2A.* J Neurochem, 1997. **68**(5): p. 2119-28.

31. Braun, A.P. and H. Schulman, *The multifunctional calcium/calmodulin-dependent protein kinase: from form to function.* Annu Rev Physiol, 1995. **57**: p. 417-45.

32. Xiao, R.P., et al., *Dual regulation of Ca2+/calmodulin-dependent kinase II activity by membrane voltage and by calcium influx.* Proc Natl Acad Sci U S A, 1994. **91**(20): p. 9659-63.

33. Dzhura, I., et al., *Calmodulin kinase determines calcium-dependent facilitation of L-type calcium channels.* Nat Cell Biol, 2000. **2**(3): p. 173-7.

34. Wehrens, X.H., et al., *Ca2+/calmodulin-dependent protein kinase II phosphorylation regulates the cardiac ryanodine receptor.* Circ Res, 2004. **94**(6): p. e61-70.

35. Maier, L.S., et al., *Transgenic CaMKIIdeltaC overexpression uniquely alters cardiac myocyte Ca2+ handling: reduced SR Ca2+ load and activated SR Ca2+ release.* Circ Res, 2003. **92**(8): p. 904-11.

36. Brittsan, A.G. and E.G. Kranias, *Phospholamban and cardiac contractile function.* J Mol Cell Cardiol, 2000. **32**(12): p. 2131-9.

37. Odermatt, A., K. Kurzydlowski, and D.H. MacLennan, *The vmax of the Ca2+-ATPase of cardiac sarcoplasmic reticulum (SERCA2a) is not altered by Ca2+/calmodulin-dependent phosphorylation or by interaction with phospholamban.* J Biol Chem, 1996. **271**(24): p. 14206-13.

38. Wagner, S., et al., *Ca2+/calmodulin-dependent protein kinase II regulates cardiac*

Na+ channels. J Clin Invest, 2006. **116**(12): p. 3127-38.

39. Maltsev, V.A., et al., *Modulation of late sodium current by Ca2+, calmodulin, and CaMKII in normal and failing dog cardiomyocytes: similarities and differences.* Am J Physiol Heart Circ Physiol, 2008. **294**(4): p. H1597-608.

40. Wagner, S., et al., *Ca/calmodulin kinase II differentially modulates potassium currents.* Circ Arrhythm Electrophysiol, 2009. **2**(3): p. 285-94.

41. H Lodish, A.B., SL Zipursky, *Molecular Cell Biology. 4th edition.* 2000, New York: W. H. Freeman.

42. Campbell, N., *Biology*. 2002, San Francisco: Benjamin Cummings.

43. Berridge, M., *(2014) Cell Signalling Biology; doi:10.1042/csb0001002.*

44. Vroling, B., et al., *GPCRDB: information system for G protein-coupled receptors.* Nucleic Acids Res, 2011. **39**(Database issue): p. D309-19.

45. Venkatakrishnan, A.J., et al., *Molecular signatures of G-protein-coupled receptors.* Nature, 2013. **494**(7436): p. 185-94.

46. *Activation of the G alpha subunit of a G-protein-coupled receptor*. Available from: http://www.nature.com/scitable/topicpage/gpcr-14047471.

47. Fimia, G.M. and P. Sassone-Corsi, *Cyclic AMP signalling.* J Cell Sci, 2001. **114**(Pt 11): p. 1971-2.

48. Willoughby, D. and D.M. Cooper, *Organization and Ca2+ regulation of adenylyl cyclases in cAMP microdomains.* Physiol Rev, 2007. **87**(3): p. 965-1010.

49. *cAMP signalling pathway.*; Available from: http://nens.yellowcouch.org/articles/CROSSTALK/CellSign.html.

50. Kamp, T.J., M.C. Sanguinetti, and R.J. Miller, *Voltage- and use-dependent modulation of cardiac calcium channels by the dihydropyridine (+)-202-791.* Circ Res, 1989. **64**(2): p. 338-51.

51. Chen, X., et al., *L-type Ca2+ channel density and regulation are altered in failing human ventricular myocytes and recover after support with mechanical assist devices.* Circ Res, 2002. **91**(6): p. 517-24.

52. McDonald, T.F., et al., *Regulation and modulation of calcium channels in cardiac,*

skeletal, and smooth muscle cells. Physiol Rev, 1994. **74**(2): p. 365-507.

53. duBell, W.H., W.J. Lederer, and T.B. Rogers, *Dynamic modulation of excitation-contraction coupling by protein phosphatases in rat ventricular myocytes.* J Physiol, 1996. **493 (Pt 3)**: p. 793-800.

54. Marx, S.O., et al., *PKA phosphorylation dissociates FKBP12.6 from the calcium release channel (ryanodine receptor): defective regulation in failing hearts.* Cell, 2000. **101**(4): p. 365-76.

55. Wegener, A.D., et al., *Phospholamban phosphorylation in intact ventricles. Phosphorylation of serine 16 and threonine 17 in response to beta-adrenergic stimulation.* J Biol Chem, 1989. **264**(19): p. 11468-74.

56. Valverde, C.A., et al., *Frequency-dependent acceleration of relaxation in mammalian heart: a property not relying on phospholamban and SERCA2a phosphorylation.* J Physiol, 2005. **562**(Pt 3): p. 801-13.

57. Talosi, L., I. Edes, and E.G. Kranias, *Intracellular mechanisms mediating reversal of beta-adrenergic stimulation in intact beating hearts.* Am J Physiol, 1993. **264**(3 Pt 2): p. H791-7.

58. MacDougall, L.K., L.R. Jones, and P. Cohen, *Identification of the major protein phosphatases in mammalian cardiac muscle which dephosphorylate phospholamban.* Eur J Biochem, 1991. **196**(3): p. 725-34.

59. Kranias, E.G. and R.J. Solaro, *Phosphorylation of troponin I and phospholamban during catecholamine stimulation of rabbit heart.* Nature, 1982. **298**(5870): p. 182-4.

60. Layland, J., R.J. Solaro, and A.M. Shah, *Regulation of cardiac contractile function by troponin I phosphorylation.* Cardiovasc Res, 2005. **66**(1): p. 12-21.

61. duBell, W.H., et al., *Effects of PP1/PP2A inhibitor calyculin A on the E-C coupling cascade in murine ventricular myocytes.* Am J Physiol Heart Circ Physiol, 2002. **282**(1): p. H38-48.

62.Wolska, B.M., *Calcineurin and cardiac function: is more or less better for the heart?* Am J Physiol Heart Circ Physiol, 2009. **297**(5): p. H1576-7.

63. Han, F., et al., *Role of phospholemman phosphorylation sites in mediating*

kinase-dependent regulation of the Na+-K+-ATPase. Am J Physiol Cell Physiol, 2010. **299**(6): p. C1363-9.

64. Kirstein, M., et al., *Dose-dependent alteration of rat cardiac sodium current by isoproterenol: results from direct measurements on multicellular preparations.* Pflugers Arch, 1996. **431**(3): p. 395-401.

65. Matsuda, J.J., H.C. Lee, and E.F. Shibata, *Acetylcholine reversal of isoproterenol-stimulated sodium currents in rabbit ventricular myocytes.* Circ Res, 1993. **72**(3): p. 517-25.

66. Dilly, K.W., et al., *Overexpression of beta2-adrenergic receptors cAMP-dependent protein kinase phosphorylates and modulates slow delayed rectifier potassium channels expressed in murine heart: evidence for receptor/channel co-localization.* J Biol Chem, 2004. **279**(39): p. 40778-87.

67. Li, G.R., et al., *Adrenergic modulation of ultrarapid delayed rectifier K+ current in human atrial myocytes.* Circ Res, 1996. **78**(5): p. 903-15.

68. Gonzalez de la Fuente, M., et al., *Chronic atrial fibrillation up-regulates beta1-Adrenoceptors affecting repolarizing currents and action potential duration.* Cardiovasc Res, 2013. **97**(2): p. 379-88.

69. Thomas, D., et al., *Deletion of protein kinase A phosphorylation sites in the HERG potassium channel inhibits activation shift by protein kinase A.* J Biol Chem, 1999. **274**(39): p. 27457-62.

70. Kockskamper, J., et al., *Emerging roles of inositol 1,4,5-trisphosphate signaling in cardiac myocytes.* J Mol Cell Cardiol, 2008. **45**(2): p. 128-47.

71. Yamada, J., et al., *[Up-regulation of inositol 1, 4, 5-trisphosphate receptor expression in atrial tissue in patients with chronic atrial fibrillation].* J Cardiol, 2002. **39**(1): p. 57-8.

72. Gorza, L., S. Schiaffino, and P. Volpe, *Inositol 1,4,5-trisphosphate receptor in heart: evidence for its concentration in Purkinje myocytes of the conduction system.* J Cell Biol, 1993. **121**(2): p. 345-53.

73. Bare, D.J., et al., *Cardiac type 2 inositol 1,4,5-trisphosphate receptor: interaction*

and modulation by calcium/calmodulin-dependent protein kinase II. J Biol Chem, 2005. **280**(16): p. 15912-20.

74. Zhou, B.Q., S.J. Hu, and G.B. Wang, *The analysis of ultrastructure and gene expression of sarco/endoplasmic reticulum calcium handling proteins in alloxan-induced diabetic rat myocardium.* Acta Cardiol, 2006. **61**(1): p. 21-7.

75. Moschella, M.C. and A.R. Marks, *Inositol 1,4,5-trisphosphate receptor expression in cardiac myocytes.* J Cell Biol, 1993. **120**(5): p. 1137-46.

76. *PIP2 cleavage to IP3 and DAG*. Available from: http://en.wikipedia.org/wiki/File:PIP2_cleavage_to_IP3_and_DAG.jpg.

77. Nosek, T.M., et al., *Inositol trisphosphate enhances calcium release in skinned cardiac and skeletal muscle.* Am J Physiol, 1986. **250**(5 Pt 1): p. C807-11.

78. Li, X., et al., *Endothelin-1-induced arrhythmogenic Ca2+ signaling is abolished in atrial myocytes of inositol-1,4,5-trisphosphate(IP3)-receptor type 2-deficient mice.* Circ Res, 2005. **96**(12): p. 1274-81.

79. Huser, J. and L.A. Blatter, *Elementary events of agonist-induced Ca2+ release in vascular endothelial cells.* Am J Physiol, 1997. **273**(5 Pt 1): p. C1775-82.

80. Parker, I., J. Choi, and Y. Yao, *Elementary events of InsP3-induced Ca2+ liberation in Xenopus oocytes: hot spots, puffs and blips.* Cell Calcium, 1996. **20**(2): p. 105-21.

81. Bootman, M., et al., *Imaging the hierarchical Ca2+ signalling system in HeLa cells.* J Physiol, 1997. **499 (Pt 2)**: p. 307-14.

82. Berridge, M.J., *Elementary and global aspects of calcium signalling.* J Physiol, 1997. **499 (Pt 2)**: p. 291-306.

83. Gassanov, N., et al., *Angiotensin II-induced changes of calcium sparks and ionic currents in human atrial myocytes: potential role for early remodeling in atrial fibrillation.* Cell Calcium, 2006. **39**(2): p. 175-86.

84. H V Huikuri, A Castellanos, and R.J. Myerburg, *Sudden death due to cardiac arrhythmias.* New England Journal of Medicine, 2001. **345**(20).

85. Stengl, M., *Experimental models of spontaneous ventricular arrhythmias and of sudden cardiac death.* Physiol Res, 2010. **59 Suppl 1**: p. S25-31.

86. Glasscock, E., et al., *Kv1.1 potassium channel deficiency reveals brain-driven cardiac dysfunction as a candidate mechanism for sudden unexplained death in epilepsy.* J Neurosci, 2010. **30**(15): p. 5167-75.

87. Aiello, E.A., R.I. Jabr, and W.C. Cole, *Arrhythmia and delayed recovery of cardiac action potential during reperfusion after ischemia. Role of oxygen radical-induced no-reflow phenomenon.* Circ Res, 1995. **77**(1): p. 153-62.

88. Kujala, K., et al., *Cell model of catecholaminergic polymorphic ventricular tachycardia reveals early and delayed afterdepolarizations.* PLoS One, 2012. **7**(9): p. e44660.

89. January, C.T. and J.M. Riddle, *Early afterdepolarizations: mechanism of induction and block. A role for L-type Ca2+ current.* Circ Res, 1989. **64**(5): p. 977-90.

90. Ferrier, G.R. and G.K. Moe, *Effect of calcium on acetylstrophanthidin-induced transient depolarizations in canine Purkinje tissue.* Circ Res, 1973. **33**(5): p. 508-15.

91. Jin, H., A.R. Lyon, and F.G. Akar, *Arrhythmia mechanisms in the failing heart.* Pacing Clin Electrophysiol, 2008. **31**(8): p. 1048-56.

92. Durrer, D., et al., *Re-entry and ventricular arrhythmias in local ischemia and infarction of the intact dog heart.* Proc K Ned Akad Wet C, 1971. **74**(4): p. 321-34.

93. Paul F. Cranefield and R.S. Aronson, *Cardiac arrhythmias : the role of triggered activity and other mechanisms.* 1988, New York: Mount Kisco.

94. Noble, D., *Cardiac action and pacemaker potentials based on the Hodgkin-Huxley equations.* Nature, 1960. **188**: p. 495-7.

95. McAllister, R.E., D. Noble, and R.W. Tsien, *Reconstruction of the electrical activity of cardiac Purkinje fibres.* J Physiol, 1975. **251**(1): p. 1-59.

96. DiFrancesco, D. and D. Noble, *A model of cardiac electrical activity incorporating ionic pumps and concentration changes.* Philos Trans R Soc Lond B Biol Sci, 1985. **307**(1133): p. 353-98.

97. Bueno-Orovio, A., et al., *Na/K pump regulation of cardiac repolarization: insights from a systems biology approach.* Pflugers Arch, 2014. **466**(2): p. 183-93.

98. Hodgkin, A.L. and A.F. Huxley, *A quantitative description of membrane current and*

its application to conduction and excitation in nerve. J Physiol, 1952. **117**(4): p. 500-44.

99. Luo, C.H. and Y. Rudy, *A dynamic model of the cardiac ventricular action potential. II. Afterdepolarizations, triggered activity, and potentiation.* Circ Res, 1994. **74**(6): p. 1097-113.

100. Soltis, A.R. and J.J. Saucerman, *Synergy between CaMKII substrates and beta-adrenergic signaling in regulation of cardiac myocyte Ca(2+) handling.* Biophys J, 2010. **99**(7): p. 2038-47.

101. Mangoni, M.E., et al., *Bradycardia and slowing of the atrioventricular conduction in mice lacking CaV3.1/alpha1G T-type calcium channels.* Circ Res, 2006. **98**(11): p. 1422-30.

102. Kharche, S., et al., *A mathematical model of action potentials of mouse sinoatrial node cells with molecular bases.* Am J Physiol Heart Circ Physiol, 2011. **301**(3): p. H945-63.

103. Bondarenko, V.E., et al., *Computer model of action potential of mouse ventricular myocytes.* Am J Physiol Heart Circ Physiol, 2004. **287**(3): p. H1378-403.

104. Li, L., et al., *A mathematical model of the murine ventricular myocyte: a data-driven biophysically based approach applied to mice overexpressing the canine NCX isoform.* Am J Physiol Heart Circ Physiol, 2010. **299**(4): p. H1045-63.

105. Yang, J.H. and J.J. Saucerman, *Phospholemman is a negative feed-forward regulator of Ca2+ in beta-adrenergic signaling, accelerating beta-adrenergic inotropy.* J Mol Cell Cardiol, 2012. **52**(5): p. 1048-55.

106. Morotti, S., et al., *A novel computational model of mouse myocyte electrophysiology to assess the synergy between Na+ loading and CaMKII.* J Physiol, 2014. **592**(Pt 6): p. 1181-97.

107. Zhang, Y., et al., *Pharmacological changes in cellular Ca2+ homeostasis parallel initiation of atrial arrhythmogenesis in murine Langendorff-perfused hearts.* Clin Exp Pharmacol Physiol, 2009. **36**(10): p. 969-80.

108. Mancarella, S., et al., *Impaired Ca2+ homeostasis is associated with atrial fibrillation in the alpha1D L-type Ca2+ channel KO mouse.* Am J Physiol Heart Circ

Physiol, 2008. **295**(5): p. H2017-24.

109. Bossen, E.H., J.R. Sommer, and R.A. Waugh, *Comparative stereology of mouse atria.* Tissue Cell, 1981. **13**(1): p. 71-7.

110. King, J.H., et al., *Atrial arrhythmia, triggering events and conduction abnormalities in isolated murine RyR2-P2328S hearts.* Acta Physiol (Oxf), 2013. **207**(2): p. 308-23.

111. Lomax, A.E., C.S. Kondo, and W.R. Giles, *Comparison of time- and voltage-dependent K+ currents in myocytes from left and right atria of adult mice.* Am J Physiol Heart Circ Physiol, 2003. **285**(5): p. H1837-48.

112. Zhou, Q., G.C. Bett, and R.L. Rasmusson, *Markov models of use-dependence and reverse use-dependence during the mouse cardiac action potential.* PLoS One, 2012. **7**(8): p. e42295.

113. Trepanier-Boulay, V., et al., *Postnatal development of atrial repolarization in the mouse.* Cardiovasc Res, 2004. **64**(1): p. 84-93.

114. Nakamura, H., et al., *Presence and functional role of the rapidly activating delayed rectifier K(+) current in left and right atria of adult mice.* Eur J Pharmacol, 2010. **649**(1-3): p. 14-22.

115. Clancy, C.E. and Y. Rudy, *Cellular consequences of HERG mutations in the long QT syndrome: precursors to sudden cardiac death.* Cardiovasc Res, 2001. **50**(2): p. 301-13.

116. Xie, L.H., et al., *Ablation of sarcolipin results in atrial remodeling.* Am J Physiol Cell Physiol, 2012. **302**(12): p. C1762-71.

117. Mahajan, A., et al., *A rabbit ventricular action potential model replicating cardiac dynamics at rapid heart rates.* Biophys J, 2008. **94**(2): p. 392-410.

118. Walden, A.P., K.M. Dibb, and A.W. Trafford, *Differences in intracellular calcium homeostasis between atrial and ventricular myocytes.* J Mol Cell Cardiol, 2009. **46**(4): p. 463-73.

119. Wang, J., et al., *Regional expression of sodium pump subunits isoforms and Na+-Ca++ exchanger in the human heart.* J Clin Invest, 1996. **98**(7): p. 1650-8.

120. Luss, I., et al., *Expression of cardiac calcium regulatory proteins in atrium v ventricle in different species.* J Mol Cell Cardiol, 1999. **31**(6): p. 1299-314.

121. Cheng, H., W.J. Lederer, and M.B. Cannell, *Calcium sparks: elementary events underlying excitation-contraction coupling in heart muscle.* Science, 1993. **262**(5134): p. 740-4.

122. Trafford, A.W., et al., *Calcium signalling microdomains and the t-tubular system in atrial mycoytes: potential roles in cardiac disease and arrhythmias.* Cardiovasc Res, 2013. **98**(2): p. 192-203.

123. Bootman, M.D., et al., *Atrial cardiomyocyte calcium signalling.* Biochim Biophys Acta, 2011. **1813**(5): p. 922-34.

124. Kirk, M.M., et al., *Role of the transverse-axial tubule system in generating calcium sparks and calcium transients in rat atrial myocytes.* J Physiol, 2003. **547**(Pt 2): p. 441-51.

125. Reckziegel, G., et al., *Electrophysiological characterization of Na+ currents in acutely isolated human hippocampal dentate granule cells.* J Physiol, 1998. **509 (Pt 1)**: p. 139-50.

126. Richmond, J.E., et al., *Slow inactivation in human cardiac sodium channels.* Biophys J, 1998. **74**(6): p. 2945-52.

127. Lemoine, M.D., et al., *Arrhythmogenic left atrial cellular electrophysiology in a murine genetic long QT syndrome model.* Cardiovasc Res, 2011. **92**(1): p. 67-74.

128. Hofmann, F., L. Lacinova, and N. Klugbauer, *Voltage-dependent calcium channels: from structure to function.* Rev Physiol Biochem Pharmacol, 1999. **139**: p. 33-87.

129. Sra, J.S., et al., *Practical Electrophysiology*. 2014: Cardiotext Publishing.

130. Rose, R.A., M.G. Kabir, and P.H. Backx, *Altered heart rate and sinoatrial node function in mice lacking the cAMP regulator phosphoinositide 3-kinase-gamma.* Circ Res, 2007. **101**(12): p. 1274-82.

131. Xiao, Y.F., et al., *Electrophysiological characterization of murine HL-5 atrial cardiomyocytes.* Am J Physiol Cell Physiol, 2006. **291**(3): p. C407-16.

132. Wickenden, A.D., et al., *Regional contributions of Kv1.4, Kv4.2, and Kv4.3 to transient outward K+ current in rat ventricle.* Am J Physiol, 1999. **276**(5 Pt 2): p. H1599-607.

133. Xu, H., H. Li, and J.M. Nerbonne, *Elimination of the transient outward current and action potential prolongation in mouse atrial myocytes expressing a dominant negative Kv4 alpha subunit.* J Physiol, 1999. **519 Pt 1**: p. 11-21.

134. Campbell, D.L., et al., *The calcium-independent transient outward potassium current in isolated ferret right ventricular myocytes. I. Basic characterization and kinetic analysis.* J Gen Physiol, 1993. **101**(4): p. 571-601.

135. Qin, M., et al., *Atrial tachyarrhythmia in Rgs5-null mice.* PLoS One, 2012. **7**(11): p. e46856.

136. Bou-Abboud, E., H. Li, and J.M. Nerbonne, *Molecular diversity of the repolarizing voltage-gated K+ currents in mouse atrial cells.* J Physiol, 2000. **529 Pt 2**: p. 345-58.

137. Wang, Z., B. Fermini, and S. Nattel, *Sustained depolarization-induced outward current in human atrial myocytes. Evidence for a novel delayed rectifier K+ current similar to Kv1.5 cloned channel currents.* Circ Res, 1993. **73**(6): p. 1061-76.

138. Xu, H., W. Guo, and J.M. Nerbonne, *Four kinetically distinct depolarization-activated K+ currents in adult mouse ventricular myocytes.* J Gen Physiol, 1999. **113**(5): p. 661-78.

139. Brouillette, J., et al., *Functional properties of K+ currents in adult mouse ventricular myocytes.* J Physiol, 2004. **559**(Pt 3): p. 777-98.

140. Hu, Y., S.V. Jones, and W.H. Dillmann, *Effects of hyperthyroidism on delayed rectifier K+ currents in left and right murine atria.* Am J Physiol Heart Circ Physiol, 2005. **289**(4): p. H1448-55.

141. Sanguinetti, M.C. and N.K. Jurkiewicz, *Two components of cardiac delayed rectifier K+ current. Differential sensitivity to block by class III antiarrhythmic agents.* J Gen Physiol, 1990. **96**(1): p. 195-215.

142. Li, G.R., et al., *Evidence for two components of delayed rectifier K+ current in*

human ventricular myocytes. Circ Res, 1996. **78**(4): p. 689-96.

143. Wang, Z., B. Fermini, and S. Nattel, *Rapid and slow components of delayed rectifier current in human atrial myocytes.* Cardiovasc Res, 1994. **28**(10): p. 1540-6.

144. Blaustein, M.P. and W.J. Lederer, *Sodium/calcium exchange: its physiological implications.* Physiol Rev, 1999. **79**(3): p. 763-854.

145. Shenoy, R., I. Klein, and K. Ojamaa, *Differential regulation of SR calcium transporters by thyroid hormone in rat atria and ventricles.* Am J Physiol Heart Circ Physiol, 2001. **281**(4): p. H1690-6.

146. Glitsch, H.G., *Electrophysiology of the sodium-potassium-ATPase in cardiac cells.* Physiol Rev, 2001. **81**(4): p. 1791-826.

147. Shannon, T.R., et al., *A mathematical treatment of integrated Ca dynamics within the ventricular myocyte.* Biophys J, 2004. **87**(5): p. 3351-71.

148. Periasamy, M. and A. Kalyanasundaram, *SERCA pump isoforms: their role in calcium transport and disease.* Muscle Nerve, 2007. **35**(4): p. 430-42.

149. Periasamy, M., P. Bhupathy, and G.J. Babu, *Regulation of sarcoplasmic reticulum Ca2+ ATPase pump expression and its relevance to cardiac muscle physiology and pathology.* Cardiovasc Res, 2008. **77**(2): p. 265-73.

150. Koss, K.L., I.L. Grupp, and E.G. Kranias, *The relative phospholamban and SERCA2 ratio: a critical determinant of myocardial contractility.* Basic Res Cardiol, 1997. **92 Suppl 1**: p. 17-24.

151. Freestone, N.S., et al., *Differential lusitropic responsiveness to beta-adrenergic stimulation in rat atrial and ventricular cardiac myocytes.* Pflugers Arch, 2000. **441**(1): p. 78-87.

152. Maier, L.S., et al., *Ca(2+) handling in isolated human atrial myocardium.* Am J Physiol Heart Circ Physiol, 2000. **279**(3): p. H952-8.

153. Bers, D.M., *Calcium fluxes involved in control of cardiac myocyte contraction.* Circ Res, 2000. **87**(4): p. 275-81.

154. Eisner, D.A., et al., *Integrative analysis of calcium cycling in cardiac muscle.* Circ Res, 2000. **87**(12): p. 1087-94.

155. Lukyanenko, V., T.F. Wiesner, and S. Gyorke, *Termination of Ca2+ release during Ca2+ sparks in rat ventricular myocytes.* J Physiol, 1998. **507 (Pt 3)**: p. 667-77.

156. Escobar, A.L., et al., *Developmental changes of intracellular Ca2+ transients in beating rat hearts.* Am J Physiol Heart Circ Physiol, 2004. **286**(3): p. H971-8.

157. Saucerman, J.J. and D.M. Bers, *Calmodulin mediates differential sensitivity of CaMKII and calcineurin to local Ca2+ in cardiac myocytes.* Biophys J, 2008. **95**(10): p. 4597-612.

158. C. B. Klee, *Interaction of calmodulin with Ca2+ and target proteins. In Calmodulin. P. Cohen and C. B. Klee, editors. Elsevier, New York. 35–56.* 1988, New York: Elsevier.

159. Linse, S., A. Helmersson, and S. Forsen, *Calcium binding to calmodulin and its globular domains.* J Biol Chem, 1991. **266**(13): p. 8050-4.

160. Stemmer, P.M. and C.B. Klee, *Dual calcium ion regulation of calcineurin by calmodulin and calcineurin B.* Biochemistry, 1994. **33**(22): p. 6859-66.

161. Gaertner, T.R., et al., *Comparative analyses of the three-dimensional structures and enzymatic properties of alpha, beta, gamma and delta isoforms of Ca2+-calmodulin-dependent protein kinase II.* J Biol Chem, 2004. **279**(13): p. 12484-94.

162. Bradshaw, J.M., et al., *An ultrasensitive Ca2+/calmodulin-dependent protein kinase II-protein phosphatase 1 switch facilitates specificity in postsynaptic calcium signaling.* Proc Natl Acad Sci U S A, 2003. **100**(18): p. 10512-7.

163. Lee, T.S., et al., *Calmodulin kinase II is involved in voltage-dependent facilitation of the L-type Cav1.2 calcium channel: Identification of the phosphorylation sites.* J Biol Chem, 2006. **281**(35): p. 25560-7.

164. Hudmon, A., et al., *CaMKII tethers to L-type Ca2+ channels, establishing a local and dedicated integrator of Ca2+ signals for facilitation.* J Cell Biol, 2005. **171**(3): p. 537-47.

165. Grueter, C.E., et al., *L-type Ca2+ channel facilitation mediated by phosphorylation of the beta subunit by CaMKII.* Mol Cell, 2006. **23**(5): p. 641-50.

166. Ono, K. and H.A. Fozzard, *Two phosphatase sites on the Ca2+ channel*

affecting different kinetic functions. J Physiol, 1993. **470**: p. 73-84.

167. Huke, S. and D.M. Bers, *Ryanodine receptor phosphorylation at Serine 2030, 2808 and 2814 in rat cardiomyocytes.* Biochem Biophys Res Commun, 2008. **376**(1): p. 80-5.

168. Simmerman, H.K. and L.R. Jones, *Phospholamban: protein structure, mechanism of action, and role in cardiac function.* Physiol Rev, 1998. **78**(4): p. 921-47.

169. Knollmann, B.C., et al., *Action potential characterization in intact mouse heart: steady-state cycle length dependence and electrical restitution.* Am J Physiol Heart Circ Physiol, 2007. **292**(1): p. H614-21.

170. Pacher, P., et al., *Electrophysiological changes in rat ventricular and atrial myocardium at different stages of experimental diabetes.* Acta Physiol Scand, 1999. **166**(1): p. 7-13.

171. Reil, J.C., et al., *Cardiac Rac1 overexpression in mice creates a substrate for atrial arrhythmias characterized by structural remodelling.* Cardiovasc Res, 2010. **87**(3): p. 485-93.

172. Lomax, A.E., R.A. Rose, and W.R. Giles, *Electrophysiological evidence for a gradient of G protein-gated K+ current in adult mouse atria.* Br J Pharmacol, 2003. **140**(3): p. 576-84.

173. Hua, R., et al., *Distinct patterns of constitutive phosphodiesterase activity in mouse sinoatrial node and atrial myocardium.* PLoS One, 2012. **7**(10): p. e47652.

174. Koh, J.T., et al., *Cardiac Characteristics of Transgenic Mice Overexpressing Refsum Disease Gene-Associated Protein within the Heart.* Biochem Biophys Res Commun, 2001. **286**(5): p. 1107-16.

175. Verheule, S., et al., *Increased vulnerability to atrial fibrillation in transgenic mice with selective atrial fibrosis caused by overexpression of TGF-beta1.* Circ Res, 2004. **94**(11): p. 1458-65.

176. Saegusa, N., et al., *Kir6.2-deficient mice are susceptible to stimulated ANP secretion: K(ATP) channel acts as a negative feedback mechanism?* Cardiovasc Res, 2005. **67**(1): p. 60-8.

177. Bagwe, S., et al., *Altered right atrial excitation and propagation in connexin40 knockout mice.* Circulation, 2005. **112**(15): p. 2245-53.

178. Odening, K.E., et al., *In vivo effect of a dominant negative Kv4.2 loss-of-function mutation eliminating I(to,f) on atrial refractoriness and atrial fibrillation in mice.* Circ J, 2009. **73**(3): p. 461-7.

179. Glukhov, A.V., et al., *Differential K(ATP) channel pharmacology in intact mouse heart.* J Mol Cell Cardiol, 2010. **48**(1): p. 152-60.

180. Dautova, Y., et al., *Atrial arrhythmogenic properties in wild-type and Scn5a+/- murine hearts.* Exp Physiol, 2010. **95**(10): p. 994-1007.

181. Choi, E.K., et al., *Triggered firing and atrial fibrillation in transgenic mice with selective atrial fibrosis induced by overexpression of TGF-beta1.* Circ J, 2012. **76**(6): p. 1354-62.

182. Chelu, M.G., et al., *Calmodulin kinase II-mediated sarcoplasmic reticulum Ca2+ leak promotes atrial fibrillation in mice.* J Clin Invest, 2009. **119**(7): p. 1940-51.

183. Huke, S. and D.M. Bers, *Temporal dissociation of frequency-dependent acceleration of relaxation and protein phosphorylation by CaMKII.* J Mol Cell Cardiol, 2007. **42**(3): p. 590-9.

184. Picht, E., et al., *CaMKII inhibition targeted to the sarcoplasmic reticulum inhibits frequency-dependent acceleration of relaxation and Ca2+ current facilitation.* J Mol Cell Cardiol, 2007. **42**(1): p. 196-205.

185. DeSantiago, J., L.S. Maier, and D.M. Bers, *Frequency-dependent acceleration of relaxation in the heart depends on CaMKII, but not phospholamban.* J Mol Cell Cardiol, 2002. **34**(8): p. 975-84.

186. Tessier, S., et al., *Regulation of the transient outward K(+) current by Ca(2+)/calmodulin-dependent protein kinases II in human atrial myocytes.* Circ Res, 1999. **85**(9): p. 810-9.

187. Ather, S., et al., *Inhibition of CaMKII phosphorylation of RyR2 prevents inducible ventricular arrhythmias in mice with Duchenne muscular dystrophy.* Heart Rhythm, 2013. **10**(4): p. 592-9.

188. Wagner, S., et al., *Reactive oxygen species-activated Ca/calmodulin kinase IIdelta is required for late I(Na) augmentation leading to cellular Na and Ca overload.* Circ Res, 2011. **108**(5): p. 555-65.

189. Wakili, R., et al., *Multiple potential molecular contributors to atrial hypocontractility caused by atrial tachycardia remodeling in dogs.* Circ Arrhythm Electrophysiol, 2010. **3**(5): p. 530-41.

190. Greiser, M., et al., *Distinct contractile and molecular differences between two goat models of atrial dysfunction: AV block-induced atrial dilatation and atrial fibrillation.* J Mol Cell Cardiol, 2009. **46**(3): p. 385-94.

191. Voigt, N., et al., *Enhanced sarcoplasmic reticulum Ca2+ leak and increased Na+-Ca2+ exchanger function underlie delayed afterdepolarizations in patients with chronic atrial fibrillation.* Circulation, 2012. **125**(17): p. 2059-70.

192. Neef, S., et al., *CaMKII-dependent diastolic SR Ca2+ leak and elevated diastolic Ca2+ levels in right atrial myocardium of patients with atrial fibrillation.* Circ Res, 2010. **106**(6): p. 1134-44.

193. Yao, L., et al., *Nav1.5-dependent persistent Na+ influx activates CaMKII in rat ventricular myocytes and N1325S mice.* Am J Physiol Cell Physiol, 2011. **301**(3): p. C577-86.

194. Macianskiene, R., et al., *Action potential changes associated with a slowed inactivation of cardiac voltage-gated sodium channels by KB130015.* Br J Pharmacol, 2003. **139**(8): p. 1469-79.

195. Bers, D.M. and E. Grandi, *Calcium/calmodulin-dependent kinase II regulation of cardiac ion channels.* J Cardiovasc Pharmacol, 2009. **54**(3): p. 180-7.

196. Communal, C., et al., *Norepinephrine stimulates apoptosis in adult rat ventricular myocytes by activation of the beta-adrenergic pathway.* Circulation, 1998. **98**(13): p. 1329-34.

197. Zhu, W.Z., et al., *Linkage of beta1-adrenergic stimulation to apoptotic heart cell death through protein kinase A-independent activation of Ca2+/calmodulin kinase II.* J Clin Invest, 2003. **111**(5): p. 617-25.

198. Zhu, W.Z., et al., *Dual modulation of cell survival and cell death by beta(2)-adrenergic signaling in adult mouse cardiac myocytes.* Proc Natl Acad Sci U S A, 2001. **98**(4): p. 1607-12.

199. Saucerman, J.J., et al., *Modeling beta-adrenergic control of cardiac myocyte contractility in silico.* J Biol Chem, 2003. **278**(48): p. 47997-8003.

200. Saucerman, J.J., et al., *Proarrhythmic consequences of a KCNQ1 AKAP-binding domain mutation: computational models of whole cells and heterogeneous tissue.* Circ Res, 2004. **95**(12): p. 1216-24.

201. Kuzumoto, M., et al., *Simulation analysis of intracellular Na+ and Cl- homeostasis during beta 1-adrenergic stimulation of cardiac myocyte.* Prog Biophys Mol Biol, 2008. **96**(1-3): p. 171-86.

202. Bondarenko, V.E., *A compartmentalized mathematical model of the beta1-adrenergic signaling system in mouse ventricular myocytes.* PLoS One, 2014. **9**(2): p. e89113.

203. Zaccolo, M. and T. Pozzan, *Discrete microdomains with high concentration of cAMP in stimulated rat neonatal cardiac myocytes.* Science, 2002. **295**(5560): p. 1711-5.

204. Vila Petroff, M.G., et al., *Glucagon-like peptide-1 increases cAMP but fails to augment contraction in adult rat cardiac myocytes.* Circ Res, 2001. **89**(5): p. 445-52.

205. Buxton, I.L. and L.L. Brunton, *Compartments of cyclic AMP and protein kinase in mammalian cardiomyocytes.* J Biol Chem, 1983. **258**(17): p. 10233-9.

206. Yue, D.T., S. Herzig, and E. Marban, *Beta-adrenergic stimulation of calcium channels occurs by potentiation of high-activity gating modes.* Proc Natl Acad Sci U S A, 1990. **87**(2): p. 753-7.

207. Sako, H., et al., *Modulation of cardiac Ca2+ channels by isoproterenol studied in transgenic mice with altered SR Ca2+ content.* Am J Physiol, 1997. **273**(5 Pt 1): p. C1666-72.

208. Mitarai, S., T.D. Reed, and A. Yatani, *Changes in ionic currents and beta-adrenergic receptor signaling in hypertrophied myocytes overexpressing G alpha(q).* Am J Physiol Heart Circ Physiol, 2000. **279**(1): p. H139-48.

209. Karczewski, P., S. Bartel, and E.G. Krause, *Differential sensitivity to isoprenaline of troponin I and phospholamban phosphorylation in isolated rat hearts.* Biochem J, 1990. **266**(1): p. 115-22.

210. Kuschel, M., et al., *Ser16 prevails over Thr17 phospholamban phosphorylation in the beta-adrenergic regulation of cardiac relaxation.* Am J Physiol, 1999. **276**(5 Pt 2): p. H1625-33.

211. Li, L., et al., *Phosphorylation of phospholamban and troponin I in beta-adrenergic-induced acceleration of cardiac relaxation.* Am J Physiol Heart Circ Physiol, 2000. **278**(3): p. H769-79.

212. Lindemann, J.P., et al., *beta-Adrenergic stimulation of phospholamban phosphorylation and Ca2+-ATPase activity in guinea pig ventricles.* J Biol Chem, 1983. **258**(1): p. 464-71.

213. Sulakhe, P.V. and X.T. Vo, *Regulation of phospholamban and troponin-I phosphorylation in the intact rat cardiomyocytes by adrenergic and cholinergic stimuli: roles of cyclic nucleotides, calcium, protein kinases and phosphatases and depolarization.* Mol Cell Biochem, 1995. **149-150**: p. 103-26.

214. Yue, L., et al., *Adrenergic control of the ultrarapid delayed rectifier current in canine atrial myocytes.* J Physiol, 1999. **516 (Pt 2)**: p. 385-98.

215. Gao, J., et al., *Isoprenaline, Ca2+ and the Na(+)-K+ pump in guinea-pig ventricular myocytes.* J Physiol, 1992. **449**: p. 689-704.

216. Tong, X., et al., *Consequences of cardiac myocyte-specific ablation of KATP channels in transgenic mice expressing dominant negative Kir6 subunits.* Am J Physiol Heart Circ Physiol, 2006. **291**(2): p. H543-51.

217. Wu, Y., et al., *Calmodulin kinase II and arrhythmias in a mouse model of cardiac hypertrophy.* Circulation, 2002. **106**(10): p. 1288-93.

218. Babu, G.J., et al., *Ablation of sarcolipin enhances sarcoplasmic reticulum calcium transport and atrial contractility.* Proc Natl Acad Sci U S A, 2007. **104**(45): p. 17867-72.

219. De Koninck, P. and H. Schulman, *Sensitivity of CaM kinase II to the frequency*

of Ca2+ oscillations. Science, 1998. **279**(5348): p. 227-30.

220. Lipp, P., et al., *Functional InsP3 receptors that may modulate excitation-contraction coupling in the heart.* Curr Biol, 2000. **10**(15): p. 939-42.

221. Mackenzie, L., et al., *The role of inositol 1,4,5-trisphosphate receptors in Ca(2+) signalling and the generation of arrhythmias in rat atrial myocytes.* J Physiol, 2002. **541**(Pt 2): p. 395-409.

222. Mackenzie, L., et al., *The spatial pattern of atrial cardiomyocyte calcium signalling modulates contraction.* J Cell Sci, 2004. **117**(Pt 26): p. 6327-37.

223. Woodcock, E.A., S.J. Matkovich, and O. Binah, *Ins(1,4,5)P3 and cardiac dysfunction.* Cardiovasc Res, 1998. **40**(2): p. 251-6.

224. Go, L.O., et al., *Differential regulation of two types of intracellular calcium release channels during end-stage heart failure.* J Clin Invest, 1995. **95**(2): p. 888-94.

225. Kockskamper, J. and L.A. Blatter, *Subcellular Ca2+ alternans represents a novel mechanism for the generation of arrhythmogenic Ca2+ waves in cat atrial myocytes.* J Physiol, 2002. **545**(Pt 1): p. 65-79.

226. Zima, A.V. and L.A. Blatter, *Inositol-1,4,5-trisphosphate-dependent Ca(2+) signalling in cat atrial excitation-contraction coupling and arrhythmias.* J Physiol, 2004. **555**(Pt 3): p. 607-15.

227. Cooling, M., P. Hunter, and E.J. Crampin, *Modeling hypertrophic IP3 transients in the cardiac myocyte.* Biophys J, 2007. **93**(10): p. 3421-33.

228. Doi, T., et al., *Inositol 1,4,5-trisphosphate-dependent Ca2+ threshold dynamics detect spike timing in cerebellar Purkinje cells.* J Neurosci, 2005. **25**(4): p. 950-61.

229. Jiang, T., et al., *Endothelin-dependent actions in cultured AT-1 cardiac myocytes. The role of the epsilon isoform of protein kinase C.* Circ Res, 1996. **78**(4): p. 724-36.

230. Llano, I., R. DiPolo, and A. Marty, *Calcium-induced calcium release in cerebellar Purkinje cells.* Neuron, 1994. **12**(3): p. 663-73.

231. Domeier, T.L., et al., *IP3 receptor-dependent Ca2+ release modulates excitation-contraction coupling in rabbit ventricular myocytes.* Am J Physiol Heart Circ

Physiol, 2008. **294**(2): p. H596-604.

232. Ramos-Franco, J., M. Fill, and G.A. Mignery, *Isoform-specific function of single inositol 1,4,5-trisphosphate receptor channels.* Biophys J, 1998. **75**(2): p. 834-9.

233. Gordienko, D.V. and T.B. Bolton, *Crosstalk between ryanodine receptors and IP(3) receptors as a factor shaping spontaneous Ca(2+)-release events in rabbit portal vein myocytes.* J Physiol, 2002. **542**(Pt 3): p. 743-62.

234. Horn, T., N.D. Ullrich, and M. Egger, *'Eventless' InsP3-dependent SR-Ca2+ release affecting atrial Ca2+ sparks.* J Physiol, 2013. **591**(Pt 8): p. 2103-11.

235. Eisner, D.A., et al., *The control of Ca release from the cardiac sarcoplasmic reticulum: regulation versus autoregulation.* Cardiovasc Res, 1998. **38**(3): p. 589-604.

236. Bassani, J.W., R.A. Bassani, and D.M. Bers, *Twitch-dependent SR Ca accumulation and release in rabbit ventricular myocytes.* Am J Physiol, 1993. **265**(2 Pt 1): p. C533-40.

237. Bootman, M.D., et al., *Temporal changes in atrial EC-coupling during prolonged stimulation with endothelin-1.* Cell Calcium, 2007. **42**(4-5): p. 489-501.

238. Kockskamper, J., et al., *Endothelin-1 enhances nuclear Ca2+ transients in atrial myocytes through Ins(1,4,5)P3-dependent Ca2+ release from perinuclear Ca2+ stores.* J Cell Sci, 2008. **121**(Pt 2): p. 186-95.

239. Dulce, R.A., et al., *Endothelin-1 induced hypertrophic effect in neonatal rat cardiomyocytes: involvement of Na+/H+ and Na+/Ca2+ exchangers.* J Mol Cell Cardiol, 2006. **41**(5): p. 807-15.

240. Zhang, Y.H. and J.C. Hancox, *Regulation of cardiac Na+-Ca2+ exchanger activity by protein kinase phosphorylation--still a paradox?* Cell Calcium, 2009. **45**(1): p. 1-10.

241. Trull, F.L. and B.A. Rich, *More regulation of rodents.* Science, 1999. **284**(5419): p. 1463.

242. Kaese, S. and S. Verheule, *Cardiac electrophysiology in mice: a matter of size.* Front Physiol, 2012. **3**: p. 345.

243. Le Grand, B., et al., *Cellular electrophysiological effects of flecainide on human*

atrial fibres. Cardiovasc Res, 1990. **24**(3): p. 232-8.

244. Wehrens, X.H., S.E. Lehnart, and A.R. Marks, *Intracellular calcium release and cardiac disease.* Annu Rev Physiol, 2005. **67**: p. 69-98.

245. Xu, L., et al., *Alterations of L-type calcium current and cardiac function in CaMKII{delta} knockout mice.* Circ Res, 2010. **107**(3): p. 398-407.

246. Despa, S., et al., *Phospholemman-phosphorylation mediates the beta-adrenergic effects on Na/K pump function in cardiac myocytes.* Circ Res, 2005. **97**(3): p. 252-9.

247. Eisner, D., et al., *Calcium flux balance in the heart.* J Mol Cell Cardiol, 2013. **58**: p. 110-7.

248. Proven, A., et al., *Inositol 1,4,5-trisphosphate supports the arrhythmogenic action of endothelin-1 on ventricular cardiac myocytes.* J Cell Sci, 2006. **119**(Pt 16): p. 3363-75.

249. Harzheim, D., et al., *Increased InsP3Rs in the junctional sarcoplasmic reticulum augment Ca2+ transients and arrhythmias associated with cardiac hypertrophy.* Proc Natl Acad Sci U S A, 2009. **106**(27): p. 11406-11.

250. Kim, J.C., et al., *Atrial local Ca2+ signaling and inositol 1,4,5-trisphosphate receptors.* Prog Biophys Mol Biol, 2010. **103**(1): p. 59-70.

251. Lloyd-Jones, D.M., et al., *Lifetime risk for development of atrial fibrillation: the Framingham Heart Study.* Circulation, 2004. **110**(9): p. 1042-6.

252. Lenaerts, I., et al., *Ultrastructural and functional remodeling of the coupling between Ca2+ influx and sarcoplasmic reticulum Ca2+ release in right atrial myocytes from experimental persistent atrial fibrillation.* Circ Res, 2009. **105**(9): p. 876-85.

253. Allessie, M.A., F.I. Bonke, and F.J. Schopman, *Circus movement in rabbit atrial muscle as a mechanism of tachycardia. III. The "leading circle" concept: a new model of circus movement in cardiac tissue without the involvement of an anatomical obstacle.* Circ Res, 1977. **41**(1): p. 9-18.

254. Burashnikov, A. and C. Antzelevitch, *Late-phase 3 EAD. A unique mechanism contributing to initiation of atrial fibrillation.* Pacing Clin Electrophysiol, 2006. **29**(3): p. 290-5.

255. Tanskanen, A.J., et al., *The role of stochastic and modal gating of cardiac L-type Ca2+ channels on early after-depolarizations.* Biophys J, 2005. **88**(1): p. 85-95.

256. Sossalla, S., et al., *Diastolic dysfunction and arrhythmias caused by overexpression of CaMKIIdelta(C) can be reversed by inhibition of late Na(+) current.* Basic Res Cardiol, 2011. **106**(2): p. 263-72.

257. Sedej, S., et al., *Na+-dependent SR Ca2+ overload induces arrhythmogenic events in mouse cardiomyocytes with a human CPVT mutation.* Cardiovasc Res, 2010. **87**(1): p. 50-9.

258. Gonano, L.A., et al., *Calcium-calmodulin kinase II mediates digitalis-induced arrhythmias.* Circ Arrhythm Electrophysiol, 2011. **4**(6): p. 947-57.

259. Sag, C.M., et al., *Calcium/calmodulin-dependent protein kinase II contributes to cardiac arrhythmogenesis in heart failure.* Circ Heart Fail, 2009. **2**(6): p. 664-75.

260. Toischer, K., et al., *Role of late sodium current as a potential arrhythmogenic mechanism in the progression of pressure-induced heart disease.* J Mol Cell Cardiol, 2013. **61**: p. 111-22.

261. Pieske, B. and J. Kockskamper, *Alternans goes subcellular: a "disease" of the ryanodine receptor?* Circ Res, 2002. **91**(7): p. 553-5.

262. Burrell, K.M., et al., *Contractile and arrhythmic effects of endothelin receptor agonists in human heart in vitro: blockade with SB 209670.* J Pharmacol Exp Ther, 2000. **292**(1): p. 449-59.

Appendix

Glossary

$[Ca^{2+}]_i$	Intracellular Ca^{2+} concentration
$[Ca^{2+}]_{dyad}$	Dyadic Ca^{2+} concentration
$[Ca^{2+}]_{SR}$	SR Ca^{2+} concentration
$[Na^{+}]_i$	Intracellular Na^{+} concentration
AC	Adenylyl cyclase
AF	Atrial fibrillation
AP	Action potential
APA	Action potential amplitude
APD	Action potential duration
APD_{25}	AP duration at 25% repolarisation
APD_{50}	AP duration at 50% repolarisation
APD_{75}	AP duration at 75% repolarisation
APD_{90}	AP duration at 90% repolarisation
ATP	Adenosine triphosphate
AV	Atrio-ventricular
AVN	Atrioventricular node
β-AR	β-adrenergic receptor
BCL	Basic cycle length
BPM	Beats per minute
CaM	Calmodulin

CaMKII	Ca^{2+}/CaM-dependent protein kinase II
cAMP	3'-5'-cyclic adenosine monophosphate
CDI	Calcium-dependent inactivation
CICR	Ca^{2+}-induced Ca^{2+} release
CSQN	Calsequestrin
DAD	Delayed afterdepolarisation
DAG	Diacylglycerol
dV/dt_{max}	Maximal upstroke velocity
EAD	Early afterdepolarisation
ECC	Excitation-contraction coupling
ET-1	Endothelin-1
FDAR	Frequency-dependent acceleration of relaxation
GDP	Guanosine diphosphate
GPCR	G-protein coupled receptor
HH	Hodgkin-Huxley
I-1	Inhibitor-1
I_{CaL}	L-type calcium current
I_{Cab}	Background Ca^{2+} current
I_{ClCa}	Ca^{2+}-activated Cl^- current
$I_{K,s}$	Rapidly activating slowly inactivating current
I_{K1}	Inward rectifier K^+ current
I_{Kr}	Delayed rectifier potassium current
I_{Ks}	Slow delayed rectifier K^+ current
I_{Kur}	Ultra-rapidly activating delayed rectifier K^+ current

I_L	Leakage current
I_{Na}	Fast Na^+ current
I_{Nab}	background Na^+ current
I_{NaK}	Na^+/K^+ pump current
I_{NaL}	Late Na^+ current
I_{NCX}	Na^+/Ca^{2+} exchange current
I_{pCa}	Ca^{2+} pump current
I_{ss}	Non-inactivating steady-state voltage-activated K^+ current
I_{stim}	External stimulation current
I_{sus}	Sustained current
I_{to}	Transient outward K^+ current
IP_3	Inositol 1,4,5-trisphosphate
IP_3R	Inositol 1,4,5-trisphosphate receptor
ISO	Isoproterenol
KO	Knockout
LVET	Left ventricular ejection time
LTCC	L-type calcium channels
NCX	Na^+-Ca^{2+} exchanger
NKA	Na^+-K^+-ATPase
OE	Overexpression
PDE	Phosphodiesterases
PF	Purkinje fibre
PI 3-K	PtdIns 3-kinase
PIP_2	Phosphatidylinositol 4,5-bisphosphate

PKA	Protein kinase A
PLB	Phospholamban
PLC	Phospholipase C
PLM	Phospholemman
PP1	Protein phosphatase 1
PP2A	Protein phosphatase 2A
ROCs	Receptor-operated channels
RP	Resting potential
RyR	Ryanodine receptor
T-tubules	Transverse tubules
SAN	Sinoatrial node
Ser	Serine
SERCA	Sarco-endoplasmic reticulum Ca^{2+} ATPase
SL	Sarcolemma
SR	Sarcoplasmic reticulum
Thr	Threonine
TnC	Troponin C
TnI	Troponin T
TnT	Troponin T
V	Voltage
VDI	Voltage-dependent inactivation
VOCs	Voltage-operated channels

Model Equations and Parameters

Excitation-contraction Coupling Modules

Fast Na^+ Current, I_{Na}

$$\alpha_m = 0.32 \times \frac{V + 47.13}{1 - e^{-0.1 \times (V + 47.13)}}$$

$$\beta_m = 0.08 \times e^{-V/11}$$

$$\alpha_h = 0.135 \times e^{\frac{80 + (V - I_{Na\_shift})}{-6.8}}$$

$$\beta_h = 1.1 \times 3.56 \times e^{0.079 \times (V - I_{Na\_shift} - 2)} + 3.1 \times 10^5 \times e^{0.35 \times (V - I_{Na\_shift} - 2)}$$

$$\alpha_j = \frac{(1 + \alpha_{CKII}) \times (-1.2714 \times 10^5 \times e^{0.2444 \times (V - I_{Na\_shift})} - 3.474 \times 10^5 \times e^{-0.04391 \times (V - I_{Na\_shift})}) \times ((V - I_{Na\_shift}) + 37.78)}{1 + e^{0.311 \times ((V - I_{Na\_shift}) + 79.23)}}$$

$$\beta_j = 0.1212 \times e^{-0.01052 \times (V - I_{Na\_shift})} / (1 + e^{-0.1378 \times ((V - I_{Na\_shift}) + 40.14)})$$

If $(V - I_{Na\_shift}) \geq -40$

$$\alpha_h = 0$$

$$\alpha_j = 0$$

$$\beta_h = 0.66 \times 1 / (0.13 \times (1 + e^{-((V - I_{Na\_shift}) + 10.66)/11.1}))$$

$$\beta_j = 0.3 \times e^{-2.535 \times 10^7 \times (V - I_{Na\_shift})} / (1 + e^{-0.1 \times ((V - I_{Na\_shift}) + 32)})$$

$$\frac{dm}{dt} = (\alpha_m \times (1 - m) - \beta_m \times m)$$

$$\frac{dh}{dt} = (\alpha_h \times (1 - h) - \beta_h \times h)$$

$$\frac{dj}{dt} = (\alpha_j \times (1-j) - \beta_j \times j)$$

$$I_{Na\_fast\_junc} = F_{junc\_Na} \times g_{Na} \times m^3 \times h \times j \times (V - E_{Na\_junc})$$

$$I_{Na\_fast\_sl} = F_{sl\_Na} \times g_{Na} \times m^3 \times h \times j \times (V - E_{Na\_sl})$$

$$I_{Na} = I_{Na\_fast\_junc} + I_{Na\_fast\_sl}$$

Late Na^+ Current, I_{NaL}

$$\bar{g}_{Nal} = 2 \times 0.0065 \times (1 + \Delta\bar{g}_{Nal\_CKII})$$

$$h_{l\_ss} = 1/(1 + e^{(V+91)/6.1})$$

$$\tau_{h\_l} = 600.0$$

$$\frac{dh_l}{dt} = \frac{h_{l\_ss} - h_l}{\tau_{h\_l}}$$

$$I_{Na\_slow\_junc} = F_{junc\_Na} \times \bar{g}_{Nal} \times m^3 \times h_l \times (V - E_{Na\_junc})$$

$$I_{Na\_slow\_sl} = F_{sl\_Na} \times \bar{g}_{Nal} \times m^3 \times h_l \times (V - E_{Na\_sl})$$

$$I_{NaL} = I_{Na\_slow\_junc} + I_{Na\_slow\_sl}$$

Na^+-K^+ Pump, I_{NaK}

$$sigma = \frac{e^{\frac{Nao}{67.3}} - 1}{7.0}$$

$$f_{NaK} = \frac{1}{1 + 0.1245 \times e^{-0.1 \times V \times F/(RT)} + 0.0365 \times sigma \times e^{-V \times F/(RT)}}$$

$$frac_{PKA_{PLMo}} = 0.116738$$

$$frac_{PKA_{PLMiso}} = 0.859251$$

$$k_{PKA_{PLM}} = K_{mNa_{ip}} \times \frac{1 - 0.7019}{\frac{frac_{PKA_{PLMiso}}}{frac_{PKA_{PLMo}}} - 1}$$

$$K_{mNa_{ipPKA}} = -k_{PKA_{PLM}} + k_{PKA_{PLM}} \times \frac{PLM_{PKAp}}{frac_{PKA_{PLMo}}}$$

$$K_{mNai_p} = K_{mNai_p} - K_{mNai_{pPKA}}$$

$$I_{NaKjunc} = \frac{Fjunc_{nak} \times I_{barNaK} \times f_{NaK} \times K_o}{(1 + Na_{ijunc}{}^4) \times (K_o + K_{mK_o})}$$

$$I_{NaKsl} = \frac{Fsl_{nak} \times I_{barNaK} \times f_{NaK} \times K_o}{\left(1 + (Na_{isl})^4\right) \times \left(K_o + K_{mK_o}\right)}$$

$$I_{Nak} = I_{NaKjunc} + I_{NaKsl}$$

Transient Outward K^+ Current, I_{to}

$$C_{3to} = 1 - C_{2to} - C_{1to} - I_{2to} - I_{1to} - I_{0to} - O_{to}$$

$$\alpha_{to} = 0.250270 \times (e^{(0.787791 \times (V + 5.00000) \times (F/RT))})$$

$$\beta_{to} = 0.168346 \times (e^{(-0.757095 \times (V + 46.0000) \times (F/RT))})$$

$$K_{fto} = 0.0233856$$

$$K_{bto} = \frac{K_{fto}}{40.0000}$$

$$K_{f_2to} = 0.430214$$

$$K_{b_2to} = \frac{360.00 \times K_{f_2to} \times K_{bto}}{K_{fto}}$$

$$\frac{dC_{2to}}{dt} = 3.0 \times \alpha_{to} \times C_{3to} - \beta_{to} \times C_{2to} + 2.0 \times \beta_{to} \times C_{1to} - 2.0 \times \alpha_{to} \times C_{2to} + K_{b_2to} \times I_{2to} - K_{f_2to} \times C_{2to}$$

$$\frac{dC_{1to}}{dt} = 2.0 \times \alpha_{to} \times C_{2to} - 2.0 \times \beta_{to} \times C_{1to} + 3.0 \times \beta_{to} \times O_{to} - \alpha_{to} \times C_{1to} + K_{bto} \times I_{1to} - K_{fto} \times C_{1to}$$

$$\frac{dO_{to}}{dt} = \alpha_{to} \times C_{1to} - 3.0 \times b_{to} \times O_{to} + K_{bto} \times I_{0to} - K_{fto} \times O_{to}$$

$$\frac{dI_{0to}}{dt} = \alpha_{to} \times I_{1to} - 3.0 \times b_{to} \times I_{0to} + K_{fto} \times O_{to} - K_{bto} \times I_{0to}$$

$$\frac{dI_{1to}}{dt} = 2.0 \times \alpha_{to} \times I_{2to} - \frac{2.0 \times \beta_{to} \times I_{1to}}{360.0} + 3.0 \times b_{to} \times I_{0to} - \beta_{to} \times I_{1to} + K_{fto} \times C_{1to} - K_{bto} \times I_{1to}$$

$$\frac{dI_{2to}}{dt} = \frac{2.0 \times \beta_{to} \times I_{1to}}{360.0} - 2.0 \times \alpha_{to} \times I_{2to} + K_{f_2 to} \times C_{2to} - K_{b_2 to} \times I_{2to}$$

$$I_{to} = g_{Kto} \times O_{to} \times (V - E_k)$$

Ultrarapidly Activating Delayed Rectifying K^+ Current, I_{Kur}

$$frac_{I_{Kur} p_0} = 0.437635$$

$$frac_{I_{Kur} p_{ISO}} = 0.718207$$

$$\alpha_{Kur} = \frac{2.20 - 1}{\frac{frac_{I_{Kur} p_{ISO}}}{frac_{I_{Kur} p_0}} - 1}$$

$$frac_{I_{Kur\_avail}} = (1 - \alpha_{Kur}) + \alpha_{Kur} \times (\frac{I_{Kur\_PKAp}}{frac_{I_{Kur} p_0}})$$

$$\alpha_{ur} = e^{(V+58.0)/90.0}$$

$$b_{ur} = e^{-(V+43.0)/90.0}$$

$$K_{fur} = 0.00862$$

$$K_{bur} = 0.00227$$

$$C_{1ur} = 1 - C_{2ur} - C_{3ur} - C_{4ur} - I_{ur} - O_{ur}$$

$$\frac{dC_{2ur}}{dt} = 4 \times \alpha_{ur} \times C_{1ur} - \beta_{ur} \times C_{2ur} + 2 \times \beta_{ur} \times C_{3ur} - 3 \times \alpha_{ur} \times C_{2ur}$$

$$\frac{dC_{3ur}}{dt} = 3 \times \alpha_{ur} \times C_{2ur} - 2 \times \beta_{ur} \times C_{3ur} + 3 \times \beta_{ur} \times C_{4ur} - 2 \times \alpha_{ur} \times C_{3ur}$$

$$\frac{dC_{4ur}}{dt} = 2 \times \alpha_{ur} \times C_{3ur} - 3 \times \beta_{ur} \times C_{4ur} + 4 \times \beta_{ur} \times O_{ur} - \alpha_{ur} \times C_{4ur}$$

$$\frac{dO_{ur}}{dt} = \alpha_{ur} \times C_{4ur} - 4 \times \beta_{ur} \times O_{ur} + K_{bur} \times I_{ur} - K_{fur} \times O_{ur}$$

$$I_{Kur} = K_{fur} \times O_{ur} - K_{bur} \times I_{ur}$$

Non-inactivating Steady-state K^+ Current, I_{ss}

$$\alpha_{ss} = 1.0 / (1.0 + (e^{(-(V-15)/34.55)}))$$

$$\tau_{Kss} = 11.5 \times (e^{(-0.03 \times V)}) + 5$$

$$\frac{d\alpha_{Kss}}{dt} = \frac{\alpha_{ss} - \alpha_{Kss}}{\tau_{Kss}}$$

$$I_{Kss} = g_{Kss} \times \alpha_{Kss} \times (V - E_K)$$

Rapid Delayed Rectifying K^+ Current, I_{Kr}

$$\alpha_0 = 0.00985942 \times e^{\frac{2.56963 \times V \times F}{R \times T}}$$

$$\alpha_1 = 0.642537$$

$$\alpha_2 = 0.105987 \times e^{\frac{2.43874 \times V \times F}{R \times T}}$$

$$\beta_0 = 0.0104051 \times e^{\frac{2.02278 \times V \times F}{R \times T}}$$

$$\beta_1 = 2.14838$$

$$\beta_2 = 0.0033 \times e^{\frac{-0.577 \times \mathrm{V} \times \mathrm{F}}{R \times T}}$$

$$\alpha_i = 0.392662 \times e^{\frac{-1.29659 \times V \times F}{R \times T}} + 0.221961$$

$$\beta_i = 0.696498 \times e^{\frac{0.35976 \times V \times F}{R \times T}}$$

$$\mu = \frac{\alpha_i + \beta_2}{\beta_i}$$

$$\frac{dtC_{3Kr}}{dt} = \beta_0 \times C_{2Kr} - \alpha_0 \times C_{3Kr}$$

$$\frac{dC_{1Kr}}{dt} = (\alpha_1 \times C_{2Kr} + \beta_2 \times O_{Kr} + \mu \times IN_{Kr}) - (\beta_1 + 2 \times \alpha_2) \times C_{1Kr}$$

$$\frac{dC_{2Kr}}{dt} = (\beta_1 \times C_{1Kr} + \alpha_0 \times C_{3Kr}) - (\alpha_1 + \beta_0) \times C_{2Kr}$$

$$\frac{dO_{Kr}}{dt} = (\alpha_1 \times I_{Kr} + \alpha_2 \times \mathrm{C}_{1Kr}) - (\beta_i + \beta_2) \times O_{Kr}$$

$$\frac{dIN_{Kr}}{dt} = (\alpha_2 \times C_{1Kr} + \beta_i \times O_{Kr}) - (\mu + \alpha_i) \times IN_{Kr}$$

$$I_{Kr} = g_{Kr} \times O_{Kr} \times (V - E_K)$$

Inward Rectifying K^+ Current, I_{K1}

$$I_{K1} = g_{K1} \times \frac{K_o}{K_o + 0.9} \times \frac{V - E_K - 5.0}{1 + e^{(0.09457 \times (V - E_K - 5.0) + 0.42984)}}$$

Na^+-Ca^{2+} Exchanger, I_{NCX}

$$K_{a_{junc}} = \frac{1}{1 + (\frac{K_{d\_act}}{Ca_{junc}})^3}$$

$$K_{a_{sl}} = \frac{1}{1 + (\frac{K_{d\_act}}{Ca_{sl}})^3}$$

$$s_{1\_junc} = e^{\mu \times V \times F/(RT)} \times {Na_{i\_junc}}^3 \times Ca_o$$

$$s_{2\_junc} = e^{(\mu - 1) \times V \times F/(RT)} \times {Na_o}^3 \times Ca_{j\_unc}$$

$$s_{3\_junc} = (K_{m\_Cai} \times {Na_o}^3 \times (1 + (\frac{Na_{i\_junc}}{K_{m\_Nai}})^3) + {K_{m\_Nao}}^3 \times Ca_{junc} + {K_{m\_Nai}}^3 \times Ca_o \times (1 + \frac{Ca_{junc}}{K_{m\_Cai}})$$
$$+ K_{m\_Cao} \times {Na_{i\_junc}}^3 + {Na_{i\_junc}}^3 \times Ca_o + {Na_o}^3 \times Ca_{junc}) \times (1 + ksat \times e^{(\mu - 1) \times V \times F/(RT)})$$

$$I_{NCX\_junc} = \frac{F_{junc\_\mathrm{NCX}} \times I_{barNCX} \times K_{a\_junc} \times (s_{1\_junc} - s_{2\_junc})}{s_{3\_junc}}$$

$$s_{1\_sl} = e^{\mu \times V \times F/(RT)} \times {Na_{i\_sl}}^3 \times Ca_o$$

$$s_{2\_sl} = e^{(\mu - 1) \times V \times F/(RT)} \times {Na_o}^3 \times Ca_{sl}$$

$$s_{3\_sl} = (K_{m\_Cai} \times Na_o^{\,3} \times (1 + (\frac{Na_{i\_sl}}{K_{m\_Nai}})^3) + K_{m\_Nao}^{\,3} \times Ca_{sl} + K_{m\_Nai}^{\,3} \times Ca_o \times (1 + \frac{Ca_{sl}}{K_{m\_Cai}})$$
$$+ K_{m\_Cao} \times Na_{i\_sl}^{\,3} + Na_{i\_sl}^{\,3} \times Ca_o + Na_o^{\,3} \times Ca_{sl}) \times (1 + ksat \times e^{(\mu - 1) \times V \times F/(RT)})$$

$$I_{NCX\_sl} = \frac{F_{sl\_NCX} \times I_{barNCX} \times K_{a_{sl}} \times (s_{1\_sl} - s_{2\_sl})}{s_{3\_sl}}$$

$$I_{NCX} = I_{NCX\_junc} + I_{NCX\_sl}$$

Background Currents

$$I_{Nab\_junc} = F_{junc\_Na} \times g_{Nab} \times (\mathrm{V} - \mathrm{E}_{Na\_junc})$$
$$I_{Nab\_sl} = F_{sl\_Na} \times g_{Nab} \times (V - E_{Na\_sl})$$
$$I_{Nab} = I_{Nab\_junc} + I_{Nab\_sl}$$

$$I_{ClCa\_junc} = \frac{F_{junc} \times g_{ClCa}}{1 + \frac{K_{dClCa}}{Ca_{junc}}} \times (V - E_{Cl})$$

$$I_{ClCa\_sl} = \frac{F_{sl} \times g_{ClCa}}{1 + \frac{K_{dClCa}}{Ca_{sl}}} \times (V - E_{Cl})$$

$$I_{ClCa} = I_{ClCa\_junc} + I_{ClCa\_sl}$$

$$I_{Clb} = g_{Clb} \times (V - E_{Cl})$$

$$I_{Cap\_junc} = \frac{F_{junc} \times \bar{I}_{pCa} \times Ca_{junc}^{1.6}}{K_{mpCa}^{1.6} + Ca_{junc}^{1.6}}$$

$$I_{Cap\_sl} = \frac{F_{sl} \times \bar{I}_{pCa} \times Ca_{sl}^{1.6}}{K_{mpCa}^{1.6} + Ca_{sl}^{1.6}}$$

$$I_{Cap} = I_{Cap\_junc} + I_{Cap\_sl}$$

$$I_{Cab\_junc} = F_{junc} \times g_{Cab} \times (V - E_{Ca\_junc})$$
$$I_{Cab\_sl} = F_{sl} \times g_{Cab} \times (V - E_{Ca\_sl})$$
$$I_{Cab} = I_{Cab\_junc} + I_{Cab\_sl}$$

Ryanodine Receptor, RyR

$$frac_{RyRo} = 0.204276$$

$$\alpha_{RyR} = \frac{1}{\frac{1}{frac_{RyRo}} - 1}$$

$$fPKA_{RyR} = 1 - \alpha_{RyR} + \alpha_{RyR} \times (RyR_{PKAp} / frac_{RyRo})$$

$$fCKII_{RyR} = 10 \times RyR_{CKp} - 1$$

$$fCKII_{EC_{50}SR} = 1.16 - \frac{4}{5} \times RyR_{CKp}$$

$$EC_{50}SR = fCKII_{EC_{50}SR} \times EC_{50}SR$$

$$MaxSR = 15.0$$

$$MinSR = 1.0$$

$$k_{CaSR} = MaxSR - \frac{MaxSR - MinSR}{1 + (\frac{EC_{50}SR}{Ca_{sr}})^{2.5}}$$

$$k_{iSRCa} = k_{iCa} \times k_{CaSR}$$

$$k_{oSRCa} = k_{oCa} / k_{CaSR}$$

$$k_{oSRCa} = (fCKII_{RyR} + fPKA_{RyR} - 1) \times k_{oSRCa}$$

$$\frac{dR}{dt} = (\mathrm{k}_{im} \times RI - k_{iSRCa} \times Ca_{junc} \times r) - (k_{oSRCa} \times Ca_{junc}^2 \times r - k_{om} \times O)$$

$$\frac{dO}{dt} = (k_{oSRCa} \times Ca_{junc}^2 \times r - k_{om} \times O) - (k_{iSRCa} \times Ca_{junc} \times O - k_{im} \times I)$$

$$\frac{dI}{dt} = (k_{iSRCa} \times Ca_{junc} \times O - k_{im} \times I) - (k_{om} \times I - k_{oSRCa} \times Ca_{junc}^2 \times RI)$$

$$J_{rel} = k_s \times O \times (Ca_{sr} - Ca_{junc})$$

Ryanodine Receptor Leak

$$k_{leak} = 1.0696 \times 10^7$$

$$J_{SRleak} = k_{leak} \times (Ca_{sr} - Ca_{junc})$$

Sarco/endoplasmic Reticulum Ca^{2+}-ATPase, SERCA

$$f_{CKII_{PLB}} = (1 - 0.25 \times PLB_{CKp})$$

$$frac_{PKA_{PLBo}} = 1 - 0.079755$$

$$f_{PKA_{PLB}} = \frac{PLB_{PKAn}}{frac_{PKA_{PLBo}}} \times 0.25 + 0.75$$

If $f_{CKII_{PLB}} <= f_{PKA_{PLB}}$

$$f_{Kmf} = f_{CKII_{PLB}}$$

else

$$f_{Kmf} = f_{PKA_{PLB}}$$

$$K_{mf} = f_{K_{mf}} \times K_{mf}$$

$$J_{serca} = K_{serca} \times V_{max_{SERCA}} \times \frac{(\frac{Ca_i}{K_{mf}})^{hillSRCaP} - (\frac{Ca_{sr}}{K_{mr}})^{hillSRCaP}}{1 + (\frac{Ca_i}{K_{mf}})^{hillSRCaP} + (\frac{Ca_{sr}}{K_{mr}})^{hillSRCaP}}$$

Na^+ Concentrations

$$Na_{Bj} = k\_on_{Na} \times Na_{i\_junc} \times (B\max_{Naj} - Na_{Bj}) - k\_off_{Na} \times Na_{Bj}$$

$$Na_{Bsl} = k\_on_{Na} \times Na_{i\_sl} \times (B\max_{Nasl} - Na_{Bsl}) - k\_off_{Na} \times Na_{Bsl}$$

$$I_{Na\_tot\_junc} = I_{Na\_junc} + I_{Nab\_junc} + 3 \times I_{NCX\_junc} + 3 \times I_{NaK\_junc} + I_{CaNa\_junc}$$

$$I_{Na\_tot\_sl} = I_{Na\_sl} + I_{Nab\_sl} + 3 \times I_{NCX\_sl} + 3 \times I_{NaK\_sl} + I_{CaNa\_sl}$$

$$Na_{i\_junc} = -I_{Na\_tot\_junc} \times C_m / (V_{junc} \times F) + J_{Na\_juncsl} / V_{junc} \times (Na_{i\_sl} - Na_{i\_junc}) - \mathrm{Na}_{Bj}$$

$$Na_{i\_sl} = -I_{Na\_tot\_sl} \times C_m / (V_{sl} \times F) + \mathrm{J}_{Na\_juncsl} / V_{sl} \times (Na_{i\_junc} - Na_{i\_sl}) - Na_{Bsl} + J_{Na\_slmyo} / V_{sl} \times Na_{i\_\mathrm{myo}} - Na_{i\_sl})$$

$$Na_{i\_myo} = J_{Na\_slmyo} / V_{myo} \times (Na_{i\_sl} - Na_{i\_myo})$$

Ca Buffers

$$\frac{dSLL_{junc}}{dt} = kon_{SLL} \times Ca_{junc} \times \left(B_{\max\_SLL\_junc} - SLL_{junc} \right) - koff_{SLL} \times SLL_{junc}$$

$$\frac{dSLH_{junc}}{dt} = kon_{SLH} \times Ca_{junc} \times \left(B_{\max\_SLh\_junc} - SLH_{junc} \right) - koff_{SLH} \times SLH_{junc}$$

$$J_{CaB\_junc} = SLL_{junc} + SLH_{junc}$$

$$\frac{dSLL_{SL}}{dt} = kon_{SLL} \times Ca_{SL} \times \left(B_{\max\_SLL\_SL} - SLL_{SL} \right) - koff_{SLL} \times SLL_{SL}$$

$$\frac{dSLH_{SL}}{dt} = kon_{SLH} \times Ca_{SL} \times \left(B_{\max\_SLh\_SL} - SLH_{SL} \right) - koff_{SLH} \times SLH_{SL}$$

$$J_{CaB\_SL} = SLL_{SL} + SLH_{SL}$$

$$\frac{dTnCL}{dt} = k\_on_{TnCL} \times Ca_i \times (B\max_{TnClow} - TnCL) - k\_off_{TnCL} \times TnCL$$

$$\frac{dTnCHc}{dt} = k\_on_{TnCHCa} \times Ca_i \times (B\max_{TnChigh} - TnCHc - TnCHm) - k\_off_{TnCHCa} \times TnCHc$$

$$\frac{dTnCHm}{dt} = k\_on_{TnCHMg} \times Mg_i \times (B\max_{TnChigh} - TnCHc - TnCHm) - k\_off_{TnCHMg} \times TnCHm$$

$$\frac{dMyosin_{Ca}}{dt} = k\_on_{myoCa} \times Ca_i \times (B\max_{myosin} - Myosin_{Ca} - Myosin_{Mg}) - k\_off_{myoCa} \times Myosin_{Ca}$$

$$\frac{dMyosin_{Mg}}{dt} = k\_on_{myoMg} \times Mg_i \times (B\max_{myosin} - Myosin_{Ca} - myosin_{Mg}) - k\_off_{myoMg} - Myossin_{Mg}$$

$$\frac{dSRB}{dt} = k\_on_{SR} \times Ca_i \times (B\max_{SR} - SRB) - k\_off_{SR} \times SRB$$

$$J_{CaB\_cytosol} = TnCL + TnCHc + Myosin_{Ca} + SRB$$

Calcium Concentrations

$$I_{Ca\_tot\_junc} = I_{Ca\_junc} + I_{Cab\_junc} + I_{Cap\_junc} + 2 \times I_{NCX\_junc}$$

$$I_{Ca\_tot\_SL} = I_{Ca\_SL} + I_{Cab\_SL} + I_{Cap\_SL} + 2 \times I_{NCX\_SL}$$

$$I_{Ca\_tot} = I_{Ca\_tot\_junc} + I_{Ca\_tot\_SL}$$

$$\frac{dCa_{SL}}{dt} = \frac{I_{Ca\_tot\_SL} \times C_{mem}}{2 \times V_{SL} \times F} + \frac{J_{Ca\_juncSL}}{V_{SL}} \times \left(Ca_{junc} - Ca_{SL}\right) - \frac{J_{Ca\_SLmyo}}{V_{SL}} \times \left(Ca_{SL} - Ca_i\right) - J_{CaB\_SL}$$

$$\frac{dCa_{junc}}{dt} = \frac{I_{Ca\_tot\_junc} \times C_{mem}}{2 \times V_{junc} \times F} + J_{SRrel} \times \frac{V_{jsr}}{V_{junc}} + J_{leak} \times \frac{V_{myo}}{V_{junc}} - \frac{J_{Ca\_juncSL}}{V_{junc}} \times \left(Ca_{junc} - Ca_{SL}\right) - J_{CaB\_junc}$$

$$\frac{dCa_i}{dt} = \frac{J_{Ca\_SLmyo}}{V_{myo}} \times \left(Ca_{SL} - Ca_i\right) - J_{CaB\_cytosol} - J_{serca}$$

CaM, CaN, CaMKII Modules

Protein Total Concentrations

Parameter	Value	Units
CaM_{TOT}	6.0	μM
$B_{TOT-CYT}$	24.5	μM
B_{TOT-SL}	$B_{TOT-CYT}$	μM
$B_{TOT-DYAD}$	1.86	mM
$CaMKII_{TOT-CYT}$	0.2(0 by default)	μM
$CaMKII_{TOT-SL}$	$CaMKII_{TOT-CYT}$	μM
$CaMKII_{TOT-DYAD}$	120	μM
$CaN_{TOT-CYT}$	0.003	μM
CaN_{TOT-SL}	$CaN_{TOT-CYT}$	μM
$CaN_{TOT-DYAD}$	3.62(0 by default)	μM
$PP1_{TOT-CYT}$	0.57	μM
$PP1_{TOT-SL}$	$PP1_{TOT-CYT}$	μM
$PP1_{TOT-DYAD}$	96.5	μM

Ca/CaM Binding and CaM Buffering Parameters

Parameter	Value	Units	Description
k_{20}	10	s^{-1}	2 Ca dissociation from CaM
k_{02}	k_{20} /K_{d02}	μM^{-2} s^{-1}	2 Ca association with CaM
k_{42}	500	s^{-1}	2 Ca dissociation from CaM
k_{24}	k_{42}/K_{d24}	μM^{-2} s^{-1}	2 Ca association with CaM
k_{0Boff}	0.0014	s^{-1}	CaM dissociation from Buffer
k_{0Bon}	k_{0Boff}/0.2	μM^{-1} s^{-1}	CaM association with Buffer
k_{2Boff}	k_{0Boff}/100	s^{-1}	Ca_2CaM dissociation from Buffer
k_{2Bon}	k_{0Bon}	μM^{-1} s^{-1}	Ca_2CaM association with Buffer

$\mathbf{k_{4Boff}}$	$k_{0Boff}/100$	s^{-1}	Ca_4CaM dissociation from Buffer
$\mathbf{k_{4Bon}}$	k_{0Bon}	$\mu M^{-1}\ s^{-1}$	Ca_4CaM association with Buffer
$\mathbf{k_{42B}}$	k_{42}	s^{-1}	2 Ca dissociation from CaMBuffer
$\mathbf{k_{24B}}$	k_{24}	$\mu M^{-2}\ s^{-1}$	2 Ca association with CaMBuffer
$\mathbf{k_{20B}}$	k_{20} /100	s^{-1}	2 Ca dissociation from CaMBuffer
$\mathbf{k_{02B}}$	k_{02}	$\mu M^{-2}\ s^{-1}$	2 Ca association with CaMBuffer

CaMKII Reaction Parameters

Parameter	Value	Units	Description
$\boldsymbol{k_{bi}}$	2.2	s^{-1}	Ca_4CaM dissociation from P_b
$\boldsymbol{k_{ib}}$	k_{bi}/33.5e-3	$\mu M^{-1}\ s^{-1}$	Ca_4CaM association with P_i
$\boldsymbol{k_{b2i}}$	$5k_{ib2}$	s^{-1}	Ca_2CaM dissociation from P_{b2}
$\boldsymbol{k_{ib2}}$	k_{ib}	$\mu M^{-1}\ s^{-1}$	Ca_2CaM association with P_i
$\boldsymbol{k_{b42}}$	k_{42}*33.5e-3/5	s^{-1}	2 Ca dissociation from P_b
$\boldsymbol{k_{b24}}$	k_{24}	$\mu M^{-2}\ s^{-1}$	2 Ca association with P_{b2}
$\boldsymbol{k_{ta}}$	k_{bi}/1000	s^{-1}	Ca_4CaM dissociation from P_t
$\boldsymbol{k_{at}}$	k_{ib}	$\mu M^{-1}\ s^{-1}$	Ca_4CaM association with P_a
$\boldsymbol{k_{t2a}}$	$5k_{ib}$	s^{-1}	Ca_2CaM dissociation from P_{t2}
$\boldsymbol{k_{at2}}$	k_{ib}	$\mu M^{-1}\ s^{-1}$	Ca_2CaM association with P_a
$\boldsymbol{k_{t42}}$	k_{42}*33.5e-6/5	s^{-1}	2 Ca dissociation from P_t
$\boldsymbol{k_{t24}}$	k_{24}	$\mu M^{-2}\ s^{-1}$	2 Ca association with P_{t2}
$\boldsymbol{k_{PP1}}$	1.72	s^{-1}	Thr^{287} dephosphorylated
$\boldsymbol{K_{mPP1}}$	11.5	μM	Thr^{287} dephosphorylated

CaN Reaction Parameters

Parameter	Value	Units	Description
$k_{CaNCaoff}$	1	s^{-1}	2 Ca dissociation from Ca_4CaN
$k_{CaNCaon}$	$k_{CaNCaoff}/0.5$	$\mu M^{-2}\ s^{-1}$	2 Ca association with Ca_2CaN
$k_{CaN4off}$	1.3e-3	s^{-1}	Ca_4CaM dissociation from CaN
k_{CaN4on}	46	$\mu M^{-1}\ s^{-1}$	Ca_4CaM association with CaN
$k_{CaN2off}$	2508 $k_{CaN4off}$	s^{-1}	Ca_2CaM dissociation from CaN
k_{CaN2on}	k_{CaN4on}	$\mu M^{-1}\ s^{-1}$	Ca_2CaM association with CaN
$k_{CaN0off}$	165 $k_{CaN2off}$	s^{-1}	CaM dissociation from CaN
k_{CaN0on}	k_{CaN2on}	$\mu M^{-1}\ s^{-1}$	CaM association with CaN
k_{20CaN}	$k_{20}/165$	s^{-1}	2 Ca dissociation from CaN
k_{02CaN}	k_{02}	$\mu M^{-2}\ s^{-1}$	2 Ca association with CaN
k_{42CaN}	$k_{42}/2508$	s^{-1}	2 Ca dissociation from CaN
k_{24CaN}	k_{24}	$\mu M^{-2}\ s^{-1}$	2 Ca association with CaN

$If\,[Mg] \le 1,$

$K_{d02} = 0.0025(1+[K]/0.94-[Mg]/0.012)(1+[K]/8.1+[Mg]/0.022)$

$K_{d24} = 0.128(1+[K]/0.64+[Mg]/0.0014)(1+[K]/13.0-[Mg]/0.153)$

$If\,[Mg] > 1,$

$K_{d02} = 0.0025(1+[K]/0.94-1/0.012+([Mg]-1)/0.06)(1+[K]/8.1+1/0.022+([Mg]-1)/0.068)$

K_{d24}=0.128(1+[K]/0.64+1/0.0014+([Mg]-1)/0.005)(1+[K]/13.0-1/0.153+([Mg]-1)/0.15);

$$Reaction_{02} = k_{02}[Ca]^2[CaM] - k_{20}[Ca_2CaM]$$

$$Reaction_{24} = k_{24}[Ca]^2[Ca_2CaM] - k_{42}[Ca_4CaM]$$

$$Reaction_{02B} = k_{02B}[Ca]^2[CaMB] - k_{20B}[Ca_2CaMB]$$

$$Reaction_{24B} = k_{24B}[Ca]^2[Ca_2CaMB] - k_{42B}[Ca_4CaMB]$$

$$Reaction_{0B} = k_{0Bon}[CaM][B] - k_{0Boff}[CaMB]$$

$$Reaction_{2B} = k_{2Bon}[Ca_2CaM][B] - k_{2Boff}[Ca_2CaMB]$$

$$Reaction_{4B} = k_{4Bon}\left[Ca_4CaM\right]\left[B\right] - k_{4Boff}\left[Ca_4CaMB\right]$$

$$[B] = \left[B_{TOT}\right] - \left[CaMB\right] - \left[Ca_2CaMB\right] - \left[Ca_4CaMB\right];$$

$$\frac{d\left[CaM\right]}{dt} = 10^{-3}\left(-Reaction_{02} - Reaction_{0B} - Reaction_{0CaN}\right);$$

$$\frac{d\left[Ca_2CaM\right]}{dt} = 10^{-3}\begin{Bmatrix} Reaction_{02} - Reaction_{24} - Reaction_{2B} - Reaction_{2CaN} \\ +CaMKII_{tot}\left(Reaction_{CKt2a} - Reaction_{CKib2}\right) \end{Bmatrix};$$

$$\frac{d\left[Ca_4CaM\right]}{dt} = 10^{-3}\begin{Bmatrix} Reaction_{24} - Reaction_{4CaN} - Reaction_{4B} \\ +\left[CaMKII_{TOT}\right]\left(Reaction_{CKta} - Reaction_{CKib}\right) \end{Bmatrix};$$

$$\frac{d\left[CaMB\right]}{dt} = 10^{-3}\left(Reaction_{0B} - Reaction_{02B}\right);$$

$$\frac{d\left[Ca_2CaMB\right]}{dt} = 10^{-3}\left(Reaction_{02B} + Reaction_{2B} - Reaction_{24B}\right);$$

$$\frac{d\left[Ca_4CaMB\right]}{dt} = 10^{-3}\left(Reaction_{24B} + Reaction_{4B}\right);$$

$$J_{CaM-DYAD/SL} = k_{0Boff}\left[CaM_{DYAD}\right] - k_{0Bon}\left[B_{DYAD}\right]\left[CaM_{SL}\right];$$

$$J_{Ca2CaM-DYAD/SL} = k_{2Boff}\left[Ca_2CaM_{DYAD}\right] - k_{2Bon}\left[B_{DYAD}\right]\left[Ca_2CaM_{SL}\right];$$

$$J_{Ca4CaM-DYAD/SL} = k_{4Boff}\left[Ca_4CaM_{DYAD}\right] - k_{4Bon}\left[B_{DYAD}\right]\left[Ca_4CaM_{SL}\right];$$

$$J_{CaM-SL/CYT} = k_{SLCYT}\left(\left[CaM_{SL}\right] - \left[CaM_{CYT}\right]\right);$$

$$J_{Ca2CaM-SL/CYT} = k_{SLCYT}\left(\left[Ca_2CaM_{SL}\right] - \left[Ca_2CaM_{CYT}\right]\right);$$

$$J_{Ca4CaM-SL/CYT} = k_{SLCYT}\left(\left[Ca_4CaM_{SL}\right] - \left[Ca_4CaM_{CYT}\right]\right);$$

$$P_i = 1 - P_b - P_{b2} - P_t - P_{t2} - P_a;$$

$$T = P_b + P_t + P_{t2} + P_a;$$

$$k_{bt} = 0.055T + 0.0074T^2 + 0.015T^3;$$

$$Reaction_{CKbt} = k_{bt}P_b - \frac{k_{pp1}\left[PP1_{tot}\right]P_t}{K_{mPP1} + \left[CaMKII_{tot}\right]P_t};$$

$$Reaction_{CKib2} = k_{ib2}\left[Ca_2CaM\right]P_i - k_{b2i}P_{b2};$$

$$Reaction_{CKb2b} = k_{b24}[Ca]^2 P_{b2} - k_{b42}P_b;$$

$$Reaction_{CKib} = k_{ib}\left[Ca_4CaM\right]P_i - k_{bi}P_b;$$

$$Reaction_{CKt2} = k_{t42}P_t - k_{t24}[Ca]^2 P_{t2};$$

$$Reaction_{CKta} = k_{ta}P_t - k_{at}\left[Ca_4CaM\right]P_a;$$

$$Reaction_{CKt2a} = k_{t2a}P_{t2} - k_{at2}\left[Ca_2CaM\right]P_a;$$

$$Reaction_{CKt2b2} = \frac{k_{pp1}\left[PP1_{tot}\right]P_{t2}}{K_{mPP1} + \left[CaMKII_{tot}\right]P_{t2}};$$

$$Reaction_{CKai} = \frac{k_{pp1}\left[PP1_{tot}\right]P_a}{K_{mPP1} + \left[CaMKII_{tot}\right]P_a};$$

$$\frac{dP_{b2}}{dt} = 10^{-3}(Reaction_{CKib2} - Reaction_{CKb2b} + Reaction_{CKt2b2})$$

$$\frac{dP_b}{dt} = 10^{-3}(Reaction_{CKib} + Reaction_{CKb2b} - Reaction_{CKbt})$$

$$\frac{dP_t}{dt} = 10^{-3}(Reaction_{CKbt} - Reaction_{CKta} - Reaction_{CKt2})$$

$$\frac{dP_{t2}}{dt} = 10^{-3}(Reaction_{CKt2} - Reaction_{CKt2a} - Reaction_{CKt2b2})$$

$$\frac{dP_a}{dt} = 10^{-3}(Reaction_{CKta} + Reaction_{CKt2a} - Reaction_{CKai})$$

$$\left[Ca_2CaN\right] = \left[CaN_{TOT}\right] - \left[Ca_4CaN\right] - \left[CaMCaN\right] - [Ca_2CaMCaN] - \left[Ca_4CaMCaN\right]$$

$$Reaction_{Ca4CaN} = k_{CaNCaon}[Ca]^2\left[Ca_2CaN\right] - k_{CaNCaoff}\left[Ca_4CaN\right]$$

$$Reaction_{02CaN} = k_{02CaN}\left[Ca\right]^2\ \left[CaMCaN\right] - k_{20CaN}\left[Ca_2CaMCaN\right]$$

$$Reaction_{24CaN} = k_{24CaN}[Ca]^2\left[Ca_2CaMCaN\right] - k_{42CaN}\left[Ca_4CaMCaN\right]$$

$$Reaction_{0CaN} = k_{CaN0on}\left[CaM\right]\left[Ca_4CaN\right] - k_{CaN0off}\left[CaMCaN\right]$$

$$Reaction_{2CaN} = k_{CaN2on}\left[Ca_2CaM\right]\left[Ca_4CaN\right] - k_{CaN2off}\left[Ca_2CaMCaN\right]$$

$$Reaction_{4CaN} = k_{CaN4on}\left[Ca_4CaM\right]\left[Ca_4CaN\right] - k_{CaN4off}\left[Ca_4CaMCaN\right]$$

$$\frac{d\left[Ca_4CaN\right]}{dt} = 10^{-3}(Reaction_{Ca4CaN} - Reaction_{0CaN} - Reaction_{2CaN} - Reaction_{4CaN})$$

$$\frac{d\left[CaMCaN\right]}{dt} = 10^{-3}\left(Reaction_{0CaN} - Reaction_{02CaN}\right)$$

$$\frac{d\left[Ca_2CaMCaN\right]}{dt} = 10^{-3}(Reaction_{2CaN} + Reaction_{02CaN} - Reaction_{24CaN})$$

$$\frac{d\left[Ca_4CaMCaN\right]}{dt} = 10^{-3}\left(Reaction_{4CaN} + Reaction_{24CaN}\right)$$

β-adrenergic Signalling System

β-adrenergic Receptor / $G_{s\alpha}$ Module

Parameter	Description	Value	Units
ISO	isoproterenol concentration (when used)	0.1	μM
b1ARtot	total β1-adrenergic receptors	0.00528	μM
Gstot	total Gs protein	3.83	μM
kf_LR	β1-AR binding to ligand	1	1/[μM ms]
kr_LR	β1-AR binding to ligand	0.285	1/ms
kf_LRG	ligand bound β1-AR associating with G-protein	1	1/[μM ms]
kr_LRG	ligand bound β1-AR associating with G-protein	0.062	1/ms
kf_RG	unbound β1-AR associating with G-protein	1	1/[μM ms]
kr_RG	unbound β1-AR associating with G-protein	33.0	1/ms
k_G_act	Gs-alpha activation	16.0e-3	1/ms
k_G_hyd	Gs-alpha hydrolysis	0.8e-6	1/ms
k_G_reassoc	Gs-alpha reassociation	1.21	1/[μM ms]
kf_bark	β1-AR desensitization by β-arrestin	1.1e-6	1/ms
kr_bark	β1-AR resensitization	2.2e-6	1/ms
kf_pka	β1-AR desensitization by PKA	3.6e-6	1/[μM ms]
kr_pka	β1-AR resensitization	2.2e-6	1/ms

$$b1ARact = b1ARtot - b1ARS\_464 - b1AR\_S301$$

$$b1AR = b1ARact - LR - LRG - RG$$

$$Gs = Gstot - LRG - RG - Gsby$$

$$\frac{dLR}{dr} = kf\_LR \cdot IS0 \cdot b1AR - kr\_LR \cdot LR$$

$$\frac{dLRG}{dt} = kf\_LRG \cdot LR \cdot Gs - kr\_LRG \cdot LRG - k\_G\_act \cdot LRG$$

$$\frac{dRG}{dr} = kf\_RG \cdot b1AR \cdot Gs - kr\_RG \cdot Gs - k\_G\_act \cdot RG$$

$$\frac{db1AR\_S464}{dt} = kf\_bARK \cdot \left(LR + LRG\right) - kr\_bARK \cdot b1AR\_S464$$

$$\frac{db1AR\_S301}{dt} = kf\_PKA \cdot PKACI \cdot b1ARact - kr\_PKA \cdot b1AR\_S301$$

$$\frac{dGsaGTPtot}{dt} = k\_G\_act \cdot \left(RG + LRG\right) - k\_G\_hyd \cdot GsaGTPtot$$

$$\frac{dGsaGDP}{dt} = k\_G\_hyd \cdot GsaGTPtot - k\_G\_reassoc \cdot GsaGDP \cdot Gsby$$

$$\frac{dGsby}{dt} = k\_G\_act \cdot \left(RG + LRG\right) - k\_G\_reassoc \cdot GsaGDP \cdot Gsby$$

cAMP Module

Parameter	Description	Value	Units
ACtot	total adenylyl cyclase	70.57e-3	µM
ATP	total ATP	5.0e3	µM
PDEtot	total phosphodiesterases	22.85e-3	µM
IBMX	isobutylmethylxanthine concentration	0.0	µM
FSK	forskolin concentration	0.0	µM
k_AC_basal	basal AC activity	0.2e-3	1/ms
Km_AC_basal	basal AC affinity for ATP	1.03e3	µM
k_AC_Gsa	AC activity with Gs-alpha activation	8.5e-3	1/ms
Km_AC_Gsa	AC:Gs-alpha affinity for ATP	315.0	µM
kf_AC_Gsa	AC activation by Gs-alpha	1	1/[µM ms]
kr_AC_Gsa	AC activation by Gs-alpha	0.4	1/ms

k_AC_FSK	AC activation by forskolin	7.3e-3	1/ms
Km_AC_FSK	AC:FSK affinity for ATP	860.0	µM
Kd_AC_FSK	AC activation by forskolin	44	1/ms
k_cAMP_PDE	cAMP degradation by PDEs	5.0e-3	1/ms
k_cAMP_PDEp	cAMP degradation by phosphorylated PDEs	10.0e-3	1/ms
Km_PDE_cAMP	PDE affinity for cAMP	1.3	µM
Kd_PDE_IBMX	PDE inhibition by IBMX	30.0	µM
k_PKA_PDE	PDE phosphorylation by PKA	7.5e-3	1/ms
k_PP_PDE	PDE inhibition by IBMX	1.5e-3	1/ms

$$cAMP = cAMPtot - \left(RCcAMP\_I + 2 \cdot RCcAMPcAMP\_I + 2 \cdot RcAMPcAMP\_I\right)$$
$$-\left(RCcAMP\_II + 2 \cdot RCcAMPcAMP\_II + 2 \cdot RcAMPcAMP\_II\right)$$

$$AC = ACtot - AC\_GsaGTP$$

$$GsaGTP = GsaGTPtot - AC\_GsaGTP$$

$$\frac{dAC\_GsaGTP}{dt} = kf\_AC\_Gsa \cdot GsaGTP \cdot AC - kr\_AC\_Gsa \cdot AC\_GsaGTP$$

$$AC\_FSK = \frac{FSK \cdot AC}{Kd\_AC\_FSK}$$

$$PDE\_IBMX = \frac{PDEtot \cdot IBMX}{Kd\_PDE\_IBMX}$$

$$PDE = PDEtot - PDE\_IBMX - PDEp$$

$$\frac{dPDEp}{dt} = k_{PKA_{PDE}} \cdot PKACII \cdot PDE - k\_PP\_PDE \cdot PDEp$$

$$PDE_{ACT} = \frac{k_{cAMP_{PDE}} \cdot PDE \cdot cAMP}{Km_{PDE_{cAMP}} + cAMP} + \frac{k\_cAMP\_PDEp \cdot PDEp \cdot cAMP}{Km\_PDE\_cAMP + cAMP}$$

$$\frac{dcAMPtot}{dt} = \frac{k\_AC\_basal \cdot AC \cdot ATP}{Km\_AC\_basal + ATP} + \frac{k\_AC\_Gsa \cdot AC\_GsaGTP \cdot ATP}{Km\_AC\_Gsa + ATP} + \frac{k\_AC\_FSK \cdot AC\_FSK \cdot ATP}{Km\_AC\_FSK + ATP}$$

PKA Module

Parameter	Description	Value	Units
PKItot	total protein kinase inhibitor	0.18	μM
kf_RC_cAMP	cAMP association with PKA	1	1/[μM ms]
kr_RC_cAMP	cAMP association with PKA	1.64	1/ms
kf_RCcAMP_cAMP	cAMP association with PKA	1	1/[μM ms]
kr_RCcAMP_cAMP	cAMP association with PKA	9.14	1/ms
kf_RcAMPcAMP_C	catalytic subunit dissociation	4.375	1/[μM ms]
kr_RcAMPcAMP_C	catalytic subunit dissociation	1	1/ms
kf_PKA_PKI	PKA inhibition by PKI	1	1/[μM ms]
kr_PKA_PKI	PKA inhibition by PKI	0.2e-3	1/ms

$$PKI = PKItot - PKACI\_PKI - PKACII\_PKI$$

$$\frac{dRC\_I}{dt} = -kf\_RC\_cAMP \cdot RC\_I \cdot cAMP + kr\_RC\_cAMP \cdot RCcAMP\_I$$

$$\frac{dRCcAMP\_I}{dt} = -kr\_RC\_cAMP \cdot RCcAMP\_I + kf\_RC\_cAMP \cdot RC\_I \cdot cAMP$$
$$-kf\_RCcAMP\_cAMP \cdot RCcAMP\_I \cdot cAMP + kr\_RCcAMP\_cAMP \cdot RCcAMPcAMP\_I$$

$$\frac{dRCcAMPcAMP\_I}{dt} = -kr\_RCcAMP\_cAMP \cdot RCcAMPcAMP\_I$$
$$+kf\_RCcAMP\_cAMP \cdot RCcAMP\_I \cdot cAMP$$
$$-kf\_RcAMPcAMP\_C \cdot RCcAMPcAMP\_I$$
$$+kr\_RcAMPcAMP\_C \cdot RcAMPcAMP\_I \cdot PKACI$$

$$\frac{dRcAMPcAMP\_I}{dt} = -kr\_RcAMPcAMP\_C \cdot RcAMPcAMP\_I \cdot PKACI$$
$$+kf\_RcAMPcAMP\_C \cdot RCcAMPcAMP\_I$$

$$\frac{dPKACI}{dt} = -kr\_RcAMPcAMP\_C \cdot RcAMPcAMP\_I \cdot PKACI$$
$$+kf\_RcAMPcAMP\_C \cdot RCcAMPcAMP\_I$$
$$-kf\_PKA\_PKI \cdot PKACI \cdot PKI + kr\_PKA\_PKI \cdot PKACI\_PKI$$

$$\frac{dPKA\_CI\_PKI}{dt} = -kr\_PKA\_PKI \cdot PKACI\_PKI + kf\_PKA\_PKI \cdot PKACI \cdot PKI$$

$$\frac{dRC\_II}{dt} = -kf\_RC\_cAMP \cdot RC\_II \cdot cAMP + kr\_RC\_cAMP \cdot RCcAMP\_II$$

$$\frac{dRCcAMP\_II}{dr} = -kr\_RC\_cAMP \, gRCcAMP\_II + kf\_RC\_cAMP \, gRC\_II \, gcAMP$$
$$-kf\_RCcAMP\_cAMP \, gRCcAMP\_II \, gcAMP + kr\_RCcAMP\_cAMP \, gRCcAMPcAMP\_II$$
$$\frac{dRCcAMPcAMP\_II}{dt} = -kr\_RCcAMP\_cAMP \, gRCcAMPcAMP\_II$$
$$+kf\_RCcAMP\_cAMP \, gRCcAMP\_II \cdot cAMP - kf\_RcAMPcAMP\_C \, gRCcAMPcAMP\_II$$
$$+kr\_RcAMPcAMP\_C \, gRcAMPcAMP\_II \, gPKACII$$

$$\frac{dRcAMPcAMP\_II}{dt} = -kr\_RcAMPcAMP\_C \cdot RcAMPcAMP\_II \cdot PKACII$$
$$+kf\_RcAMPcAMP\_C \cdot RCcAMPcAMP\_II$$

$$\frac{dPKACII}{dr} = -kr\_RcAMPcAMP\_C \cdot RcAMPcAMP\_II \cdot PKACII$$
$$+kf\_RcAMPcAMP\_C \cdot RCcAMPcAMP\_II - kf\_PKA\_PKI \cdot PKACII \cdot PKI$$
$$+kr\_PKA\_PKI \cdot PKACII\_PKI$$

I-1/PP1 Module

Parameter	Description	Value	Units
PP1tot	total phosphatase 1	0.89	μM
I1tot	total inhibitor 1	0.5	μM
k_PKA_I1	PKA phosphorylation of inhibitor 1	60e-3	1/ms
Km_PKA_I1	PKA phosphorylation of inhibitor 1	1.0	μM
Vmax_PP2A_I1	PP2A dephosphorylation of phospholamban	14.0e-3	μM/ms
Km_PP2A_I1	PP2A dephosphorylation of phospholamban	1.0	μM

kf_PP1_I1	PP1 inhibition by inhibitor 1	1.0	1/[μM ms]
kr_PP1_I1	PP1 inhibition by inhibitor 1	1.0e-3	1/ms

$$I1 = I1tot - Ilptot$$

$$PP1 = PP1tot - I1p\_PP1$$

$$I1p = I1ptot - I1p\_PP1$$

$$\frac{dI1p\_PP1}{dt} = kf\_PP1\_I1 \cdot PP1 \cdot I1p - kr\_PP1\_I1 \cdot I1p\_PP1$$

$$\frac{dI1ptot}{dt} = \frac{k\_PKA\_I1 \cdot PKACI \cdot I1}{Km\_PKA\_I1 + I1} - \frac{V\max\_PP2A\_I1 \cdot I1ptot}{Km_{PP2A_{I1}} + I1pToT}$$

LCC Module

Parameter	Description	Value	Units
LCCtot	total L-type Ca channel	0.025	μM
PKACII_LCCtot	total PKA local to L-type Ca channel	0.025	μM
PP1_LCC	total PP1 local to L-type Ca channel	0.025	μM
PP2a_LCC	total PP2A local to L-type Ca channel	0.025	μM
epsilon	AKAP-mediated scaling factor	10	-
k_PKA_LCC	PKA phosphorylation of LCC	54e-3	1/ms
Km_PKA_LCC	PKA phosphorylation of LCC	21	μM
k_PP1_LCC	PP1 dephosphorylation of LCC	8.52e-3	1/ms
Km_PP1_LCC	PP1 dephosphorylation of LCC	3	μM
k_PP2A_LCC	PP2A dephosphorylation of LCC	10.1e-3	1/ms
Km_PP2A_LCC	PP2A dephosphorylation of LCC	3	μM
PKAIItot	Total type 2 protein kinase A	0.059	μM

$$PKACII\_LCC = \frac{PKACII\_LCCtot}{PKAIIToT} \cdot PKACII$$

$$LCCa = LCCtot - LCCap$$

$$\frac{dLCCa}{dt} = \frac{epsilon \cdot k\_PKA\_LCC \cdot PKACII\_LCC \cdot LCCa}{Km\_PKA\_LCC + epsilon \cdot LCCa} - \frac{epsilon \cdot k\_PP2A\_LCC \cdot PP2A\_LCC \cdot LCCap}{Km\_PP2A\_LCC + epsilon \cdot LCCap}$$

$$LCCb = LCCtot - LCCbp$$

$$\frac{dLCCb}{dt} = \frac{epsilon \cdot k\_PKA\_LCC \cdot PKACII\_LCC \cdot LCCb}{Km\_PKA\_LCC + epsilon \cdot LCCb} - \frac{epsilon \cdot k\_PP1\_LCC \cdot PP1\_LCC \cdot LCCbp}{Km\_PP1\_LCC + epsilon \cdot LCCbp}$$

PLB Module

Parameter	Description	Value	Units
PLBtot	total phospholamban	60.6	μM
k_PKA_PLB	PKA phosphorylation of phospholamban	54e-3	1/ms
Km_PKA_PLB	PKA phosphorylation of phospholamban	21	μM
k_PP1_PLB	PP1 dephosphorylation of phospholamban	8.5e-3	1/ms
Km_PP1_PLB	PP1 dephosphorylation of phospholamban	7	μM

$$PLB = PLBtot - PLBp$$

$$\frac{dPLBp}{dt} = \frac{k\_PKA\_PLB \cdot PKACI \cdot PLB}{Km\_PKA\_PLB + PLB} - \frac{k\_PP1\_PLB \cdot PP1 \cdot PLBp}{Km\_PP1\_PLB + PLBp}$$

PLM Module

Parameter	Description	Value	Units
PLMtot	total phospholemman	48	μM
k_PKA_PLM	PKA phosphorylation of phospholemman	54e-3	1/ms
Km_PKA_PLM	PKA phosphorylation of phospholemman	21	μM
k_PP1_PLM	PP1 dephosphorylation of phospholemman	8.5e-3	1/ms

Km_PP1_PLM	PP1 dephosphorylation of phospholemman	7.0	μM

$$PLM = PLMtot - PLMp$$

$$\frac{dPLMp}{dt} = \frac{k\_PKA\_PLM \cdot PKACI \cdot PLB}{Km\_PKA\_PLM + PLB} - \frac{k\_PP1\_PLM \cdot PP1 \cdot PLBp}{Km\_PP1\_PLM + PLBp}$$

TnI Module

Parameter	Description	Value	Units
TnItot	total troponin I	70	μM
PP2a_TnI	total PP2A local to troponin I	0.67	μM
k_PKA_TnI	PKA phosphorylation of troponin I	54e-3	1/ms
Km_PKA_TnI	PKA phosphorylation of troponin I	21	μM
k_PP2A_TnI	PP2A dephosphorylation of troponin I	10.1e-3	1/ms
Km_PP2A_TnI	PP2A dephosphorylation of troponin I	4.1	μM

$$TnI = TnItot - TnIp$$

$$\frac{dTnIp}{dt} = \frac{k\_PKA\_TnI \cdot PKACI \cdot TnI}{Km\_PKA\_TnI + TnI} - \frac{k\_PP2A\_TnI \cdot PP2a\_TnI \cdot TnIp}{Km\_PP2A\_TnI + TnIp}$$

RyR Module

Parameter	Description	Value	Units
epsilon	AKAP- mediated scaling factor	10	none
RyR_{tot}	Total RyR	0.135	μM
$PKAII_{RyRtot}$	Total PKA local to RyR	0.034	μM
$PP1_{RyRtot}$	Total PP1 local to RyR	0.034	μM
$PP2A_{RyRtot}$	Total PP2A local to RyR	0.034	μM
$k_{m\_pka\_RyR}$	PKA phosphorylation of RyR	21.0	μM
$k_{m\_PP1\_RyR}$	PP1 dephosphorylation of RyR	7.0	μM

$\mathbf{k_{m\_PP2A\_RyR}}$	PP2A dephosphorylation of RyR	4.1	μM
$\mathbf{k_{PKA\_RyR}}$	PKA phosphorylation of RyR	$54.0e^{-3}$	ms^{-1}
$\mathbf{k_{PP1\_RyR}}$	PP1 dephosphorylation of RyR	$8.52e^{-3}$	ms^{-1}
$\mathbf{k_{PP2A\_RyR}}$	PP2A dephosphorylation of RyR	$10.1e^{-3}$	ms^{-1}

$$PKAII\_RyR = \frac{PKAII_{RyRtot}}{PKAII_{tot}} \cdot PKACII$$

$$RyR = RyR_{tot} - RyRp$$

$$\frac{dRyRp}{dt} = \frac{epsilon \cdot k_{PKA\_RyR} \cdot PKACII\_RyR \cdot RyR}{k_{m\_PKA\_RyR} + epsilon \cdot RyR}$$
$$- \frac{epsilon \cdot k_{PP1\_RyR} \cdot PP1_{RyR_{tot}} \cdot RyRp}{k_{m\_PP1\_RyR} + epsilon \cdot RyRp} - \frac{epsilon \cdot k_{PP2A\_RyR} \cdot PP2A_{RyR_{tot}} \cdot RyRp}{k_{m\_PP2A\_RyR} + epsilon \cdot RyRp}$$

I_{Kur} Module

Parameter	Description	Value	Units
epsilon	AKAP- mediated scaling factor	10	none
$\mathbf{Kur_{tot}}$	Total I_{Kur}	0.025	μM
$\mathbf{PKAII_{RyRtot}}$	Total PKA local to I_{Kur}	0.025	μM
$\mathbf{PP1_{Kurtot}}$	Total PP1 local to I_{Kur}	0.025	μM
$\mathbf{k_{m\_pka\_Kur}}$	PKA phosphorylation of I_{Kur}	21	μM
$\mathbf{k_{m\_PP1\_Kur}}$	PP1 dephosphorylation of I_{Kur}	7.0	μM
$\mathbf{k_{PKA\_Kur}}$	PKA phosphorylation of I_{Kur}	$54.0e^{-3}$	ms^{-1}
$\mathbf{k_{PP1\_Kur}}$	PP1 dephosphorylation of I_{Kur}	$8.52e^{-3}$	ms^{-1}

$$PKAC_{\mathrm{Kur}} = \frac{PKAII_{Kurtot}}{PKAII_{tot}} \times PKACII$$

$$Kur = Kur_{tot} - Kur_p$$

$$\frac{dKur_p}{dt} = \frac{epsilon \cdot Kur_n \cdot PKAC_{Kur} \cdot k_{PKA\_Kur}}{k_{m\_PKA\_\mathrm{Kur}} + epsilon \cdot Kur_n} - \frac{epsilon \cdot k_{PP1\_\mathrm{Kur}} \cdot PP1_{Kur_{tot}} \cdot Kur_p}{k_{m\_PP1\_Kur} + epsilon \cdot Kur_p}$$

IP_3 Production System

IP_3 Signal Transduction System

Parameters	Description	Units	Value
$\mathbf{k_{f,1}}$	R1 forward rate constant	$\mu M^{-1}s^{-1}$	3.00×10^{-4}
$\mathbf{K_{d,1}}$	R1 dissociation constant	μM	3.00×10^{-5}
$\mathbf{k_{f,2}}$	R2 forward rate constant	$\mu m^2 s^{-1}$	2.75×10^{-4}
$\mathbf{K_{d,2}}$	R2 dissociation constant	μm^{-2}	27,500
$\mathbf{k_{f,3}}$	R3 forward rate constant	$\mu m^2 s^{-1}$	1.00
$\mathbf{k_{r,3}}$	R3 reverse rate constant	s^{-1}	1.00×10^{-3}
$\mathbf{k_{f,4}}$	R4 forward rate constant	$\mu M^{-1}s^{-1}$	3.00×10^{-1}
$\mathbf{K_{d,4}}$	R4 dissociation constant	μM	3.00×10^{-5}
$\mathbf{k_{f,5}}$	R5 forward rate constant	s^{-1}	4.00×10^{-4}
$\mathbf{k_{f,6}}$	R6 forward rate constant	s^{-1}	1.00
$\mathbf{k_{f,7}}$	R7 forward rate constant	s^{-1}	1.50×10^{-1}
$\mathbf{k_{f,8}}$	R8 forward rate constant	$\mu M^{-1}s^{-1}$	1.67×10^{-2}
$\mathbf{k_{r,8}}$	R8 reverse rate constant	s^{-1}	1.67×10^{-2}
$\mathbf{k_{f,9}}$	R9 forward rate constant	$\mu m^2 s^{-1}$	4.20×10^{-3}
$\mathbf{k_{r,9}}$	R9 reverse rate constant	s^{-1}	1.00
$\mathbf{k_{f,10}}$	R10 forward rate constant	$\mu m^2 s^{-1}$	4.20×10^{-2}
$\mathbf{k_{r,10}}$	R10 reverse rate constant	s^{-1}	1.00
$\mathbf{k_{f,11}}$	R11 forward rate constant	$\mu M^{-1}s^{-1}$	3.34×10^{-2}
$\mathbf{K_{d,11}}$	R11 dissociation rate constant	μM	1.00×10^{-1}
$\mathbf{k_{f,12}}$	R12 forward rate constant	s^{-1}	6.00
$\mathbf{k_{f,13}}$	R13 forward rate constant	s^{-1}	6.00
$\mathbf{k_{f,14}}$	R14 forward rate constant	s^{-1}	4.44×10^{-1}
$\mathbf{K_{m,14}}$	R14 K_m value	μM	19.8
$\mathbf{k_{f,15}}$	R15 forward rate constant	s^{-1}	3.80
$\mathbf{K_{m,15}}$	R15 K_m value	μM	5.00

$\mathbf{k_{f,16}}$	R16 forward rate constant	s^{-1}	1.25
$\mathbf{L_s}$	Ligand stimulation concentration	μM	varies
PIP2	PIP2 density	μm^{-2}	4000
$\mathbf{t_s}$	Time of stimulation	s	varies
$\mathbf{V_c}$	Cytosolic volume	μm^3	2549.3
Ca	Cytosolic Ca^{2+} concentration	μM	1.00×10^{-1}
$\mathbf{G_d}$	G_αGDP density	μm^{-2}	10,000
$\mathbf{G_t}$	G_αGTP density	μm^{-2}	0.00
IP3	IP3 concentration	μM	0.015
L	Ligand concentration (extracellular)	μM	0.00
P	PLCβ density	μm^{-2}	90.9
$\mathbf{P_c}$	PLCβ-Ca^{2+} density	μm^{-2}	9.09
$\mathbf{P_g}$	PLCβ-G_αGTP density	μm^{-2}	0.00
$\mathbf{P_{cg}}$	PLCβ- Ca^{2+}-G_αGTP density	μm^{-2}	0.00
R	Noncoupled receptor density	μm^{-2}	13.9
$\mathbf{R_g}$	Precoupled receptor density	μm^{-2}	5.06
$\mathbf{R_l}$	Ligand-bound receptor density	μm^{-2}	0.00
$\mathbf{R_{lg}}$	Active receptor density	μm^{-2}	0.00
$\mathbf{R_{lgp}}$	Phosphorylated receptor density	μm^{-2}	0.00
$\mathbf{R_{pc}}$	Plasma membrane/cytosolic volume ratio	μm^{-1}	4.61

$$c_c = \frac{1}{V_c \times 6.022 \times 10^2}$$

$$c_p = \frac{1}{V_c \times R_{pc}}$$

$$c_{pc} = \frac{c_c}{c_p}$$

$$L = \frac{L_s}{\left(1.0 + e^{-800\times\left((t-t_s)-0.05\right)}\right)}$$

$$if\ \ (t < (t_s + 0.15))(t \geq t_s), Ls;$$

$$if\ I \geq (t_s + 0.15), 0 \text{ otherwise}$$

$$k_{r,1} = k_{f,1} \times K_{d,1}$$

$$J_1 = k_{f,1} \times R \times L - k_{r,1} \times R_1$$

$$k_{r,2} = k_{f,2} \times K_{d,2}$$

$$J_2 = \left(k_{f,2} \times R \times G_d - k_{r,2} \times R_g\right)$$

$$\frac{dR}{dt} = -\left(J_1 + J_2\right)$$

$$J_3 = k_{f,3} \times R_1 \times G_d - k_{r,3} \times R_{1g}$$

$$\frac{dR_1}{dt} = J_1 - J_3 + J_6$$

$$k_{r,4} = k_{f,4} \times K_{d,4}$$

$$J_4 = k_{f,4} \times L \times R_g - k_{r,4} \times R_{1g}$$

$$\frac{dR_g}{dt} = J_2 - J_4$$

$$\frac{dG_d}{dt} = J_{12} + J_7 + J_{13} - \left(J_2 + J_3\right)$$

$$J_5 = k_{f,5} \times R_{1g}$$

$$\frac{dR_{1gp}}{dt} = J_5$$

$$J_6 = k_{f,6} \times R_{1g}$$

$$\frac{dR_{1g}}{dt} = J_3 + J_4 - \left(J_5 + J_6\right)$$

$$J_7 = k_{f,7} \times G_t$$

$$\frac{dG_t}{dt} = J_6 - J_7 - J_9 - J_{10}$$

$$J_9 = k_{f,9} \times P \times G_t - k_{r,9} \times P_g$$

$$J_8 = k_{f,8} \times P \times Ca - k_{r,8} \times P_c$$

$$J_{10} = k_{f,10} \times P_c \times G_t - k_{r,10} \times P_{cg}$$

$$k_{r,11} = k_{f,11} \times K_{d,11}$$

$$J_{11} = k_{f,11} \times P_g \times Ca - k_{r,11} \times P_{cg}$$

$$J_{12} = k_{f,12} \times P_{cg}$$

$$J_{13} = k_{f,13} \times P_g$$

$$J_{14} = \frac{k_{f,14} \times P_c \times PIP2}{\left(\frac{K_{m,14}}{c_{pc}} + PIP2 \right)}$$

$$J_{15} = \frac{k_{f,15} \times P_{cg} \times PIP2}{\left(\frac{K_{m,15}}{c_{pc}} + PIP2 \right)}$$

$$\frac{dP}{dt} = J_{13} - \left(J_9 + J_8 \right)$$

$$\frac{dP_g}{dt} = J_9 - \left(J_{11} + J_{13} \right)$$

$$\frac{dP_c}{dt} = J_8 + J_{12} - J_{10}$$

$$\frac{dP_{cg}}{dt} = J_{10} + J_{11} - J_{12}$$

$$J_{16} = k_{f,16} \times IP3$$

$$\frac{dIP3}{dt} = \left(J_{14} + J_{15} \right) \times C_{pc} - J_{16}$$

$$\frac{dCa}{dt} = C_{pc} \times -1 \times \left(J_8 + J_{11} \right)$$

IP_3 Receptor

Parameters	Description	Units	Value
$\mathbf{k_{f,1}}$	R1 forward rate constant	$\mu M^{-1}ms^{-1}$	27.7325
$\mathbf{k_{d,1}}$	R1 dissociation constant	ms^{-1}	1.5786
$\mathbf{k_{f,2}}$	R2 forward rate constant	$\mu M^{-1}ms^{-1}$	0.9530
$\mathbf{k_{d,2}}$	R2 dissociation constant	ms^{-1}	0.1047
$\mathbf{k_{f,3}}$	R3 forward rate constant	$\mu M^{-1}ms^{-1}$	0.009331
$\mathbf{k_{d,3}}$	R3 reverse rate constant	ms^{-1}	0.0005794
$\mathbf{k_{f,4}}$	R4 forward rate constant	$\mu M^{-1}ms^{-1}$	0.001424
$\mathbf{k_{d,4}}$	R4 dissociation constant	ms^{-1}	1.1972
$\mathbf{k_{f,5}}$	R5 forward rate constant	$\mu M^{-1}ms^{-1}$	0.2099
$\mathbf{k_{d,5}}$	R5 dissociation constant	ms^{-1}	2.1135
$\mathbf{k_{f,6}}$	R6 forward rate constant	$\mu M^{-1}ms^{-1}$	11.5643
$\mathbf{k_{d,6}}$	R6 dissociation constant	ms^{-1}	7.0688

$$\frac{dO}{dt} = RI \times Ca \times k_{f,1} - O \times k_{d,1}$$

$$\frac{dRI}{dt} = \left(O \times k_{\mathrm{d},1} + R \times IP3 \times k_{f,2} \right) - RI \times \left(Ca \times k_{f,1} + k_{d,2} \right)$$

$$\frac{dR}{dt} = \left(RI \times k_{\mathrm{d},2} + RC \times k_{d,3} \right) - R \times \left(IP3 \times k_{f,2} + Ca \times k_{\mathrm{f},3} \right)$$

$$\frac{dRC}{dt} = \left(R \times Ca \times k_{\mathrm{f},3} + RC2 \times k_{d,4} \right) - RC \times \left(k_{\mathrm{d},3} + Ca \times k_{\mathrm{f},4} \right)$$

$$\frac{dRC2}{dt} = \left(R \times Ca \times k_{\mathrm{f},4} + RC3 \times k_{d,5} \right) - RC2 \times \left(k_{\mathrm{d},4} + Ca \times k_{\mathrm{f},5} \right)$$

$$\frac{dRC3}{dt} = \left(RC2 \times Ca \times k_{\mathrm{f},5} + RC4 \times k_{d,6} \right) - RC3 \times \left(k_{\mathrm{d},5} + Ca \times k_{\mathrm{f},6} \right)$$